

**A Search for Galaxy Clusters Using
the Sunyaev-Zel'dovich Effect**

Thesis by
Marcus C. Runyan

In Partial Fulfillment of the Requirements
for the Degree of
Doctor of Philosophy

California Institute of Technology
Pasadena, California

2002

(Submitted December 20, 2002)

© 2002

Marcus C. Runyan

All Rights Reserved

Abstract

This thesis describes the instrumental design and observations with the Arcminute Cosmology Bolometer Array Receiver (ACBAR). We have used ACBAR to make very sensitive, high resolution maps of the Cosmic Microwave Background (CMB) and have searched within these maps for previously unknown massive clusters of galaxies through the Sunyaev-Zel'dovich effect. ACBAR is a 16-pixel, millimeter-wave, 240 mK bolometer array that is configurable to observe simultaneously at 150, 220, 280, and 350 GHz. The receiver observes from the 2m Viper telescope at the South Pole from which it has beam sizes of $\sim 4 - 5'$ at all frequencies. We have taken advantage of improvements in bolometric detector technology and the superb observing conditions at the South Pole to image the microwave sky at multiple millimeter wavelengths. Here we present the results of observing $\sim 20 \text{ deg}^2$ for 16 weeks in 2002. These represent the deepest CMB observations to date with a sensitivity of $\sim 5 \mu\text{K}$ per $5'$ beam at 150 GHz in the deepest part of the map. We present the results from 150 GHz and employ an optimal filter to remove the primary CMB. We detect no clusters above $4\times$ the post-filter map RMS in the most sensitive 10 deg^2 of the maps. We perform a Monte Carlo simulation to determine the cluster detection efficiency of the survey using the measured noise covariance and realizations of the CMB. We use the results of the simulation to estimate the expected cluster yield of the survey as a function of cosmological parameters. The non-detection of clusters allows us to place a 2σ upper limit upon the variance of the smoothed density field of $\sigma_8 < 1.10 (\Omega_M/0.3)^{-0.23}$ in a flat- Λ CDM concordance cosmology.

Acknowledgments

Countless people have contributed to my graduate education and the success of ACBAR. I owe a debt of gratitude of Andrew Lange for hiring me – even though my “references” were less than perfect – as well as teaching me the most valuable skill I have learned in graduate school: networking. Thanks for getting me involved in a great thesis project while it was still on the drawing board. The co-PIs of ACBAR have lead by example. Bill Holzapfel is a tireless lab god that can make just about anything work by force of will. John Ruhl comes up with brilliant solutions to problems and is a shockingly nice person (a trait not common in our field). Another person critical to my graduate career was Kathy Deniston, who worked behind the scenes but kept me out of trouble and always got what needed to be done, done.

Many other people worked hard to make ACBAR a success. “The Boys of ACBAR” Mike Daub, Jon Goldstein, and Chao-lin Kuo: ACBAR would not have happened without you and it has been a pleasure working with you. Jeff Peterson was responsible for overseeing the construction of the fine Viper telescope. Bob Pernic and the rest of polar support kept things running smoothly at the Pole. Eric Torbet, Jon Leong, and Georges Sirbi all contributed their expertise. A huge thanks to Jamie Bock for providing the bolometers and for being a terrific officemate. Thanks to Carole and Vic for getting filters to us when we needed them most. Thanks to Joe Mohr for providing the cluster simulations that feature prominently in this thesis. The CMU crew of Kathy Romer, Percy Gomez, and Chris Cantalupo lent me their valuable expertise on galaxy clusters. ACBAR was largely built by the machine shops at UCB, UCSB, and Caltech, and I would especially like to thank Rick, Terry, Ricardo, and Armando. Thanks to Giles Novak for giving up his time on the telescope so that we could collect what ended up forming the bulk of my thesis data. And a huge thanks to our intrepid winter over for 2001 and 2002, Matt Newcomb.

There are many people around the Lange lab that made coming to work easy. Thanks to Byron Holmes Philhour for being the nicest person I know and for “stepping aside.” What little conscience I have, I owe to discussions with him. Thanks to Brendan Crill for being a lab badass and for measuring the geometry of the Universe. Thanks to Pete Mao for sharing my interest in cars and always being up for FMC. Thanks for Phil Mauskopf for teaching me CodeV and leaving used gym clothes in what was to become my desk. Thanks to Sarah Church for convincing Andrew to hire me and for teaching me about filtering and the value of maintaining good interpersonal relationships. Thanks to Eric Hivon and Ken Ganga for countless discussions of noise covariance and the CMB. Thanks to Viktor Hristov for helping me out with electronics and for teaching the world that the alligator is more green than long.

Thanks to Bill Jones for being a great lab amigo, getting me into running, and showing me a truly great haircut. I still can’t tell you what “the god damn hold-up” is. Thanks to Jing Xu for being the coolest person I know, teaching me about lock-in amplifiers, and “storing” my QM book for five years. Thanks to Sam Edgington for being a swell officemate and supporting my caffeine addiction. Thanks to pimp Kiwon Reginald Yoon for not putting meat on my BBQ and getting me into Korean soccer. Thanks to Cindy Hunt (who is all class!) for having good taste and for not stinking after consuming dairy products. Thanks to Christian Reichardt for taking over for me; I’m sure you’ll find ACBAR a fun project to

work on. Thanks to Sunil Golwala for being a dedicated badass and for knowing the answer to every question I asked.

A few brave souls met the challenge of reading this thesis in its entirety. The quality of this tome was vastly improved by their efforts. In particular, Andrew Lange, Kathy Romer, Byron, Brendan, Cindy The Great, Andrew Benson, and Christian had incredibly useful comments and suggestions. I was fortunate to receive the support of a NASA Graduate Student Researchers Fellowship during much of this research.

Thanks to the shepherd who first noticed his goats went berserk after eating coffee beans and to the Starbucks baristas (especially the ones who gave me free coffee) for crafting the finest caramel macchiatos in town. Thanks to the city of Woodland Hills (south of The Boulevard, at least) for being a tranquil oasis in this synthetic land of car chases and celebrities. I would especially like to thank Barbara Lundy for not understanding the concept of “buy low, sell high.” I must tearfully acknowledge the companionship of the finest cats in the world, Vixen and Scampi, who were always glad to see me when I got home at o’dark-thirty and will be sorely missed. Thanks to the fake meat chinese (FMC) restaurant Vegetarian Delight for making the best food I’ve ever had; please move back from Taiwan.

Many people outside of work have had a strong influence on my life and career. Thanks to my mom for not sending me to “the home for wayward bozos,” saving me from getting expelled from high school, and always supporting me. Thanks to my dad for giving me a telescope when I was young and largely fueling my interest in science. Thanks to Jon for turning into a really great brother and for understanding why I’m going to lose The Bet. Thanks to Dave Denny for being a great friend since high school, for getting me into triathlon, and for explaining how sunlight reflects off police car lights. Thanks to Suzi Clarke for being a great mother-in-law and for the care packages to the pole. Thanks to Dan Clarke for putting me up while we were putting ACBAR together and for keeping up the pressure with the graduation bet; I will enjoy the dinner. To properly thank Kelly would require more pages than this entire thesis. So to you I’ll simply say: Thanks for everything!

Contents

Abstract	iii
Acknowledgments	iv
1 Introduction	1
1.1 Motivation	1
1.2 CMB Power Spectrum	2
1.3 The Sunyaev-Zel'dovich Effect	7
1.4 Surveying for Galaxy Clusters	11
1.4.1 Clusters as Cosmological Probes	12
1.4.2 SZ Cluster Surveys	20
1.4.3 Confusion	22
1.5 Previous Work	23
2 The ACBAR Instrument	25
2.1 Optics	25
2.1.1 Scalar Feeds	25
2.1.2 Feed Structure	29
2.1.3 Filtering	31
2.1.4 Detectors	39
2.1.5 Telescope Optics	42
2.2 Cryogenics	49
2.2.1 Dewar	49
2.2.2 Fridge	51
2.2.3 Thermal Isolation and Heat Sinking	55
2.2.4 Thermometry	58
2.3 Electronics	58
2.3.1 Signal Electronics	58
2.3.2 Microphonic Response	61
2.3.3 Computer Control and Housekeeping	62
3 Observations and Performance	63
3.1 The South Pole Environment	63
3.2 Observational Parameters	63
3.2.1 Chopper Functions	64
3.2.2 Beam Sizes	67
3.2.3 Chopper Synchronous Offsets	74
3.2.4 Snow	77
3.2.5 Optical Loading	78
3.2.6 Scan Strategies	81
3.2.7 Field Selection	82
3.3 Calibration	84
3.3.1 Planetary Observations	84

3.3.2	Atmospheric Opacity	85
3.3.3	Responsivity	86
3.3.4	Galactic Source Cross-Calibration	87
3.3.5	Calibration Procedure	88
3.3.6	Calibration Stability	89
3.4	Noise and Sensitivity	91
3.4.1	Photon Noise	94
3.4.2	Detector and Electronics Noise	95
4	Signal Processing	99
4.1	Time Domain Filtering	99
4.2	Spike Removal	103
4.3	Map Binning	105
4.4	Offset Removal	106
4.5	Data Cuts	109
4.6	Coadding Maps	110
5	Data Analysis	119
5.1	Jackknife Tests	119
5.2	Source Extraction	124
5.2.1	Optimal Filtering	124
5.2.2	Noise Power Spectrum Estimation	126
5.2.3	Cluster Sizes	130
5.2.4	Application of Optimal Filters	134
5.3	False Detection Rate	141
5.4	Bias and Detection Efficiency	148
5.4.1	Cluster Realizations	149
5.4.2	Bias	150
5.4.3	Average Signal-to-Noise Ratio	152
5.4.4	Cluster Detection Efficiency	154
5.4.5	Expected Cluster Yield	155
5.5	Results	159
5.5.1	Source Catalog	159
5.5.2	Comparison with Expectations	164
6	Other ACBAR Science	168
6.1	CMB Power Spectrum	168
6.2	Pointed Cluster Observations	169
7	Conclusions and Future Prospects	171
A	Bolometer Parameters	174
A.1	Load Curve Analysis	174
A.2	Bolometer Optimization	179
B	Atmosphere	182
B.1	Spectrum	182
B.2	Skydip Analysis	184

C Optics	190
C.1 Gaussian Telescope Optics	190
C.2 Viper Telescope and Tertiary Redesign	192
D Transfer Functions	195
D.1 Introduction	195
D.2 Filters	195
D.3 Transfer Function Measurement	198
D.4 Effects of Transfer Function	202
E CMB Realizations	206
E.1 Correlation Function Method	206
E.2 FFT Method	208
Bibliography	211

List of Figures

1.1	Model CMB Power Spectra	5
1.2	CMB Power Spectrum Measured by ACBAR	8
1.3	Intensity Spectra of the SZ Effects	9
1.4	Angular Diameter Distance and Comoving Volume Element	14
1.5	Evolution of σ_8	17
1.6	Differential and Integrated Number Counts of Massive Clusters	19
1.7	Integrated Number Counts for Varying σ_8	20
1.8	Number Counts versus Limiting Cluster Mass	21
2.1	Photos of ACBAR Feed Arrays for 2001 and 2002	26
2.2	150 GHz Corrugated Feed Detail	26
2.3	Beams Measured from Dewar	28
2.4	Overview of 150 GHz Feed Structure	30
2.5	Atmospheric Transmission and Measured Spectral Bands	32
2.6	Zenith Brightness Temperature	32
2.7	SZ Spectra and Measured Bands	33
2.8	Warm Filter Optics Arrangement	36
2.9	Photo of Microlithographed Spider-Web Bolometer	40
2.10	Load Curves for D-row (150 GHz)	43
2.11	Load Curves for B-row (150 GHz)	44
2.12	Load Curves for C-row (220 GHz)	45
2.13	Load Curves for A-row (280 GHz)	46
2.14	Photo of Viper Telescope	46
2.15	Telescope Optics Arrangement	47
2.16	Cryostat	50
2.17	$^4\text{He}/^3\text{He}/^3\text{He}$ Sorption Fridge	52
2.18	Fridge Cycle Temperatures	53
2.19	Fridge Load Curves	54
2.20	Baseplate Temperature Stability	55
2.21	Skydip Baseplate Temperature Stability	56
2.22	Photo of Focal Plane Structure	56
2.23	Signal Electronics	59
2.24	PCB Module	60
3.1	Chopper Voltage Offset for 2001	65
3.2	Chopper Gain Fluctuations for 2001	66
3.3	Raster Map of Mars in 2001	69
3.4	Raster Map of Venus in 2002	70
3.5	Changing Chopper Offsets	75
3.6	Effect of Baffle upon Chopper Offsets	76
3.7	Average RJ Temperature Loading	79
3.8	Optical Loading versus Atmospheric Opacity	80
3.9	Chop Sky Coverage	81

3.10	Dust Map and CMB Fields	83
3.11	Raster Map of RCW38	88
3.12	Detector Responsivity versus Temperature and Zenith Angle	89
3.13	Calibrator Signal versus Time	90
3.14	Calibrator Signal versus Optical Loading	92
3.15	Integrated 150 GHz RCW38 Signal versus Time	93
3.16	Ratio of Integrated RCW38 Signals	93
3.17	Electronics Noise PSD	97
3.18	Calibrated Telescope <i>NET</i> at 150 GHz	98
4.1	Data Processing Flow Chart	99
4.2	Model Scan PSD	101
4.3	Blackman Windowed Sinc Filter	102
4.4	Comparison of Filter Kernels	103
4.5	Cosmic Ray	104
4.6	CMB Field Offset Removal	108
4.7	Masked Offset Removal	109
4.8	Integrated RCW38 Signal versus Offset RMS	111
4.9	Offset RMS versus CMB5 Observation	112
4.10	Quasar Position Offsets	113
4.11	Coadded CMB5 MAIN Field with Quasar	115
4.12	Coadded CMB5 MAIN Field without Quasar	116
4.13	CMB5 Sky Coverage at 150 GHz	117
5.1	CMB5 LEAD Field Jackknife	120
5.2	CMB5 MAIN Field Jackknife	121
5.3	CMB5 TRAIL Field Jackknife	122
5.4	Multi-frequency Jackknife	123
5.5	Noise Correlation Function	128
5.6	Measured and Model Power Spectra	131
5.7	Cluster Mass and Core Radius versus Convolved ΔT	133
5.8	Convolved FWHM versus Core Radius	135
5.9	Optimal Filter with Measured and Model Power Spectra	136
5.10	Filtered Map RMS versus Beam FWHM	137
5.11	Fourier Space Optimal Filter versus Core Radius	138
5.12	Filtered Map RMS versus Integration Time	140
5.13	Real Space Optimal Filter	140
5.14	CMB5 Filtered with $r_c = 0'$ Optimal Filter	142
5.15	CMB5 Filtered with $r_c = 0.4'$ Optimal Filter	143
5.16	CMB5 Filtered with $r_c = 0.7'$ Optimal Filter	144
5.17	CMB5 Filtered with $r_c = 1.0'$ Optimal Filter	145
5.18	Efficacy of Optimal Filter	146
5.19	False Detection Rate	147
5.20	Bias of Optimal Filter	150
5.21	S/N Ratio for “Incorrect” Core Radii	151
5.22	S/N versus Integrated Cluster Flux	153
5.23	S/N versus Central Comptonization	153
5.24	S/N versus Convolved Cluster Decrement	155

5.25	Detection Efficiency with 4σ Threshold	156
5.26	Detection Efficiency with 3σ Threshold	156
5.27	Cluster Mass versus In-Beam Flux for Λ CDM Simulations	157
5.28	Expected Cluster Redshift Distribution	160
5.29	Expected Survey Yield and Probability of Zero Detections versus σ_8	165
5.30	Probability of Zero Detections on σ_8 - Ω_M Plane	166
6.1	CMB Removed SZ Image of A3266	170
A.1	Contributions to Total NEP	180
A.2	Minimum NEP versus Thermal Conductivity	181
B.1	Model Atmospheric Transmission	183
B.2	FET Offset Comparison	186
B.3	Measured Skydips	187
B.4	Measured In-Band Opacity versus $350\ \mu\text{m}$ Tipper	188
B.5	Histogram of Effective 150 GHz Opacity During 2001	189
C.1	Viper Telescope Optics	193
D.1	VXI Transfer Function and Aliasing	199
D.2	Cumulative Transfer Function	200
D.3	Detector Transfer Function Fit	203
D.4	Impulse Response	204
D.5	Beam Smearing Effects of Transfer Function	205
E.1	CMB Simulations	209

List of Tables

2.1	Feed Geometry and Beam Widths	29
2.2	Filters	36
2.3	Measured Optical, Electrical, and Thermal Bolometer Properties	38
2.4	Thick Grill Results for 2001	39
3.1	Galactic Source Coordinates	64
3.2	Beam Sizes for 2001	68
3.3	Beam Sizes for 2002	68
3.4	Estimated Loading Contributions	78
3.5	CMB Field Central Point Sources	83
3.6	Bootstrapped Flux of RCW38	88
3.7	Estimated Photon Noise	95
3.8	Noise Budget	96
5.1	CMB5 Jackknife RMS	119
5.2	Filtered Map RMS versus Core Radius	139
5.3	Map RMS versus Core Radius	141
5.4	Average In-beam Cluster Fluxes Yielding 3 and 4 σ Detections	155
5.5	Detection Efficiency Function Parameters	158
5.6	Catalog of Candidate Decrement Sources in CMB5	162
5.7	Catalog of Candidate Increment Sources in CMB5	163
5.8	Expected versus Detected Source Counts	164
B.1	Liner Fit Parameters for Opacity versus $\tau_{350\mu\text{m}}$ for 2001	188
B.2	Liner Fit Parameters for Opacity versus $\tau_{350\mu\text{m}}$ for 2002	189

Chapter 1 Introduction

1.1 Motivation

Cosmology is concerned with understanding the composition, structure, and evolution of our Universe. By this we mean cosmology attempts to answer the following questions: What types of matter and energy populate the Universe and how are they distributed? How has the geometry of the Universe evolved with time? How did the Universe transition from a reasonably smooth distribution to the complex structures that we observe today?

Until recently, cosmology was a theorist's playground in which the boundaries from observational data extended to virtually any model of the Universe that predicted a microwave background, nucleosynthesis, and the existence of large-scale structure. However, cosmology has made the transition from a data-starved science to one of precision measurement. We are carving away vast regions of parameter space to leave just a few cosmological models with reasonably well constrained parameters.

Unlike most of the sciences, cosmology is an observational (rather than experimental) science; our interaction with the Universe is one-sided. Everything we learn about the Universe is limited to what we can *observe*. We cannot put the Universe in a test tube and shoot particles at it or mix it with chemicals and see what happens. We also have only one universe to investigate which makes a statistical study of the laws of Nature that govern the Universe as a whole all but impossible. Because of this, we need to exploit every available piece of observational information to expand our understanding. Observations of the Universe cover photon energies spanning roughly ten orders of magnitude and include phenomena as diverse as black holes and the Big Bang. What is remarkable is that these disparate observations are beginning to reveal a coherent picture of the Universe. It is likely that cosmology will soon make the transition to a science that is not only precise but accurate as well [85].

In the spirit of constraining cosmological parameters through complementary observations, we have embarked on a program to survey for clusters of galaxies using the Sunyaev-Zel'dovich (SZ) effect as well as to measure the angular power spectrum of primary

anisotropies of the Cosmic Microwave Background (CMB). This thesis will be concerned mainly with surveying for clusters of galaxies as probes the growth of structure and evolution of the cosmological volume element. However, our ability to find clusters with the SZ effect is, as we shall see, intimately tied to the distribution of CMB anisotropies. Although the CMB power spectrum is not the main topic of this thesis, it was the driving science goal behind the Arcminute Cosmology Bolometer Array Receiver (ACBAR) and so we discuss it first.

The remainder of Chapter 1 will discuss the scientific rationale behind ACBAR as well as establish the cluster abundance formalism that we will use to constrain cosmological parameters within the modern picture of adiabatic density perturbations in a Cold Dark Matter (CDM) framework. The instrumental design of ACBAR is presented in detail in Chapter 2. Chapter 3 describes the CMB observations made at the South Pole in 2001 and 2002 as well as the performance of the instrument. Chapter 4 details the processing of the raw data and 5 details the development of our cluster detection methodology. We also report the results of the cluster survey in Chapter 5 and place these results in the context of a Λ CDM cosmology. We discuss other science from ACBAR in Chapter 6 and present our conclusions and future prospects for SZ cluster surveys in Chapter 7. We include appendices on the analysis of bolometer load curves and sky dips, re-design of telescope optics, transfer functions, and the generation of CMB realizations at the end of this thesis.

1.2 CMB Power Spectrum

The Cosmic Microwave Background (CMB) is the sea of thermal photons left over from the hot ionized plasma of the early Universe. The spectrum of the CMB is very well fit by a blackbody of temperature 2.73 K and peaks at millimeter wavelengths [74]. We believe that shortly after our Universe emerged in the Big Bang, the energy field formed elementary particles, such as photons and electrons, in a tightly bound plasma. These were not distributed uniformly, but instead conformed to the primordial density perturbation field. Although the temperature of the Universe was too hot for the photons and charged baryons to decouple, the weakly interacting dark matter had no such pressure support and collapsed into the overdensities to enhance the potential wells.

The other charged particles were gravitationally attracted to these potential wells but the

photon pressure prevented their collapse. This induced acoustic oscillations in the photon-baryon plasma until about $z \sim 1100$ when the Universe expanded and cooled enough that the electrons were able to bind to the baryons (the so-called “epoch of re-combination”), thus decoupling from the photons. The baryons then settled into the dark matter potential wells to form gravitationally bound structures and the photons free-streamed from this “surface of last scattering” and cooled with the expanding Universe to form the CMB we observe today.

The CMB is a snapshot of the Universe when it was only about 300,000 years old and encodes much information about the temperature and distribution of matter at that epoch. With sensitive instruments we can measure the tiny variations in CMB temperature from one point on the celestial sphere to the next. If we define the temperature of the sky in the direction $\hat{\theta}$ as $T(\theta, \phi)$, we can decompose the temperature field into a spherical harmonic expansion as

$$T(\theta, \phi) = \sum_{\ell m} a_{\ell m} B_{\ell} Y_{\ell m}(\theta, \phi),$$

where the $Y_{\ell m}(\theta, \phi)$ are the spherical harmonics and $B_{\ell} = e^{-\ell(\ell+1)\sigma^2}$ is the window function for a Gaussian beam of width σ . The angular power spectrum is then defined as

$$C_{\ell} = \langle a_{\ell m} a_{\ell m}^* \rangle = \frac{1}{2\ell + 1} \sum_{m=-\ell}^{\ell} |a_{\ell m}|^2.$$

In the equations above, ℓ is the order of Legendre polynomials; smaller values of ℓ correspond to larger spatial scales on the sky. The C_0 term is the monopole and set by the average temperature measured by the FIRAS instrument on COBE to be 2.73 K [74]. The dipole term ($\ell = 1$) is dominated by the motion of the earth with respect to the CMB rest frame caused by our motion about the sun, the sun’s motion about the Milky Way, and the Milky Way’s motion towards what has been termed “The Great Attractor” in the direction of the constellation Leo. What is usually referred to as the CMB power spectrum is the set of C_{ℓ} ’s starting with $\ell = 2$.

The shape of the CMB power spectrum encodes the distribution of density perturbations as a function of angular scale. The primordial density field may have originated from the quantum fluctuations in the Big Bang which were amplified by inflation and processed by the oscillations in the plasma of the early Universe. If the age of the Universe at photon-baryon

decoupling is denoted t_{dec} , then regions larger than ct_{dec} (the horizon size at decoupling) cannot have causally interacted since inflation. Scales smaller than the horizon have had sufficient time to interact and the peaks and troughs in the power spectrum reflect the state of the acoustic oscillations in the plasma at decoupling. However, we also measure anisotropy in the CMB on scales larger than the horizon size and believe these fluctuations originate from the period before inflation.

One should note that the peaks in the power spectrum are anisotropy *power* and thus correspond to both compression and rarefaction peaks in the distribution. The first peak in the power spectrum at $\ell \sim 220$ corresponds to the physical scale that has just had time to compress once; objects of this size subtend an angle of roughly one degree on the sky. The second peak has collapsed and rarefied to maximum expansion at decoupling.

The different cosmological parameters affect the predicted power spectrum in different ways. For example, the total density of matter and energy (Ω_{total}) determines the angular size of fluctuations on the sky by setting the angular diameter distance to the surface of last scattering as well as the horizon size at decoupling. A larger (smaller) value of Ω_{total} shifts the power spectrum to larger (smaller) angular scale. The density of baryons affects the depth of gravitational potential wells, thus enhancing the amplitude of compression peaks while reducing rarefaction peaks. An interesting feature of these power spectra is that different sets of cosmological parameters can produce virtually identical power spectra. These parameter degeneracies can be broken by complementary measurements such as those described in the next section. Model power spectra generated with CMBFAST¹ [102] for three different cosmologies (Λ CDM, SCDM, OCDM) are shown in Figure 1.1.

The epoch of re-combination was not instantaneous and so the surface of last scattering has a finite thickness. The thickness is determined by the photon diffusion distance near decoupling which is proportional to $\Omega_M^{-1/2}h^{-1}$ [65]. Fluctuations that are small compared to this thickness (corresponding to a few arcminutes) will be averaged out as one looks through the surface. This smoothing results in the damping tail of the CMB power spectrum at $\ell \gtrsim 1000$. The steepness of the damping tail is also shaped by the spectral index of the primordial perturbation spectrum which has led to the term “tilt” meaning a non-flat primordial spectrum. The existence of the damping tail was recently measured by the Cosmic Background Imager experiment [83] and is in good agreement with the predictions

¹Available from <http://www.physics.nyu.edu/matiasz/CMBFAST/cmbfast.html>

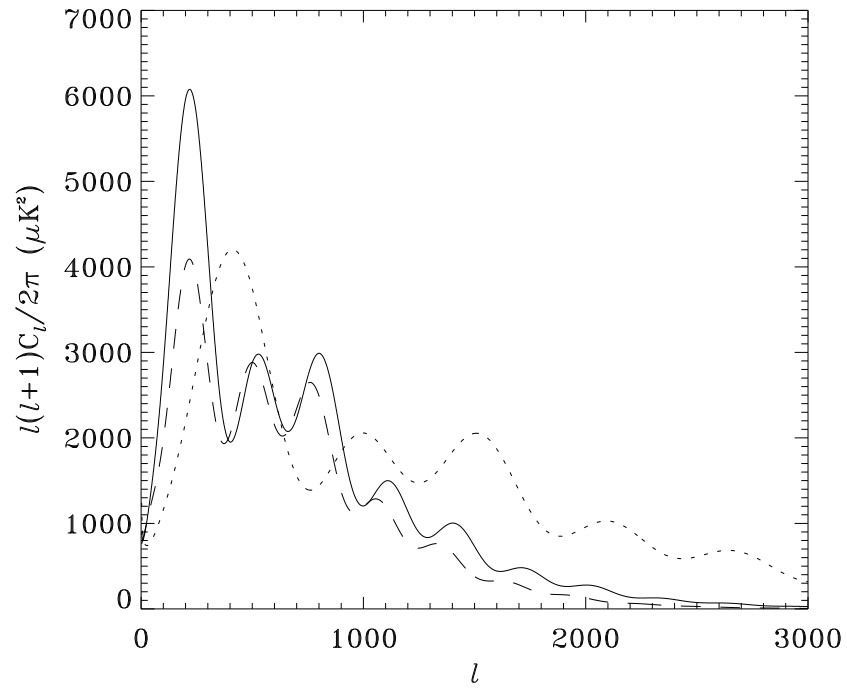


Figure 1.1: Shows the model CMB power spectrum for three different cosmologies: Λ CDM (solid line, $\Omega_M = 0.3$, $\Omega_\Lambda = 0.7$, $h = 0.7$), SCDM (dashed line, $\Omega_M = 1$, $\Omega_\Lambda = 0$, $h = 0.5$), and OCDM ($\Omega_M = 0.3$, $\Omega_\Lambda = 0$, $h = 0.7$). All models assume $\Omega_B h^2 = 0.021$, $n = 1$, and no reionization.

of the Λ CDM cosmology in which $\sim 70\%$ of the energy density of the Universe is in the form of a mysterious “Dark Energy”, $\sim 25\%$ in non-baryonic cold dark matter, and $\sim 5\%$ in ordinary baryonic matter.

At $\ell \gtrsim 2000$ – and frequencies far from 218 GHz – the primary CMB power spectrum is expected to be dominated by an unresolved background of secondary CMB anisotropies from the Sunyaev-Zel’dovich (SZ) effect in clusters of galaxies [46]. The SZ effect will be discussed in the next section and recent results from the CBI [15] and BIMA [23] suggest that this high- ℓ power may have been detected. A conclusive measurement of this SZ power spectrum will require measuring the high- ℓ power spectrum at multiple frequencies – including ~ 218 GHz where the clusters should not contribute significantly – to separate the primary from the secondary CMB anisotropies. The amplitude of the SZ power spectrum is expected to scale very strongly with the normalization of the matter power spectrum (σ_8^7) [15].

There are simply too many CMB mapping experiments to list, but a few Web sites have compiled all of the available data to illustrate the state of the field of CMB power spectrum measurement². It should be noted that most of the recent experiments have focused on the large to moderate angular scales ($\ell < 1000$) where the CMB is believed to have the most power. Experiments such as Boomerang, MAXIMA, DASI, and Archeops have done a remarkable job of measuring the position and amplitude of the first few peaks in the power spectrum and have placed very tight limits on most of the cosmological parameters. However, the sensitivity of these large beam experiments falls off rapidly for $\ell \gtrsim 1000$. Only a handful of experiments have attempted to measure the CMB power spectrum on smaller angular scales: SuZIE placed an upper limit around $\ell \sim 2500$ [19], OVRO placed an upper limit at $\ell \sim 2000$ [94], BIMA detected power at $\ell \sim 7000$ [23], and CBI definitively detected the damping tail [72]. It is this region of the power spectrum that ACBAR was designed to measure with high precision.

In Figure 1.2 we show the state of the observed CMB power spectrum as measured by a selection of instruments. This figure incorporates the data from stratospheric balloon instruments ARCHEOPS [7], Boomerang [101], and MAXIMA [42] as well as ground-based experiments CBI [72], DASI [91], VSA [105], and ACBAR [59]. One can see from the figure that ACBAR has measured the CMB damping tail across a wide range of angular scales

²<http://background.uchicago.edu/~whu>, <http://www.hep.upenn.edu/~max/cmb/experiments.html>

with good precision.

1.3 The Sunyaev-Zel'dovich Effect

The Sunyaev-Zel'dovich (SZ) effect is the scattering of CMB photons from energetic electrons in the shock-heated, gravitationally bound plasma in clusters of galaxies [107, 10]. Low energy CMB photons travel from the (in this case, misnamed) surface of last scattering and are boosted in energy by the few keV thermal electrons via Thomson scattering. The probability of scattering depends on the electron density of the cluster and is of order 1% for any given photon. This is the *thermal* SZ effect and it results in unique spectral distortion to the CMB intensity spectrum (see Figure 1.3). The CMB thus acts as a backlight to the cluster, which appears as a cold patch at frequencies below ~ 218 GHz and a hot patch above ~ 218 GHz.

The temperature spectrum of the thermal SZ effect is given by

$$\frac{\Delta T_{thermal}}{T_{CMB}} = y f(x) = f(x) \int d\ell \frac{kT_e}{m_e c^2} n_e(\ell) \sigma_T,$$

where the integral is along the line of sight through the cluster, y is referred to as the Compton y -parameter and is proportional to the integrated electron pressure in the cluster, k is Boltzmann's constant, T_e is the electron temperature, m_e is the mass of an electron, c is the speed of light, n_e is the electron number density profile, and σ_T is the Thomson scattering cross-section. The factor $f(x)$ encodes the frequency dependence and is given by

$$f(x) = x \frac{e^x + 1}{e^x - 1} - 4,$$

where $x = h\nu/kT_{CMB}$ and we have neglected higher order relativistic corrections (see, for example, Itoh 1998).

The thermal SZ effect spectrum can be re-written in terms of specific intensity to give

$$\Delta I_{SZ} = \frac{dB(T_{CMB})}{dT} \Delta T_{SZ} = I_0 g(x) y,$$

where $B(T)$ is the Planck blackbody equation, T_{CMB} is the temperature of the CMB,

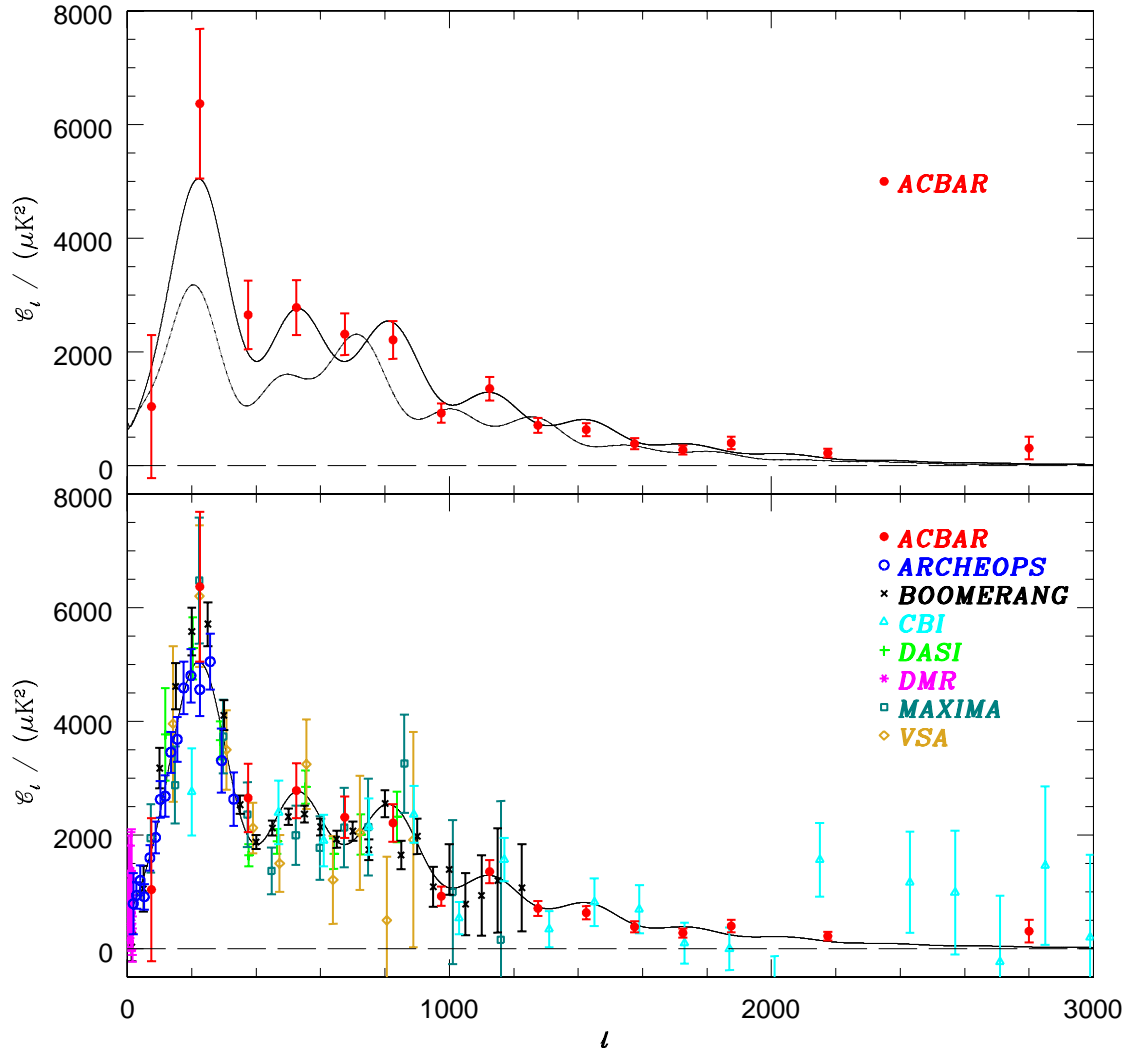


Figure 1.2: The upper panel shows the power spectrum measured by ACBAR with two model power spectra. The solid line is a Λ CDM model and the dotted line is an SCDM model. The ACBAR data points are uncorrelated. The lower panel compares the ACBAR results to the power spectrum measured by previous bolometric and interferometric instruments. The solid line is a flat- Λ CDM cosmology. The figure is taken from the ACBAR cosmological parameter paper of Goldstein et al. (2002).

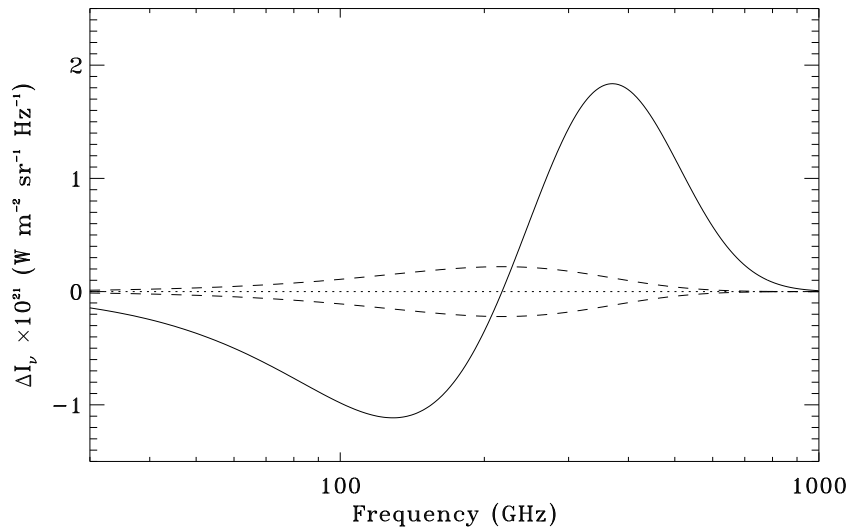


Figure 1.3: Intensity spectrum of both the thermal (solid) and kinetic (dashed) Sunyaev-Zel'dovich effects for a massive cluster of galaxies. The model cluster is characterized by a central comptonization of $y = 10^{-4}$, an optical depth of $\tau = 0.01$, and peculiar velocity of ± 500 km/s.

$I_0 = 2(kT_{CMB})^3/(hc)^2$, and

$$g(x) = \frac{x^4 e^x}{(e^x - 1)^2} f(x).$$

The SZ intensity spectrum is plotted in Figure 1.3 for a cluster with $y = 10^{-4}$ which is typical for massive clusters.

There is a second SZ effect due to the bulk motion of a cluster with respect to the CMB rest frame. This *kinetic* SZ effect acts like a Doppler shift and the sign of the distortion depends on the direction of the peculiar velocity with respect to the line of sight. The temperature spectrum of the kinetic effect (ignoring relativistic corrections) is given by

$$\frac{\Delta T_{kinetic}}{T_{CMB}} = -\tau \left(\frac{\vec{v}_{pec} \cdot \hat{r}}{c} \right),$$

where τ is the optical depth of electrons, $\vec{v}_{pec} \cdot \hat{r}$ is the component of the peculiar velocity along the line of sight, and the negative sign indicates that a cluster moving away from us will cause a decrement. The kinetic effect is also shown in Figure 1.3 and one can see that the optimum frequency band to observe the kinetic effect is near the thermal null at ~ 218 GHz, thus reducing contamination from the thermal signal.

In addition to thermal effect contamination, the kinetic effect has the unfortunate fea-

ture of an intensity spectrum identical to the CMB. This means that CMB fluctuations cannot be distinguished from kinetic SZ emission. This suggests that small beam sizes are advantageous when trying to measure the kinetic effect because this will reduce the amount of primary CMB confusion. The amplitude of the kinetic SZ signal is also quite small and has not been conclusively detected as of the time of this writing. The strongest upper limits on cluster peculiar velocities from the kinetic effect come from the SuZIE instrument which observes from Mauna Kea and suffers from atmospheric noise contamination [49]. The latest incarnation of SuZIE employs multi-frequency photometers that enable thorough atmospheric removal and may permit significant detections of cluster peculiar velocities.

It is important to note that the SZ effect is not really an emission mechanism but a scattering processes that preserves photon number. The SZ effect results in a fractional change in the surface brightness of the CMB by boosting photons to higher energy. Although the photons we observe from a cluster at redshift z interacted with the intra-cluster plasma when the Universe was $(1+z)$ hotter, those photons have undergone the same $(1+z)^{-1}$ redshift as the rest of the CMB as the Universe expanded. The SZ surface brightness inherits the remarkable property of redshift independence from the CMB; a specific cluster (fixed temperature and electron density) will have the same surface brightness independent of its redshift of observation. The total flux from a cluster will, however, depend upon redshift through the angular diameter distance relation. As will be shown below, the angular size of a cluster of fixed proper dimension is expected to initially fall off but will eventually flatten out and even increase at $z > 2$ in currently acceptable cosmologies.

It is the redshift independence of surface brightness that makes the SZ effect such a powerful cosmological probe. One of the most powerful uses of the SZ effect is as a cosmological distance measure without the use of standard candles (such as Cepheid variables). The SZ signal is proportional to the integrated column depth of the electron pressure, $\int n_e T_e dl$. This can be combined with both X-ray surface brightness observations, which are proportional to the integral of the electron density squared, $\int n_e^2 T_e^{1/2} dl$, and X-ray spectra which give the temperature of the intra-cluster electrons, T_e . By eliminating the electron density and temperature one obtains a measurement of the depth of a cluster. If the assumption of spherical symmetry is valid, one can assume the proper width of the cluster is the same as the depth and use the angular diameter distance relation to determine the Hubble constant,

H_0 [71, 95]. With sufficient cluster statistics to reduce cluster orientation bias, the cluster derived angular diameter distance relationship at high redshift can be used to measure the matter and vacuum energy densities (Ω_M and Ω_Λ , respectively).

We can integrate the thermal SZ surface brightness of a cluster over solid angle using $d\Omega = dA/d_A^2(z)$ to get the total flux density

$$S_{total} = I_0 g(x) \frac{\sigma_T k T_{CMB} \langle T_e \rangle_n N_e}{m_e c^2 d_A^2(z)},$$

where $\langle T_e \rangle_n$ is the mean density weighted electron temperature of the cluster, N_e is the total number of free cluster electrons, and $d_A(z)$ is the angular diameter distance relation. The total number of electrons is related to the cluster mass by

$$N_e = \frac{f_g M}{\mu_e m_p},$$

where M is the total cluster mass, f_g is the gas mass fraction, $\mu_e = 1.142$ is the mean molecular weight per electron assuming cosmic abundances plus 30% of the solar abundance in metals [2], and m_p is the proton mass. The gas mass fraction should be approximately equal to the cosmological value of $\Omega_B/\Omega_M \sim 0.15$ from BBN if clusters reflect the universal partition of matter; it is measured to be $f_g h \sim 0.081$ assuming a Λ CDM cosmology [36].

1.4 Surveying for Galaxy Clusters

The second science goal of ACBAR is to conduct an untargeted survey for clusters of galaxies using the Sunyaev-Zel'dovich effect. The success of this project is a more uncertain than measuring the CMB power spectrum because it has not been attempted on a large patch of sky before and the level of expected SZ signal is still unknown. Fortunately, the power spectrum measurement and cluster search are derived from the same CMB maps resulting in two science data sets from one set of observations. In the following subsections we will discuss the usefulness of galaxy clusters as probes for measuring the cosmological parameters as well as why the Sunyaev-Zel'dovich effect provides a powerful tool for surveying for clusters [5, 48]. We follow the prescription outlined in Vianna and Liddle (1996) and Holder et al. (2000) for modeling the cluster abundance but incorporate a modified cluster mass function that better fits numerical simulations.

1.4.1 Clusters as Cosmological Probes

For a model of structure formation to be considered successful it must predict the observed number density of galaxy clusters at the present epoch as well as at higher redshifts. Massive clusters of galaxies presently correspond to rare peaks in the density perturbation field (much like galaxies at a redshift of a few) and their number depends strongly on the normalization of the matter power spectrum. It has been suggested by many authors that measuring the evolution of the number density of galaxy clusters would be a powerful probe of some cosmological parameters; in particular, the matter density (Ω_M), power spectrum normalization (σ_8), and the density (and possibly equation of state) of dark energy (Ω_Λ) should be well constrained by such a survey [48]. The observed number density of clusters is considered the strongest evidence against the standard CDM model ($\Omega_M = 1$) because it under-predicts the number of rich clusters at intermediate redshifts by several orders of magnitude [3] when normalized to the local cluster abundance as measured by X-ray satellites [26, 27].

The evolution of the number density of clusters, $n(z)$, can be separated into two effects: 1) the change in the comoving volume element, $dV/d\Omega dz$, and 2) the growth of structure in the Universe as parameterized by the cluster mass function, dn/dM . The definitions of the density parameters, Ω_i , comes from the Friedmann equation

$$\left(\frac{\dot{a}}{a}\right)^2 = H(z)^2 = H_0^2 E^2(z) = \frac{8\pi G\rho(z)}{3} + \frac{\Lambda}{3} - K(1+z)^2,$$

which can be re-written as

$$E^2(z) = \frac{8\pi G\rho(z)}{3H_0^2} + \frac{\Lambda}{3H_0^2} - \frac{K(1+z)^2}{H_0^2}.$$

At the current epoch, $z = 0$ and $E(z = 0) = 1$, from which we have

$$\frac{8\pi G\rho_0}{3H_0^2} + \frac{\Lambda}{3H_0^2} - \frac{K}{H_0^2} = 1 = \Omega_M + \Omega_\Lambda + \Omega_K.$$

In the matter dominated epoch, the density term scales like $(1+z)^3$ and we can explicitly

write down the evolution of the density parameters with redshift as

$$\begin{aligned}\Omega_M(z) &= \frac{8\pi G\rho_0(1+z)^3}{3H_0^2 E^2(z)} \\ \Omega_\Lambda(z) &= \frac{\Lambda}{3H_0^2 E^2(z)} \\ \Omega_K(z) &= -\frac{K(1+z)^2}{H_0^2 E^2(z)}.\end{aligned}$$

We can re-write the function $E(z)$ as

$$E^2(z) = \Omega_M^0(1+z)^3 + \Omega_\Lambda^0 + \Omega_K^0(1+z)^2,$$

where the superscript 0 denotes the present value.

The comoving volume element is given by (see, for example, Hogg 2000)

$$\frac{dV}{d\Omega dz} = \frac{c(1+z)^2 d_A^2(z)}{H_0 E(z)},$$

where the angular diameter distance, $d_A(z)$, is given by

$$d_A(z) = \frac{1}{1+z} \int_0^z \frac{dz'}{E(z')}$$

for the spatially flat case ($\Omega_K = 0$). The angular diameter distance relates the physical size of an object, D , to its angular size on the sky by $\theta = D/d_A(z)$. We have plotted the dimensionless angular diameter distance relation and comoving volume element as a function for redshift for three cosmologies in Figure 1.4. The interesting feature of the angular diameter distance is that it flattens out at a redshift of 1–2 and even decreases past this point. This means if a standard yardstick were taken to higher and higher redshift it would at first appear smaller on the sky but eventually would begin to appear larger as it is taken further away.

The cluster mass function, $dn/dM(M, z)$, gives the number density of collapsed objects of a given mass as a function of cosmology and redshift [120]. Press and Schechter (1974) were the first to derive an expression for the mass function by making the assumption that the fraction of matter in collapsed objects is proportional to the fraction of the density field – smoothed on scale $M = 4\pi R^3 \bar{\rho}/3$ – that exceeds a critical threshold δ_c for collapse. The

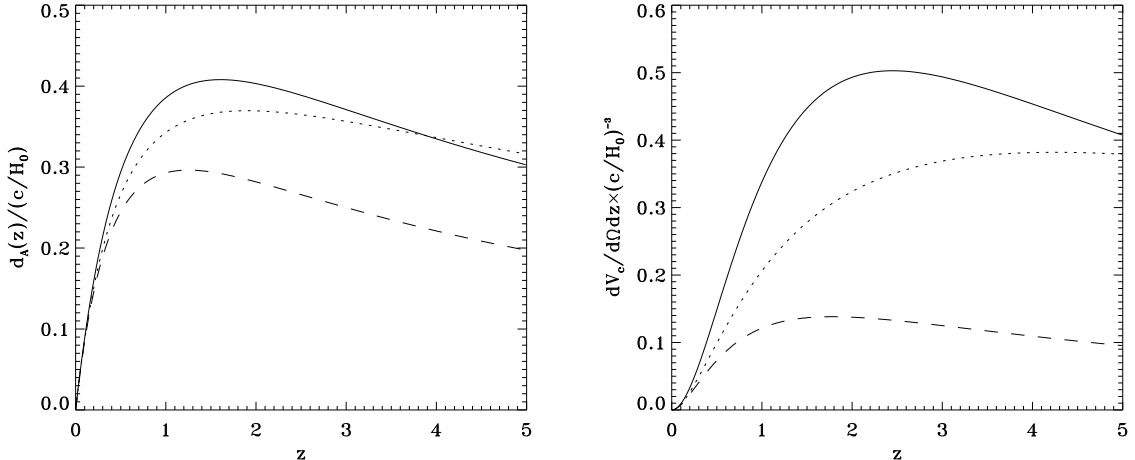


Figure 1.4: Shows the dimensionless angular diameter distance (left panel) and comoving volume element (right panel) as a function of redshift. The three cosmologies are Λ CDM with $\Omega_M = 0.3$ and $\Omega_\Lambda = 0.7$ (solid), critical density SCDM (dashed), and OCDM Universe with $\Omega_M = 0.3$ (dotted).

Press-Schechter (PS) comoving mass function is given by

$$\frac{dn(M, z)}{dM} dM = -\sqrt{\frac{2}{\pi}} \frac{\bar{\rho}}{M} \frac{\delta_c}{\sigma^2(M, z)} \frac{d\sigma(M, z)}{dM} e^{-\delta_c^2/2\sigma^2(M, z)} dM,$$

where M is the mass of the object, $\bar{\rho}$ is the mean comoving matter density, $\sigma^2(M, z)$ is the variance of the density field smoothed on scale M corresponding to a size $R = (3M/4\pi\bar{\rho})^{1/3}$, δ_c is the linear density contrast at collapse and is found to be ~ 1.69 for a top-hat smoothing window (fairly independent of cosmology) [69]. The dispersion on mass scale M is determined by smoothing the matter power spectrum $P(k, z)$ with a window function $W(kR)$ is

$$\sigma^2(M, z) = \int_0^\infty P_\delta(k, z) W^2(kR) \frac{dk}{k}.$$

The power spectrum is $P_\delta(k) \propto k^4 T^2(k) \delta_H^2(k)$, where $\delta_H^2(k) \propto k^{n-1}$ is the primordial power spectrum of density contrast ($\delta = \delta\rho/\rho$) – with $n = 1$ corresponding to the Harrison-Zel’dovich spectrum – and $T(k)$ is the transfer function [14]. The power spectrum is usually normalized to the variance of the density field smoothed with a top-hat window function on $R = 8h^{-1}$ Mpc scales, designated $\sigma_8(z)$, where h is the dimensionless Hubble constant defined as $H_0 = h$ 100 km/s/Mpc. The top-hat window function in Fourier space is given

by [65]

$$W(kR) = 3 \left[\frac{\sin(kR)}{(kR)^3} - \frac{\cos(kR)}{(kR)^2} \right].$$

High resolution numerical simulations [120, 55, 103] indicate that the Press-Schechter (P-S) mass function over-predicts the number of low mass halos and under-predicts the most massive halos. Since we are interested in the number density of the most massive clusters of galaxies, we elect to use the modified P-S mass function given by Sheth and Tormen (S-T) (1999); the functional form of the S-T mass function was verified by Jenkins et al. (2000) and White (2002). This form of the modified mass function was determined by fitting to the results of numerical cluster simulations. The modified comoving mass function is given by

$$\frac{dn(M, z)}{dM} dM = -A \sqrt{\frac{2a}{\pi}} \frac{\bar{\rho}}{M} \frac{\delta_c}{\sigma^2(M, z)} \frac{d\sigma(M, z)}{dM} \left[1 + \left(\frac{\sigma^2(M, z)}{a\delta_c^2} \right)^p \right] e^{-\delta_c^2/2\sigma^2(M, z)} dM,$$

where we will use the best fit values of $A = 0.3222$, $a = 0.707$, and $p = 0.3$. We note that [117] contains an error in the evaluation of $d\sigma(M, z)/dM$ but this has a minimal effect on the mass function.

To determine the dispersion on an arbitrary mass scale, we can either integrate the smoothed power spectrum for every mass or we can use a fitting function in the region of interest to massive clusters ($\sim 8h^{-1}$ Mpc). This should provide an accurate analytic function for the dispersion in the mass region of interest. We use the power law fit of Vianna and Liddle (1996) given by

$$\sigma(R, z = 0) = \sigma_8 \left(\frac{R}{8h^{-1} \text{ Mpc}} \right)^{-\gamma(R)},$$

where for CDM spectra the power law is fit by

$$\gamma(R) = (0.3\Gamma + 0.2) \left[2.92 + \log \left(\frac{R}{8h^{-1} \text{ Mpc}} \right) \right].$$

Γ is the shape parameter used in the power spectrum transfer function and is equal to

$$\Gamma = \Omega_M h e^{-\Omega_B(1+1/\Omega_M)},$$

and is evaluated at the current epoch. For a power spectrum with $n = 1$, the shape

parameter is found to be $\Gamma \sim 0.23 \pm 0.04$ from the galaxy correlation function. We note that the latest measurements of $\Omega_M \sim 0.3$ from supernova and the CMB [101, 91, 7, 86] and $\Omega_M h^2 \sim 0.02$ from Big Bang nucleosynthesis [114] predict a value of $\Gamma \sim 0.21$ which is consistent with the value derived from galaxy correlation.

The evolution of the dispersion with redshift is given by the linear growth suppression factor, $g(\Omega_M, \Omega_\Lambda)$; this compares the growth of linear density perturbations in an arbitrary cosmology at a redshift z to SCDM ($\Omega_M = 1$, in which structure growth is proportional to the scale factor $a = (1+z)^{-1}$). A useful analytic fit to the growth suppression factor is given by Carroll, Press, and Turner (1992)

$$g(\Omega_M(z), \Omega_\Lambda(z)) = \frac{5}{2} \frac{\Omega_M(z)}{\left[\Omega_M^{4/7}(z) - \Omega_M(z) + (1 + \Omega_M(z)/2)(1 + \Omega_\Lambda/70) \right]},$$

where the redshift dependence of Ω_M and Ω_Λ are given above. The redshift dependence of the dispersion on $8h^{-1}$ Mpc scales is then given by

$$\sigma_8(z) = \frac{\sigma_8(0)}{(1+z)} \frac{g(\Omega_M(z), \Omega_\Lambda(z))}{g(\Omega_M(0), \Omega_\Lambda(0))},$$

which uses the fact that the density contrast of structures grows proportional to $(1+z)^{-1}$ in a critical density Universe. We plot $\sigma_8(z)$ for three different cosmologies in Figure 1.5. The figure shows that the dispersion in the density field was larger at high redshift in low matter density cosmologies compared to SCDM. This means that the structure we observe today formed at higher redshift in low matter density cosmologies.

The local abundance of massive clusters has been measured well by X-ray satellites. Eke et al. (1996) derive limits on the present power spectrum normalization of $\sigma_8 \Omega_M^{0.46-0.10\Omega_M} = 0.52$ if $\Omega_\Lambda = 0$ and $\sigma_8 \Omega_M^{0.52-0.13\Omega_M} = 0.52$ if $\Omega_\Lambda = 1 - \Omega_M$. Note that if $\Omega_M = 1$ we have $\sigma_8 = 0.52$ to reproduce the local cluster abundance; but this set of parameters underpredicts the number of clusters observed between redshift 0.5 to 0.8 by about two orders of magnitude [3]. For $\Omega_M = 0.3$ we have $\sigma_8 \sim 0.9 \pm 0.03$ depending on the value of Ω_Λ . The degeneracy between σ_8 and Ω_M can be broken by measuring the *evolution* of the number density of galaxy clusters. Ω_M effectively sets the normalization of the mass function and $\sigma_8(z)$ determines how the mass function varies with redshift. It should be noted that optical cluster surveys, such as the Sloan Digital Sky Survey, measure a substantially lower value

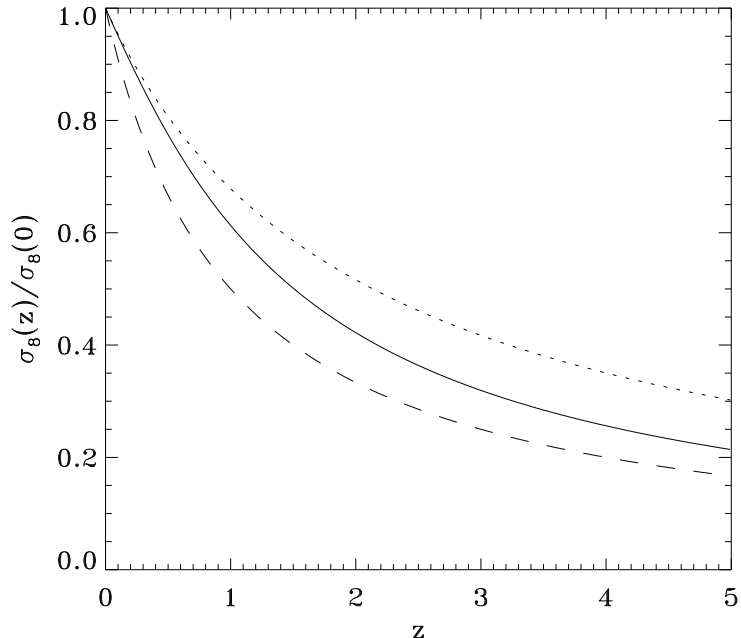


Figure 1.5: Shows the dispersion in the power spectrum smoothed with an $8h^{-1}$ Mpc top-hat window as a function of redshift normalized to the value at $z = 0$. The three cosmologies are Λ CDM with $\Omega_M = 0.3$ and $\Omega_\Lambda = 0.7$ (solid), critical density SCDM (dashed), and an open CDM Universe with $\Omega_M = 0.3$ (dotted).

of σ_8 for a given value of the matter density. The SDSS constraint given in Bahcall et al. (2002) is $\sigma_8 \Omega_M^{0.6} = 0.35 \pm 0.03$ for values of Ω_M in the range of 0.1-0.4 which implies $\sigma_8 = 0.72$ if $\Omega_M = 0.3$. It will be shown below that the expected yield from a cluster survey depends very strongly on the value of σ_8 ; this is the cosmological parameter likely to have the strongest constraints placed upon it by near-future cluster surveys.

We can now put this all together to estimate the number density of clusters above a given mass limit. Multiplying the comoving number density of objects of mass M by the comoving volume element and integrating from a lower mass limit M_{lim} to ∞ gives the evolution of the differential number density of objects above the limiting mass

$$\frac{dn(> M_{lim}, z)}{d\Omega dz} = \int_{M_{lim}}^{\infty} \frac{dn(M, z)}{dM} \frac{dV}{d\Omega dz} dM.$$

This last equation assumes that a cluster survey will detect all objects above a given mass limit, independent of cluster redshift. The cluster selection function (or detection efficiency) of a survey, $f(M, z)$, encodes the fraction of clusters that will be detected as a function of

mass and redshift. Incorporating the selection function of a survey into the differential number density yields

$$\frac{dn(z)}{d\Omega dz} = \int f(M, z) \frac{dn(M, z)}{dM} \frac{dV}{d\Omega dz} dM.$$

More realistic than a simple step-function in mass, the selection function of a cluster survey will vary with both cluster mass and redshift and must be determined from Monte Carlo simulations. The simulations incorporate the background noise properties of the survey and assumptions about the evolution of galaxy cluster properties. As will be discussed below, it is the relative simplicity of the selection function of SZ cluster surveys versus X-ray or optical cluster surveys that makes the SZ effect such a potentially powerful probe of cosmology. For the remainder of this introduction, we will use the redshift-independent step selection function with $f(M, z) = 1$ for $M \geq M_{lim}$ and $f(M, z) = 0$ for $M < M_{lim}$. We determine the ACBAR cluster selection function in Chapter 5 and use this to estimate the cluster yield as a function of cosmological parameters. We then compare the expected cluster yield with the number of objects detected to place constraints on the cosmological parameters σ_8 and Ω_M within the CDM paradigm.

Assuming the simple step selection function, we can integrate the differential number density over redshift to get the total surface number density of massive objects at redshift higher than z ,

$$\frac{dN(> M_{lim}, > z)}{d\Omega} = \int_z^\infty \frac{dn(> M_{lim}, z')}{d\Omega dz'} dz'.$$

We plot $dn(> M_{lim}, z)/d\Omega dz$ and $dN(> M_{lim}, > z)/d\Omega$ versus redshift for three cosmological models in Figure 1.6. The three cosmologies are SCDM ($\Omega_M = 1$, $\Omega_\Lambda = 0$, $h = 0.5$, $\sigma_8 = 0.52$), Λ CDM ($\Omega_M = 0.3$, $\Omega_\Lambda = 0.7$, $h = 0.7$, $\sigma_8 = 0.93$), and OCDM ($\Omega_M = 0.3$, $\Omega_\Lambda = 0$, $h = 0.7$, $\sigma_8 = 0.87$). The values of σ_8 were chosen to be consistent with the Eke et al. (1996) constraints from local abundance of X-ray clusters and we have used $\delta_c = 1.69$ and $\Gamma = 0.23$ for all cosmologies. We have chosen a uniform cluster mass limit of $10^{15} M_\odot$ for these figures.

One of the most interesting features of Figure 1.6 is that most of the massive clusters in a SCDM cosmology will form at a redshift around $z \sim 0.2$ whereas most of the $> 10^{15} M_\odot$ clusters in either a Λ CDM or OCDM cosmology will form at $z \sim 0.4$. The mere existence of $> 10^{15} M_\odot$ clusters past $z \sim 0.6$ is enough to exclude SCDM as a viable model of structure

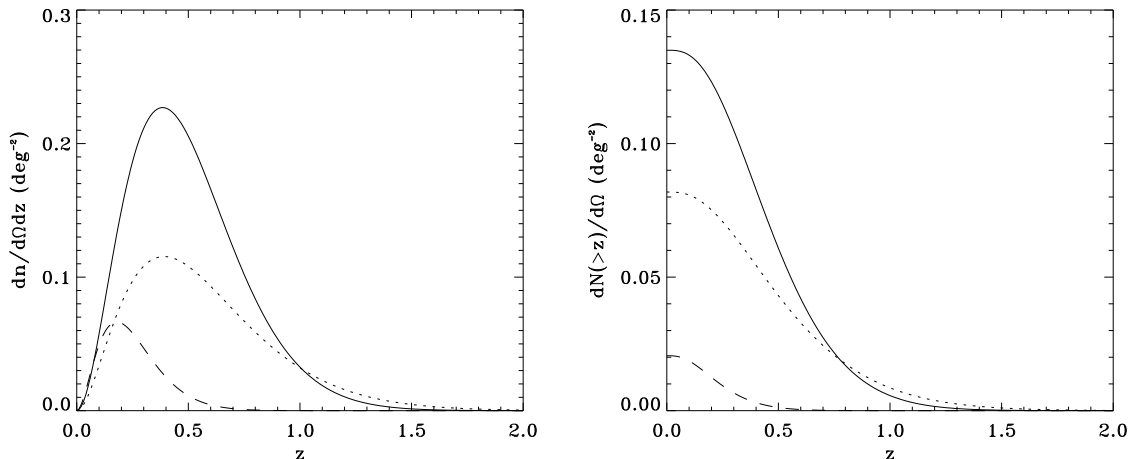


Figure 1.6: Left panel shows the differential number counts of massive clusters ($> 10^{15} M_{\odot}$) versus redshift for the three cosmologies defined in the text: Λ CDM (solid), SCDM (dashed), and OCDM (dotted). The right panel shows the integrated number counts for clusters above the redshift z for the same three cosmologies. The value at $z = 0$ represents the visible surface density of massive clusters on the sky.

formation. One also glean from these figures that massive clusters of galaxies are quite rare objects on the sky with a surface density of a few per 10 deg^2 . However, the number density is a strong function of the power spectrum normalization, σ_8 . This is illustrated in Figure 1.7, which shows the integrated number density of $> 10^{15} M_{\odot}$ clusters in a Λ CDM cosmology with varying σ_8 . We expect more than a factor of two difference in the density of massive clusters on the sky between cosmologies with $\sigma_8 = 0.9$ and $\sigma_8 = 1.0$.

The cluster mass function has an exponential dependence upon the dispersion of the smoothed density field. As we increase the smoothing radius – equivalent to increasing the mass scale – the dispersion decreases resulting in a sharp reduction of the expected number of objects on that scale. Thus, the expected cluster yield from a survey will depend strongly on the limiting mass of the survey, or equivalently, the survey selection function. As will be discussed below, the selection function of SZ cluster surveys should not depend strongly upon redshift [48]. We illustrate the effect of limiting cluster mass (assuming a step selection function) upon expected cluster yield for the three cosmologies listed above in Figure 1.8. It can be seen from the figure that expected cluster yield depends very strongly upon limiting mass; especially at the high-mass end where clusters become quite scarce. Another interesting feature of Figure 1.8 is that the difference in expected cluster yield between low-density and critical density universes becomes most pronounced at the high-

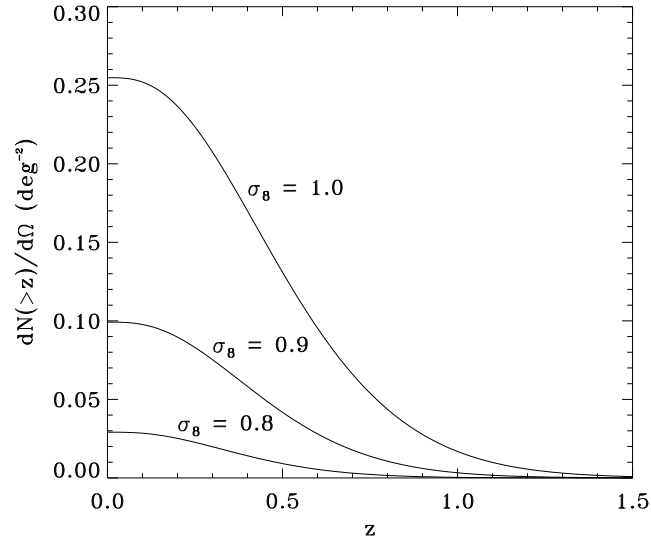


Figure 1.7: Illustrates the strong dependence on power spectrum normalization of the integrated surface density of massive clusters ($M > 10^{15} M_{\odot}$) with redshift for a Λ CDM cosmology and varying σ_8 . All other parameters are held fixed at the values given in the text.

mass end. This suggests that massive clusters of galaxies that will provide the strongest constraints on Ω_M from galaxy cluster surveys. In fact, it is the abundance of massive clusters at moderate redshifts that provides one of the strongest pieces of evidence against the SCDM model.

1.4.2 SZ Cluster Surveys

The total SZ flux equation given above tells us that a flux limited survey will have a cluster selection function that is proportional to $T_e N_e / d_A^2(z)$. The angular diameter distance relation is quite flat with redshift. Both T_e and N_e are determined by the cluster mass; in virial equilibrium the cluster mass sets the velocity dispersion, and hence the temperature, of the cluster gas. Taken together this implies that the selection function for a flux limited SZ survey should be almost independent of redshift with cluster mass being the limiting factor [47]. Holder et al. (2000) show that the limiting mass for an upcoming interferometric SZ survey is expected to vary with redshift by less than a factor of 2–3 for $z > 0.5$ (if there is no cluster evolution); independent of the underlying cosmology. ACBAR has large beams compared to most galaxy clusters and should be sensitive to the integrated cluster flux. However, smaller beam experiments that resolve clusters will be sensitive to the cluster

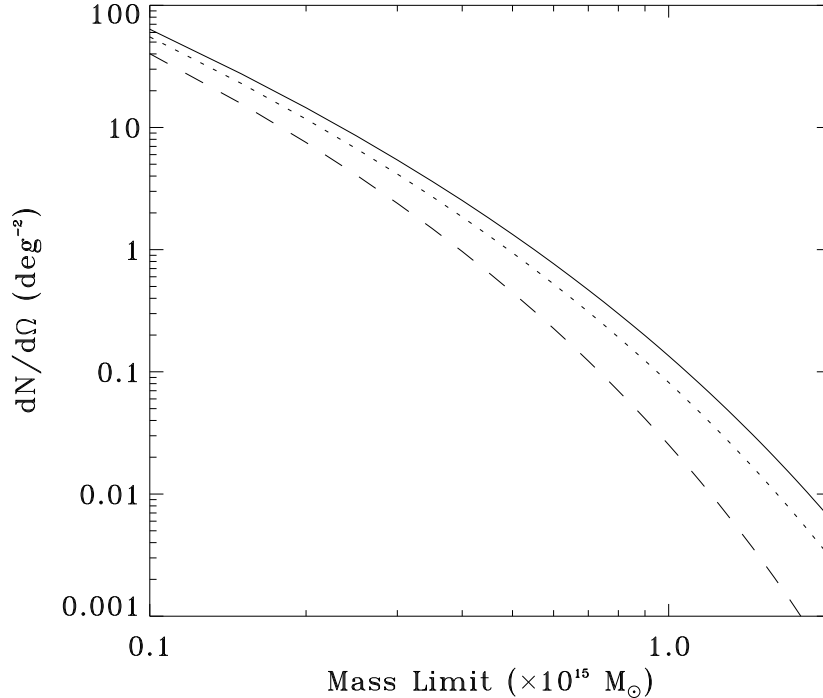


Figure 1.8: Shows the very strong dependence of expected cluster survey yield versus uniform limiting cluster mass for Λ CDM (solid), SCDM (dashed), and OCDM (dotted).

core radius. For fixed cluster mass, a cluster that formed earlier will tend to be more compact (and consequently hotter) reflecting the higher density of the Universe at the epoch of formation. The selection function for such an experiment will be a more complicated function of redshift. This last point depends strongly upon the cluster detection method employed and will be discussed in more detail in the Analysis chapter.

Unlike the SZ effect, the integrated cluster surface brightness in both optical and X-ray falls off rapidly with redshift like $(1+z)^{-4}$. This implies that the cluster selection function for a flux limited sample will depend strongly upon redshift for optical and X-ray observations but remain constant for an SZ survey (see, for example, Rosati et al. 2002). Cluster surveys conducted in X-ray and optical are usually limited in depth to $z \lesssim 1$ [100]. However, the forthcoming XMM Cluster Survey (XCS) [99] should detect many X-ray clusters out to $z \sim 2$. Because of the redshift independence of the SZ surface brightness, an SZ survey will be limited only by the existence of massive galaxy clusters. As daunting of a task as extracting cosmological parameters from X-ray and optical surveys may appear to be, it is important to stress that unlike future large-scale SZ surveys, optical and X-ray surveys have

actually been conducted [e.g., ROSAT All-Sky Survey (RASS), Einstein Extended Medium Sensitivity Survey (EMSS), and Sloan Digital Sky Survey (SDSS)] and have been used to place strong constraints on σ_8 and Ω_M [100, 43, 96, 58, 4].

Once a survey has identified a set of candidate clusters, they must be followed up (either optically or with X-ray spectra [66]) to obtain redshifts to extract the most information from the survey. The measured evolution of the number density of clusters allows the separation of otherwise degenerate cosmological parameters. A program to measure the angular diameter distance relation with an unbiased sample of clusters will require pointed X-ray observations to obtain electron temperatures in addition to cluster redshifts. Distance measures (such as angular diameter and luminosity distances) are sensitive to cosmological parameters in a way that is complementary to CMB and cluster abundance measurements [52].

1.4.3 Confusion

The dominant source of confusion for an SZ survey depends strongly upon the frequency of observation and the angular scales probed by the experiment. Observations conducted below the thermal null (< 218 GHz) will detect clusters as a decrement compared to the CMB. At radio frequencies, however, point source emission will “fill in” the SZ signal decrement making a cluster much less detectable [67] (or even completely dominate the signal). A novel way to avoid this problem at radio frequencies is through the use of interferometry which uses the differences in the Fourier transform of clusters and point sources to separate their signals. Since point sources have a flat spectrum and clusters have a steeply falling spectrum, one can use the signal from the longest baselines (which should have very little cluster signal) as a point source monitor [16].

At frequencies above the thermal null (> 218 GHz), the dominant source of confusion is from dusty infrared sources such as distant star forming galaxies. This has the opposite effect of radio sources in that it makes the inferred SZ signal appear larger than it really is. In fact, the problem is compounded by the gravitational lensing effect of clusters upon the background of high redshift dusty galaxies [11] which collects more sources in the field of the cluster than appear in the uniform background. As an aside, we mention that the gravitational lensing of background galaxies has recently been used to detect clusters of galaxies through reconstruction of the projected matter distribution of a cluster by the shear distortion of background galaxy images [113]. This method shows great promise for

measuring the mass of lensing clusters because the optical deviation of the background galaxy images depends only on the cluster mass and requires no information about cluster physics.

Observations at 100–200 GHz are relatively free of contaminating sources and are dominated by confusion from fluctuations in the CMB itself. If an experiment has sufficient sensitivity at frequencies on either side of the thermal null (ideally with a frequency channel straddling the null), then the contribution from the intrinsic CMB anisotropy can be removed from the SZ sensitive channels. The amount of confusion for experiments with sensitivity at only one frequency depends strongly on the angular resolution of the instrument because the CMB power spectrum is steeply falling on small angular scales. However, pushing instrument resolution to too fine of a scale in an attempt to escape the CMB will resolve the clusters and lose the copious extended emission to the background noise. A beam size of a couple arcminutes allows one to survey a reasonable amount of sky in a fixed amount of time while still coupling well to extended cluster emission and avoiding most of the primary CMB confusion.

One last source of confusion is the effect of interpreting the projected emission of separate sources that happen to lie along a common line-of-sight as a single object. This has historically been a major problem for optical surveys such as the Abell cluster catalogs. Recent multi-color and spectroscopic surveys add the power to discriminate objects in redshift as well which dramatically reduces the number of spurious detections. The X-ray emission from clusters depends very strongly on the degree of gas concentration ($S \propto n_e^2$) which greatly reduces projection effects. The SZ effect is proportional to the integrated electron pressure along the line of sight and – because of the redshift independence – will suffer from projection effects. However, massive clusters of galaxies have a rather low surface density on the sky and thus chance projections are unlikely to be a major source of false cluster characterization for ACBAR.

1.5 Previous Work

Although surveys for galaxy clusters have been conducted at X-ray and optical wavelengths for some time, instruments with sufficient sensitivity to conduct untargeted surveys using the SZ effect have only recently been constructed. Much like ACBAR, these experiments

have focused on measuring the CMB power spectrum on small angular scales. Although a handful have detected power attributed to small-scale CMB anisotropy (either primary or secondary), so far none have identified a previously unknown object as an SZ cluster detection. There are reported detections of previously unknown galaxy clusters near clusters of radio sources (see for example [22]). However, these searches are not unbiased surveys and there is some debate over the efficacy of the technique [51].

The Cosmic Background Imager experiment operates at 30 GHz in the Atacama desert in Chile [83]. They measured the CMB power spectrum to $\ell \sim 3500$ and report a significant excess of power in the ℓ range of 2000-3000 which they also attribute to a background of unresolved SZ sources [72, 15]. Although the CBI has made SZ images of known galaxy clusters as part of program to measure the Hubble constant [115], they do not report the detection of previously unknown SZ clusters.

Receivers operating at 28.5 GHz were used with the Berkeley-Illinois-Maryland-Association (BIMA) array to detect small-scale CMB power of $\Delta T = 14.3_{-6.0}^{+4.8} \mu\text{K}$ at $\ell \sim 7000$ [23]. Their survey covered ten $6.6'$ circular fields for a total area of approximately $1/8 \text{ deg}^2$. The team performed a radio point source survey with the VLA to remove all point sources well below the level that could explain the detected power. At this ℓ the damping tail of the CMB should yield very little primary CMB power. They report their detection is consistent with level of power predicted from a background of unresolved SZ clusters.

In the most relevant work to the ACBAR cluster survey, Lin and Mohr (2002) analyzed the non-detection of SZ clusters above 2σ in 7 of the early BIMA fields. They performed a Monte Carlo simulation of the cluster detection efficiency and determined that the limiting cluster mass of the survey was $\sim 1.3 \times 10^{14} h^{-1} M_{\odot}$. This was a very deep survey but its power to discriminate cosmological parameters is limited by the size of the survey ($\sim 250 \text{ arcmin}^2$). Using these results they place constraints on the power spectrum normalization and matter density of $\sigma_8 < 1.00 \Omega_M^{-0.43 \Omega_M - 0.22}$ at 95% confidence for flat- Λ CDM models over a reasonable range of Ω_M . If the matter density is indeed $\Omega_M = 0.3$ then this constraint translates to $\sigma_8 < 1.52$ at 95% confidence.

Chapter 2 The ACBAR Instrument

The Arcminute Cosmology Bolometer Array Receiver (ACBAR) is a multi-frequency millimeter-wave instrument optimized for observations of small angular scale fluctuations in the Cosmic Microwave Background (CMB) from the South Pole.

2.1 Optics

The focal plane optics are designed to couple the ACBAR receiver to the Viper telescope and produce diffraction limited beams at 150 GHz. The angular resolution at higher frequencies is intentionally degraded to produce nearly matched beam sizes at all frequencies. This beam size matching results in equal sampling on the sky at all frequencies while mapping and simplifies multifrequency analysis.

Figure 2.1 shows the layout of the ACBAR focal plane as deployed in 2001 and 2002. In 2001, the focal plane was arranged with common frequencies aligned in columns so that each row observed at 150, 220, 280, and 350 GHz. For 2002, the focal plane is arranged with rows of common frequency to concentrate the declination extent of the 150 GHz channels; the 350 GHz feeds were replaced with an additional set of 150 GHz feeds because of poor noise performance and large beam size. The main optical elements of the focal plane are beam defining scalar feeds, expanding and reconcentrating conical feed structure, filtering, and bolometric detectors. Each of these will be described in the following sections.

2.1.1 Scalar Feeds

The corrugated feeds used in ACBAR are designed to produce single moded (e.g., scalar), nearly Gaussian beams with very low sidelobes. Low sidelobes reduce optical loading from telescope spillover as well as decrease offset signals from modulation of the spillover by the chopping flat of Viper (see Figure 2.15). Figure 2.2 shows an enlargement of the ACBAR 150 GHz scalar feed. The feeds were fabricated by Thomas Keating, Ltd.¹ and performed within specification. The geometry of the conical section of the scalar feeds (aperture diameter and

¹Billingshurst, England, <http://josephson.terahertz.co.uk/homepage.HTM>



Figure 2.1: Images of the ACBAR focal plane layout for 2001 (left) and 2002 (right).

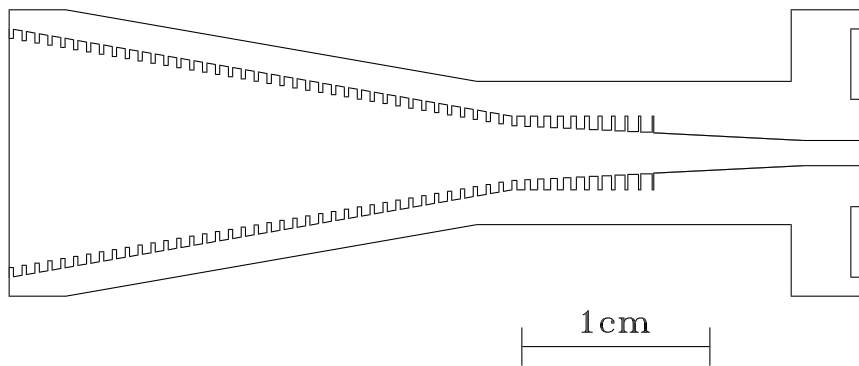


Figure 2.2: Detail of the ACBAR 150 GHz scalar feed horn showing corrugation geometry in cone and throat.

length, see Table 2.1) is designed to produce beams from the telescope of $\sim 4 - 5'$ FWHM with reasonable sidelobe structure. We modeled the expected beam patterns by assuming balanced hybrid conditions at the aperture and used the Fourier transform of a Gauss-Laguerre expansion of the HE_{11} mode as described in [121]. The corrugation geometry within the conical section is designed in accordance with [21]; the corrugation depth is $\lambda/4$ and the groove pitch is three grooves per wavelength to preserve the desirable HE_{11} mode.

Because ACBAR is not intended measure to polarization, we are not concerned about instrumental cross-polarization from mode conversion after the beam defining section and are thus able to transition from corrugated to smooth walled waveguide. Smooth walled structures are much easier to fabricate and significantly less expensive. The transition to

smooth walled waveguide occurs in the throat of scalar feed and must gradually convert the $\lambda/3$ pitch corrugations to smooth wall without abrupt changes in waveguide impedance that can cause mode conversion and thus degrade the beam quality.

We implement the throat prescription of Zhang (1993) which varies both the corrugation thickness and depth through the throat. This proved quite challenging to fabricate, particularly at the higher frequencies. The feeds are manufactured by electroforming copper onto aluminum mandrels with corrugations as narrow as 0.003". It is very difficult to etch away the aluminum mandrel to the bottom of the small corrugations after electroforming because of the aspect ratio of the small corrugation structures at the back of the throat. Incomplete etching degrades the performance of the throat transition causing mode conversion. The measured beam patterns agree quite well with the model predictions and we believe that the machining and etching of the throats were well done.

When designing the 350 GHz feeds, we determined that their length was prohibitively long and would be extremely expensive to manufacture. We decided that the 350 GHz channel science was less sensitive to increased sidelobe structure and decided to shorten the feed by putting a lens at the aperture as described in [20]. Using a beam forming lens can significantly shorten the length of a feed but this comes at a cost of higher sidelobe structure, which we deemed acceptable.

The measured beam patterns of the ACBAR scalar feeds – as well as the model beam patterns – are shown in Figure 2.3. These beam patterns were measured during the instrument integration at U.C. Berkeley in the Fall of 2000. To measure the beams, we place ACBAR on a custom built metal table with a hole for the dewar window. Below this hole is a chopped thermal load on a computer controlled rotating arm that sweeps the load across the beam. Integration times at each arm angle are set by the user. The axis of rotation of the arm is adjustable and is approximately centered on the phase center of the scalar feeds. Table 2.1 lists the measured Gaussian FWHM of the ACBAR beams exiting the dewar as well as the model Gaussian widths. For the non-lensed feeds (this includes all frequencies except 350 GHz), the agreement between the model predicted Gaussian widths and measured widths is within a fraction of a percent. As discussed in more detail in Appendix C, to achieve equal beam sizes on the sky the beam widths on the primary mirror should scale proportionally with wavelength.

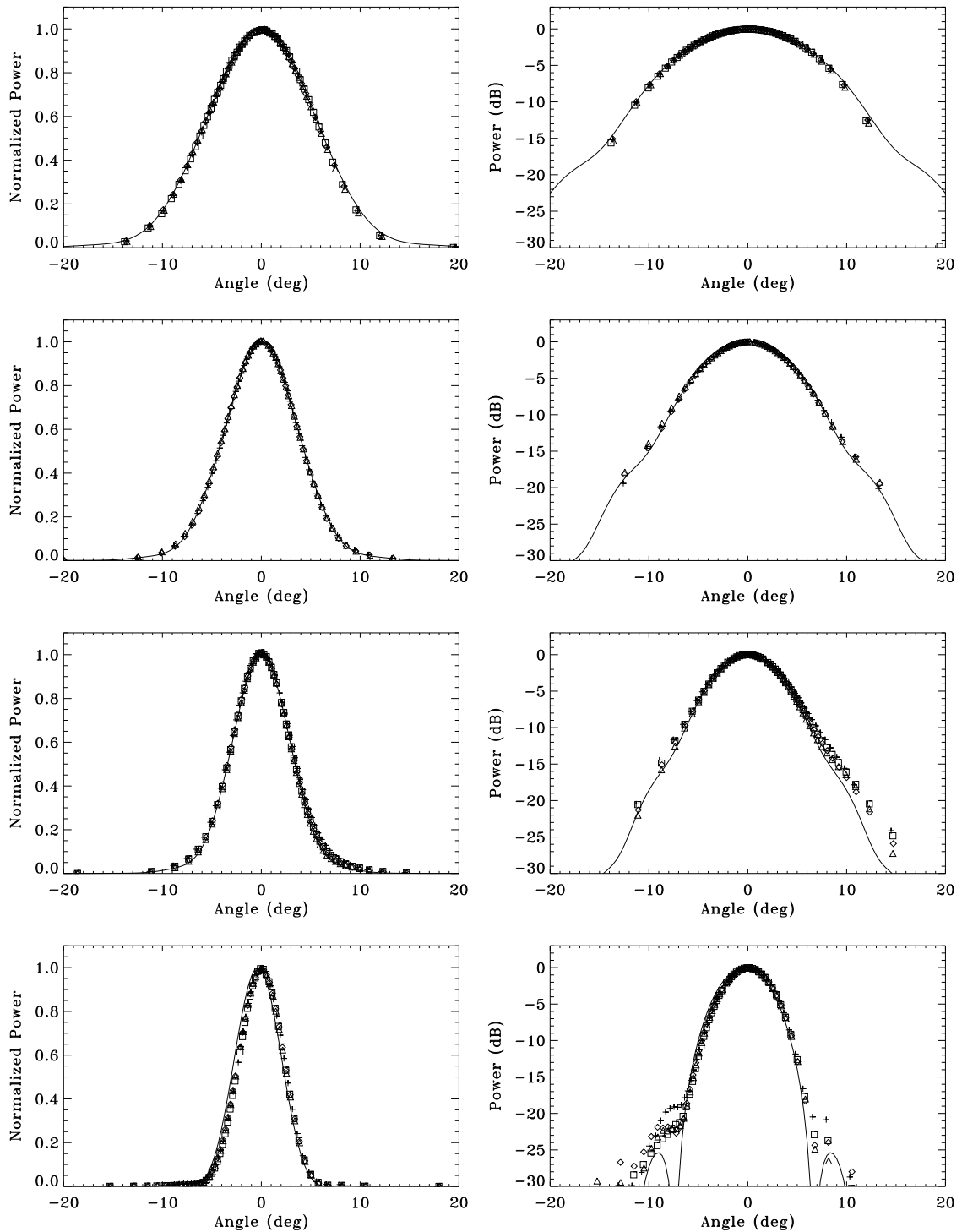


Figure 2.3: ACBAR beams measured from the dewar along with model beam patterns. The beams were measured along the direction of the azimuth chop. From top to bottom, the frequencies are 150, 220, 280, and 350 GHz. The agreement in most cases is seen to be quite good. The 280 GHz beams appear to deviate slightly on one side which is probably due to diffraction through the cryostat vacuum window. The finite size of the source ($\sim 1^\circ$) will smooth the model beam pattern which explains why the measured 350 GHz beams do not follow the deep nulls in the response pattern.

Frequency (GHz)	a (mm)	L (mm)	Gaussian Fit FWHM	Model FWHM
150	6.1	35.0	$12.52^\circ \pm 0.01^\circ$	12.57°
220	6.1	45.0	$8.65^\circ \pm 0.03^\circ$	8.66°
280	6.2	53.0	$6.79^\circ \pm 0.08^\circ$	6.81°
350	5.9	22.1	$5.14^\circ \pm 0.02^\circ$	5.27°

Table 2.1: Corrugated feed dimensions and average measured and model Gaussian FWHM for all four ACBAR frequency feeds.

2.1.2 Feed Structure

The design of the ACBAR feed structure is based on the *Planck* satellite prototype design of Church et al. (1996) (see Figure 2.4). Light enters the feed structure through the beam defining scalar feed and encounters a waveguide cutoff that high pass filters the incoming light. Cylindrical waveguide supports TE modes with the dispersion relation

$$k^2 = \frac{\omega^2}{c^2} - \frac{\nu_{ni}^2}{a^2},$$

where a is the radius of the waveguide and ν_{ni} is the i th root of the first derivative of the n th order Bessel function and is equal to 1.841 for the lowest frequency mode (TE_{11}). For ν less than $\nu_{ni}c/2\pi a$ the wavenumber becomes imaginary and the wave is damped exponentially. The length of the waveguide cutoff is approximately three times the cutoff wavelength in order to fully attenuate low frequencies. During testing we observed that material in the waveguide (from incomplete cleaning) greatly affected the waveguide edge frequency. The steep waveguide cutoffs of properly cleaned waveguide edges can be seen in the transmission spectra in Figure 2.5 below.

After waveguide filtering, the smooth walled section re-expands to a diameter of a few wavelengths before reaching the edge defining and blocking filters. This re-expansion is necessary to make the guide wavelength equal to the free space wavelength where the upper band edge filters are designed. At this point we also have a thermal break to separate the relatively warm 4 K front end of the feeds from the ultra-cold detector side of the feed structure (which sits at 240 mK).

The optical coupling between two front-to-front conical feeds is reduced because the phase caps for the two feeds have opposite curvature and small radii resulting in a large

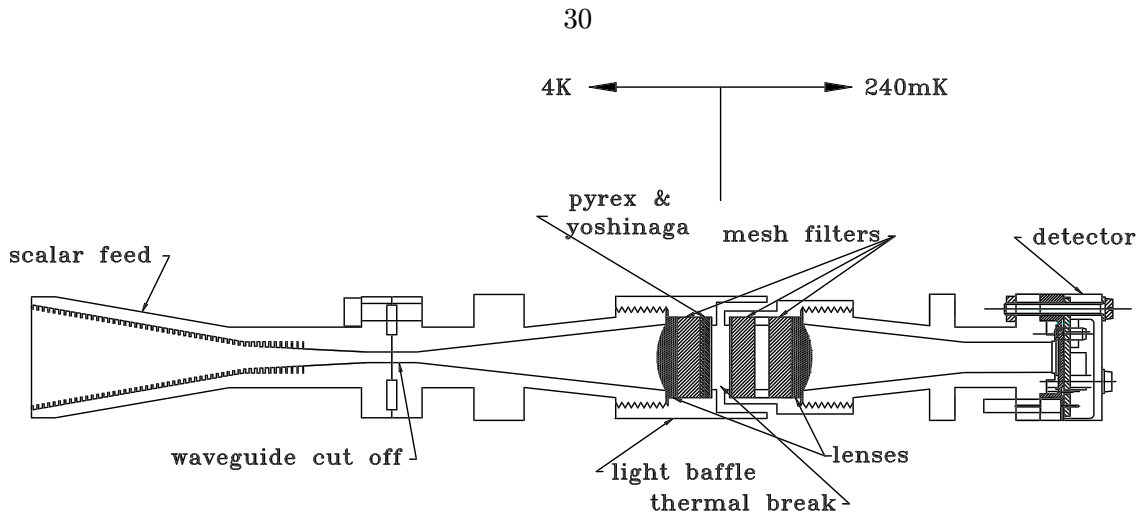


Figure 2.4: ACBAR 150 GHz feed horn structure for 2002.

phase mismatch. To improve the coupling we employ coupling lenses at the apertures of both conical feeds. These are designed to place a common beam waist midway between the two feed apertures. The design of these coupling lenses was developed by for use in *Planck* [18] and were machined on a CNC lathe. There is a difficulty using focusing elements in Gaussian optics because they do not obey the same object/image distance relationship as geometric optics. When designing coupling lenses one finds that for short “object” distances there is a maximum separation distance beyond which there is no solution. Because of the large thickness of the filters in the ACBAR feed structure, the spacing between the apertures slightly exceeds this maximum limit at 220 GHz. We use lenses designed for the maximum separation with apparently no ill effects. We tested the efficacy of the coupling lenses at 150 GHz by measuring the optical efficiency of the feed structure with and without the lenses and found that the lenses improved the relative optical efficiency by $\sim 40\%$ (a significant improvement).

The light is reconcentrated and fed into the detector cavity where it is absorbed by a bolometer. Since the light sets up a standing mode with the reflective cavity backshort, the detectors are spaced an odd number of $\lambda_0/4$ away from the front and back surfaces of the cavity to maximize the electric field at the absorber [56]. The initial design of the reconcentrating feeds tapered down to the waveguide diameter before entering the integrating cavity. This was done because, historically, Winston concentrators in many moded systems were used at millimeter wavelengths; many moded systems obey geometric ray tracing optics. In

the geometric optics limit, light enters the integrating cavity and reflects until it is either absorbed by the detector (or the cavity wall) or goes back out the cavity entrance. The probability of detection would then go roughly as $\sim A_{\text{absorber}}/A_{\text{hole}}$ from which it can be seen that making the cavity hole as small as possible is advantageous.

On the other hand, ACBAR (and many other contemporary millimeter instruments) operates single moded; in which case the Gaussian beams do not obey geometric optics. We believe that the beam suffers reflection from the small cavity entrance hole as well as diffraction upon entering the integrating cavity; both of these effects reduce the optical efficiency of the system. To test this we gradually opened up the diameter of the entrance to the integrating cavity until the diameter was as large as the absorber and measured the optical efficiency in each case. This resulted in an additional improvement in relative optical efficiency of $\sim 40\%$ at 150 GHz and $\sim 80\%$ at 350 GHz. This is a significant improvement because light that is not absorbed by the detector is reflected back through the feed structure, thus degrading the system sensitivity.

2.1.3 Filtering

The ACBAR filter bands were selected to maximize the ratio of astrophysical signal to the sum of detector and atmospheric noise. Although the atmospheric transmission from the South Pole is arguably the best on the earth's surface for millimeter-wave observation, care still must be taken to avoid the deep molecular lines that pervade the atmospheric spectrum. Figure 2.5 shows a model of transmission spectrum at the South Pole in the winter generated with the AT² atmospheric model program. This model assumes an elevation of 2835 m, temperature of -60°C , precipitable water vapor of 0.25 mm, and pressure of 530 torr. Also shown are the three frequency bands of ACBAR in 2002. The lines at 183, 325, and 380 GHz are generated by rotational transitions of water vapor and the lines at 56, 119, and 368 GHz are due to a rotational transitions of molecular oxygen [41]. The forest of narrow lines is due almost entirely to ozone. Figure 2.6 shows the brightness temperature contribution to each of the 2002 spectral bands from the atmosphere.

To determine the ACBAR frequency bands we used this model atmospheric transmission spectrum and combined it with an estimate of the atmospheric fluctuation noise as described in Lay and Halverson (2000). For each of our spectral bands we estimated the detector

²E. Grossman, Airhead Software, Boulder, CO 80302

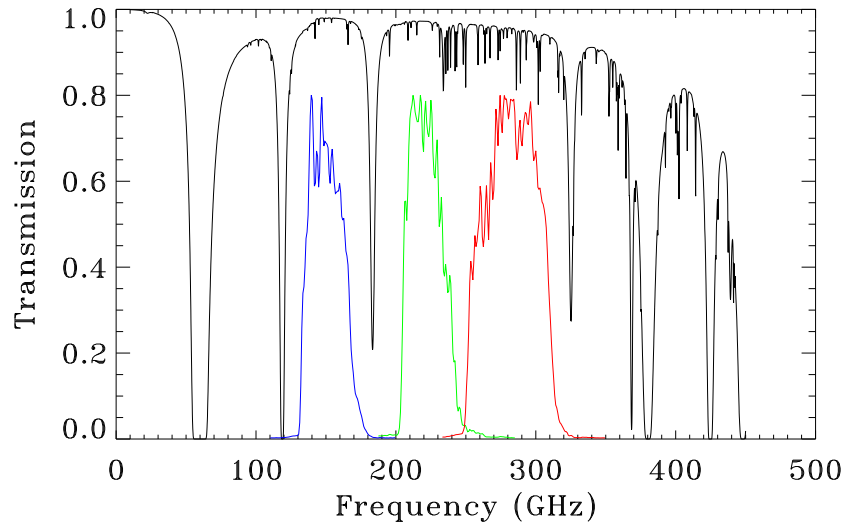


Figure 2.5: Model transmission spectrum for the South Pole during the winter (thin line) generated with the AT atmospheric modeling program [40]. Overplotted are the average of the 2002 ACBAR observing bands at 150, 220, and 280 GHz (colored lines). The spectral bands have been normalized to 0.8 for ease of visibility.

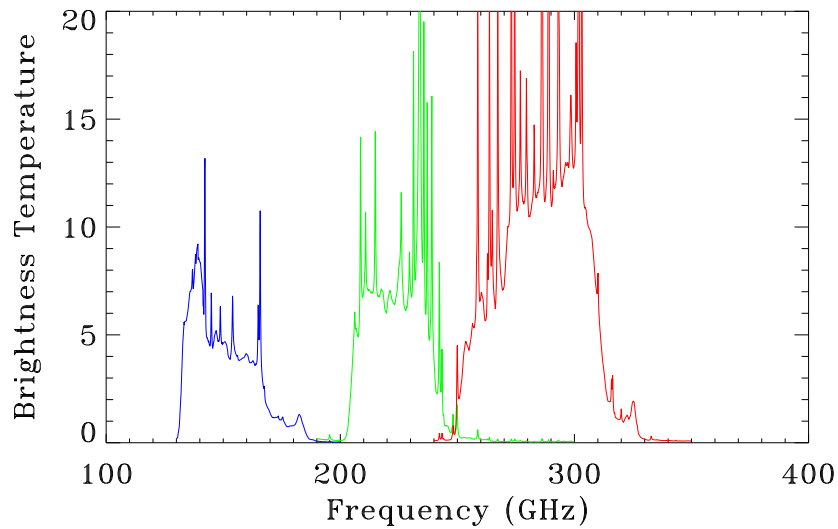


Figure 2.6: Zenith brightness temperature contribution to each of the 2002 frequency bands assuming a sky temperature of 260 K. The plot shows the continuum contribution along with a forest of narrow transition lines of ozone and other minor species. This plot was made by convolving the measured spectral bands of ACBAR with the model South Pole emission spectrum generated with the AT atmospheric modeling program.

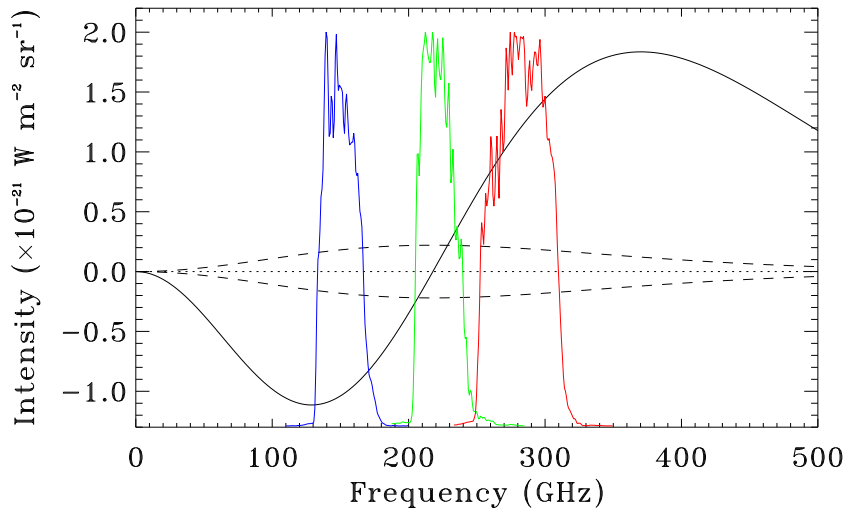


Figure 2.7: Shows the ACBAR spectral bands for 2002 over plotted on the thermal (solid) and kinetic (dashed) SZ intensity spectra. The model cluster parameters used are: Compton y parameter of 10^{-4} , optical depth of $\tau = 0.01$, and peculiar velocity of 500 km/s.

noise of our system and found the ratio of astrophysical signal to the quadrature sum of the detector noise and atmospheric noise as a function of band center and bandwidth. The 150, 280, and 350 GHz bands were optimized for detection of the SZ thermal effect by maximizing the SZ signal to the total estimated noise contribution as a function of band center and bandwidth. The 220 GHz band was optimized for detection of the SZ kinetic effect (which has the same spectrum as primary CMB anisotropies) while minimizing the contribution from the SZ thermal effect. In practice, however, relativistic corrections to the thermal spectrum will prevent the 220 band from cancelling the thermal emission for all cluster electron temperatures. Because of the constraints placed by atmospheric emission lines, the 150, 280, and 350 GHz bands are also well optimized for primary CMB fluctuations as well. Figure 2.7 shows the spectrum of the kinetic and thermal SZ effects along with the measured ACBAR frequency bands. One can see that the 220 GHz band straddles the SZ thermal null resulting in very little thermal contamination for measurements of either the kinetic SZ effect or primary CMB anisotropy.

As described above, the lower edges of the frequency bands are set by the diameter of waveguide cutoffs in the feed structures. The upper edges of the bands are defined with resonant metal-mesh filters [62] which are provided by the Astronomy Instrumentation group at Cardiff University. Metal-mesh filters suffer from resonant leaks at harmonics of

the cutoff frequency; these leaks must be blocked with additional filters. If left unblocked these high-frequency transmission leaks will couple to either warmer stages of the cryostat, or worse yet, hot objects outside the cryostat.

High-frequency leaks are particularly insidious because the thermal emission of warm objects in the Rayleigh-Jeans limit rises as ν^2 and the higher frequencies couple to multiple spatial modes ($A\Omega/\lambda^2 > 1$). If high-frequency leaks are not blocked at cold temperatures, their cumulative effects can rapidly increase the loading on the detector as well as couple to undesirable high-frequency astrophysical sources such as dust. These higher order modes also cause significant problems in polarization sensitive experiments by increasing cross-polarization response.

To block high-frequency leaks in ACBAR we use a combination of additional reflective metal-mesh filters and absorptive dielectric filters. There are very few filters available other than resonant metal-meshes for frequencies below about 1 THz. The ACBAR feed structure employs a combination of two metal-mesh filters to block the harmonic leaks of the band defining edge filter. The band defining edge filter and one blocking metal-mesh are mounted at 240 mK and the third metal-mesh and dielectrics are installed at 4 K (see Figure 2.4).

At very high frequencies the transmission of metal-mesh filters opens up. To block this high-frequency transmission we installed Pyrex disks in the 4 K feed structures which absorb light between 40 cm^{-1} and around 2000 cm^{-1} . The thickness of the Pyrex (and all of the dielectrics) is tuned for maximum transmission. For a slab of lossless dielectric in free space, the condition for maximum transmission (or equivalently, minimum reflection) is

$$t = \frac{m\lambda}{2n},$$

where n is the index of refraction of the material and m is an integer. The thickness of all of the dielectric filters in ACBAR is tuned to first or second order.

The combination of Pyrex and metal-mesh filters will still transmit above 2000 cm^{-1} and so we also installed a 55 cm^{-1} Yoshinaga filter [123] (otherwise known as an alkali halide filter). The Yoshinaga filter is a combination of powdered Thallium Bromide salt and carbon lampblack embedded in polyethylene. This filter is quite useful because it absorbs everything above 55 cm^{-1} (at least as far as 300 K blackbody emission is concerned). The full contingent of filters is listed in Table 2.2 starting from the detector.

All of the filters at 4 K and colder are held in place with threaded filter caps as seen in Figure 2.4. The filters are thermally sunk to their respective feeds using beryllium copper spring washers inside the filter caps. Proper heat sinking of the filters is very important because (at low temperatures) the heat capacity of the focal plane is dominated by the dielectrics in the filters. We also employ a blackened re-entrant light baffle across the thermal break between the 4 K feeds and 240 mK feeds. We use a thin layer of Stycast³ epoxy mixed with carbon lampblack known as “Bock Black” as the blackening agent [12]. This is applied to the 240 mK side of the light baffle to reduce optical loading from stray light coupling from high-frequency multimoded leaks exiting the sub-Kelvin feed.

During early feed structure testing, we measured a substantial ($\sim 3\%$) high-frequency leak in the system. We believed that some fraction of the leak could be from stray light making its way around the metal-mesh filters in the sub-Kelvin feed. The spacer between the two filters was originally made from OFHC copper because we were concerned about heat sinking the filters (see Figure 2.4). We decided to replace the copper spacer with a light absorbing material to try to damp any high-frequency light from making its way around the filters. We had new spacers fabricated from what we believed to be machinable Eccosorb but turned out to be grey polyurethane. The effect was as desired; the high-frequency leak vanished. The final feed design includes polyurethane spacers between the band-edge and first blocking metal-mesh filters.

The set of filters thus described provides sufficient filtering for the feed structure, but the cryostat itself requires additional filters to reduce thermal loading on the 4 K helium stage from the 300 K vacuum jacket. In 2002 we used a single 14 cm^{-1} metal-mesh blocker ($\varnothing 100\text{ mm}$ clear aperture) at 77 K to reduce the load from 300 K (see Figure 2.8). In 2001 we had an additional Yoshinaga filter at 77 K but we determined this filter was adding significant optical loading to our detectors and was thus removed. Although filters at 77 K are necessary to reduce helium boil off, they can be a tremendous source of optical loading and can even dominate over the loading from outside of the cryostat (as was the case for ACBAR in 2001). The key considerations for filters at 77 K are to minimize in-band absorption and/or reflection and to attempt to block all high-frequency multimoded leaks at cold temperatures before they are intercepted at 77 K.

The transmission spectra of ACBAR were measured with a Fourier transform spec-

³Emerson & Cuming, Billerica MA

Filter	Temp (K)	150 GHz	220 GHz	280 GHz
Blocker #1	240 mK	255 GHz	360 GHz	420 GHz
Edge	240 mK	169 GHz	235 GHz	300 GHz
Yoshi	4 K	1.6 THz	1.6 THz	1.6 THz
Pyrex	4 K	1.2 THz (0.019")	1.2 THz (0.026")	1.2 THz (0.021")
Blocker #2	4 K	234 GHz	360 GHz	420 GHz
Waveguide	4 K	131 GHz (0.053")	204 GHz (0.034")	252 GHz (0.0275")
Blocker #3	77 K	420 GHz	420 GHz	420 GHz

Table 2.2: Filter elements of ACBAR in the 2002 configuration. Frequencies denote approximate 50% transmission point of blocker, edge, and waveguide filters but correspond to roughly 10% points of Pyrex and Yoshi. Numbers in parentheses are thicknesses for Pyrex and diameter for the waveguide. The 77 K filter is one large metal-mesh filter mounted on the nitrogen can that all of the feeds look through. This upgraded filter arrangement differs from the 2001 configuration which did not have Blockers #2 or #3 or the Pyrex but instead used black-poly disks at 4 K. In 2001 the Yoshinaga filter was located in front of the feed structure at 77 K and contributed significantly to the internal loading of the system; it was replaced with smaller Yoshinaga disks within the feeds at 4 K for 2002.

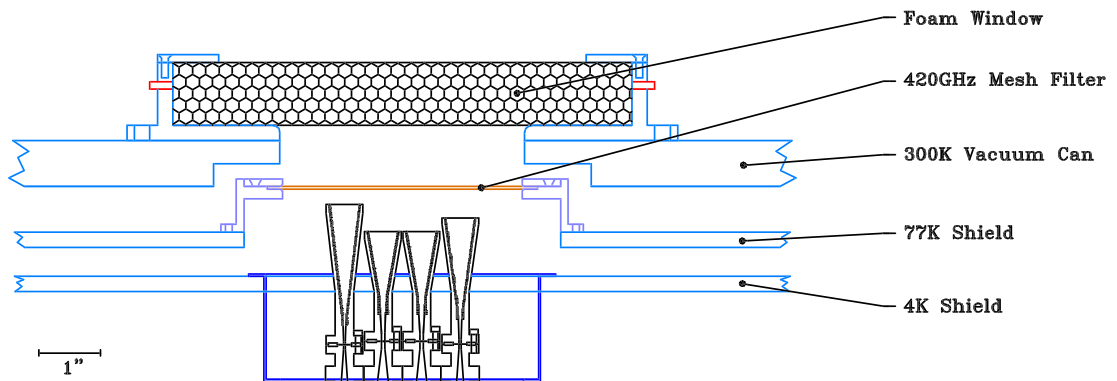


Figure 2.8: Shows the arrangement of the ACBAR warm filter optics in 2002.

trometer (FTS) at the South Pole and are shown in Figure 2.7. The measured transmission spectrum, $f_i(\nu)$, of band i has been corrected for the emission of the FTS source (ν^2 for RJ sources). The band centers are determined by

$$\nu_0^i = \frac{\int \nu f_i(\nu) d\nu}{\int f_i(\nu) d\nu}.$$

Measurements of bandwidth, such as the span in frequency at half the maximum value, tend to be qualitative since they depend strongly on the smoothness of the spectrum and its gross features. Spikes in a high resolution spectrum will affect the overall normalization, and hence, the half power points. In Table 2.3 we present the measured band centers and approximate bandwidths of the ACBAR 2002 frequency bands. The optical parameters during 2001 were approximately the same as those listed for 2002.

A very important parameter for characterizing an optical system is its optical efficiency, η , otherwise referred to as the quantum efficiency; this is the fraction of incident optical power that is transmitted through the filter stack and absorbed by the detector. Losses due to absorption or reflection from filters or poorly matched optical structures will degrade the optical efficiency of a system. The optical efficiency provides a normalization to the measured transmission spectrum from which a band averaged optical efficiency is calculated.

The optical efficiency can be determined by measuring the optical power incident on a detector by looking into two blackbody loads at different temperatures. One then compares the measured optical power difference with the optical power calculated by convolving the transmission spectrum with the spectral intensity of the two loads. The spectrum normalization optical efficiency is thus defined as

$$\eta_i = \frac{Q_1 - Q_2}{\int f_i(\nu) [B(\nu, T_1) - B(\nu, T_2)] A(\nu) \Omega(\nu) d\nu},$$

where $B(\nu, T)$ is the black body spectral energy density of an object at temperature T , Q is the measured optical power, and $A(\nu)\Omega(\nu)$ is the system throughput which is equal to λ^2 in the limit the system is single moded. For this measurement we used Eccosorb⁴ microwave absorbing foam (AN-72) at both room temperature (300 K) and liquid nitrogen temperature (77 K).

The band average optical efficiency is calculated by integrating the product of η_i and

⁴Emerson & Cuming, Randolph, MA 02368

Channel name	Bolo name	R_0 (Ω)	G_0 (pW/K)	β	ν_0 (GHz)	$\Delta\nu_0/\nu_0$ (%)	$\bar{\eta}$ (%)	τ (ms)
D5	150-02	128.3	390.4	1.10	150.1	21.0	40.5	2.2
D6	JPL-14	93.8	563.1	1.21	150.7	17.9	39.4	5.2
D4	150-07	139.4	351.6	1.12	150.3	21.0	39.8	2.3
D3	JPL-18	82.3	338.6	1.17	150.7	19.9	39.6	7.2
D2	345-05	159.8	668.4	0.99	-	-	-	-
B1	150-08	158.6	342.8	1.10	150.8	19.9	39.0	4.6
B2	150-12	198.4	365.4	1.07	151.1	17.9	43.9	2.0
B3	219-01	187.5	334.0	1.06	150.9	18.4	37.9	2.2
B6	150-09	216.4	325.7	1.05	150.4	18.4	37.1	3.4
B4	219-06	181.9	366.4	0.98	-	-	-	-
C4	219-08	179.3	359.9	1.14	222.1	15.2	26.2	7.2
C3	JPL-12	89.5	595.2	1.19	221.5	13.5	33.3	9.0
C2	219-11	114.4	324.0	1.20	224.2	13.4	28.9	2.3
C1	219-05	188.4	332.6	1.03	220.6	12.2	40.1	4.8
C6	274-02	144.4	859.7	1.05	-	-	-	-
A4	274-05	136.6	692.8	1.16	279.7	18.2	33.4	1.8
A6	274-03	159.0	539.9	1.11	282.3	18.3	28.1	1.4
A3	274-07	121.4	587.7	1.17	283.1	19.6	31.8	1.8
A5	274-09	134.0	699.5	1.17	285.4	15.2	29.2	2.0
A2	JPL-11	92.2	650.3	1.16	-	-	-	-

Table 2.3: ACBAR bolometer and optical parameters for the 2002 season. Dark bolometers have hyphens in the optical parameters. The detector impedance follows $R(T) = R_0 e^{\Delta/T}$ and the Δ for all of the bolometers is approximately 41.8 K. The thermal conductivity is defined as $G(T) = G_0 (T/T_0)^\beta$ where G_0 are normalized to $T_0 = 300$ mK. ν_0 is the measured band center and $\Delta\nu$ is the approximate half power bandwidth. $\bar{\eta}$ is the average optical efficiency across the $\Delta\nu$ bandwidth. τ are the effective optical time constants under operating conditions.

Channel	Taped	200 GHz	300 GHz	380 GHz	500 GHz
150 GHz	0.23%	0.59%	0.22%	0.19%	0.11%
220 GHz	0.07%	23.57%	0.72%	0.08%	0.07%
280 GHz	0.03%	25.71%	6.88%	0.06%	0.04%
350 GHz	0.09%	10.40%	28.77%	0.22%	0.14%

Table 2.4: Measured thick grill results for the 2001 season. Shows the ratio of the measured signal voltage for each thick grill (denoted by its nominal cutoff frequency in GHz) to the unfiltered signal voltage. The “Taped” column refers to the signal measured with a piece of aluminum tape over the source aperture rather than a thick grill and represents a baseline point for each frequency. The bold values are the most important for that frequency because they are the closest grill to the nominal upper band edge.

the transmission spectrum across the frequency band and dividing by the bandwidth. This number is also somewhat qualitative because it depends on one’s choice of the limits of integration and assumed bandwidth. The band averaged optical efficiencies for ACBAR’s 2002 configuration are also given in Table 2.3 where we have used the approximate half power points of the spectra as the limits of integration.

Another important characteristic of a feed system is the integrated above-band response (otherwise known as a “blue leak”). This measures the power response at frequencies above the nominal band edge that will couple to undesirable sources. To measure the out-of-band response of ACBAR we use a chopped thermal load with a small aperture and measure the signal with and without thick grill filters of varying cutoff frequency. Thick grill filters are plates of metal which have been densely drilled with many cylindrical waveguide holes. The filter acts like waveguide passing all light above the waveguide cutoff (modulo the filling factor of the drilled holes). Table 2.4 summarizes the average results of the thick grill tests for a chopped RJ source. The inclusion of additional blocking filters in 2002 reduced the high-frequency leakage to a level not measurable above the noise. Note that the thick grills do not isolate the frequency of the leak but merely give a lower frequency bound. Determining the actual magnitude of a leak requires knowing its frequency and correcting for the ν^2 brightness of the source.

2.1.4 Detectors

ACBAR detects optical power with extremely sensitive micro-mesh spiderweb bolometers developed by the Micro Devices Laboratory at JPL for the *Planck* satellite [75, 112].

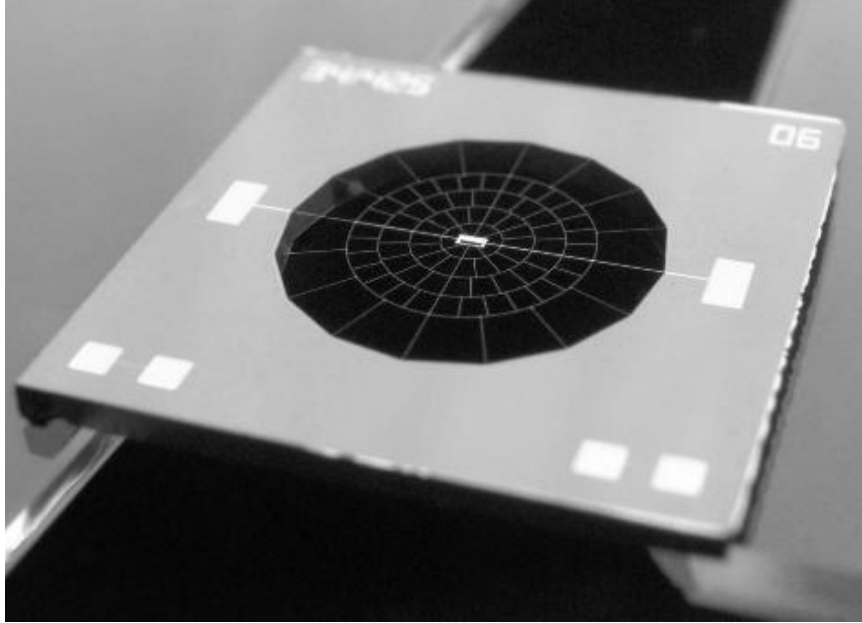


Figure 2.9: Closeup image of a bolometer very similar to those used in ACBAR. The spider web absorber is easily seen along with the NTD thermistor chip in the center. Image courtesy of J. J. Bock of the Microdevices Laboratory at JPL.

These detectors are optimized to detect broadband emission across millimeter-wavelengths. Bolometers provide the highest sensitivity and largest bandwidth in the far infrared through sub-millimeter wavelength range. The ACBAR bolometers are background photon noise limited (see the Noise section below) which allows us to take advantage of the excellent atmospheric conditions of the South Pole without being dominated by detector noise.

The ACBAR bolometers have silicon nitride micro-mesh absorbers with neutron transmutation doped (NTD) germanium thermistors. A picture of a bolometer very similar to the ones used in ACBAR is shown in Figure 2.9. The spiderweb geometry has very low heat capacity; this results in short detector time constants as well as reduces the cosmic ray cross section while efficiently coupling to millimeter-wave photons.

In steady state, a bolometer will obey the power balance equation

$$P + Q = \int_{T_{base}}^{T_{bolo}} G(T) dT,$$

where $P = IV$ is the electrical power applied to the bolometer, Q is the incident optical power, $G(T) = G_0(T/T_0)^\beta$ is the thermal conductivity referenced to some temperature T_0 , T_{base} is the baseplate temperature to which the bolometer is heat sunk, and T_{bolo} is the

operating temperature of the bolometer. Typical values of G_0 normalized to 300 mK for ACBAR range from 300-700 pW/K. The impedance of the NTD thermistor at temperature T is given by

$$R(T) = R_0 e^{\sqrt{\Delta/T}},$$

where R_0 depends on the geometry of the thermistor and Δ is a property of the doping of the Germanium. Typical values for ACBAR are $R_0 \sim 150 \Omega$ and $\Delta \sim 41.8 \text{ K}$.

These bolometers are normally current biased by placing them in series with load resistors with impedance large compared to the operating impedance of the thermistor and applying a bias voltage across the stack. Bolometers respond to increases in optical power by heating up, which lowers the impedance of the thermistor and causes a drop in the output voltage. The drop in detector impedance means there is less electrical power applied resulting in a slight cooling. This is referred to as electrothermal feedback and results in a shortening of the detector response time.

The time constant, τ , of a bolometer determines how quickly it will respond to changes in power [97, 73]. The nominal time constant of a bolometer of heat capacity C and thermal conductivity G is $\tau = C/G$. The effect of electrothermal feedback is to increase the effective thermal conductivity. This results in a smaller effective detector time constant, $\tau_e = C/G_e$, where G_e is given by $G_e = G - I^2(dR/dT)$. This is usually rewritten as $G_e = G - \alpha I^2 R$ with $\alpha = R^{-1}(dR/dT)$. For NTD thermistors obeying the impedance versus temperature relation above, we have $\alpha \sim -16 \text{ K}^{-1}$ for detectors with $\Delta = 41.8 \text{ K}$ operating at 350 mK. The effective detector time constant is a single pole filter in the detector responsivity, $S(\omega)$, to variations in optical power of frequency ω as

$$S(\omega) = \frac{S_0}{1 + i\omega\tau_e}.$$

The value of the DC responsivity, S_0 , for the operating conditions of ACBAR is typically $\sim -2.5 \times 10^8 \text{ V/W}$. The time constants of the optical bolometers during operation are also listed in Table 2.3.

The time constants of the detectors were measured on the telescope using a chopped compact thermal source mounted behind a hole in the tertiary mirror. The frequency of the chopper is varied from 5 to 200 Hz and we perform a digital lock-in to measure the detector signals at each chop frequency. The signals are then corrected for the measured

transfer function of the electronics and fit to the equation above to determine the *in situ* detector time constants. A more detailed discussion of measured detector time constants is provided in the Transfer Function Appendix.

The properties of a bolometer can be measured by slowly ramping the bias voltage and measuring the output voltage of the detector to produce a load curve. Analysis of load curves can provide all of the bolometer parameters of interest (R_0 , Δ , G_0 , β) including the absorbed optical power. The analysis of load curves is discussed in detail in the Appendix. Examples of load curves, responsivity curves, and detector noise versus bias measured with ACBAR on the telescope in 2002 are shown for each of the four rows of detectors in Figures 2.10 through 2.13. The non-ohmic shape of the load curve is due to the applied electrical power heating the thermistor and causing a decrease in DC signal voltage. The bias current applied to the ACBAR detectors on the telescope is about 2–3 nA which puts the operating point near the peak of the load curve. This is beneficial because it makes the response of the detector insensitive to small changes in atmospheric loading while achieving near minimum detector noise (as discussed below). The measured bolometer parameters for all of the ACBAR detectors used in the 2002 season are listed in Table 2.3.

2.1.5 Telescope Optics

The Viper telescope (Figure 2.14) is located at the South Geographic Pole and is administered by the Center for Astrophysical Research in Antarctica. Viper is an off-axis aplanatic Gregorian telescope which has a re-imaging tertiary mirror to reduce the effective focal length. Viper has a 2 m diameter primary mirror and additional 0.5 m skirt around the primary to reduce ground spillover. There is a chopping flat mirror located at the image of the primary formed by the secondary mirror which sweeps the beams approximately 3° on the sky without modulating the beams on the primary.

The re-imaging tertiary on the Viper telescope was originally designed for low frequency (45 GHz) observations of the CMB for which aberrations were not significant. The tertiary had to be redesigned to provide sufficient optical quality across a large field of view at ACBAR's higher frequencies. The redesign of the Viper telescope optics is described in more detail in the Appendix. After the redesign, the telescope has an effective focal length

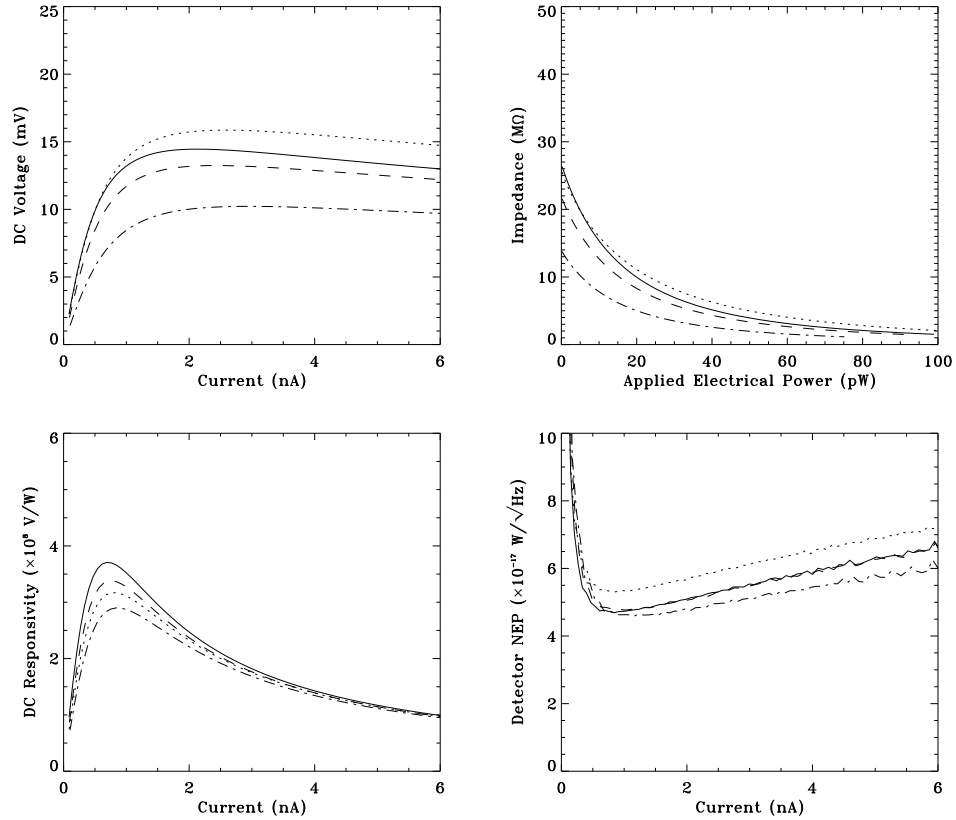


Figure 2.10: Load curves from one channel (D row - 150 GHz) of ACBAR on 03/21/02. These are for the four optically loaded detectors while on the Viper telescope with a base-plate temperature of 232 mK looking at 60° elevation. The different line types separate the four detectors in each row. The upper left panel is the signal voltage versus bias current load curve. The upper right panel shows the impedance of the detectors versus applied electrical power. The lower left panel is the DC responsivity of the detectors versus bias current. The lower right panel is the detector NEP which includes both the Johnson and Phonon noise contributions versus bias current. The detector is shunted by two $30\text{ M}\Omega$ load resistors as illustrated in Figure 2.23.

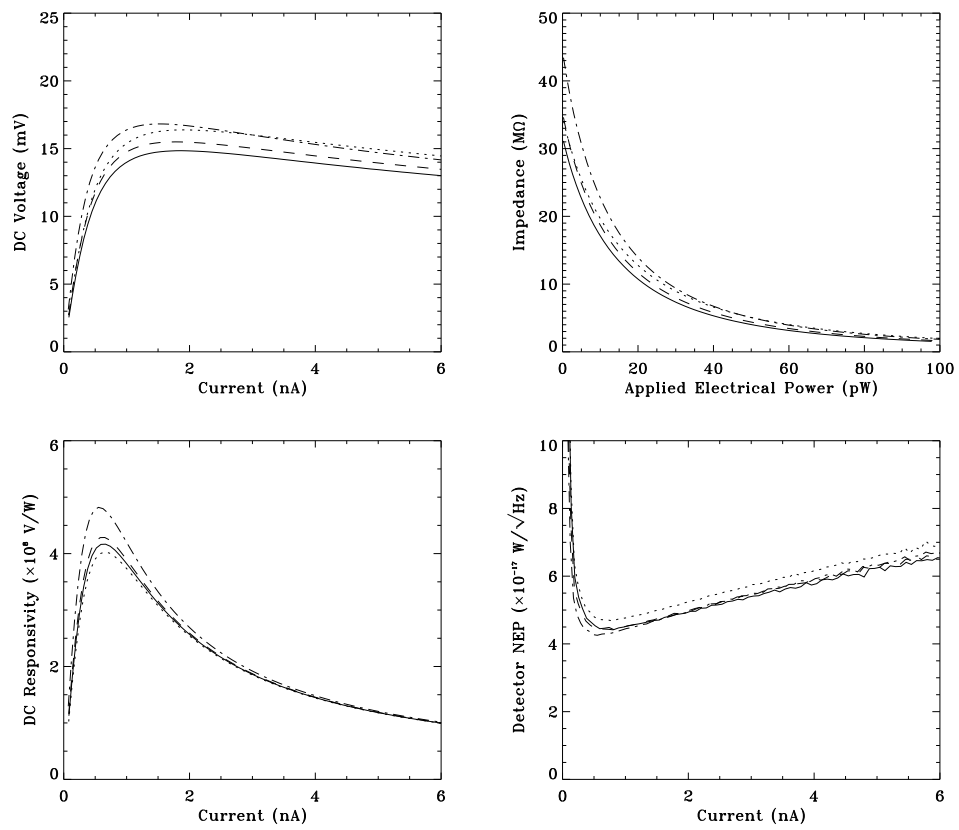


Figure 2.11: Same as Figure 2.10 but for the B-row of 150 GHz detectors.

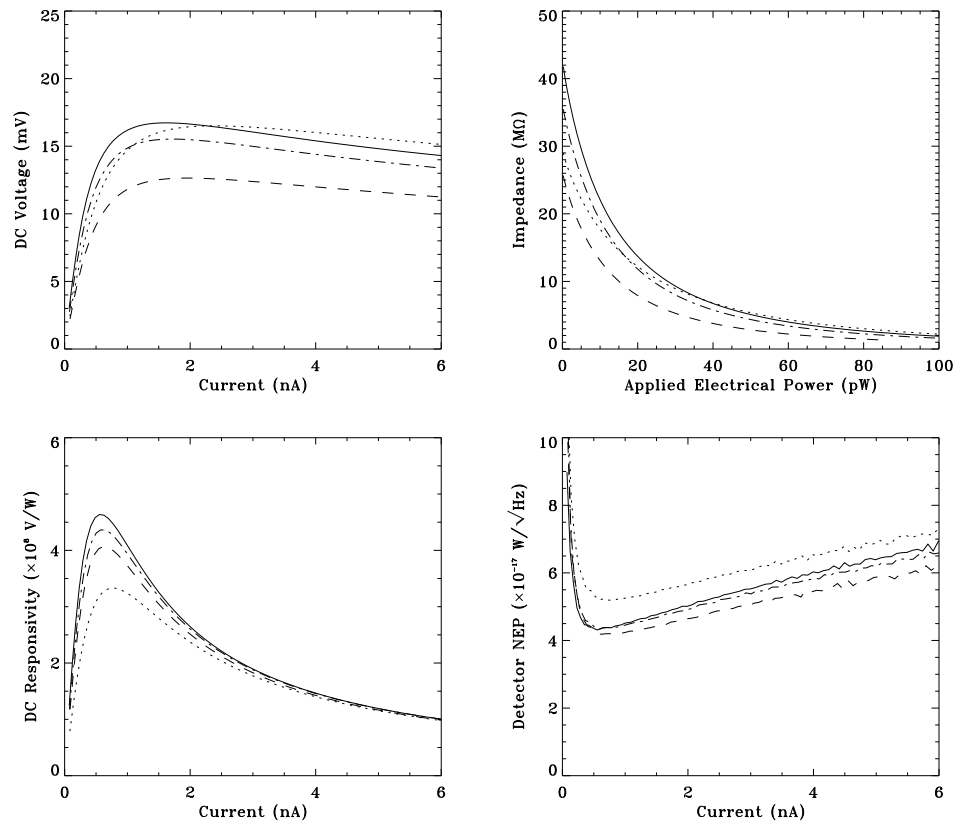


Figure 2.12: Same as Figure 2.10 but for the C-row of 220 GHz detectors.

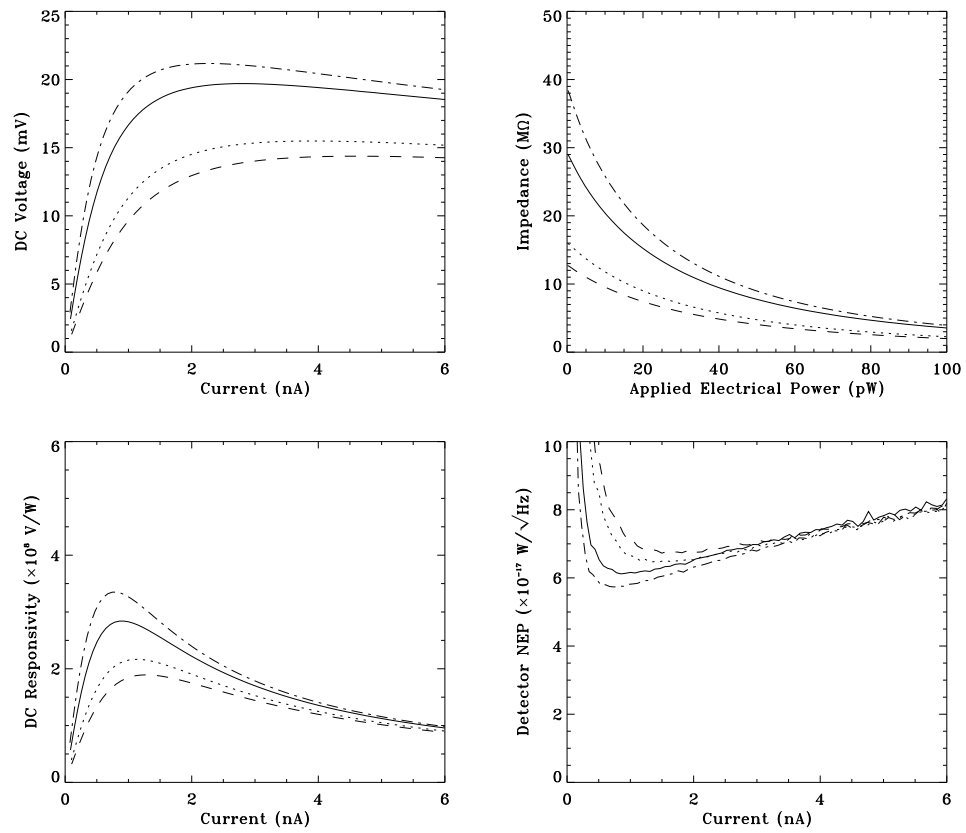


Figure 2.13: Same as Figure 2.10 but for the A-row of 280 GHz detectors.

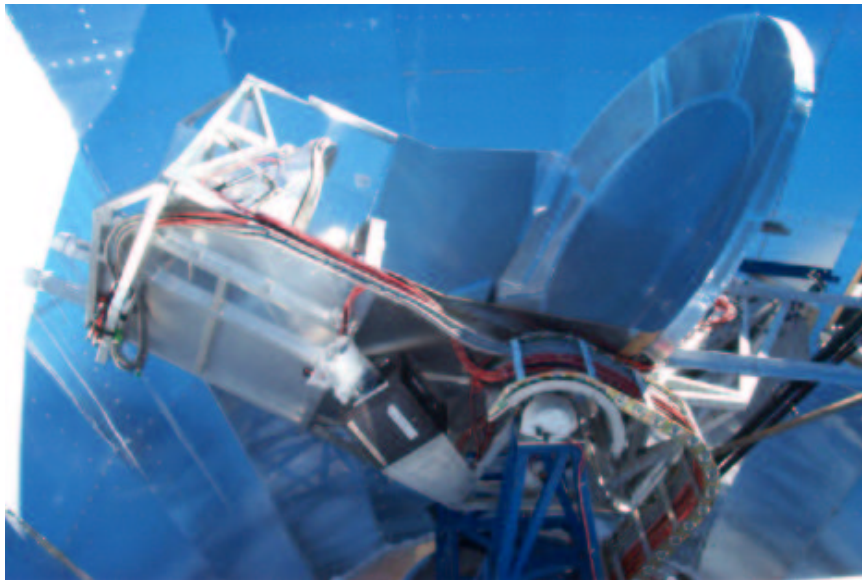


Figure 2.14: The Viper telescope without an instrument installed.

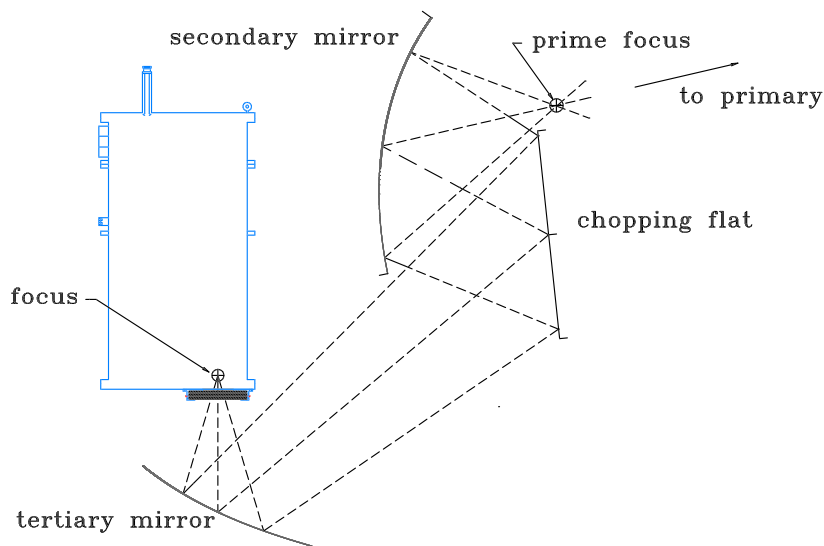


Figure 2.15: Most of the Viper telescope optics along with the ACBAR dewar. The light rays are the geometrical optic rays for full illumination of the primary and are shown to illustrate the tight clearance around the prime focus.

of 3.44 m yielding a plate scale of

$$PS = \frac{1}{F_{eff}} \sim 10' / \text{cm}.$$

This means that the 16 mm separation of feeds on the ACBAR focal plane will produce beams separated by roughly $16'$ on the sky.

Figure 2.15 shows a schematic of a subsection the Viper telescope optics along with the ACBAR receiver. The rays drawn are the extreme geometric optical rays to illustrate the tight clearances of the system; the actual Gaussian beam widths are much more narrow than the lines drawn. With full illumination of the 2 m primary, the focal plane is fed at $f/1.7$ in the geometric optics limit. The dewar is mounted on a sliding pillow-block mount with a linear actuator for controlling the distance between the tertiary and the dewar for focusing.

The chopping flat mirror sweeps the beams across the sky approximately 1° for every 2.2° of chopper rotation. The position of the chopper is read out with an encoder and is controlled to trace a triangular chop with a PID loop. The triangle wave results in a constant velocity chop across the sky. During the 2001 season we used an RVDT encoder⁵

⁵Schaevitz Sensor, model #R30A

as both the control signal and position signal which turned out to be a critical mistake.

The RVDT suffered from two major problems that caused the dominant source of pointing error. First, a drift in the zero point voltage of the encoder caused the position on the sky corresponding to zero volts to change with time. This drift was rather slow (about $10'$ per month) and we were able to fit for it because we observed bright galactic sources multiple times per day. The second more serious problem was that the gain of the encoder, in volts per degree of rotation, fluctuated with time on the level of about 8%. The gain of the chopper was roughly bimodal, falling into a high gain or low gain state. The only way to determine the gain state the chopper was to look at the separation of a bright object (in volts) between two adjacent channels and determine the scaling. The gain was observed to change during the course of a multi-hour observation and thus the 8% gain uncertainty will produce an error of approximately $7'$ at the edge of the chop. The RVDT encoder gain is also nonlinear which significantly complicates the conversion of volts to degrees with a drifting voltage offset and fluctuating gain. To remedy this we installed an optical encoder⁶ for 2002 which solved all of these problems. The gain of the optical encoder is very linear with the quadratic term approximately 0.1% of the linear term and no measurable gain fluctuation. The RMS pointing error during 2001 was approximately $1.3'$ and the RMS for 2002 is slightly less than $30''$.

The telescope is enclosed in a large conical ground shield that reflects telescope spillover to the sky. This reduces both loading and modulated sidelobe signal. We determined that the ground shield only obstructs observations below $\sim 25^\circ$ elevation by measuring the angle at which skydips deviated from the nominal equation. However, one section of the ground shield – known as the “moon door” – lowers to allow observations of low elevation sources; this is necessary to observe planets which do not rise higher than $\sim 30^\circ$ above the horizon at the pole. Unfortunately, the duration of unobstructed observation of a source through the moon door is limited to ~ 90 minutes per day. This is enough time to make high signal to noise maps of bright sources such as planets.

Viper sits atop a six legged diagonal mount with a walkway to the control room. It was discovered during summer of 2001 observations that as the sun circles around the horizon the thermal contraction of the support legs causes a differential tilt of a few arcminutes. To mitigate this effect we wrapped the support legs in reflective foil to reduce their emissivity.

⁶Gurley Precision Instruments, model #A25S

Differential thermal contraction is not an issue during winter observations when the sun is below the horizon.

The telescope rides on three wheels atop a hardened steel azimuth bearing. This bearing is leveled to a few arcminutes with respect to the celestial equator and the residual tilt must be corrected for in the pointing model. In addition, the telescope is approximately 1 km away from the actual geographic pole; this is also accounted for in the pointing model. The actual geographic coordinates were measured using a GPS unit to be $-89^{\circ}59'34.9''$ latitude and $45^{\circ}31'30''$ west longitude.

The elevation is controlled by a combination of two screw actuators. The “fine actuator” controls the elevation of the telescope during observations with a 45° range and the “course actuator” is set to either the lower position (allowing 0° to 45° elevation) or the upper position (allowing 45° to 90°). A servo-controlled PID loop controls the positioning of the AZ and EL positions with power supplied by Techron amplifiers. All temperature sensitive components of the telescope are temperature controlled to ~ 300 K. All of the mirrors are equipped with heaters for sublimating the thin layer of ice that accumulates over time. Blowing snow collects on most mirrors and must be cleaned off daily because it contributes to chopper synchronous offsets as well as signal attenuation, as discussed below.

We developed a telescope pointing model using frequent observations of both galactic and extragalactic sources. This allows us to reconstruct the position of each beam on sky using the reported AZ and EL encoder positions. The pointing model incorporates the distance of the telescope from the geographic pole, the tilt of the azimuth ring, flexure of the telescope with elevation, and the collimation offsets between the radio beams and nominal telescope boresight position. As discussed below, the RA and DEC chopper functions are then used to translate the measured chopper position into an instantaneous beam position for all 16 optical channels.

2.2 Cryogenics

2.2.1 Dewar

The ACBAR dewar (Figure 2.16) is a liquid helium/liquid nitrogen cryostat. The environs at the South Pole are quite harsh with the outside temperature routinely dropping below -100°F during the austral winter. To minimize the frequency of cryogen transfers, we made

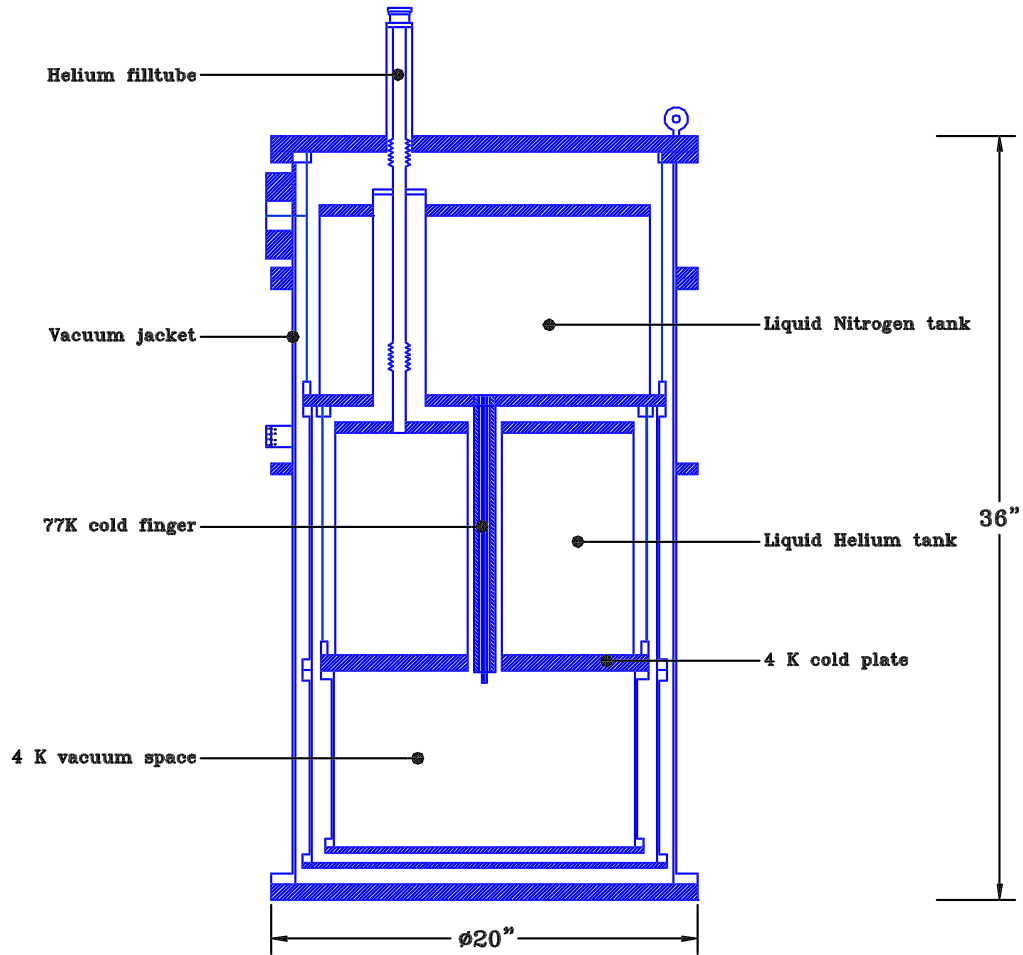


Figure 2.16: Schematic of the ACBAR dewar.

the cryogen capacity of the dewar as large as would reasonably fit on the telescope structure. The dimensions of the ACBAR dewar are $\varnothing 20''$ in diameter and 36'' in length (excluding cryogen fill tubes). Both the helium and nitrogen tanks hold 25 liters of liquid and the 4 K cold space is $\varnothing 14.15''$ by 8.25'' high. During normal operation the liquid helium holds three days including fridge cycles (described below) and the liquid nitrogen holds about one week.

Because the ambient temperature outside is so cold, we mounted adhesive sheet heaters to the dewar and electronics boxes as well as surrounded the instrument with custom-made insulating blankets to keep the temperature above 260 K; a single cool-down to -100°F could permanently damage the electronics. This nominal temperature is still quite cold and could freeze ordinary rubber o-rings. A leak in the dewar during the winter would

halt observations for at least a few weeks. Hence, we needed o-rings with a low operating temperature and low permeability to helium gas. We selected Ethylene Propylene (EPDM) o-rings⁷ which are rated to below 250 K. After nine months of observing, ACBAR had a mere 15 torr of pressure at room temperature upon warm-up. We noticed that the o-rings had permanently deformed after nine months of observing and so we replaced all of them for the second season.

The ACBAR 4 K radiation shield design uses a re-entrant section to meet the 4 K scalar feed plate rather than mount a large filter in the top of the 4 K shield with the feeds looking through it. This design has two main advantages. First, only the 16 small waveguide apertures of the feeds enter the 4 K cold space; these are heavily filtered which greatly reduces stray optical power in the 4 K space that could load the fridge or bolometers. The second benefit comes from the reduction of RFI entering the 4 K space by forming a contiguous Faraday shield.

A number of factors influenced the decision to use a foam vacuum window on the dewar rather than a thin sheet of dielectric (such as Mylar). Our first concern was scattering of the beam from thin dielectrics which would result in increased spillover and modulated sidelobe response. The dewar window is also quite large (4" clear aperture; see Figure 2.8) and we were concerned about the strength of the window as well as its permeability to helium gas. We measured the off-axis scattering, transmission, and helium permeability of many materials and selected 1.2" thick Zotefoam PPA30 as our window material. This foam is a nitrogen extruded polypropylene that has very good transmission ($\sim 99\%$ at 150 GHz) and low scattering at millimeter wavelengths. The foam is quite strong and has an unmeasurably low permeability to helium gas. We used Stycast to seal the foam to an aluminum mounting ring. The window deformed permanently when the dewar was first evacuated with an inward deviation of $\sim 0.75''$ for the 4" aperture.

2.2.2 Fridge

The sensitivity and speed of bolometers depend strongly on their operating temperature. We want to run the bolometers at an operating point where the detector noise is below the expected photon background limit. This requires a base temperature below ~ 300 mK which is not difficult to achieve with a ^3He sorption fridge. ^3He fridges have historically

⁷Valley Seal Co., Woodland Hills, CA 91367

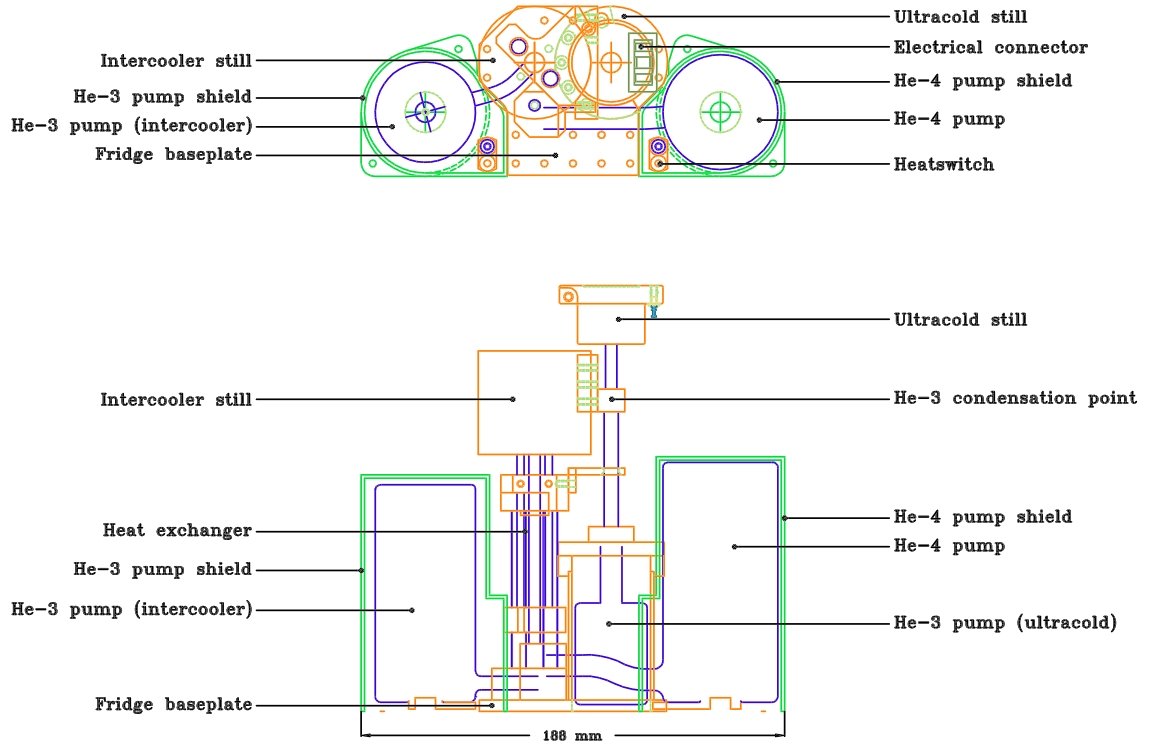


Figure 2.17: Schematic of the $^4\text{He}/^3\text{He}/^3\text{He}$ fridge built by Chase Research employed in ACBAR for cooling the detectors to 240 mK. Figure courtesy of S. Chase.

operated from pumped liquid helium baths. The added complexity of pumping on the ACBAR helium bath while mounted on the telescope was unattractive and thus we sought an alternative solution for our detector cooling requirements.

In collaboration with the Polatron [88] and Bolocam [31] projects, Chase Research has developed a three stage $^4\text{He}/^3\text{He}/^3\text{He}$ fridge system – affectionately referred to as the ^{10}He fridge – that achieves base temperatures below 240 mK from an unpumped helium bath and was selected for cooling the ACBAR bolometers. The fridge is described in detail in Bhatia et al. (2001) and is shown schematically in Figure 2.17.

The fridge is cycled by first condensing ^4He and using the enthalpy of that liquid to condense the ^3He in the ultracold stage. The ^4He section is then re-cycled and used to condense the ^3He in the intercooler stage. The ^4He liquid is exhausted in this process and does not contribute to steady-state base temperatures. During normal operation the intercooler stage operates at ~ 370 mK for approximately 32 hours and the ultracold stage operates near 240 mK for a longer duration. The fridge is recycled when the intercooler is

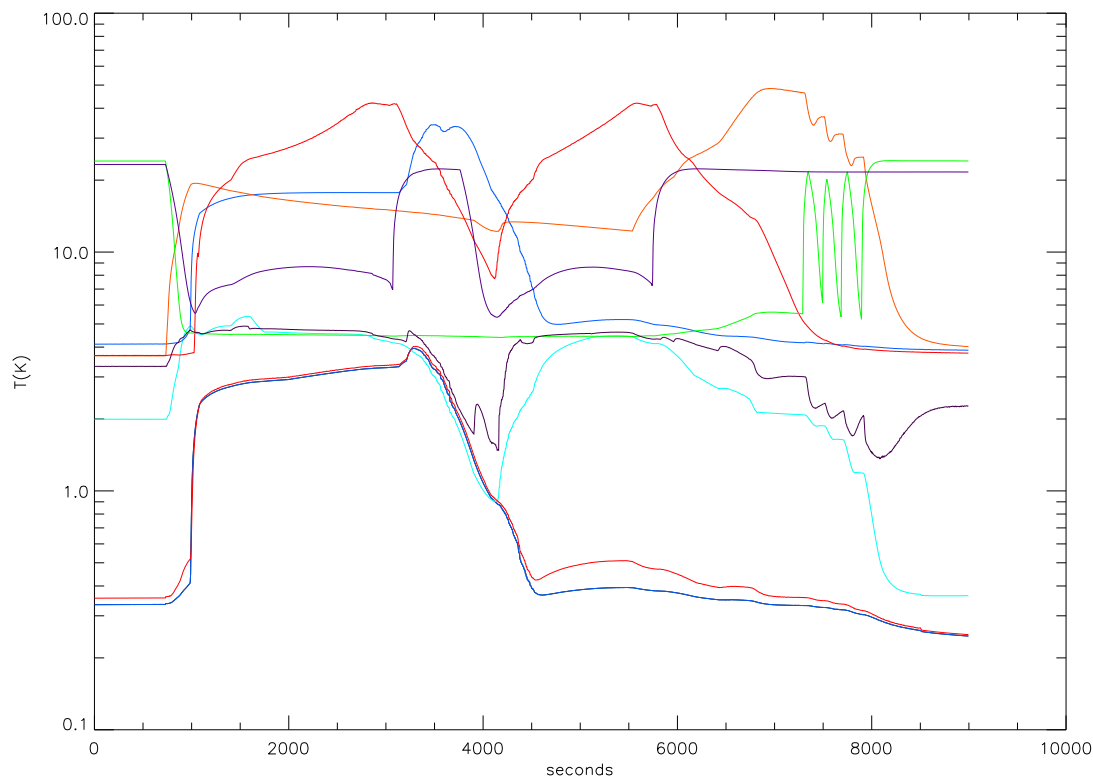


Figure 2.18: Shows all of the temperatures of the fridge during a cycle while attached to the focal plane. Lines below 4 K correspond to (royal) ultra still, (red) bolometer stage, (aqua) inter still, (black) heat exchanger. Lines above 4 K are (red) ^4He pump, (orange) inter pump, (royal) ultra pump, (green) inter pump heatswitch, (navy) ^4He pump heatswitch. The vertical axis is temperature in Kelvin and the horizontal axis is time in seconds.

exhausted and takes about three hours from the start of the cycle to below 250 mK. A plot showing the temperatures of the various fridge elements during the cycle is shown in Figure 2.18. Figure 2.19 shows load curves taken on the intercooler and ultracold stages without the focal plane attached. The load curves were generated by dissipating a known amount of power on a resistive heater mounted to each cold still and measuring the corresponding still temperature with a GRT thermometer.

Sorption fridges work on the principle that lowering the pressure above a liquid allows the molecules with more kinetic energy to escape thus cooling the liquid until the vapor pressure equals the pressure above the liquid. This is the same principle that makes cooking pasta at higher elevations difficult because water boils at a substantially lower temperature. This effect has an added benefit for ACBAR at the Pole because the 9,200' elevation pumps the liquid helium bath and drops its temperature to ~ 3.9 K instead of the 4.2 K at sea level pressure. This small change in baseplate temperature greatly improves the condensation

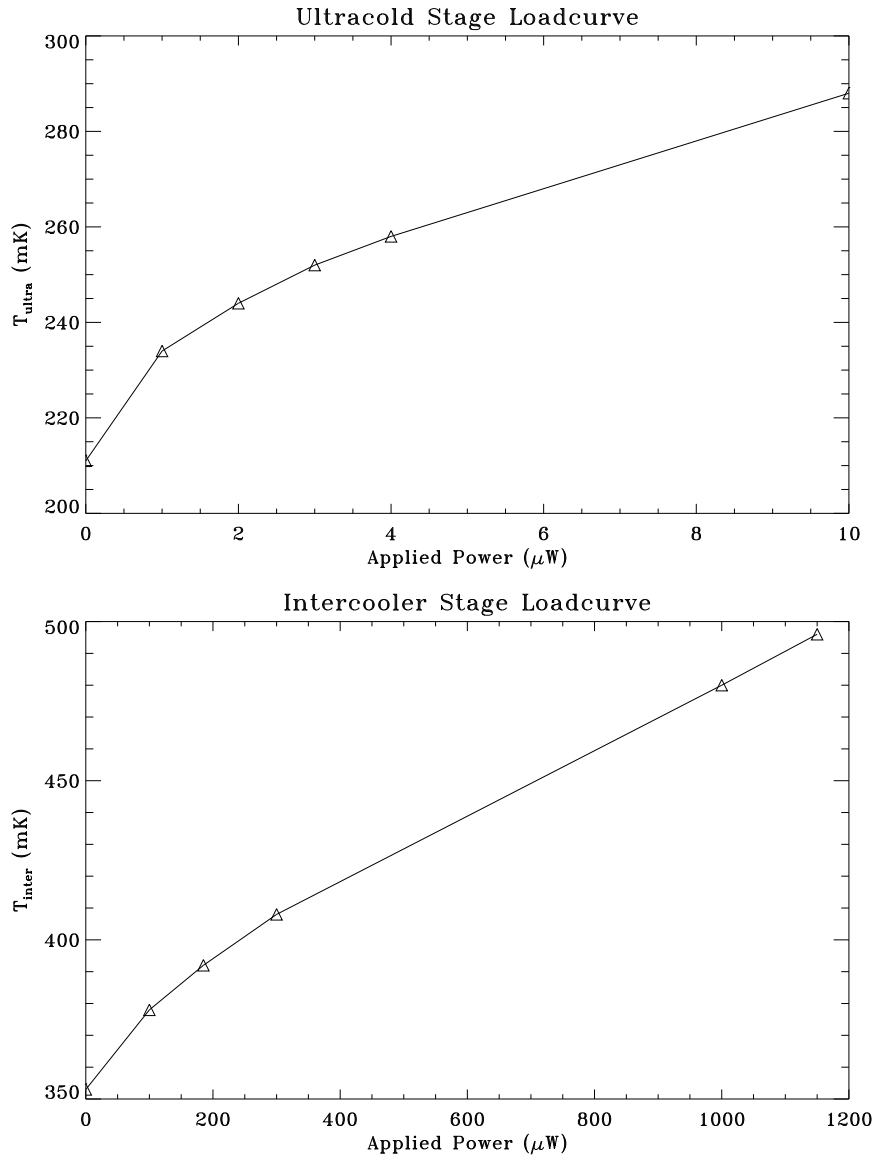


Figure 2.19: Fridge load curves for both the intercooler and ultracold stages of the ACBAR fridge. The plots show the temperature of the stages as a function of applied electrical power. Power is only applied to one stage at a time.

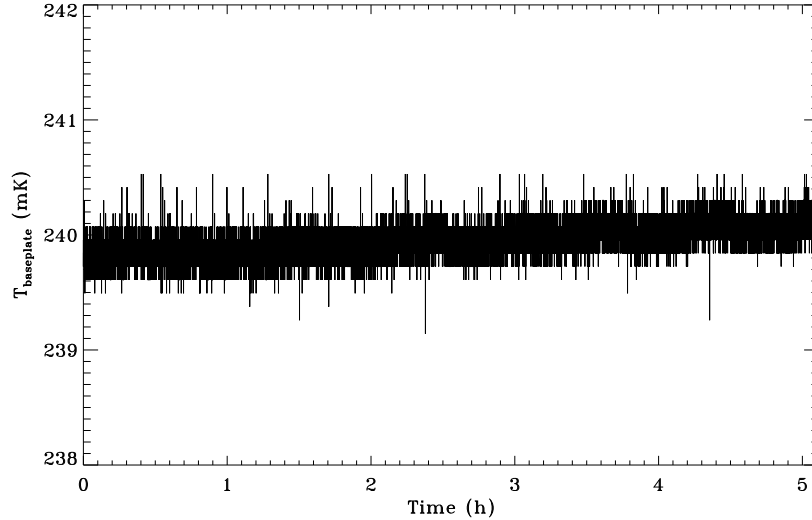


Figure 2.20: Shows the stability of the bolometer baseplate temperature over the course of a 5 hour observation. The RMS of the temperature is about 0.1 mK. Digitization noise in the A/D can be seen in the data.

efficiency of the fridge cycle which doubled the hold time of fridge compared to the hold time achieved in Berkeley during system integration.

The bolometer baseplate temperature provided by the ultracold still is remarkably stable. Figure 2.20 shows the temperature of the baseplate over the course of a 5 hour observation. One can see that there is very little drift in the baseplate temperature and the scatter has an rms of $\sigma \sim 0.1$ mK. Because ACBAR is mounted directly on the telescope, we were concerned about variations in baseplate temperature with the angle of the telescope. We requested that copper sinter be included in the stills to improve the coupling of the liquid in the stills to the metal housing. Figure 2.21 shows the baseplate temperature as a function of zenith angle during the course of a skydip which shows that there is very little change in bolometer baseplate temperature over 75° of dewar angle change.

2.2.3 Thermal Isolation and Heat Sinking

The limited cooling capacity of the fridge requires us to restrict the thermal loading on the bolometer stage to a few microwatts of power. The challenge is to rigidly support the massive copper focal plane as well as read out all 24 bolometer channels and associated thermometry while keeping the thermal load on the fridge to a few μW .

Figure 2.22 shows an image of the ACBAR focal plane structure. The scalar feeds are

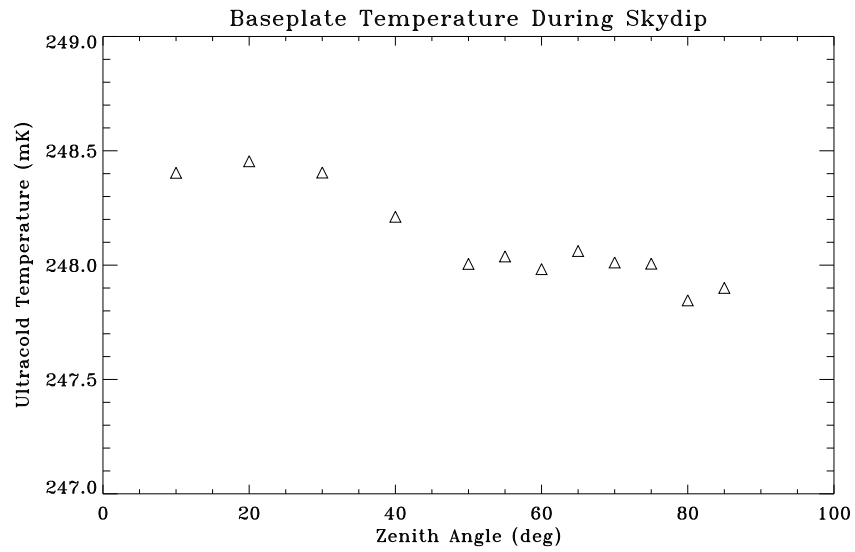


Figure 2.21: Shows the temperature of the ultracold bolometer baseplate during a skydip. The variation in temperature is less than 1 mK over 75° of elevation change.

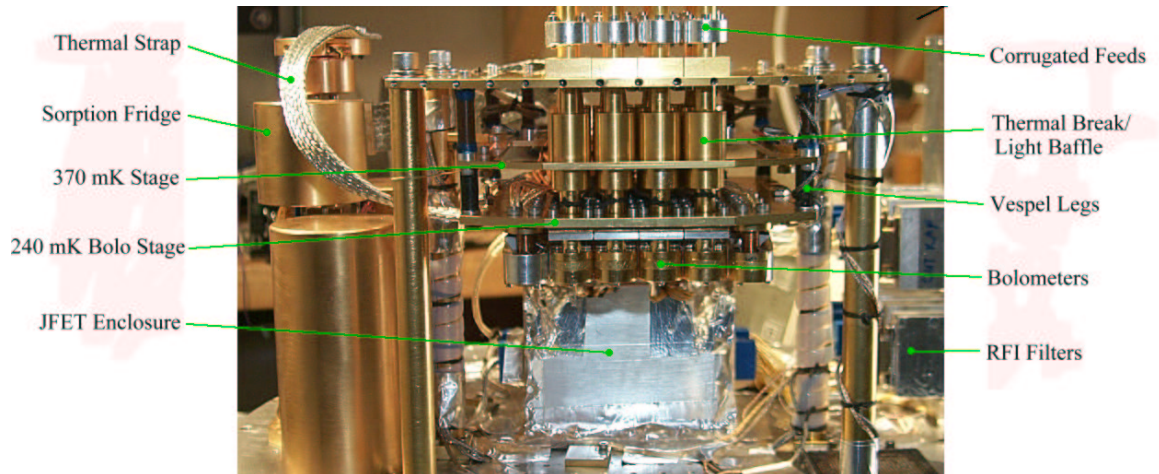


Figure 2.22: Picture showing the different elements of the ACBAR focal plane.

mounted on a gold plated aluminum plate which is rigidly fixed to the 4 K helium cold plate via $\varnothing 0.5$ " gold plated copper rods. The structural support of the cold focal plane is provided via Vespel⁸ stand-offs machined to $\varnothing 0.25$ " and 0.015" thickness with aluminum end caps. Vespel is a low thermal conductivity plastic which can be easily machined to thicknesses as small as 0.01". We use the cooling power of the 370 mK intercooler still as a thermal buffer ring between the 4 K horn plate and the 240 mK detector stage. This intercepts most of the thermal power that would otherwise overwhelm the small heat lift of the ultracold stage.

There are multiple types of Vespel available with different temperature indices for the thermal conductivity. Vespel SP-1 (brown) has a thermal conductivity below 4 K of approximately $1.8 \times 10^{-5} T^{1.21} \text{ W cm}^{-1} \text{ K}^{-1}$ and Vespel SP-22 (black) is $1.7 \times 10^{-5} T^{2.0} \text{ W cm}^{-1} \text{ K}^{-1}$ [25]. We use SP-1 between 4 K and 370 mK and SP-22 between 370 mK and 240 mK. We estimate the thermal loads from the Vespel legs to be $\sim 40 \mu\text{W}$ on the Interhead (370 mK) and $\lesssim 0.1 \mu\text{W}$ on the Ultrahead (240 mK).

Flexible thermal straps (see Figure 2.22) are used to couple the fridge stills to the two thermal stages. These are made from nickel-plated copper-braid shields that were lying around the lab in which indium is embedded at each end for clamping. We originally used OFHC copper straps between the fridge and focal plane cold stages but found that the mechanical resonances of the fridge strongly coupled to the focal plane inducing microphonics in the signal band.

All of the isothermal wiring inside ACBAR is Teflon-coated gold-plated copper wire and all of the wiring that traverses multiple temperature regions is Teflon-coated stainless wire. Both of these are surgical quality wires manufactured by Cooner Wire⁹. The stainless wiring is bundled into six twisted pairs within a common stainless shield (corresponding to the six bolometer channels per bias) with no outer jacket. Stainless wiring has low thermal conductivity but also has relatively high resistance; all of the wiring for high current devices (such as pump heaters) must be doubled up to reduce the thermal power dissipation in the wiring. All of the wires joining stages at different temperatures are heat sunk at each stage by embedding the wires in a gold-plated copper tab with Stycast¹⁰ epoxy. The stainless wiring is estimated to contribute less than $50 \mu\text{W}$ of power on the intercooler stage and

⁸DuPont Engineering Polymers, Newark, DE 19714-6100

⁹Chatsworth, CA 91311

¹⁰Emerson & Cuming, Randolph, MA 02368

around $0.5 \mu\text{W}$ on the ultracold stage.

2.2.4 Thermometry

ACBAR uses three different types of thermometers inside the cryostat; all of these are manufactured by Lake Shore Cryotronics, Inc¹¹. For temperatures between ~ 4 K and 300 K we use two-wire silicon diode thermometers. These are used on both cryogen tanks, the JFET module, all three fridge pumps, and the two heat switches. On the cold stills of the fridge, we use calibrated four-wire germanium resistance thermometers (GRT) which are useful for temperatures below 4 K. The ultracold bolometer stage is equipped with a calibrated four-wire Cernox RTD which is only accurate to ~ 5 mK but has a useful dynamic range from 230 mK to a few hundred Kelvin. This Cernox thermometer is particularly useful because we can monitor the temperature of the bolometer stage during cool down as well as measure its temperature during normal operation with the same sensor. Note that a typical Silicon diode thermometer biased with $10 \mu\text{A}$ dissipates $\sim 20 \mu\text{W}$ at sub-Kelvin temperatures which, as seen in Figure 2.19, would warm the bolometer baseplate well above 300 mK.

2.3 Electronics

2.3.1 Signal Electronics

The ACBAR electronics system is designed to provide DC bias across the bolometers and read out all 24 channels with clean signal bandwidth from DC to ~ 100 Hz. Figure 2.23 shows a schematic of the ACBAR signal electronics chain. The DC bias board supplies a low noise voltage between 0 to 0.5 V symmetrically across the bias resistor stack. There are four bias voltages – one for each row of detectors – which can be set independently and are applied to six detectors each. Two sets of twisted pair stainless wires (one set for redundancy) bring each of the bias voltages to the focal plane where they are broken out to six detectors each. All isothermal cabling on the focal plane is gold-plated high-purity copper.

In addition to the optically loaded bolometers, each of the four biases is also applied to a “dark bolometer” (a bolometer which has been blanked off with a blackened load at 240

¹¹Westerville, OH 43082

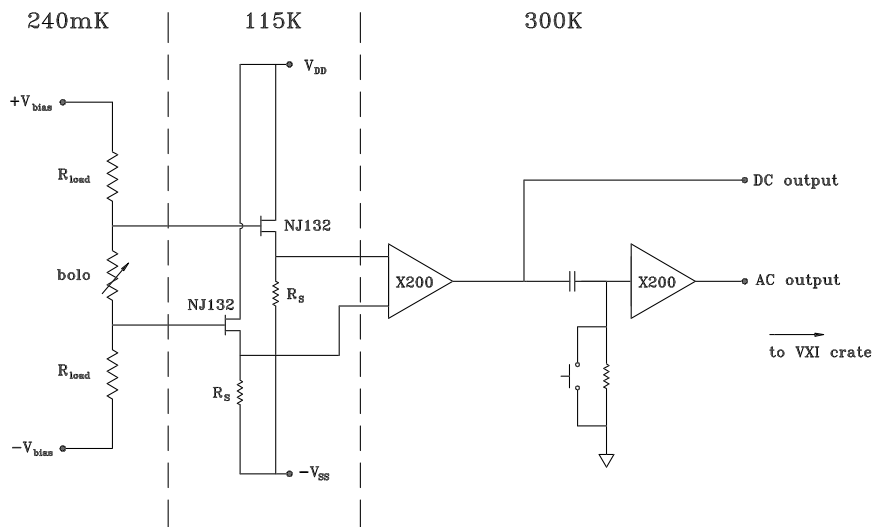


Figure 2.23: A schematic of the ACBAR signal electronics chain. Dashed vertical lines denote thermal boundaries.

mK) and a “fake bolometer” (a resistor in place of the bolometer) for use as monitors of baseplate thermal drifts and electronics noise.

Each bolometer is in series with two 30 M Ω precision etched metal film load resistors which were custom made by Mini-systems, Inc.¹² The load resistor package is surface mounted to a PCB board (shown in Figure 2.24), which is epoxied directly to the back of the bolometer module at 240 mK. Also mounted on the PCB board is an EMI filter on each side of the bolometer composed of surface mount 47 nH inductors¹³ and 10 pF capacitive feed-through filters¹⁴ which provides filtering above a few hundred MHz directly on the bolometer module.

The bolometer signal voltages are sent to the JFET modules on twisted pair stainless wires. All bolometer signals of a common bias are carried out in a single bundle of six twisted pairs. Each side of the bolometer voltage is sent into one side of a matched NJ132 JFET follower pair. The JFETs were manufactured by Interfet¹⁵ and were matched to have less than ~ 20 mV difference in offset voltages. The JFETs buffer the bolometers by reducing their output impedance. This significantly reduces the susceptibility to sources of current noise such as microphonic pickup and RFI. The JFET module is housed in a blackened box mounted on the 4 K cold plate. It is thermally isolated from a 77 K cold

¹²Attleboro, MA 02703

¹³muRata part #LQP21A47NG14

¹⁴muRata part #NFM839R02C100R470

¹⁵Garland, TX 75042

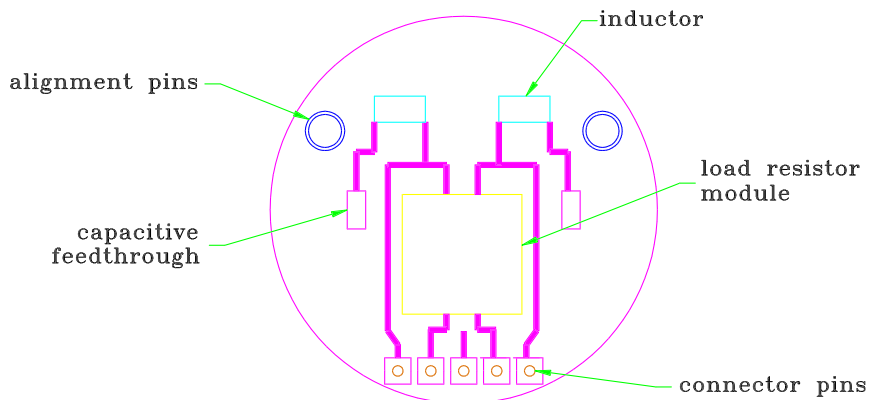


Figure 2.24: Schematic of the ACBAR bolometer module PCB board which provides load resistance and RFI filtering directly at the bolometer. Figure provided by R. S. Bhatia.

finger that extends from the nitrogen can through a hole in the helium can (see Figure 2.16) with G-10 fiberglass legs. A heater on the JFET module warms the temperature to the operating point of $\sim 110 - 120$ K.

Radio frequency interference (RFI) entering the 4 K vacuum space can couple to the high impedance wiring on the focal plane and heat the detectors, thus degrading their sensitivity. To prevent this, all wires entering the 4 K vacuum space pass through additional RFI filter modules mounted in the wall of the liquid helium radiation shield. The filters used in these modules are muRata EMI π -filters¹⁶ which have been embedded in castable Eccosorb. These RFI filter modules were measured to attenuate signals above 1 GHz at ~ -60 dB [64].

The signal wires then exit the dewar and enter the warm electronics signal box where they are filtered and amplified. The signal boxes have RF shielding gaskets at all mating surfaces. The raw signals are amplified by a factor of 200 and then the DC and AC components are separated with a filter at ~ 16 mHz (10 s time constant). The AC signals are further amplified another factor of 200 (for a total gain of 40,000) and low pass filtered at 650 Hz. The signals are then sent to VXI data acquisition system housed in a heated enclosure on the back of the telescope primary mirror. There the signals are sampled at ~ 2400 Hz and averaged over 8 samples to save disk space. This averaging puts the Nyquist frequency at 150 Hz. The signals are finally converted to digital form and written to disk. The complete transfer function of the ACBAR signal chain is described in detail in the

¹⁶muRata part #VFM41R01C222N16-27

Appendix. We transfer the data to the US using the TDRSS network. This allows the local science team to monitor the state of the instrument and analyze data within a day of acquisition. This rapid turnaround proved invaluable because we were able to identify problems very quickly rather than discovering them after the end of the season.

2.3.2 Microphonic Response

Early into the system integration at U.C. Berkeley, we discovered a forest of lines in the noise spectra of all high impedance channels. We measured the *in situ* electronics noise to be very clean using a low impedance short across one of the pairs of JFET gates in place of a detector. We believed these lines were due to microphonic pickup in the system and this was borne out by further investigation.

Variable capacitance between vibrating wires will drive a current through our high impedance detectors resulting in a noise spike at the resonant frequency. To measure the microphonic response of the system, we used mechanically vibrating load called the “Whomper”; similar to a speaker with a mass attached to the coil. We bolted the Whomper to the dewar and swept the vibration frequency between a few Hz to a kHz while measuring the noise spectrum of the detectors. This test revealed many strong resonances within our signal band.

The two ways to reduce microphonic response are 1) lower the output impedance of the detectors with FET buffers, or 2) tighten down the wiring to push the microphonic response to frequencies well above the signal band. We had already employed option #1 with a JFET stage mounted to the 77 K cold finger on the cold plate. Unfortunately, the path length from detectors to the JFETs left approximately 2 feet of high impedance wiring that was free to vibrate. We made every effort to secure the high impedance wiring but the microphonics persisted. This was particularly insidious because we could not measure the microphonic response with the bolometers at room temperature because our detectors have very little impedance at 300 K.

To locate the source of the microphonics we constructed “fake bolometers” using 30 M Ω load resistors as the detectors and installed them on the focal plane. We then attached the Whomper to the open room temperature dewar and measured the noise spectrum while trying to isolate the source of the microphonics. The dominant sources of microphonic response were discovered to be the vibration of the entire 240 mK stage of the focal plane

and the JFET module. To reduce the vibration of these we installed a set of radial kevlar supports which we tensioned by compressing belleville spring washers. Kevlar has the unfortunate property of expanding upon cooling so the spring washers were necessary to keep tension on the stages as the strands relax. The kevlar system successfully moved the microphonic resonances of the system well above the ACBAR signal band.

2.3.3 Computer Control and Housekeeping

ACBAR can be configured for either manual or computer control of all system elements by flipping large toggle switches for ease of use with gloved hands. Under manual control, all settings are modified with turn pots. Under computer control the settings are changed with a digital bus. The digital bus allows remote setting of all of the following: bolometer bias levels, all heaters on fridge and cold stages, calibrator temperature and modulation frequency, and all thermometer settings (reference impedance and excitation voltage). This allows the observer to control virtually all aspects of the instrument from within the main station dome located approximately 1 km away from the telescope. All of the housekeeping information is read by the VXI crate at 2 Hz and saved to disk. This includes all bias levels, thermometry readings, DC levels of all 24 bolometers, and the two-axis tilt meter mounted on the telescope.

Chapter 3 Observations and Performance

3.1 The South Pole Environment

ACBAR observes from the Viper telescope located at the Southern Geographic Pole in Antarctica. The South Pole provides a remarkable platform for terrestrial far-infrared observations [60]. The Amundsen-Scott South Pole Station is located on top of the Ross ice shelf at an elevation of 9,300' which lowers the column depth of atmosphere above the telescope. The pressure elevation at the Pole routinely exceeds 11,000' because of the thinning of the polar atmosphere as air bulges at the equator. The extreme cold freezes out most of the precipitable water vapor from the atmosphere greatly reducing emission and absorption from the sky. The ambient temperature averages around -80°F in the Austral winter with a precipitable water vapor less than 0.32 mm 75% of the time [60]. In addition, the atmosphere is very stable with long periods of good observing weather punctuated by occasional weather events (usually associated with a warming of the ambient temperature) [61]. The entire Southern celestial hemisphere is available year round allowing indefinite integration times on small patches of sky. These attributes combine to make the South Pole arguably one of the best locations on the planet for far-infrared observation.

3.2 Observational Parameters

A full characterization of the system requires precise measurement of the projected beams on the sky; both the right ascension (RA) and declination (DEC) position of the beams as the chopper swings and how the beams themselves change with chopper angle must be measured. We measure these beam properties by making raster maps of compact objects at multiple RA offsets to position the source at different chopper locations. Because these raster map sets take a very long time, the telescope pointing can change a significant fraction of a beam width over the course of an observation. Thus, many of these maps are required to determine the true chopper functions as well as characterize the telescope pointing model.

Source	Other Name	RA (J2000)	DEC (J2000)
RCW38	IRAS 08573-4718	134.768°	-47.510°
RCW57	NGC 3576	167.886°	-61.362°
MAT6a	IRAS 12073-6233	182.501°	-62.832°

Table 3.1: Reported IRAS coordinates of the galactic HII regions used to develop the ACBAR/Viper pointing model.

3.2.1 Chopper Functions

The RA and DEC of each beam as a function of chopper angle can be measured on any bright and reasonably compact source because, for this measurement, we are only interested in the location of the center of the beam as a function of chop and not the details of how the beam itself changes. However, the source cannot be so large or have complicated sub-structure such that the measured centroids depend on small changes to the beam shape. For these observations we use the bright galactic HII regions RCW38, RCW57, and MAT6a; we have listed the IRAS reported coordinates for these sources in Table 3.1. The complete chopper maps are made by starting with the source near the center of the chop and performing a full raster map with 1' declination steps through the entire array. The telescope is then shifted in RA to put the source at a different chop position as recorded by the chopper encoder voltage. We make raster maps with RA spacings of about $0.5^\circ \sec \delta$, where δ is the declination of the observation, across the full $\sim 3^\circ$ chop to build up the chopper functions. The beam centroids are determined by fitting a Gaussian to the source position in each of the raster maps.

The RA and DEC as functions of chopper voltage are well fit by second order polynomials of chopper voltage in the form

$$\alpha(V) = \alpha_0 + \alpha_1 V' + \alpha_2 V'^2$$

$$\delta(V) = \delta_0 + \delta_1 V' + \delta_2 V'^2$$

$$V' = [V - \Delta V(t)]/g(t),$$

where the zeroth-order terms are boresight position offsets for each channel, first-order terms are linear coefficients for the number of degrees per volt of chop, and the second-order terms are the quadratic corrections.

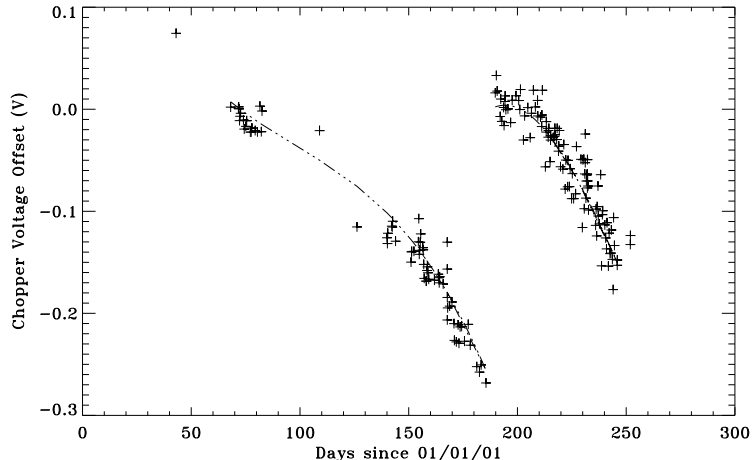


Figure 3.1: Measured chopper voltage offset for 2001 versus time. The large jump in offset back to zero volts around day 186 is a result of re-zeroing the encoder. The two lines are polynomial fits to the chopper voltage with time for the two periods. Note that in 2001 the full chopper range of motion was ± 1 V over $\sim 3^\circ$ which means that a 0.2 V offset corresponds to a shift in position of approximately $18'$ on the sky.

There are two additional variables in these functions which unfortunately were time variable for 2001; these remained static for 2002 because of an overhaul of the chopper encoder system. The $\Delta V(t)$ term is a drift in the zero point voltage of the RVDT chopper encoder with time. This voltage drift caused the actual angular position of the chopper corresponding to zero volts on the encoder output to drift with time, meaning that 0V was not a fixed angle on the sky. Fortunately, we performed limited raster maps of galactic sources multiple times a day and are able to parameterize the drift in chopper voltage with time from the change in source location within the maps. Figure 3.1 shows the measured drift in chopper voltage with time for the 2001 observing season.

The second time-varying term, $g(t)$, is the gain correction of the chopper encoder with time and is a far more serious problem than the monotonic slowly drifting voltage offset. It was noticed in 2001 that the difference in source chopper voltage between two fixed pixels ($\Delta V_{AC} = V_{A3} - V_{C3}$ and $\Delta V_{BD} = V_{B3} - V_{D3}$) varied with time for raster maps made with the source near the center of the chop. This implied that the chopper encoder gain (the voltage difference for a fixed change in chopper rotation angle) was not a constant. The encoder gain is seen to vary by as much as 10% (see Figure 3.2) and has been observed to change during the course of a single raster map. The variation in chopper gain is roughly bi-modal with a high and low state. A 10% change in chopper gain over the course of a 3°

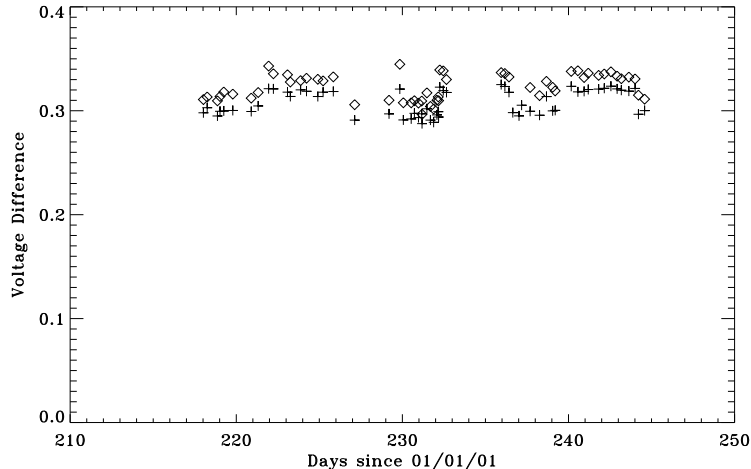


Figure 3.2: Measured source position voltage differences $\Delta V_{AC} = V_{A3} - V_{C3}$ (pluses) and $\Delta V_{BD} = V_{B3} - V_{D3}$ (diamonds) versus time for approximately one month during 2001. The two differences are highly correlated indicating the variation is due to gain fluctuations common to both differences and not merely scatter due to centroiding uncertainty. Note that the slight difference between ΔV_{AC} and ΔV_{BD} (which are equally spaced on the focal plane) is due to distortion in the optical system.

chop means that the position of the beam at the edge of the chop can be off by as much as $9'$ (roughly two beam widths) from the expected position. This position uncertainty has a very detrimental impact on our ability to search for compact objects in 2001 and was the dominant source of pointing error during the season.

The only way to measure the current gain state of the chopper is to make a raster map and compare the measured two-channel chopper voltage difference to the nominal value. Fortunately, the frequent galactic source maps also provide a reasonably frequent measurement of the gain. However, without a bright object in the blank field maps to determine the *in situ* encoder gain, we are forced to discard any observation for which the gain measured from galactic sources on either side of an observation disagree (indicating a gain change occurred) or during periods of time when the gain is seen to vary on short time scales. As mentioned above, the RVDT encoder on the chopper was replaced with an absolute optical encoder which eliminated both the voltage offset drift and gain variation problems for the 2002 season.

3.2.2 Beam Sizes

Accurately measuring the beam sizes on the sky is important for calibrating the instrument and generating window functions. Ideally, this requires a source with angular size much less than the beam but can also be done using a source with well-characterized extended emission that can be deconvolved from the resulting beam map. In addition, the source should be very bright so that an accurate map can be made in a short period of time; this prevents pointing jitter from the telescope from contributing significantly to the measured beam size. The planets Mars and Venus satisfy these criteria with sizes less than an arcminute and (depending on distance) fluxes greater than 100 Jy at all frequencies; these are our objects of choice for measuring beam parameters. Figure 3.3 shows a raster map of Mars made on 07/17/01 when it was very near the Earth and Figure 3.4 shows a raster map of Venus on 09/22/02.

Using the measured chopper functions, one can convert a raster map into proper sky coordinates and measure the solid angle of the beam. A raw raster map is first flat fielded to remove chopper offsets before calculating the solid angle. To flat field the maps, we mask out the pixels in the region of the source and then remove a common offset and third order polynomial from each RA stare. The effect of this procedure is illustrated in Figure 4.7 which shows a raw raster map on RCW38 and the corresponding flat fielded image.

The solid angle is then found by integrating the source voltage over the flat fielded map and dividing by the source amplitude:

$$\Omega_{beam} \equiv \frac{1}{V_{norm}} \int V(\Omega') d\Omega' = \frac{1}{V_{norm}} \sum_{ij} V_{ij} \Delta\alpha_i \Delta\delta_j,$$

where V_{norm} is the best fit Gaussian voltage amplitude of the beam map, and $\Delta\alpha$ and $\Delta\delta$ are the right ascension and declination widths of each bin, respectively. The measured beam sizes from the 07/17/01 Mars raster map are listed in Table 3.2. Mars subtended $19''$ on the sky for this observation which results in an error of $< 0.5\%$ in the measured solid angle. The average beam FWHM from the table are $4.80'$, $4.00'$, $3.97'$, and $5.66'$ at 150, 220, 280, and 350 GHz, respectively. For 2002 we used the planet Venus to measure the beam sizes. These are listed in Table 3.3 from an observation of Venus on 09/22/02. The average beam FWHM in 2002 were $4.69'$, $4.25'$, and $3.95'$ at 150, 220, and 280 GHz, respectively.

The 150 and 350 GHz beam sizes differ substantially from the design of $4'$. The 150

Chan	Freq (GHz)	Ω ($\times 10^{-6}$ sr)	FWHM ($'$)
A1	280	1.86	4.41
A2	280	1.47	3.92
A3	280	1.33	3.74
A4	280	1.38	3.81
B1	220	1.78	4.31
B2	220	1.44	3.88
B3	220	1.51	3.84
B4	220	1.43	3.97
C1	150	2.43	5.05
C2	150	2.12	4.71
C3	150	2.10	4.69
C4	150	2.17	4.76
D1	350	3.26	5.84
D2	350	3.60	6.14
D3	350	2.94	5.55
D4	350	2.49	5.10

Table 3.2: Measured 2001 beam sizes from Mars on 07/17/01. The angular diameter of Mars was $19''$ which is substantially smaller than the beams. The FWHM quoted in the table is calculated assuming a Gaussian shape with $\theta_{FWHM} = \sqrt{(4 \ln 2)\Omega/\pi}$.

Chan	Freq (GHz)	Ω ($\times 10^{-6}$ sr)	FWHM ($'$)
A4	280	1.74	4.26
A6	280	1.49	3.95
A3	280	1.47	3.92
A5	280	1.28	3.65
D5	150	2.29	4.89
D6	150	2.23	4.83
D4	150	1.97	4.53
D3	150	2.08	4.67
B1	150	2.22	4.82
B2	150	2.12	4.71
B3	150	1.89	4.44
B6	150	2.08	4.66
C4	220	2.05	4.63
C3	220	1.88	4.44
C2	220	1.38	3.80
C1	220	1.64	4.13

Table 3.3: Measured 2002 beam sizes from Venus on 09/22/02. The angular diameter of Venus was $37.0''$ which is substantially smaller than the beams. The FWHM quoted in the table is calculated assuming a Gaussian shape with $\theta_{FWHM} = \sqrt{(4 \ln 2)\Omega/\pi}$.

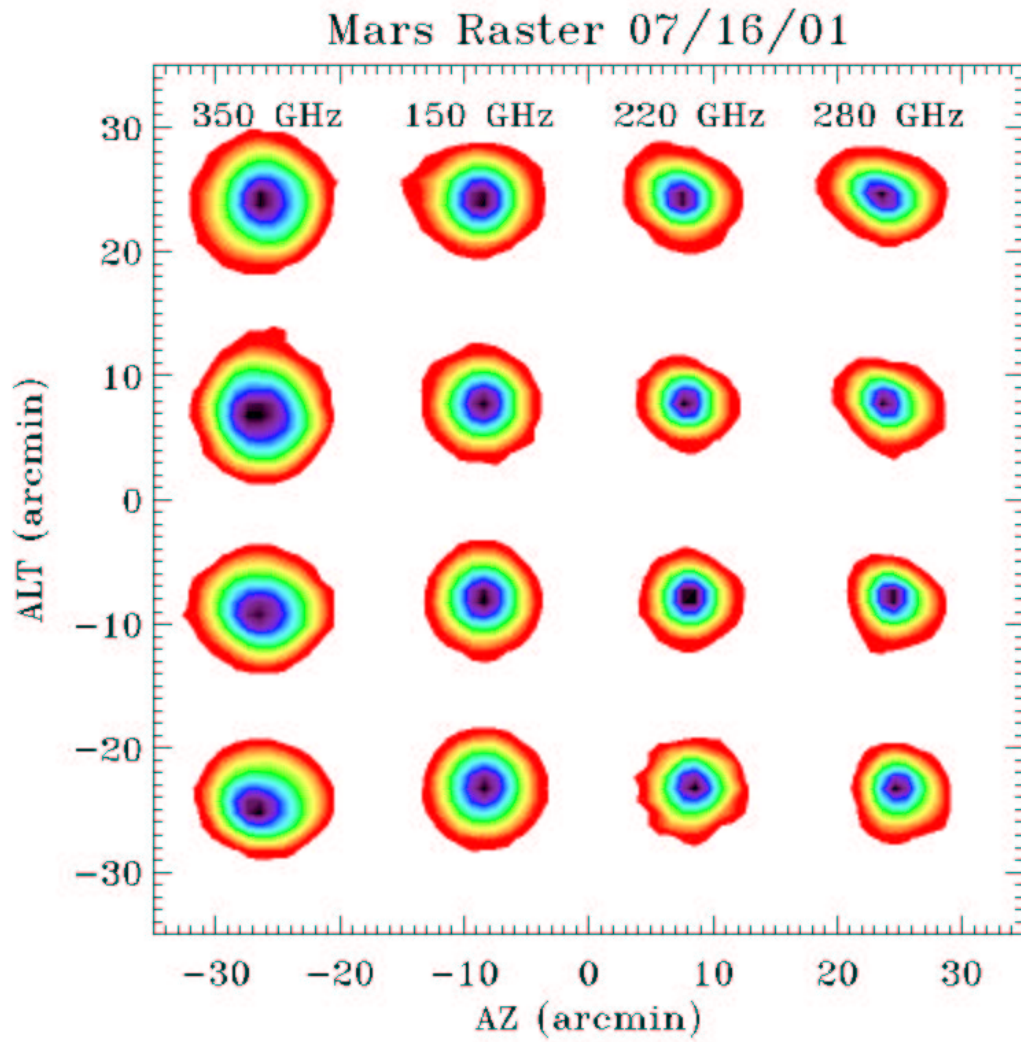


Figure 3.3: Raster map of Mars at an elevation of approximately 26.5° taken on 07/16/01. The angular diameter of Mars was $19''$ on this date.

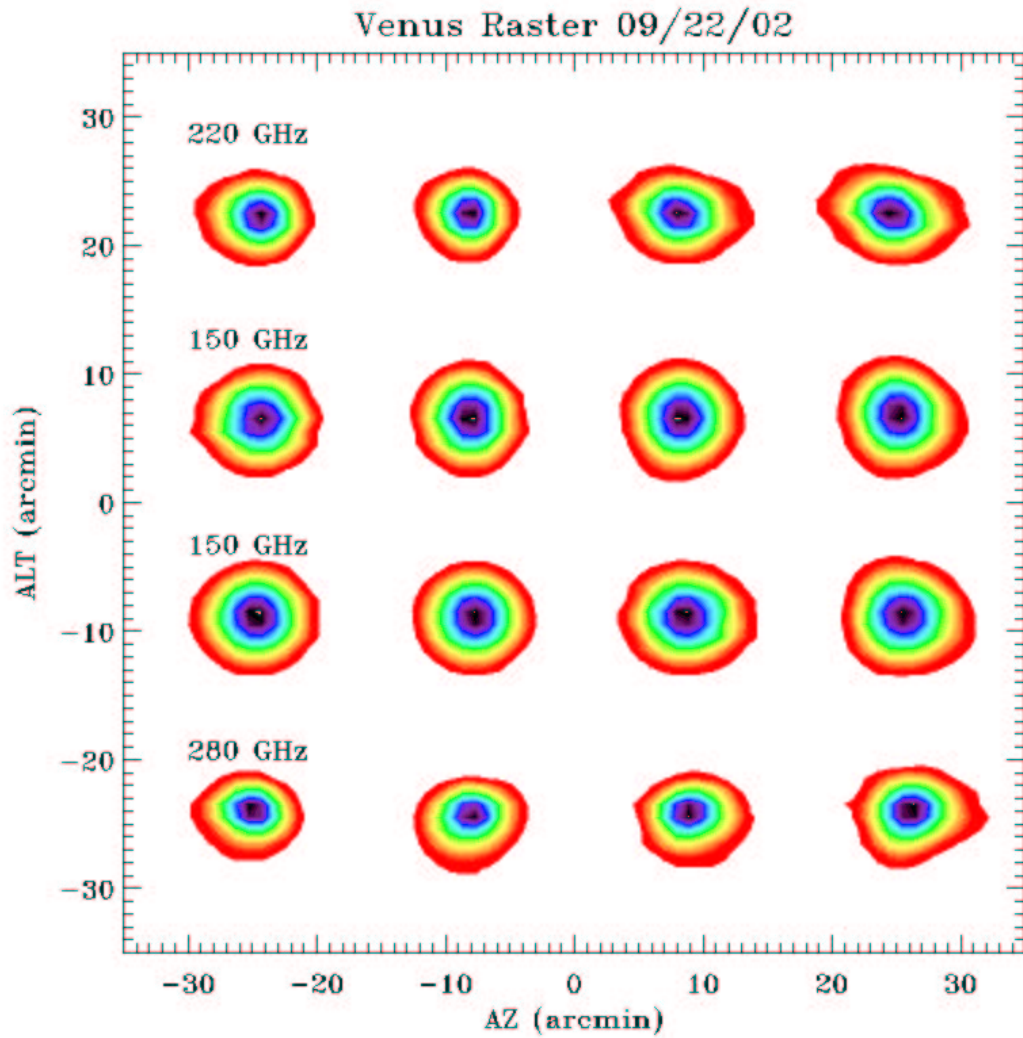


Figure 3.4: Raster map of Venus at an elevation of 19.8° taken on 09/22/02. The angular diameter of Venus was $37''$ on this date.

GHz beams suffer from diffraction because of the aggressive edge taper on the 2 m primary mirror. The $\sim 20\%$ spread in 150 GHz beam size is consistent with the level expected for a -18dB edge taper. In retrospect, under-illuminating the primary at 150 GHz would have achieved effectively the same beam size without the risk of spillover. The very large 350 GHz beam sizes are somewhat of a mystery because the beams exiting the dewar are very close to specification to produce a 4' beam. It is believed that the surface roughness of the mirrors contributes to the smearing, but an abrupt change between 280 and 350 GHz seems unrealistic. It is also possible that the fine dusting of snow on the mirrors scatters the beam and this is bolstered by the fact that the 350 GHz chopper synchronous offset is most sensitive to the accumulation of snow on the mirrors.

One may also note from the beam size tables that the beam size varies within a frequency column/row indicating some curvature of the focal plane. The focus of the dewar is set with a linear actuator mounted between the telescope structure and the dewar cart which rides on rails parallel to the optic axis. We chose the dewar focus position that, on average, resulted in the maximum signal from galactic source raster maps. Since the optical throughput is conserved, the maximum signal voltage should correspond well with minimum beam size. We made a particular effort to minimize the beam size of the 150 GHz channels because it is our strongest science frequency.

While analyzing galactic source chopper maps from 2001, we noticed that the voltage amplitude of a source depended on its location in the chop. Upon further investigation we found that the measured solid angle of a source also changed with chop angle indicating that the beams are distorted as the chopper rotation changes the optical path through the telescope. This effect means that the calibration will change as a function of chop for compact objects but remain effectively constant for beam filling sources (if the throughput is conserved).

To be more specific about how the effects of a changing beam size depend on the source distribution, consider the following examples. Assume the beam gain is Gaussian and is given by

$$B(\vec{\theta}) = G_0 e^{-\theta^2/2\sigma_B^2} \quad (\text{V/Jy}),$$

where $\vec{\theta} = \theta_x \hat{x} + \theta_y \hat{y}$, $\theta^2 = \theta_x^2 + \theta_y^2$, G_0 is the gain in V/Jy, and σ_B is the Gaussian width

of the beam. For a point source with intensity profile of

$$I(\vec{\theta}) = S_0 \delta(\vec{\theta}) \quad (\text{Jy/sr}),$$

where δ is the Kronecker delta function and the total source flux density is $S_0 = \int I(\vec{\theta}) d^2\theta$ (Jy), the voltage map of the source is the convolution of the beam and source profiles and is given by

$$V(\vec{\theta}) = B(\vec{\theta}) \star I(\vec{\theta}) = G_0 S_0 e^{-\theta^2/2\sigma_B^2} \quad (\text{V}).$$

Similarly, for a compact Gaussian object of width σ_S with intensity profile

$$I(\vec{\theta}) = \frac{S_0}{2\pi\sigma_S^2} e^{-\theta^2/2\sigma_S^2} \quad (\text{Jy/sr}),$$

(again with integrated flux density $S_0 = \int I(\vec{\theta}) d^2\theta$) the voltage profile from the source is

$$V(\vec{\theta}) = \frac{2\pi\sigma_B^2 G_0 S_0}{2\pi(\sigma_S^2 + \sigma_B^2)} e^{-\theta^2/2\pi(\sigma_S^2 + \sigma_B^2)} \quad (\text{V}).$$

Lets also consider a uniform intensity distribution given by $I(\vec{\theta}) = \Sigma$ (Jy/sr), where Σ is a constant, in which case the voltage map is

$$V(\vec{\theta}) = \Sigma G_0 \Omega_B \quad (\text{V}).$$

If the bolometer responsivity and source flux density remain static, the condition for throughput conservation is $G_0 \Omega_B$ is constant. Performing the integral of the voltage map over solid angle on the sky in both the point source case and Gaussian source case gives

$$\int V(\vec{\theta}) d^2\theta = S_0 (G_0 \Omega_B) \quad (\text{V sr}).$$

We see that the integrated signal will be constant regardless of the change in beam size if throughput is conserved. The actual voltages in the map will depend explicitly on the value of the gain ($G_0 \propto \Omega_B^{-1}$) which in turn depends on chopper angle. However, for a diffuse source (much larger than the beam size) of intensity Σ , the voltage map only depends on the product $G_0 \Omega_B$ which is independent of chopper position if the throughput is conserved. It is therefore important to 1) verify that the throughput is conserved with chopper rotation,

and 2) depending on the spatial extent of the source under observation, correct for the change in gain with chopper angle.

To test the conservation of throughput we made complete raster maps of galactic sources at multiple chopper offset positions and measured whether the integrated signal was constant for all chopper offset positions. Ideally, one would like to use a bright point source for this measurement, but the limited availability of planets and bright quasars made this impossible. Most of our chopper map data is from RCW38 which has complex extended structure and is not a good candidate for verifying throughput conservation since the changing beam size will couple to different regions of the source. The compact HII region MAT6a [92] is better suited for this measurement because of its limited extended emission. The integrated source voltage of MAT6a versus chopper position are found to be quite flat indicating good conservation of throughput.

In late September 2002, we performed a sequence of beam maps on Venus. The winter telescope operator (“winter over”) noticed that some ice crystals had accumulated on the dewar window and carefully scrapped them off with a finger nail. From the Venus maps on either side of the ice removal we discovered a significant change in some of the beams; the ice on the curved surface of the window acted like a lens, distorting the focal plane. The average beam sizes before the ice removal were 4.89', 4.30', and 4.23' FWHM at 150, 220, and 280 GHz, respectively. After the ice removal the average beams measured 4.69', 4.25', and 3.95'. The solid angle of a few of the beams towards the middle of the focal plane changed by almost a factor of two. In addition, the positions of some of the beams were shifted by a few arcminutes on the sky. Both of these effects tend to smear the effective beam size of the coadded maps and reduce the sensitivity to compact sources. Unfortunately, the presence of ice on the window and its effects were only discovered after the CMB observations.

The accumulation of ice on the window appears to have been a very gradual process. Although we were only able to view planets at the very end of the 2002 season, we can monitor the change in beam size with the galactic source raster maps. Using raster maps on RCW38 we found that the change in beam size was roughly monotonic with time during the course of CMB observations. For beam filling sources like the CMB, we do not need to change the calibration with varying beam size but must correct for the changing CMB window functions [59]. The calibration for point sources, however, will change linearly with solid angle. Using the measured galactic source solid angles it should be possible to

partially correct the calibration for those channels most affected by the ice. Because most of the 150 GHz beams were not strongly affected by the ice we opt to leave the calibration fixed and use the measured beam sizes of quasars in the final coadded maps for determining the window function.

3.2.3 Chopper Synchronous Offsets

When the chopper is running the bolometer signals are dominated by a roughly parabolic chopper synchronous offset (see Figures 3.5 and 3.6). Since the chop across the sky is roughly constant latitude at the horizon, we would expect an offset at other elevations because the beams no longer sweep at constant elevation. The amplitude of the temperature offset due to motion through the atmosphere at 45° elevation is approximately equal to

$$\Delta T \sim 3 \text{ mK} \left(\frac{T_{sky}}{220 \text{ K}} \right) \left(\frac{\tau}{0.03} \right) \left(\frac{\Delta\delta}{1.2'} \right),$$

where T_{sky} is the temperature of the atmosphere, τ is the atmospheric opacity, $\Delta\delta$ is the elevation change from the chop which is $1.2'$ for a $\pm 1.5^\circ$ chop at 45° . The key point is that as the chopper swings, the beam will travel through a higher air mass and thus see a temperature increase of a few mK. However, one sees from Figure 3.5 that the temperature change can be much larger than the predicted amplitude as well as change sign, indicating the offset is due to something other than the path of the beams across the sky.

The offset structure is observed to depend on a number of factors. Modulated spillover, accumulation of snow on the telescope, and atmospheric conditions appear to be the dominant sources of offset amplitude. The first two offset sources are somewhat within our ability to control and we take steps to mitigate their effects. To reduce modulated mirror spillover we mounted a blackened circular light baffle between the tertiary mirror and the chopper. This light baffle is somewhat smaller than the projected area of the chopper and intercepts beam power which would otherwise spillover and modulate as the chopper rotates. The baffle significantly reduced the offset amplitude as can be seen in Figure 3.6 which shows the offsets before and after baffle installation in 2001. As discussed below in the optical loading section, this warm baffle contributes to the loading of the system because it intercepts beam power at ambient temperature. We decided that the increase in loading was worth the reduction in possible systematics and thus left the baffle installed.

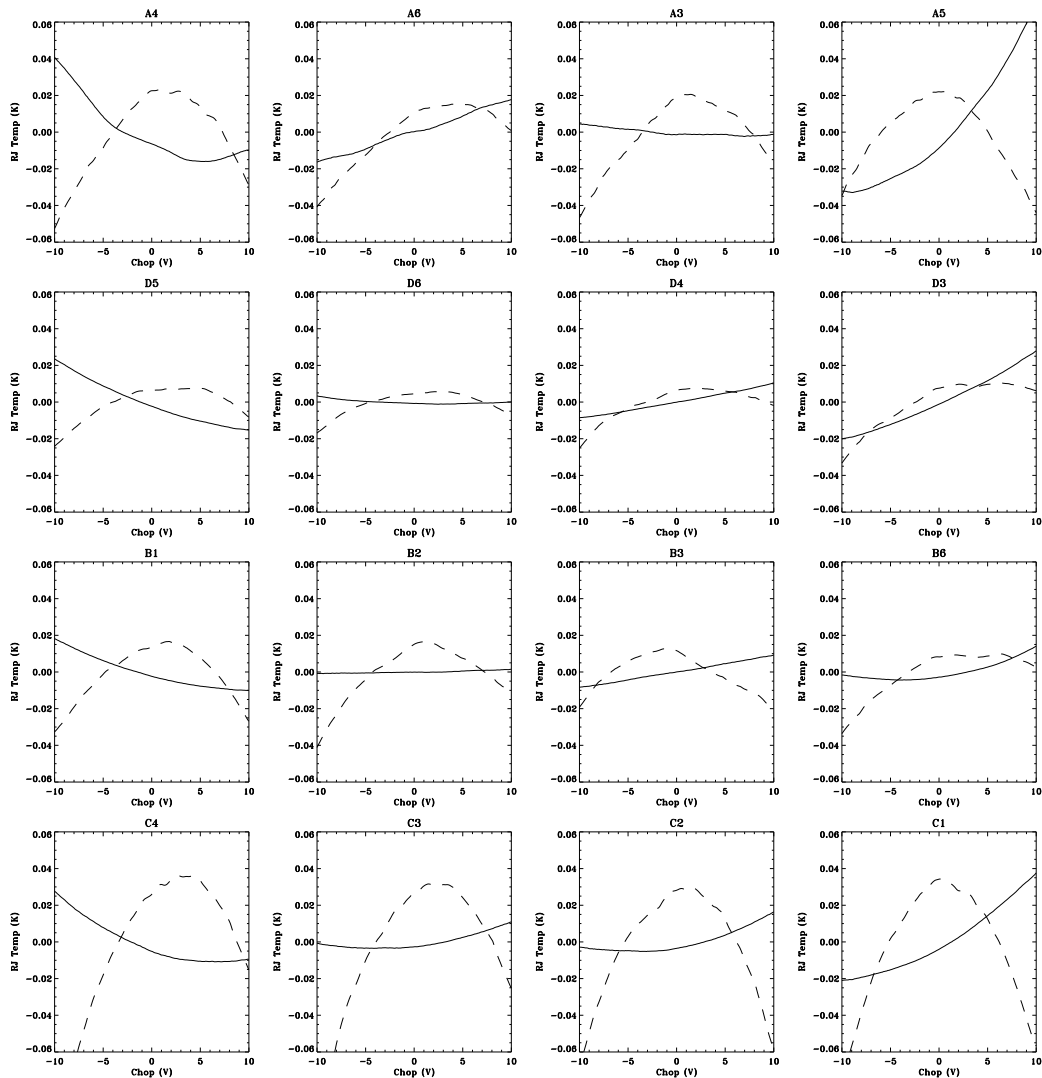


Figure 3.5: Shows the measured average RJ sky temperature offsets of all optical channels during observations of the CMB5 blank field (elevation 55°) versus chop on 04/14/02 (solid lines) and 06/19/02 (dashed lines). All channels are set to the same vertical scale for ease of comparison. The frequencies are 280, 150, 150, and 220 GHz from top to bottom. The $350 \mu\text{m}$ zenith opacity for this observation was approximately 2.0 on 04/14/02 and 1.0 on 06/19/02.

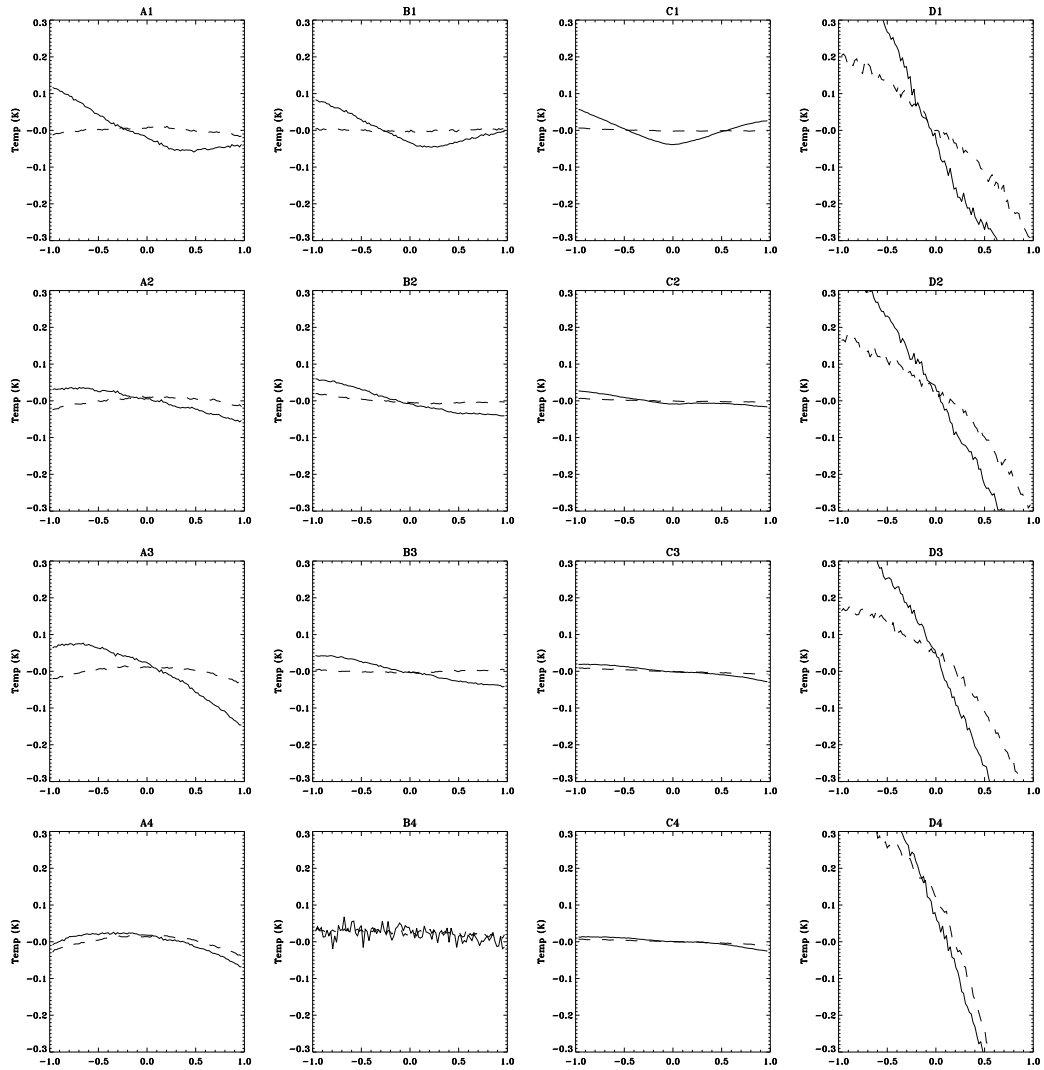


Figure 3.6: Chopper synchronous offsets before and after baffle installation on 02/04/01. Shows the measured temperature versus chop for all optical bolometers before (solid) and after (dashed) baffle installation. The columns are (from left to right) 280, 220, 150, and 350 GHz.

Snow accumulation is another large contributor to the chopper synchronous offsets. The mirror surfaces collect blowing snow as well as develop a thin layer of frost. The rate of accumulation depends on the ambient temperature and the amount of blowing snow. As the chopper rotates, the beams sweep across the secondary mirror, view different projections of the chopper mirror, and move slightly (a few cm) on the primary mirror. The warm snow then contributes an optical signal to the system as the beams move across it. The only solution to this is to clean and defrost the mirrors frequently.

3.2.4 Snow

In addition to contributing to offset structure, snow accumulation also attenuates astronomical signals. The method of signal loss is either power absorption or scattering by crystals with size comparable to λ . This signal attenuation was discovered by comparing the measured amplitude of galactic sources versus chopper offset amplitude. To test the effects of snow on signal attenuation we performed raster maps on RCW38 with the mirrors quite snowy and then repeated the observation with the mirrors cleaned. The average signal ratios for RCW38 with the mirrors snowy versus clean were 70%, 45%, and 20% at 150, 220, and 280 GHz, respectively, indicating a strong frequency dependence consistent with absorption. The beam solid angles are effectively unchanged between the snowy versus clean measurements indicating the scattering would have to be relatively isotropic to explain the signal loss without an appreciable broadening of the beams. This signal loss is very serious (particularly in the high frequency channels) and needs to be mitigated by identifying periods when the data may be contaminated from snow attenuation.

To develop a criteria for cutting data with snow contamination, we investigated the correlation of chopper offset amplitude with source signal and found a strong correlation at high frequency and a much weaker correlation at low frequency (see Figure 4.8). This frequency dependence allows us to tune the level of tolerable snow attenuation to the science goal being investigated. For example, the weaker dependence at 150 GHz means that a more aggressive snow cut threshold can be used for science only incorporating the low frequency channels, such as CMB power spectrum estimation. However, pointed cluster observations rely on the higher frequency data to remove the CMB contribution from the maps and must therefore employ a more conservative snow cut threshold to prevent severe signal attenuation at higher frequencies. The snow cut is discussed more quantitatively in the

Frequency (GHz)	T_{RJ} (K)	$T_{internal}$ (K)	$T_{mirrors}$ (K)	T_{baffle} (K)	T_{atm} (K)
150	38.5 ± 3.8	11	4	5	15
220	36.7 ± 6.8	16	5	~ 0	22
280	63.0 ± 10.4	16	6	~ 0	40

Table 3.4: Average Rayleigh-Jeans (RJ) temperature loading at 60° elevation for the 2002 season and estimates of various contributions to the loading. These values were generated from measurements of loading from load curves taken roughly twice daily. The mirror contribution is estimated to be $3\times$ the theoretical emissivity [122] at 260 K to account for surface roughness. The atmospheric contribution is estimated from an average 350 μm tipper value of 1.5 and a sky temperature of 220 K.

Data Cuts section below.

3.2.5 Optical Loading

The optical loading on all channels can be determined at any time from the DC level of bolometer and the measured cold plate temperature using the power balance equation and the previously measured properties of the bolometers (refer to §A.1). Figure 3.7 shows the average Rayleigh-Jeans (RJ) optical loading versus time of all three observing frequencies for part of the 2002 season. One can see the stability of the optical loading at 150 GHz but the higher frequencies have significantly more scatter because of a stronger dependence upon atmospheric conditions. The average RJ loading temperature for 2002 at all three frequencies is listed in Table 3.4.

The bulk features in Figure 3.7 are the result of changes in atmospheric emissivity as seen in Figure 3.8 which shows the correlation between RJ loading and $\tau_{350\mu\text{m}}$ tipper measurements. The higher frequency channels are more strongly correlated than 150 GHz as would be expected from the emissivity profile of the atmosphere.

There are many contributors to the total optical loading of the system. The dominant sources of loading for ACBAR are warm filter optics, atmosphere, and a hot telescope. We took great pains to reduce the internal optical loading from the dewar by maximizing the in-band transmission of the warm filters and blocking high-frequency leaks at cold temperatures. The atmospheric contribution is given by

$$T_{atm} = T_{sky}(1 - e^{-\tau/\cos\zeta}),$$

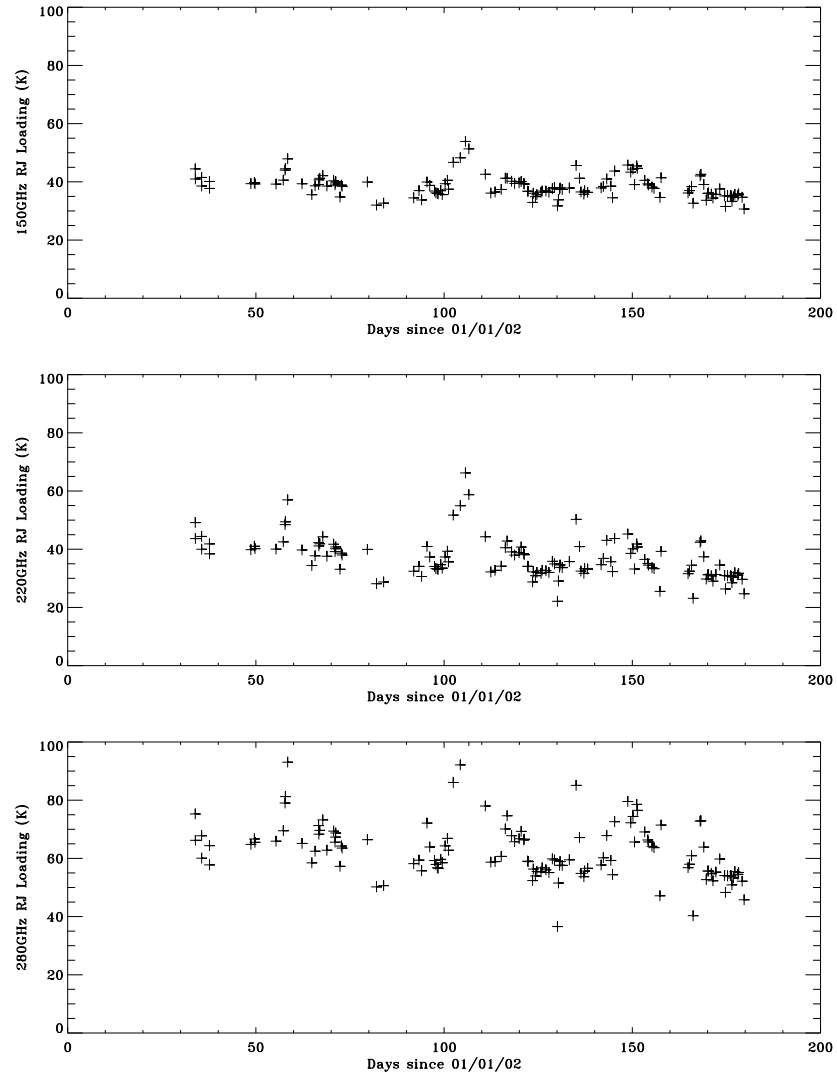


Figure 3.7: Average Rayleigh-Jeans temperature loading at (from top to bottom) 150, 220, and 280 GHz versus time since January 1, 2002. The points represent the average optical loading during load curves and were all taken at 60° elevation. Notice the strong correlation between the frequency channels.

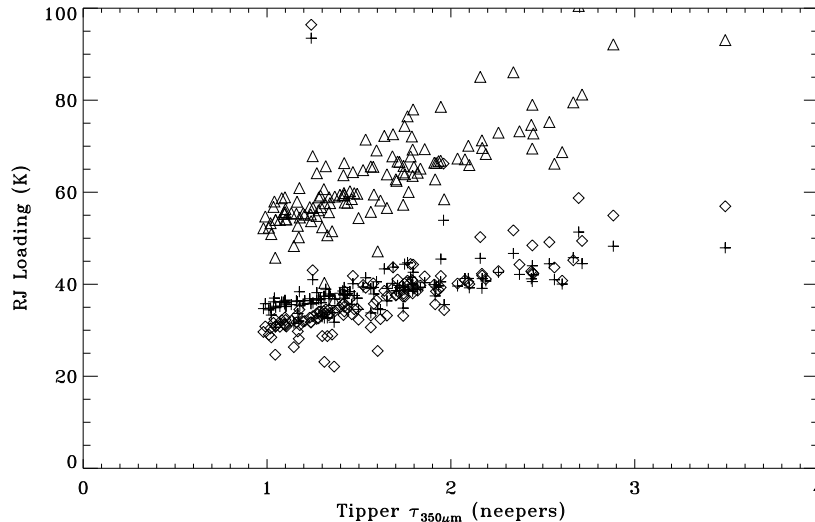


Figure 3.8: Shows the average Rayleigh-Jeans temperature loading at 150 (pluses), 220 (diamonds), and 280 GHz (triangles) versus 350 μm zenith opacity for 2002.

where T_{sky} is the temperature of the atmosphere, τ is the average in-band zenith opacity, and ζ is the zenith angle of the observation. The telescope consists of four warm aluminum mirrors, each of which has an approximate emissivity of [122]

$$\epsilon = \sqrt{\frac{16\pi c\epsilon_0}{\lambda\sigma}},$$

where c is the speed of light, ϵ_0 is the permittivity of free space, λ is the observing wavelength, and σ is the conductivity of the metal ($3.7 \times 10^7 \Omega^{-1}\text{m}^{-1}$ for aluminum). The actual emissivity of the surface is usually a few times this value because of surface roughness. The contribution from all four mirrors is roughly

$$T_{mirrors} \sim \text{few} \times 4\epsilon T_{ambient}.$$

The introduction of the light baffle to reduce chopper synchronous offsets also contributes to the optical loading. The large beams of the 150 GHz channels are truncated at the baffle aperture at a level which contributes ~ 5 K but the beams from the higher frequencies are sufficiently small that the baffle contribution is negligible. Estimates of the various contributions to the optical loading are also given in Table 3.4.

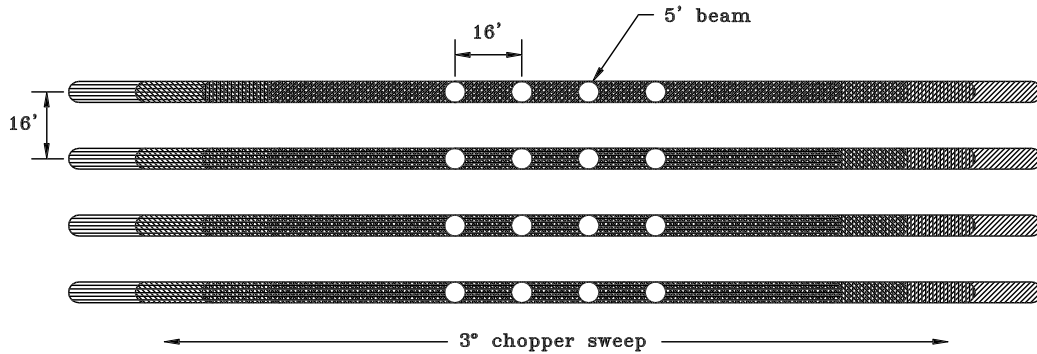


Figure 3.9: Illustrates the sky coverage geometry of a single declination stare. The 16 pixels are swept $\sim 3^\circ$ on the sky and the darkness of the cross hatch indicates the degree of overlap of the four channels within each row.

3.2.6 Scan Strategies

When taking CMB data with ACBAR we perform an elevation raster map. This means we fix the telescope elevation and observe with the chopper running for some period of time – this is referred to as a “stare”. We then tilt the telescope down in elevation (usually $1'$) and continue the process. We usually perform ~ 100 elevation steps which gives a large patch of sky sampled by all four rows of focal plane. The sky coverage of the array during a single DEC stare is illustrated in Figure 3.9. As described above, the dominant signal in the raw raster maps is a roughly parabolic signal a few mK in amplitude. The chopper synchronous offsets change with time and we were concerned that changing small-scale variations in the offset signal could contaminate the CMB maps. We devised an observing strategy to remove as much chopper synchronous offset as possible – even if slowly time varying – while preserving the large-scale CMB power in the map.

We employ a LEAD-MAIN-TRAIL observing strategy which breaks the raster map into three $\sim 3^\circ$ fields that overlap roughly 0.5° in RA. The raster progresses by observing the three fields in succession at fixed elevation before proceeding to the next elevation. The fields are usually observed for 30 seconds on LEAD, 60 seconds on MAIN, and 30 seconds on TRAIL. If the offset is changing linearly with time then the average offset of the LEAD and TRAIL fields should equal the offset in MAIN. By forming the difference $LMT = M - (L + T)/2$ we eliminate both a common offset as well as linear drift.

The three fields are separated by about 3° on the sky which is larger than the $\sim 1^\circ$ peak correlation of the CMB; the LMT subtraction should not remove much CMB power.

In fact, if the CMB fluctuations are Gaussian and uncorrelated, then the *LMT* map should have $\sqrt{3/2}$ times the CMB RMS of the MAIN field alone. This observing strategy does come at the price of sensitivity because the integration time is divided amongst three fields. The ratio of instrumental noise in the LMT field compared to spending all of the time on a single field is a factor of 2 resulting in a reduction of the signal to noise on the CMB of $\sqrt{3/8}$.

We are not concerned with preserving the large-scale CMB power if we are searching for SZ clusters. We can treat the three fields as separate and remove an average offset plus higher order polynomial to eliminate the chopper synchronous signal. For cluster searching, this has a tremendous advantage over LMT subtraction because the spectrum of SZ clusters is preserved. This means that clusters will always appear as decrements at 150 GHz in the three separate fields but could appear as hot or cold spots in an LMT subtracted image. As mentioned above, the offsets are mostly due to accumulating snow on the telescope optics. When searching for clusters we implement an aggressive snow cut based on the amplitude of the offset. This excludes the large chopper offset data as well as those periods of time when the offsets are changing rapidly.

3.2.7 Field Selection

When selecting fields for deep CMB observations at millimeter wavelengths, the primary foreground contaminant of concern is dust emission [109]. With most of the southern celestial hemisphere available for continuous observation we were able to choose the very best regions of dust contrast for our observations. The IRAS/DIRBE dust map of [28] provides an excellent template of galactic dust emission and we found that the best region of the southern hemisphere lies roughly between 21^h to 5^h in RA and -20° to -70° in DEC (see Figure 3.10). The Viper telescope must change coarse elevation actuator positions to observe sources with $\text{DEC} > -45^\circ$ ($< 45^\circ$ elevation) and so we decided to limit our DEC range between -45° and -70° to avoid coarse actuator changes.

With so much clean sky available we decided to select our fields by centering them on flat-spectrum mm bright radio point sources. These objects are typically blazars which are a subset of AGN and highly time variable. They provide a continuous monitor of pointing as well as a bright point source for measuring the final beam size in the coadded maps; the coadded point source image incorporates the physical extent of the beams as well as beam

FIELD	name	α (J2000)	δ (J2000)
CMB2/3/4	PMN J0455-4616	73.962°	-46.266°
CMB5	PMN J0253-5441	43.372°	-54.698°
CMB6	PMN J0210-5101	32.692°	-51.017°
CMB7	PMN J2235-4835	338.805°	-48.600°

Table 3.5: Central reference sources for each CMB observation. The quasar names and positions are from the Parkes-MIT-NRAO Radio Survey as reported by the NASA/IPAC Extragalactic Database [81].

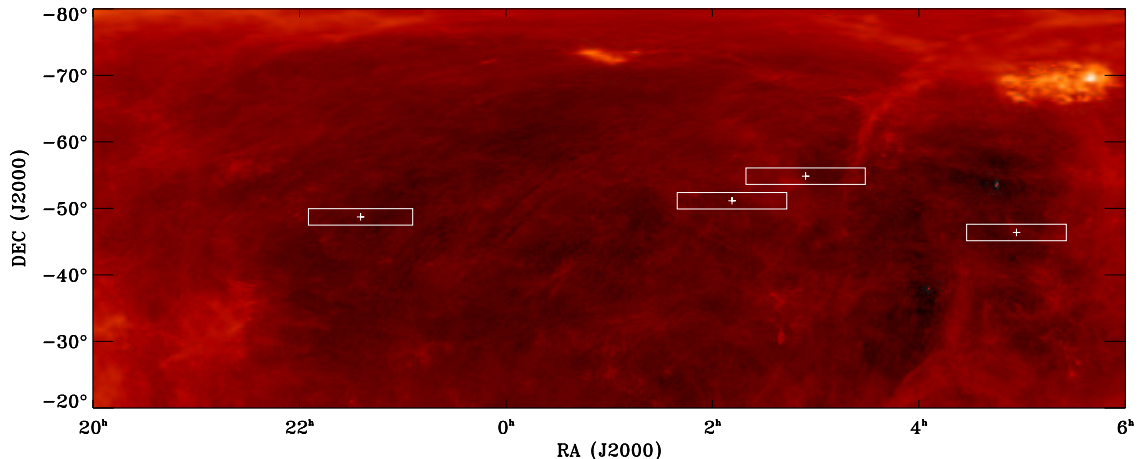


Figure 3.10: Shows the lowest dust region of the southern sky along with the CMB fields observed by ACBAR in 2001 and 2002 (field centers are listed in Table 3.5). The map was generated with the IRAS/DIRBE projection of [28] to 150 GHz and is plotted with a logarithmic intensity scale. The two very bright regions are the Magellanic Clouds.

smearing due to pointing jitter. The coadded quasar size in the CMB5 field at 150 GHz is $5.1'$ FWHM which should be compared with the $\sim 4.8'$ average instantaneous beam size. This indicates an average smearing RMS of $\sim 0.7'$.

A bright radio source in the middle of the field adds a degree of complexity to the analysis because one must remove or mask out the object from the map; the pointing knowledge gained far outweighs this inconvenience. We surveyed many of the flat-spectrum radio sources in the southern hemisphere observed by SEST [6, 110, 111] searching for candidates bright enough to detect with good S/N in a single raster map. We detected a handful with good S/N and list the sources selected for each of the CMB fields in Table 3.5. A map of the dust emission extrapolated to 150 GHz along with the CMB fields observed with ACBAR during 2001 and 2002 is shown in Figure 3.10.

3.3 Calibration

3.3.1 Planetary Observations

To convert the measured signal voltages to physically meaningful units we need to observe an object of known flux. Our primary calibration source for the 2001 season is the planet Mars which has been well studied at millimeter wavelengths [37]. We observed Mars multiple times during the year in an effort to develop a consistent calibration and check for systematic effects. For the 2002 season we used the planet Venus as our primary calibrator. Much less is known about Venus at millimeter wavelengths, and its complicated atmosphere makes the uncertainty of its brightness temperature quite high ($\sim 8\%$ at 150 GHz) [119]. To determine the calibration we made raster maps of Mars and Venus (see Figures 3.3 and 3.4) and integrated the voltage maps, which, as shown above, give

$$\int V_P(\vec{\theta}) d^2\theta = S_P G_0 \Omega_B \quad (\text{V sr}),$$

where S_P is the planetary flux density (Jy), G_0 is the boresight gain (V/Jy), and Ω_B is the beam solid angle (sr).

To determine the flux of Mars during an observation we use the FLUXES software package [29], developed for the JCMT telescope on Mauna Kea. FLUXES provides the brightness temperature of some planets on any date across a range of mm and sub-mm wavelengths. FLUXES incorporates a model for the correction of Martian brightness temperature with the Sun-Mars distance. For Venus we use the table of published Venus brightness temperatures listed in Eric Weisstein's thesis [119]. We determine the location and solid angle of the planet, Ω_P , from the online NASA planetary ephemeris¹. Typical brightness temperatures for Mars were between 205 to 211 K at 150 GHz during our CMB observations in 2001 with a reported error of 5%. The brightness temperature of Venus is approximately 300 K at 150 GHz [116] with an error of 8%. The planetary brightness temperatures as a function of frequency, $T_B(\nu)$, are well fit by a straight line between 100 and 400 GHz. For each observation we convolve this linear fit with the frequency response

¹NASA Reference Publication 1349: Twelve Year Planetary Ephemeris: 1995 - 2006 by Fred Espenak (<http://lep694.gsfc.nasa.gov/code693/TYPE/TYPE.html>)

of our detectors, $\tilde{f}_i(\nu)$, to determine the band average flux density for each channel, i ,

$$\bar{S}_P^i = \frac{\int 2kT_B(\nu)\Omega_P(\nu/c)^2\tilde{f}_i(\nu)d\nu}{\int \tilde{f}_i(\nu)d\nu}.$$

In the absence of atmosphere, the ratio

$$R^i = \frac{\bar{S}_P^i}{\int V_P^i(\vec{\theta})d^2\theta} \quad (\text{Jy V}^{-1}\text{sr}^{-1}),$$

would give us the responsivity of the each channel. However, we observe the planet through an attenuating atmosphere and must correct for the atmospheric opacity to determine the actual planetary flux arriving at the instrument.

3.3.2 Atmospheric Opacity

To determine the actual planetary flux incident on our detectors – as well as source flux during normal observations – we need to characterize the transmission of the atmosphere. To do this we perform a skydip before and after planetary observations to determine the atmospheric zenith opacity for each channel, τ_i . The details of measuring the in-band opacity from a skydip are presented in the Appendix. Typical measured values of zenith opacity are 0.035, 0.05, and 0.10 at 150, 220, and 280 GHz, respectively.

Because skydips are a time-consuming process, we developed a method which avoids having to perform skydips regularly but still permits frequent monitoring of the atmospheric transmission. We determined the relationship between our measured in-band opacities and a 350 μm tipper experiment located on the adjacent AST/RO building [93] which measures the sub-mm opacity of the South Pole atmosphere approximately every 15 minutes. This was done by performing many skydips and correlating the measured in-band zenith opacities with those measured by the 350 μm tipper. The relationship is quite linear, as is seen in Figure B.4 which shows the measured in-band opacity of ACBAR observing bands versus the 350 μm tipper values.

3.3.3 Responsivity

Once we have determined the atmospheric transmission, we can re-write the corrected instrumental responsivity in for each channel,

$$R^i = \frac{\bar{S}_P^i e^{-\tau_i^P / \cos(\zeta_P)}}{\int V_P^i(\vec{\theta}) d^2\theta} = \frac{1}{G_0 \Omega_B} \quad (\text{Jy V}^{-1} \text{sr}^{-1}),$$

For this calibration to be useful for subsequent observations we need to correct for the atmospheric transmission of the observation as well as any change in bolometer responsivity due to changes in optical loading at different zenith angles. The correction for the atmospheric transmission of the observation is simply $e^{-\tau_i^{obs} / \cos(\zeta_{obs})}$.

After each planetary observation we run a small chopped thermal source mounted behind a hole in the tertiary. The source is an IR-41 etched metal film emitter manufactured by Boston Electronics². The active area of the source is only a few square mm in area but was measured to emit roughly 200 K above ambient at 150 GHz. This provides a reference signal for each channel, $V_{cal_i}^P$, that is used to scale the bolometer responsivity for future observations. To correct the change in bolometer responsivity with elevation, we run the chopped calibrator source again at the elevation of the CMB observations and multiply the responsivity by the measured ratio of the observation calibrator voltage, $V_{cal_i}^{obs}$, to the planetary calibrator voltage.

Because of the gradual accumulation of snow around the hole in the tertiary and ice on the dewar window, this responsivity transfer is only useful for closely spaced observations. However, the measured signal from RCW38 has an RMS scatter of $< 4\%$ which implies that the detector responsivity is very stable. The resulting responsivity for each channel for a given observation is then

$$R_i = \frac{\bar{S}_P^i}{\int V_P^i(\vec{\theta}) d^2\theta} \frac{e^{-\tau_i^P / \cos(\zeta_P)}}{e^{-\tau_i^{obs} / \cos(\zeta_{obs})}} \frac{V_{cal_i}^P}{V_{cal_i}^{obs}} \quad (\text{Jy V}^{-1} \text{sr}^{-1}).$$

Observations of the cosmic microwave background are usually calibrated into CMB temperature units. Since we are looking at fluctuations in the CMB the conversion between

²Brookline, MA 02445, <http://www.boselec.com>

flux density and temperature is given by

$$\Delta S = \frac{dB_\nu}{dT} \Omega_B \Delta T,$$

where B_ν is the black body spectral energy density given by

$$B_\nu(T) = \frac{2h\nu^3}{c^2} \frac{1}{e^{h\nu/kT} - 1} \quad (\text{Jy sr}^{-1}),$$

and dB_ν/dT is evaluated at T_{CMB} . Thus, the desired calibration from signal voltage to CMB temperature units is given by

$$R_i^{CMB} = R_i \left(\frac{\int \frac{dB_\nu}{dT} \tilde{f}_i d\nu}{\int \tilde{f}_i d\nu} \right)^{-1} \quad (\text{K V}^{-1}),$$

where we have averaged the conversion from flux density to Kelvin over the band. We estimate the total uncertainty on the calibration for the 2002 CMB observations to be 10% which is dominated by the 8% uncertainty in the brightness temperature of Venus.

3.3.4 Galactic Source Cross-Calibration

During the 2002 observing season, there were no bright planets available until September 2002 and we were forced to use a bootstrapped calibration from galactic sources. When the throughput is conserved, the integrated voltage map is equal to $S_0(G_0\Omega_B)$. We can determine the band averaged flux density of an object S_2 from an object of known flux density S_1 by

$$S_2 = S_1 \frac{\int V_2 d\Omega \frac{V_1^{cal} e^{-\tau_1/\cos\zeta_1}}{V_2^{cal} e^{-\tau_2/\cos\zeta_2}}}{\int V_1 d\Omega \frac{V_1^{cal} e^{-\tau_1/\cos\zeta_1}}{V_2^{cal} e^{-\tau_2/\cos\zeta_2}}},$$

where the ratio $V_1^{cal} e^{-\tau_1/\cos\zeta_1} / V_2^{cal} e^{-\tau_2/\cos\zeta_2}$ accounts for the change in atmospheric transmission and bolometer responsivity between the two observations.

We apply this method to observations of RCW38 in both 2001 with Mars and 2002 with Venus where a planet was observed within one day of RCW38 and both observations have calibrator runs for scaling the responsivity. We integrate the flux within $8'$ of the source center. These results are given in Table 3.6. The agreement between the integrated flux is quite good at 150 and 280 GHz but the 220 GHz observations in 2001 suffer from low number statistics and are unreliable. A raster map of RCW38 taken on 06/09/01 is shown

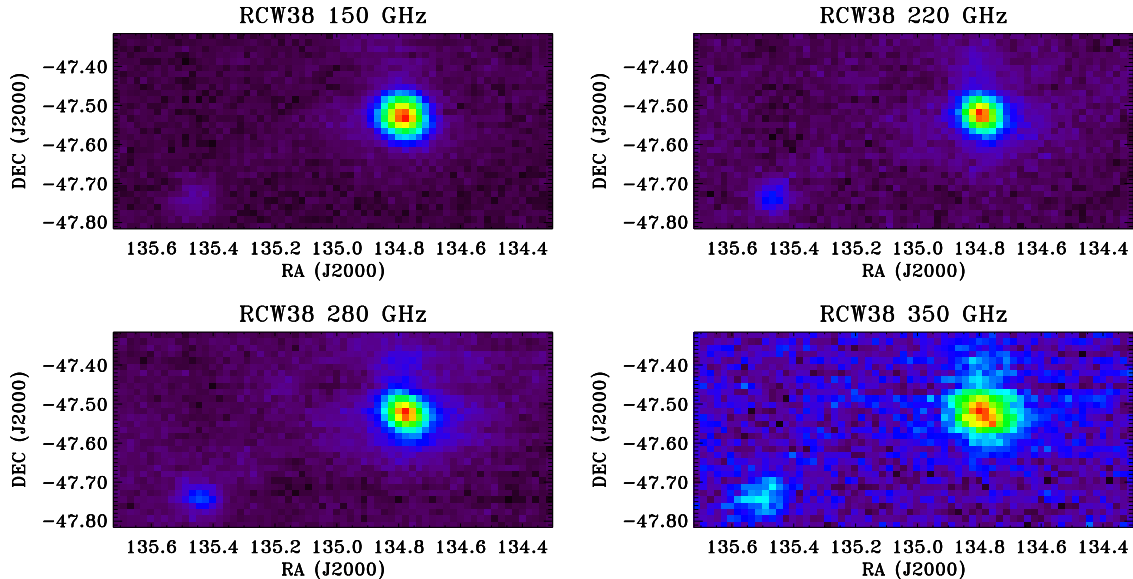


Figure 3.11: Raster map of RCW38 taken on 06/09/01.

Freq (GHz)	S_{RCW38}^{2001} (Jy)	S_{RCW38}^{2002} (Jy)
150	146 ± 15	144 ± 14
220	229 ± 30	260 ± 26
280	318 ± 32	323 ± 32

Table 3.6: Bootstrapped flux densities for RCW38 within $8'$ radius for 2001 and 2002. The 10% error bars on S_{RCW38} include planetary brightness temperature, voltage integral, and responsivity uncertainties.

in Figure 3.11. The complex extended structure of RCW38 – particularly at 220 and 280 GHz – is apparent even in a single raster image. We estimate the total error including planetary calibration, voltage integral uncertainty, and responsivity scaling to be $\sim 10\%$ for both 2001 and 2002.

3.3.5 Calibration Procedure

To determine the calibration for all channels for a given observation we use the following procedure: We impose a limit to the change in baseplate temperature during the course of an observation of 20 mK; this would result in a responsivity change of less than 10% for the 150 GHz detectors (see Figure 3.12). If the fridge is still cooling down or is warming up past 250 mK during an observation, we exclude it. Next we determine the atmospheric opacity during the observation. Because we cannot perform skydips regularly we use the most recent

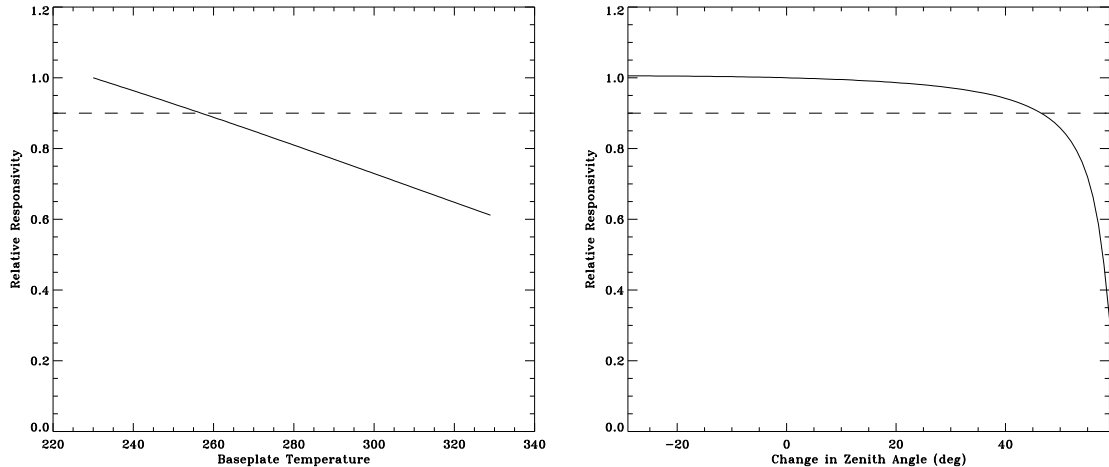


Figure 3.12: Shows the change in relative responsivity for an average 150 GHz detector with varying baseplate temperature (left panel) and zenith angle (right panel). The fiducial parameters are $R_0 = 150 \Omega$, $\Delta = 41.8 \text{ K}$, $G_0 = 300 \text{ pW/K}$, $\beta = 1.1$, $Q = 10 \text{ pW}$, $\zeta = 30^\circ$, $T_{base} = 240 \text{ mK}$, $T_{sky} = 220 \text{ K}$, $\tau = 0.03$, $\nu = 150 \text{ GHz}$, $\Delta\nu = 30 \text{ GHz}$, and $\eta = 0.4$. If we impose the constraint that the responsivity change must be less than 10% we find that the baseplate temperature must rise no more than $\sim 20 \text{ mK}$.

350 μm tipper value and the measured scaling relations (see Appendix B) to determine the in-band zenith opacity of each channel. The 350 μm tipper takes measurements quite regularly, and thus, we have a frequent measure of atmospheric opacity that we can use to correct our observations. With these two measurements in hand, we then calculate the calibration for each channel using the measured planetary responsivity and apply it to the signal voltages.

3.3.6 Calibration Stability

The stability of the calibration depends on the change in detector responsivity and atmospheric attenuation. Figure 3.13 shows the measured calibrator signal (which we originally implemented to measure *in situ* detector responsivity) versus time for all optical bolometers during the 2002 season. Changes in calibrator signal of 50% occur in the 280 GHz channels, whereas the 150 GHz channels fluctuate at the level of $\sim 10\%$. One can also see the strong dependence of responsivity upon bias – the first group of points were taken in the summer at slightly lower bias voltages than are currently being used for the remainder of the season.

We originally believed that the stability of the detector responsivity would significantly depend upon the optical loading. Figure 3.14 shows the normalized calibrator signal from all

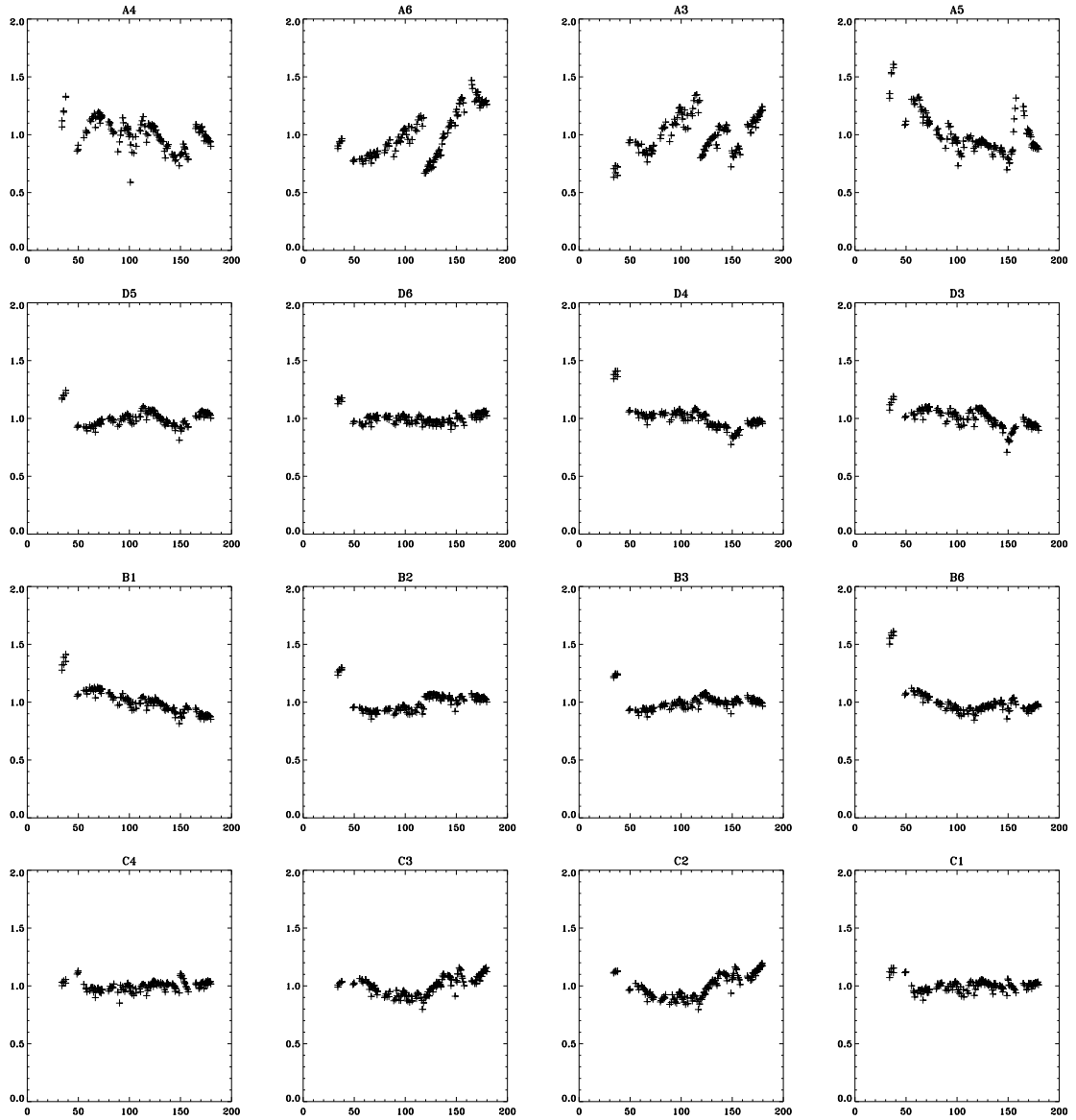


Figure 3.13: Measured calibration source voltages versus days since January 1, 2002. From top to bottom, the rows are 280, 150, 150, and 220 GHz, respectively. The data for each channel have been normalized to have an average value of unity. The first six data points were taken with different bias settings than the rest of the data which explains their departure from the general trend. The large variations in calibrator signal (particularly at 280 GHz) are due to the gradual accumulation of ice on the window.

optical detectors in 2002 versus RJ optical loading as measured from load curves. Although there is some correlation – particularly at the lower frequencies – between the calibrator signal and optical loading, the correlation does not appear to be very strong. The trends in the calibrator versus time (Figure 3.13) are too strong for the lack of correlation to be due to measurement error. This indicates that some physical process is responsible for the lack of correlation. At the end of the 2002 season we discovered that the changes in calibrator signal were due to ice accumulation on dewar window. This renders the calibrator signal useless as a long-term responsivity correction.

As mentioned above, the variation in optical responsivity of the system with changing atmospheric conditions is not very large once the data taken when the telescope is snowy is removed. This snow cut is discussed in detail in §4.5 below. We show the average integrated signal voltage from RCW38, corrected for atmospheric attenuation, for the B-row (150GHz) in 2002 versus time in Figure 3.15. We have applied the snow cut to the data and the dispersion of the integrated signal is less than 4% indicating the responsivity at 150 GHz is quite stable. In Figure 3.16 we show the ratio of the average integrated signals of rows D (150 GHz) and C (220 GHz) to row B (150 GHz) versus time; the correlations between different rows is also stable with time after applying the snow cut. As will be discussed below in the Data Analysis chapter, the snow cut used for 150 GHz is not adequate for 280 GHz because of the steep frequency dependence of snow attenuation and so the results for 280 GHz are not shown in the figure. Because of the stability of the detector responsivity – as measured from the integrated galactic source maps – we elect to use the planetary calibration and correct for changes in opacity and the average change in responsivity between the low-elevation planet observations and the CMB fields.

3.4 Noise and Sensitivity

There are multiple sources of noise that contribute to the limiting system sensitivity of an instrument. The sensitivity of a well-designed system should not be limited by sources of noise inherent to the instrument but by the random arrival time of background photons, in which case, the system is said to be “background noise limited” (or “BLIP limited”). Instrument characteristics that determine whether a system will be background limited are optical power incident on a detector, bandwidth of observed light, optical efficiency, detector

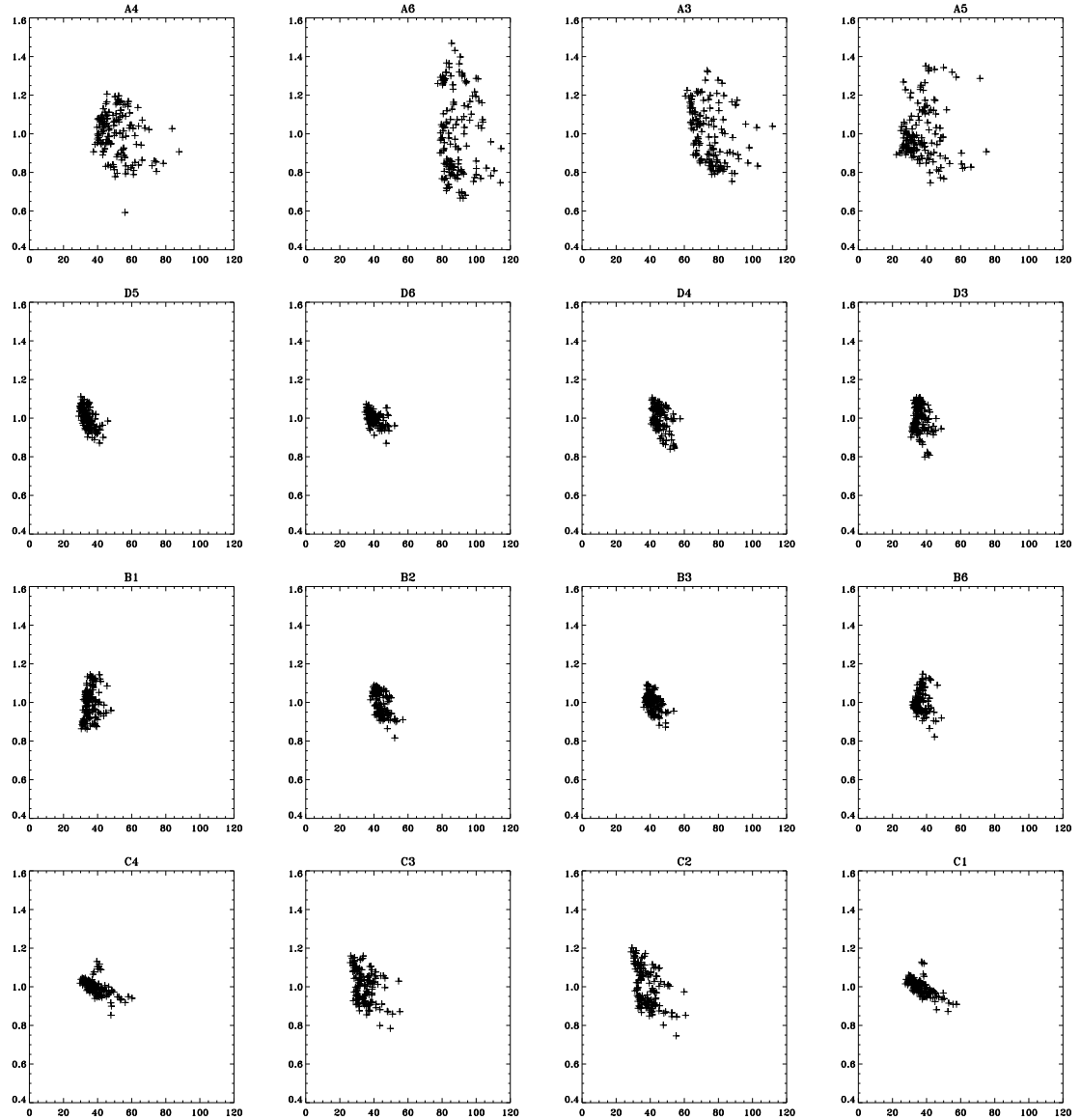


Figure 3.14: Correlation between the measured calibrator signal (normalized to have an average of unity) versus RJ optical loading in Kelvin for all optical bolometers in 2002. From top to bottom, the rows are 280, 150, 150, and 220 GHz, respectively. Although there is some correlation at the lower frequencies, the correlation at 280 GHz is very weak.

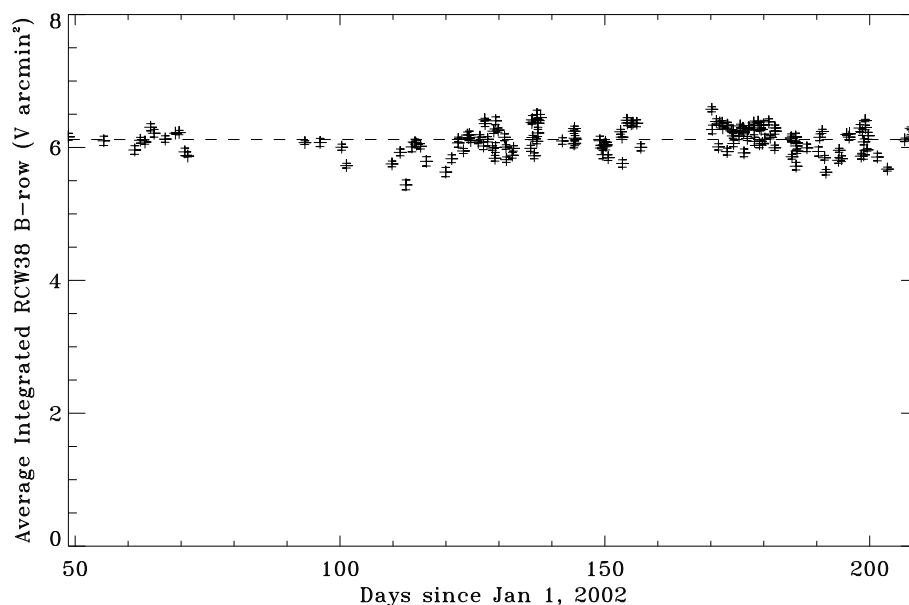


Figure 3.15: Shows the average integrated signal from the B-row (150 GHz) versus time for RCW38 measured in limited raster maps in 2002. The signals have been corrected for atmospheric attenuation and the error bars are purely statistical variance with the integrated signals in the row. The strong snow cut was applied to this data and is discussed in the Data Analysis section.

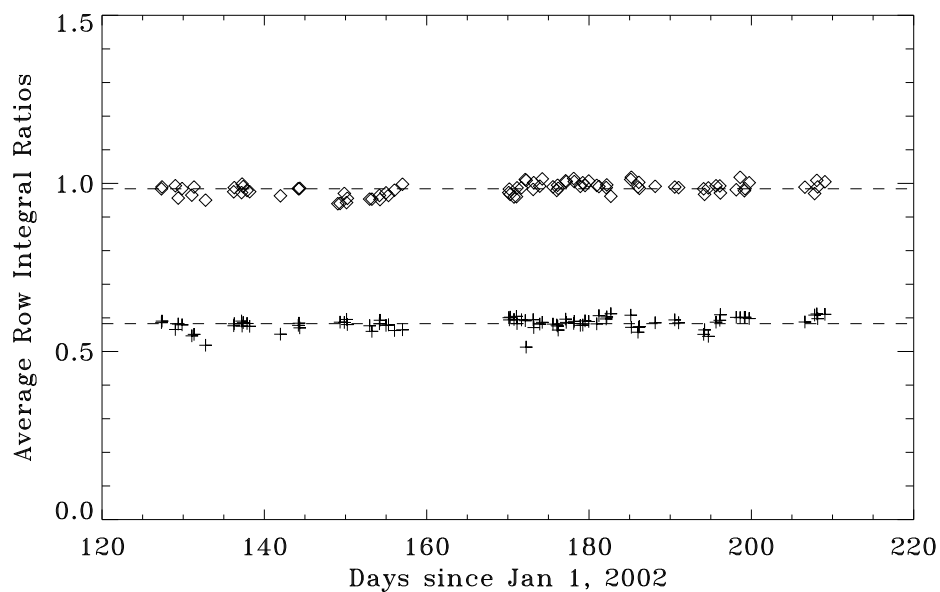


Figure 3.16: Shows the stability of the ratios of the average integrated RCW38 signal from the D-row (150 GHz, diamonds) and C-row (220 GHz, pluses) to the B-row (150 GHz) measured in full raster maps in 2002. The signals have been corrected for atmospheric attenuation and the strong snow cut was applied to this data.

impedance, detector thermal conductivity, operating temperature, electronics noise, as well as the atmospheric conditions of the site.

3.4.1 Photon Noise

Bolometers are effectively photon integrators and are sensitive to the variance in the number of photons arriving in a given length of time. For a detailed discussion, refer to Richards (1994). The number of photons detected per second per Hz of bandwidth per spatial mode is given by the Planck law

$$n = \frac{\epsilon\eta}{e^{h\nu/kT} - 1},$$

where ν is the frequency of the radiation, T is the temperature of the source, ϵ is the source emissivity, and η is the optical efficiency of the system. The variance of this number is $\langle(\Delta n)^2\rangle = n + n^2$. Given an energy per photon of $h\nu$ the mean square fluctuation in power in 1 s of integration is $2Nh^2\nu^2\langle(\Delta n)^2\rangle$ where the factor of 2 accounts for both polarizations of the photons and N is the number of spatial modes, $N = A\Omega/\lambda^2$, which is 1 for ACBAR's single moded feeds.

If we define the power spectral density as $P_\nu = 2Nnh\nu = \epsilon\eta B_\nu(T)A\Omega$ and use the fact that for an integration time t the bandwidth is $1/2t$, we have that the mean square noise per unit bandwidth is given by the integral over the infrared bandwidth:

$$NEP_\gamma^2 = 2 \int P_\nu h\nu d\nu + \int P_\nu^2/N d\nu.$$

The first term represents the random arrival times due to a Poisson process and the second term (referred to as the ‘‘Bose term’’ or ‘‘bunching term’’) encodes the penchant for photons (which are bosons) to bunch together. There is some debate about whether an additional factor of $q = 2Nt\Delta\nu$ should be included in the denominator, where t is the integration time and $\Delta\nu$ is the infrared spectral bandwidth. This factor is in excess of 10^{11} for ACBAR and, if true, would render the second term negligible.

If we can assume that the power spectral density does not vary significantly over the band, the mean square power fluctuation is given approximately by

$$NEP_\gamma^2 \sim 2Qh\nu_0 + Q^2/\Delta\nu,$$

Frequency (GHz)	Q_{total} (pW)	$Q_{internal}$ (pW)	$Q_{external}$ (pW)	$NEP_{\gamma 1}$ ($\times 10^{-17} W/\sqrt{Hz}$)	$NEP_{\gamma 2}$ ($\times 10^{-17} W/\sqrt{Hz}$)
150	11.1	3.7	7.4	4.7	6.4
220	12.1	4.7	7.4	5.9	7.0
280	25.1	7.0	18.1	9.7	11.2

Table 3.7: Average estimated photon noise contributions for each of the three ACBAR frequencies. The total loading was measured with a load curve on a relatively good day $\tau_{350\mu m} = 1.2$, EL=60° (05/06/02). $NEP_{\gamma 1} = \sqrt{2Qh\nu_0}$ and $NEP_{\gamma 2} = \sqrt{Q^2/\Delta\nu}$.

where Q is the total optical power given by $Q = \int P_\nu d\nu$.

ACBAR has roughly equal contributions to the total optical power from warm telescope optics and sky with $T \sim 260$ K and $\epsilon \sim 0.05$ and sources inside the dewar with T between 4 K and 77 K and $\epsilon \sim 0.2$, where ϵ is the emissivity of the surface. Table 3.7 lists the average optical loading for each frequency from inside and outside the dewar along with an estimate of the two photon noise terms. If the second term exists, it would dominate the photon noise contribution for ACBAR. The complete noise budget is presented in Table 3.8. The measured $NEPs$ appear in-between the predicted total $NEPs$ with and without the additional photon bunching term.

3.4.2 Detector and Electronics Noise

Bolometric detectors suffer from two main sources of noise intrinsic to the detector. Johnson noise arises from the thermal fluctuations of a warm resistance and is derived in Richards (1994). The mean square voltage noise per unit bandwidth of a resistor of impedance R at temperature T is given by

$$NEV_J^2 = 4kTR.$$

This can be converted to an NEP using the electrical responsivity of the detector S (V/W) to give

$$NEP_J = \frac{\sqrt{4kTR}}{|S|},$$

where the absolute value is taken because the responsivity of some detectors, including those used in ACBAR, is negative. Johnson voltage noise has a flat spectrum but inherits the frequency dependence of the responsivity when converted to noise power.

The second type of detector noise arises from the quantization of the energy carriers

Frequency (GHz)	150	220	280
$\Delta\nu$ (GHz)	30	30	50
η (%)	40	32	30
$FWHM$ (l)	4.8	3.9	3.9
Q_{total} (pW)	12.8	9.6	26.4
T_{RJ} (K)	39	36	64
R (M Ω)	7.1	7.7	7.3
T_{bolo} (mK)	359	351	355
$G(T)$ (pW/K)	470	485	760
S ($\times 10^8$ V/W)	-2.4	-2.6	-1.9
$NEP_{\gamma\text{ counting}} \times 10^{17}$ (W/ \sqrt{Hz})	5.0	5.3	9.9
$NEP_{\gamma\text{ bose}} \times 10^{17}$ (W/ \sqrt{Hz})	7.4	5.5	11.8
$NEP_J \times 10^{17}$ (W/ \sqrt{Hz})	2.5	2.4	3.4
$NEP_G \times 10^{17}$ (W/ \sqrt{Hz})	4.5	4.5	5.8
$NEP_A \times 10^{17}$ (W/ \sqrt{Hz})	1.2	1.2	1.6
$NEP_{total\ w/o\ bose} \times 10^{17}$ (W/ \sqrt{Hz})	7.3	7.4	12.1
$NEP_{total\ w/\ bose} \times 10^{17}$ (W/ \sqrt{Hz})	10.4	9.3	16.9
$NEP_{achieved} \times 10^{17}$ (W/ \sqrt{Hz})	9.4	7.9	14.6
NET_{CMB} ($\mu K \sqrt{s}$)	345	640	1400
NET_{RJ} ($\mu K \sqrt{s}$)	200	210	250
$NEFD$ (mJy \sqrt{s})	290	530	890

Table 3.8: Average bolometer parameters and noise budget for all three frequencies based on telescope noise data taken with the chopper stopped and a load curve performed at EL=60°; both on 06/14/02. The amplifier and FET voltage noise contribution is estimated to be 3×10^{-9} V/ \sqrt{Hz} at 10 Hz and is scaled to NEP_A by dividing by the responsivity, S . The total NEP is the quadrature sum of all noise components listed. The achieved $NEPs$ are determined from the average calibrated noise power spectra between 10 and 20 Hz.

(phonons) between the bolometer and the thermal bath and depends on the thermal conductivity G and temperature of the bolometer. The phonon noise, or “ G noise,” is given by

$$NEP_G = \sqrt{4kT^2G}.$$

The contribution of these detector noise sources under telescope operating conditions is listed in Table 3.8 for the 2002 season detectors.

The bolometer bias voltage circuit as well as the readout electronics will also contribute to the total system noise. Current noise in the bias circuit will produce voltage noise across the high impedance thermistor. The amplifier chain also contributes through the JFET buffers and warm amplification stages. During the 2001 observing season we shorted one of the JFET pair gates together along with a 10 k Ω shunt to ground. This shorted pair

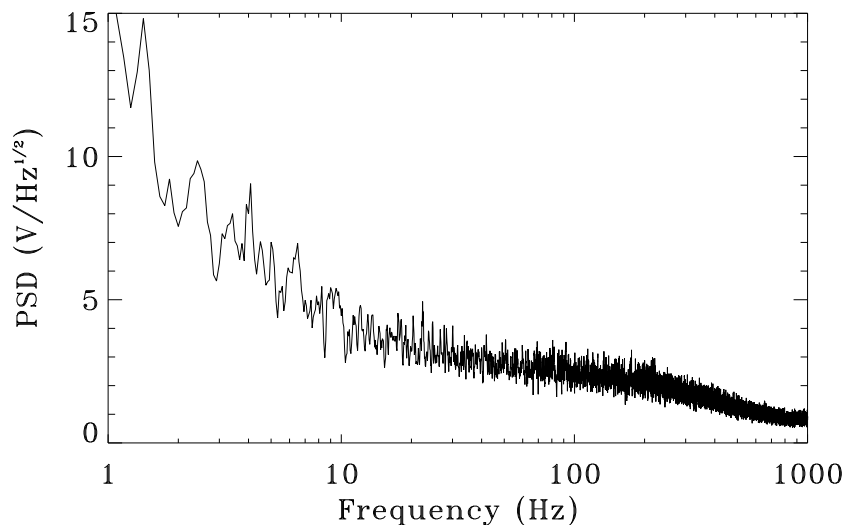


Figure 3.17: Amplifier and FET noise PSD from ACBAR while on the telescope for a shorted pair of FETs. The PSD has been smoothed. The effect of the 650 Hz AC filter can be seen at high frequency.

provides an *in situ* measurement of the noise from one path through the JFET + amplifier chain and a typical noise PSD is shown in Figure 3.17. The noise level is $\sim 3 \text{ nV}/\sqrt{\text{Hz}}$ down to $\sim 10 \text{ Hz}$ where the $1/f$ noise starts to rise. To convert the noise voltage PSD to an *NEP* one needs to divide by the electrical responsivity which is approximately $-2.5 \times 10^8 \text{ (V/W)}$ at low frequencies for ACBAR but does decrease with frequency as $(1 + \omega^2 \tau_{\text{bolo}}^2)^{-1/2}$.

We plot the average calibrated telescope NET_{CMB} of the 150 GHz channels – after correcting for the complete transfer function – versus frequency in Figure 3.18. Also plotted are the expected frequency spectra of the primary CMB and a point source assuming a chopper speed of 3° at 0.3 Hz. This figure indicates that the chopping rate could probably be increased by a factor of ~ 4 without significant loss of sensitivity from the rise in *NET* due to detector time constants.

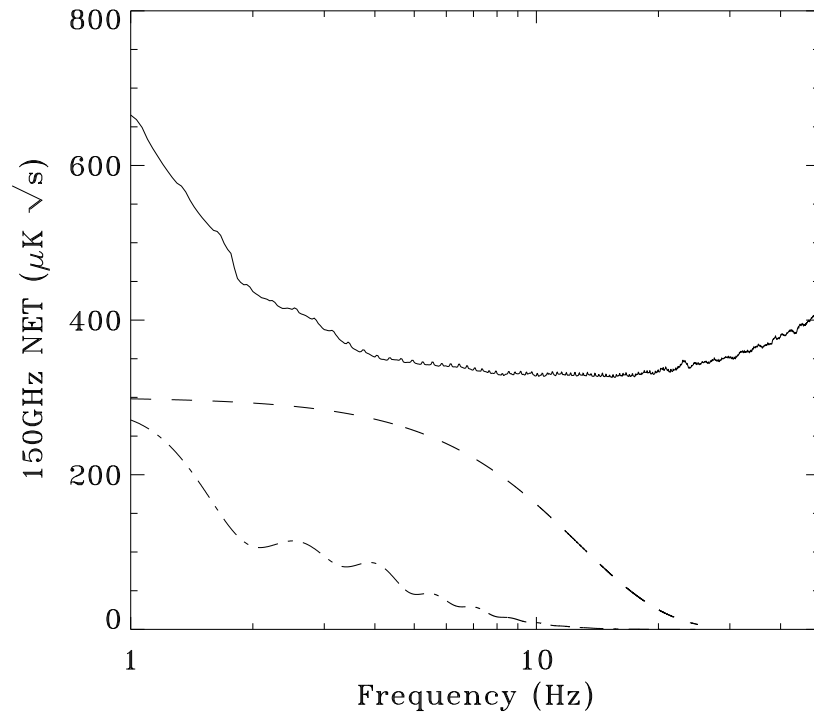


Figure 3.18: Average calibrated NET_{CMB} (solid line) of the eight 150 GHz detectors during observations of the CMB. Also shown are the arbitrarily normalized frequency spectra of Λ CDM CMB anisotropies (dot-dashed) and a point source convolved with a $4.5'$ beam (dashed). We have assumed a telescope chop of 3° at 0.3 Hz (108 arcmin/s).

Chapter 4 Signal Processing

A considerable amount of signal processing must be performed on the raw voltage time stream data to generate a map of the microwave sky. Figure 4.1 shows a schematic flow diagram of the data path from raw time ordered data to the final coadded maps.

4.1 Time Domain Filtering

As described in detail in the Transfer Function Appendix, the raw signal voltages have undergone a significant amount of filtering due to the response of the detectors and transfer function of the signal electronics. We correct the raw time ordered data (TOD) for the complete system transfer function to recover the incident optical signal time stream. The correction of the transfer function in frequency space is given by

$$\tilde{s}(\omega) = \tilde{T}^{-1}(\omega)\tilde{v}(\omega),$$

where v is the raw signal voltage, T is the transfer function of the system, s is the desired incident signal, $\omega = 2\pi\nu$ is the frequency, and the tilde denotes Fourier Transform.

The advantage of correcting for the transfer function in Fourier space rather than by convolution in time is computation speed. However, spikes in the TOD will then spill power

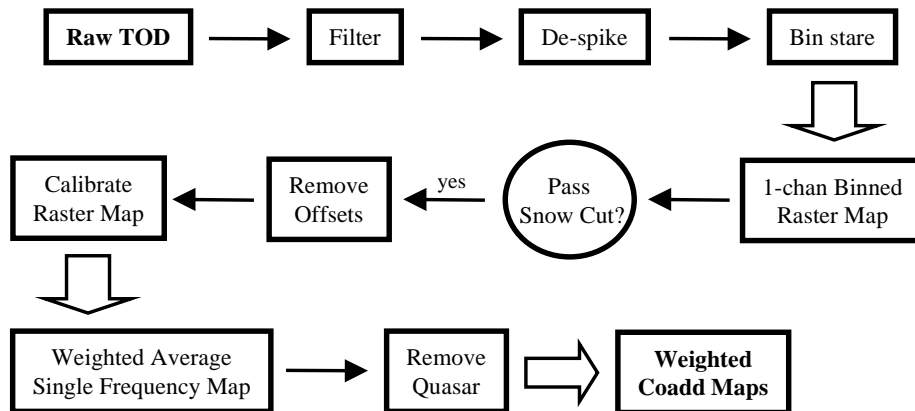


Figure 4.1: ACBAR data processing flow chart.

into the entire “corrected” time stream because the filter has the same length as the data. We mitigate this by accepting an increase in computing time and perform the correction directly on the TOD by convolving the data with a filter kernel of finite length. The full filter kernel is given by a Fourier transform of inverse transfer function in frequency space

$$K(t) \iff \tilde{T}^{-1}(\omega).$$

Using the full Nyquist sampled transfer function will generate a kernel of length equal to that of the TOD. By truncating the filter kernel at some length, the spillover from cosmic ray spikes is limited to the data points within the kernel length. Truncating the kernel also decreases the frequency resolution of the filter. This is not an issue because the Fourier domain transfer function filters are slowly varying so errors introduced by using the truncated kernel are very small.

In addition to correcting for the transfer function of the system, we also want to limit the signal bandwidth to the range where astrophysical signals will contribute. This is because the white noise level will blow up at high frequency after dividing by the steeply falling transfer function. The highest frequency component in the time stream comes from scanning the beam across a point source. An estimate of the signal bandwidth is obtained by dividing the scan speed by the beam width. For the 2002 season we chop the $\sim 4.5'$ (FWHM) beams $\sim 3^\circ$ (peak-to-peak) at 0.3 Hz giving a scan speed of about 108 $'/s$ and a “signal bandwidth” of about 22 Hz.

One can generate a better estimate of the signal bandwidth by modeling the time stream of the scan and taking the Fourier transform (see Figure 4.2). The figure shows a model time stream with beam and chop parameters given in the previous paragraph. The source is placed at both the center and edge of the chop. One notes that regardless of the source position, the signal bandwidth is about 30 Hz; frequencies above this will contribute noise power but no signal power.

To filter out the noise above the signal band, we use a Blackman-windowed sinc filter [106]. Windowing the sinc filter allows us to truncate the filter kernel without causing ripples in the pass-band from an abrupt discontinuity at the edges of the kernel. The Blackman

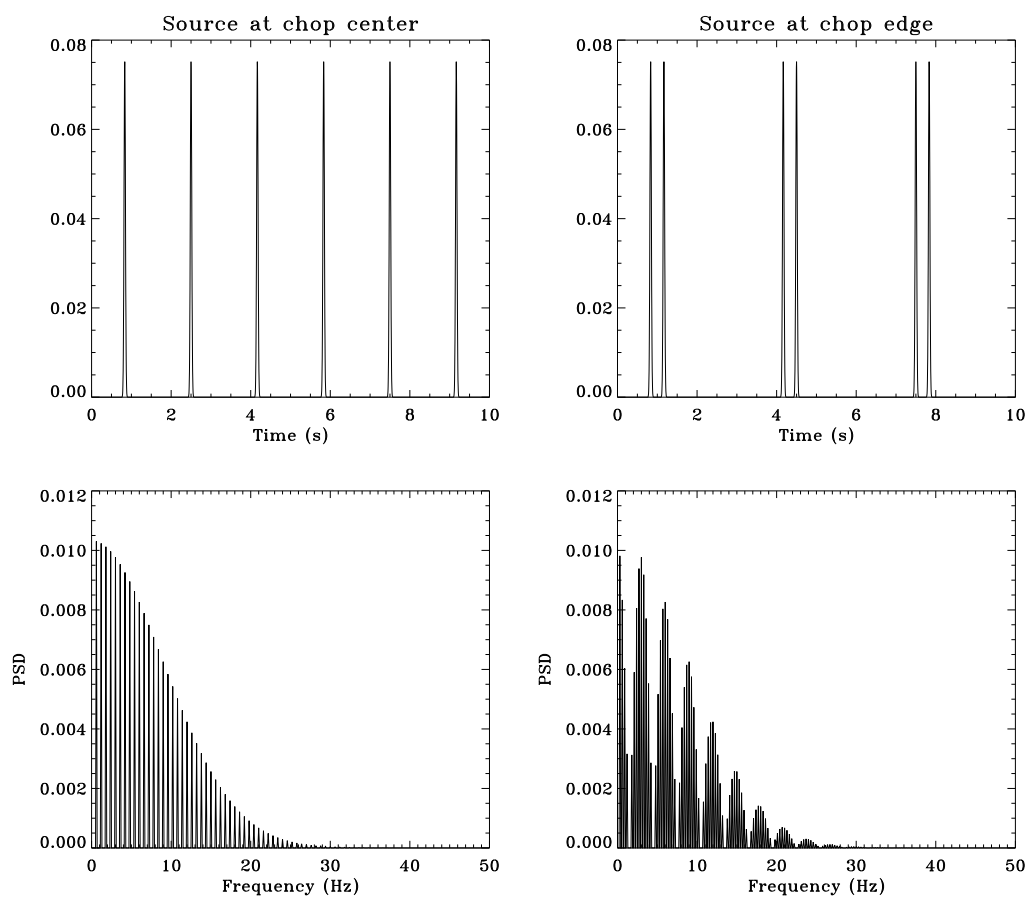


Figure 4.2: Modeled scan time stream and resulting PSD for a $\sim 4.5'$ (FWHM) beam chopped $\sim 3^\circ$ (peak-to-peak) at 0.3 Hz. The left-hand panels have the source located in the center of the chop and the right-hand panels have the source at the edge of the chop. One notes that the details of the comb-like structure in the PSD depend on the source position but the full signal bandwidth depends only on the chop speed and beam size.

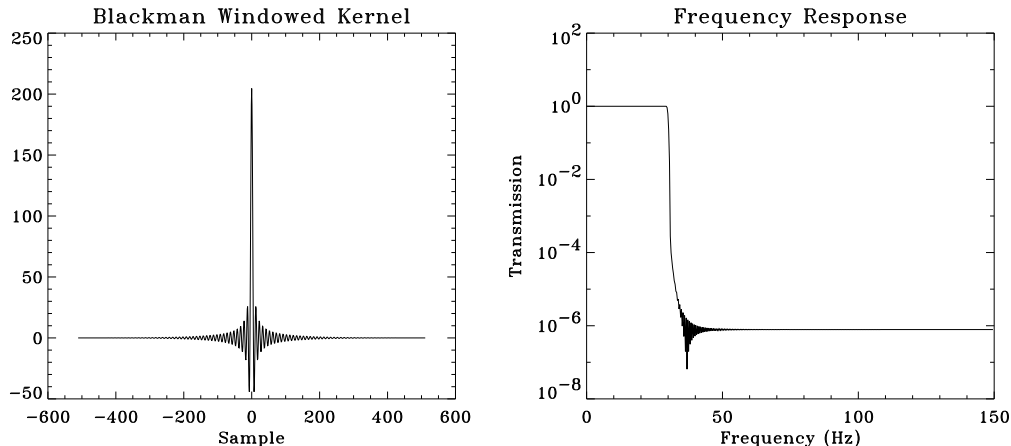


Figure 4.3: Blackman windowed sinc filter kernel (left panel) for a 30 Hz cutoff. The frequency response of this kernel (right panel) shows the steep drop in power and good stop-band attenuation. The kernel length used here is 1023 samples.

windowed sinc kernel (see Figure 4.3) is generated by the equation

$$h_i = K \frac{\sin 2\pi f_c (i - M/2)}{(i - M/2)\pi} [0.42 - 0.5 \cos(2\pi i/M) + 0.08 \cos(4\pi i/M)],$$

where f_c is the desired cutoff frequency (scaled to the sample period), K is a normalization constant to give unity gain in band, and M is the kernel length (we use a kernel length of 1023 samples).

The use of a time-domain filter introduces correlations in the otherwise statistically independent data samples (see Figure 4.4). This figure shows the windowed sinc filter kernel for 30 and 50 Hz edges translated into spatial extent assuming a scan speed of 108 arcmin/s. As can be seen in the figure, for a map pixelated at $1'$ resolution the 30 Hz filter will introduce significant correlation between adjacent pixels, but there will be significantly less correlation with a 50 Hz filter. As an example of the effect of pixel-to-pixel correlation, consider averaging five adjacent data points together that are correlated at the 50% level. The variance in the average will be 40% larger than if the data points were uncorrelated. On the other hand, if the data is only correlated at the 10%, the increase in variance of the average is $< 2\%$. Correlated noise can greatly reduce the significance level of detecting sources a few pixels in size.

Note that because ACBAR scans in RA, the correlations introduced by the time domain filters are only within rows and that different DEC observations are left uncorrelated. This

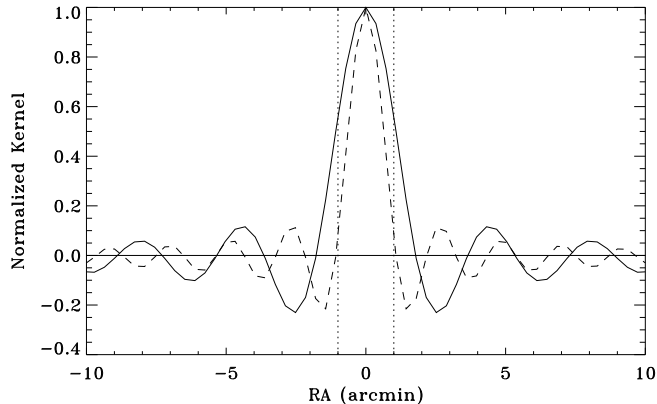


Figure 4.4: Spatial structure of the Blackman windowed sinc filter at both 30 (solid) and 50 Hz (dashed) assuming a scan speed of 108 arcmin/s. The vertical dotted lines correspond to $\pm 1'$ and illustrate the large pixel-to-pixel correlation introduced with a 30 Hz filter.

is borne out in the noise covariance matrix and will be discussed further below. Using a 50 Hz filter has the added benefit of leaving the 2-D spatial noise power spectrum (almost) rotationally symmetric; whereas the 30 Hz filter will remove all noise power in RA with spatial frequency higher than $2\pi/(108/30) \sim 1.74 \text{ arcmin}^{-1}$. Although it is possible to use an asymmetric power spectrum to generate an optimal filter, the optimal filter will zero the spatial structure where there is no signal power. It is convenient to leave the additional high-frequency noise power in the map because of the mathematical simplicity provided by rotational symmetry and the fact that it will be removed by the optimal filter.

4.2 Spike Removal

The next step is to identify and remove signal spikes due to cosmic ray hits in the bolometers or data drop-outs. Spikes are found by taking a pointwise difference of the time ordered data, x_i , as

$$\Delta_i = x_{i+1} - x_i.$$

This differencing is effectively a high-pass filter; slowly varying signals (*e.g.*, chopper offsets) do not appear in the difference signal. The time constant of the electronics is short compared to sample rate and so the signal from cosmic rays rise over one or two samples and thus appear as significant departures from the mean in Δ_i . We take the RMS of the difference data and look for spikes above a fixed σ threshold. For the data presented here we use a 5σ

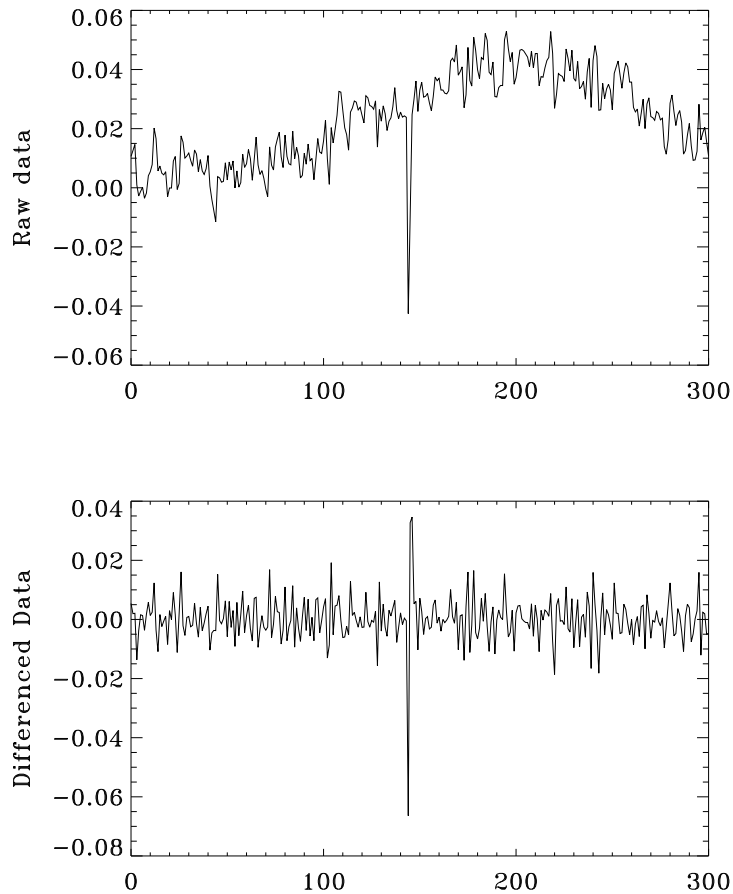


Figure 4.5: Raw time stream and pointwise differenced signal during a cosmic ray hit. Notice that the large slowly rolling offset in the raw time stream does not appear in the difference signal but the quick change from the cosmic ray is very prominent.

cutoff for spike identification. An example of a cosmic ray hit and the associated difference signal is shown in Figure 4.5.

Once the data spikes are identified, the data in the vicinity must be removed. The spike cannot simply be removed from the time stream before filtering because the TOD would no longer be contiguous. However, leaving the spike in the TOD during Fourier domain filtering will spill power into all of the adjacent points. To eliminate this problem we perform all filtering by convolving a time domain filter kernel of finite length with the TOD and removing all of the data within one kernel length of the spike. Because of the high sample rate of the system, this conservative spike removal retains the vast majority of the TOD and prevents any contamination of data spikes in the final maps. The very low cosmic ray cross section of the spider-web bolometers results in an insignificant loss of data

from cosmic ray removal.

4.3 Map Binning

For each observation, the telescope tracks a point on the sky for a fixed amount of time while the chopper sweeps the beams across the same strip of sky many times. This is referred to as a “stare”. For a 60 second stare integration with a chop frequency of 0.3 Hz, each point in the strip is observed 36 times per stare. The data are divided into bins in chopper encoder voltage and averaged to produce a binned stare. Explicitly, for time ordered data x_i and chopper encoder voltage v_i we bin the stare as

$$\bar{x}_m = \frac{\sum_j x_j}{N_j},$$

with the sum over all encoder voltages v_j that satisfy

$$(v_{min} + m\Delta v) \leq v_j < (v_{min} + (m + 1)\Delta v).$$

The chopper encoder sweeps ± 10 V corresponding to about $3^\circ = 180'$. The sample rate of ~ 300 Hz with a chop frequency of 0.3 Hz yields about 500 samples per left- or right-going sweep, or roughly 3 samples per arcminute per sweep. The data are binned into 180 bins per chop corresponding to roughly $1'$ on the sky. The beam width is significantly larger than $1'$ which means the noise in the bins will be correlated if there is noise power on the sky.

Each stare, n , in a multi-position raster map undergoes the same binning procedure to produce a binned map for each channel, X_{mn} . The stares are separated by $1'$ in declination, and thus, each map bin corresponds to about one square arcminute on the sky. After binning, the pointing model generates RA and DEC coordinates for each bin and writes the binned data and pointing information to a file. These individual raster maps then undergo offset removal and are coadded to produce a final map of the sky.

4.4 Offset Removal

The dominant feature of the individual coadded maps is a large, roughly parabolic, chopper synchronous offset (see Figure 3.5). The offsets are due to modulation of the beams through the optical system as the chopping flat rotates. The dominant contributors to the offset structure are movement of the beams on mirror optics (which is amplified by the presence of snow on the mirrors), spillover from the chopper, and atmospheric conditions. As described in §3.2.3 above, we installed a blackened light baffle between the tertiary and chopper to reduce the spillover contribution to the offsets. The baffle does not affect the offset due to motion of the beams on the mirrors; this is only improved by frequent cleaning of snow from the mirror surfaces.

During periods of good weather (and when the mirrors are free of snow), the amplitudes of the offsets are quite small and very stable. During poor weather, the offsets are observed to change with time. We have optimized our CMB observation strategy to mitigate the effects of time varying offsets while preserving the CMB signal by performing a LEAD-MAIN-TRAIL (LMT) observing sequence. The LMT differencing strategy works well for removing linearly drifting offsets by generating the vector

$$\vec{X} = \vec{M} - \frac{1}{2}(\vec{L} + \vec{T}),$$

for each declination. Because the stars are observed in the sequence L-M-T, one sees that the average offset of LEAD and TRAIL should equal the offset in MAIN if the offset is stable or changing linearly with time.

The LMT technique has the additional benefit that large-scale structures (such as those expected from the CMB) that are not repeated in L, M, and T are not removed in the difference. The main disadvantage of the LMT technique is that it is not easy to distinguish whether decrement sources in the LMT map are either actual decrements in the MAIN field or increments (such as from radio point sources) in the LEAD or TRAIL fields unless there is sufficient sensitivity in all three maps to make the distinction. This is not an issue for measuring the CMB power spectrum because it is the CMB power (not amplitude) in the map that is of interest. To find SZ clusters in the maps, however, we need to employ a different technique to remove the offsets.

Unlike large-scale CMB fluctuations, clusters are compact objects and we are not con-

cerned with preserving the large-scale structures in the maps. We can therefore compute an average offset for each of the L, M, and T raster maps independently and remove the offset from each stare in the three maps. Given n declination stares of a field, we calculate the average offset as

$$\mu_i = \frac{1}{n} \sum_j X_{ij},$$

where i denotes the bin number in the chop and j is the declination stare number. The resultant average subtracted map, X' , is then

$$X'_{ij} = X_{ij} - \mu_i.$$

Because the offsets can vary with time, this technique does not perfectly remove the offset in each stare; it removes the small-scale offset structure due to snow on the mirrors which does not change rapidly with time unless the weather is particularly poor. However, it leaves the large-scale variations caused by the atmosphere which do not have much small-scale power. To remove this residual power we fit and subtract an additional polynomial from each of the stares after average offset subtraction. After RA offset removal we perform the same procedure in declination, removing both a common “offset” as well as a polynomial. There is usually very little residual large-scale structure in the maps after RA offset removal except for large-scale CMB fluctuations. Thus, the DEC offset removal only has a modest effect on the map RMS. The resultant maps are very flat and quite random in appearance. An example of common offset plus polynomial removal for a CMB raster map is shown in Figure 4.6.

Although the offset and polynomial removal is necessary to remove undesirable spatial structure, it also effects the data in a number of ways which must be accounted. The first possible issue is removal of the desired cluster signal. The pixel noise in a single observation map is typically a few hundred μK RMS and a massive cluster of galaxies will only produce a signal $\sim 50 \mu\text{K}$ in amplitude. It could be argued that the offset removal would be dominated by the large statistical variance in the map and the cluster signal would remain effectively unchanged. However, the offset removal is a linear process and thus removes cluster signal. In a noiseless map with a cluster at the center, the offset removal truncates the cluster signal by a factor which depends on the size of the map and weakly upon the degree of

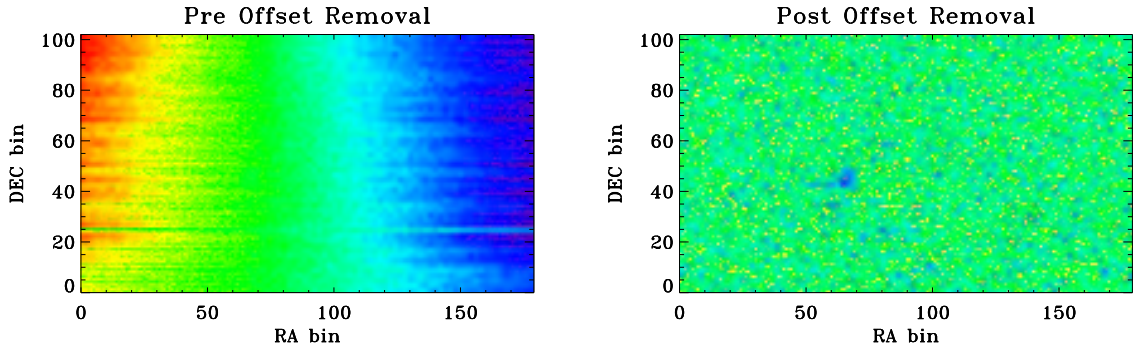


Figure 4.6: Illustrates the effectiveness of offset removal upon a single channel raster map of the MAIN CMB5 field. A common offset plus third-order RA polynomial were removed. The collection of dark points around (65,45) is the central pointing quasar. The scale was reduced by a factor of 5 between the left and right hand figures.

polynomial removed. For the 180' by 103' CMB5 maps we remove a third-order polynomial in RA and a first-order polynomial in DEC. For a 5' FWHM Gaussian beam on a flat field, the offset plus polynomial removal would reduce the peak signal by $\sim 10\%$. We will discuss this issue more thoroughly in the Detection Efficiency section below.

The offset removal eliminates a significant fraction of the primary CMB anisotropy from the map. Although this is beneficial to cluster searching because it reduces the “background” noise in the map, the change in the CMB power spectrum should be accounted for when developing an optimal filter and this will be discussed further below. The last concern from offset removal is the introduction of correlation between pixels. This will produce off-diagonal elements in the noise covariance matrix and reduce the significance of a cluster detection. This too will be discussed more fully in the Power Spectrum Estimation section.

We have an additional degree of complexity for offset removal because our fields include a bright quasar as a pointing reference. If neglected, the quasar will contaminate the average offset and cause ringing in the map from polynomial removal. Ideally, we would fit to the quasar and remove it from each binned map but the sensitivity in the individual maps is not sufficient to completely remove the quasar from the binned map. Simply subtracting the quasar from the map using its known position is not possible either because quasar fluxes are highly time variable and the pointing jitter causes its location to vary slightly with time. To eliminate this we flag the pixels within 10' of the quasar and exclude them from the offset removal process; we then remove the quasar after coadding. The efficacy of masked offset removal is illustrated in Figure 4.7 which shows a 150 GHz raster map of

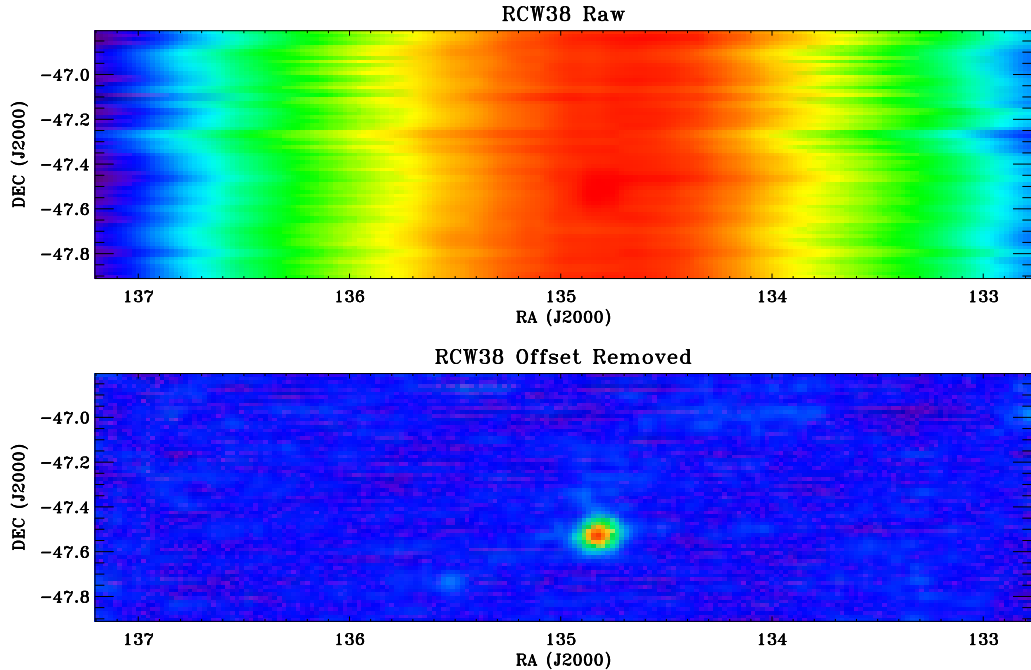


Figure 4.7: Shows the ability to remove large, time-varying offsets from a raster map in an area with a known source. This figure is a 150 GHz raster map of RCW38 and the offsets are atypically large and variable. We masked out the $8'$ surrounding the known position of RCW38 and removed a fourth-order polynomial in RA and a constant in DEC.

RCW38 with particularly large offsets that change with time.

4.5 Data Cuts

In this section, we describe the various cuts applied to the raw data set before inclusion in the coadded maps. The first cut is based on the reliability of the pointing solution for a given observation. There are brief periods of time where the observation of galactic sources does not yield a consistent pointing solution and CMB observations during these periods are excluded. We also verify that the chopper is chopping during the entire observation. We next verify that the fridge base temperature is cold (< 250 mK) during the entire observation to prevent significant changes in detector responsivity. If the fridge is still cooling down during an observation or is warming up before the end of an observation, we do not include it.

Our final cut is referred to as the “snow cut.” As mentioned above, accumulation of snow on the telescope mirrors causes a large chopper synchronous signal. Snow also attenuates

the astrophysical signal before reaching the detectors. This is an especially sinister effect because the signal from the responsivity calibrator mounted in the tertiary is not affected by snow on the telescope mirrors and one may naively assume the system responsivity has not changed. The effect was discovered by measuring the integrated RCW38 flux with time and noticing that the reduction in signal was correlated with an increase in map variance from the chopper offset. Figure 4.8 shows the average integrated RCW38 signal at 150, 220, and 280 GHz versus the average RMS of the C row (220 GHz). One can see from the plot that the magnitude of signal attenuation is a strong function of frequency. We determined that an average C row RMS of 0.02 V provided a reasonably conservative cut level below which the 150 GHz row has very little attenuation. As seen in the figure, this cut level is also acceptable for the 220 GHz channels but completely unacceptable at 280 GHz where the average signal has fallen dramatically by this point. Approximately 650 of the original 1280 hours of CMB5 data survive all of the cuts and is included in the final coadded maps.

In this thesis we will primarily concern ourselves with the 150 and 220 GHz data but will not use the 280 GHz for cluster searching because of its poor sensitivity (approximately 6 times worse than the 150 GHz maps). Thus, we implement the C row RMS ≤ 0.02 V snow cut for the deep CMB and cluster observations. Figure 4.9 shows the average C row RMS versus CMB5 observation along with a horizontal line representing the 0.02 V threshold. One can see that there are very clean periods punctuated by severe snow accumulation. The 0.02 V cutoff level removes 40% of the available CMB5 data and is our largest source of data loss.

4.6 Coadding Maps

The individual raster maps are then calibrated (as described above) and coadded into a map for that observation at each of the observing frequencies. For each spectral frequency we generate a rectangularly gridded empty master map, M , large enough in spatial extent to encompass all of the points from the raster maps. We then cycle through the individual raster maps and determine which bin within the master map (for that observing frequency) to include each sample using the reported pointing model RA and DEC of each raster map point $(\alpha_{ij}, \delta_{ij})$. The location of a given binned map point in the master map depends on

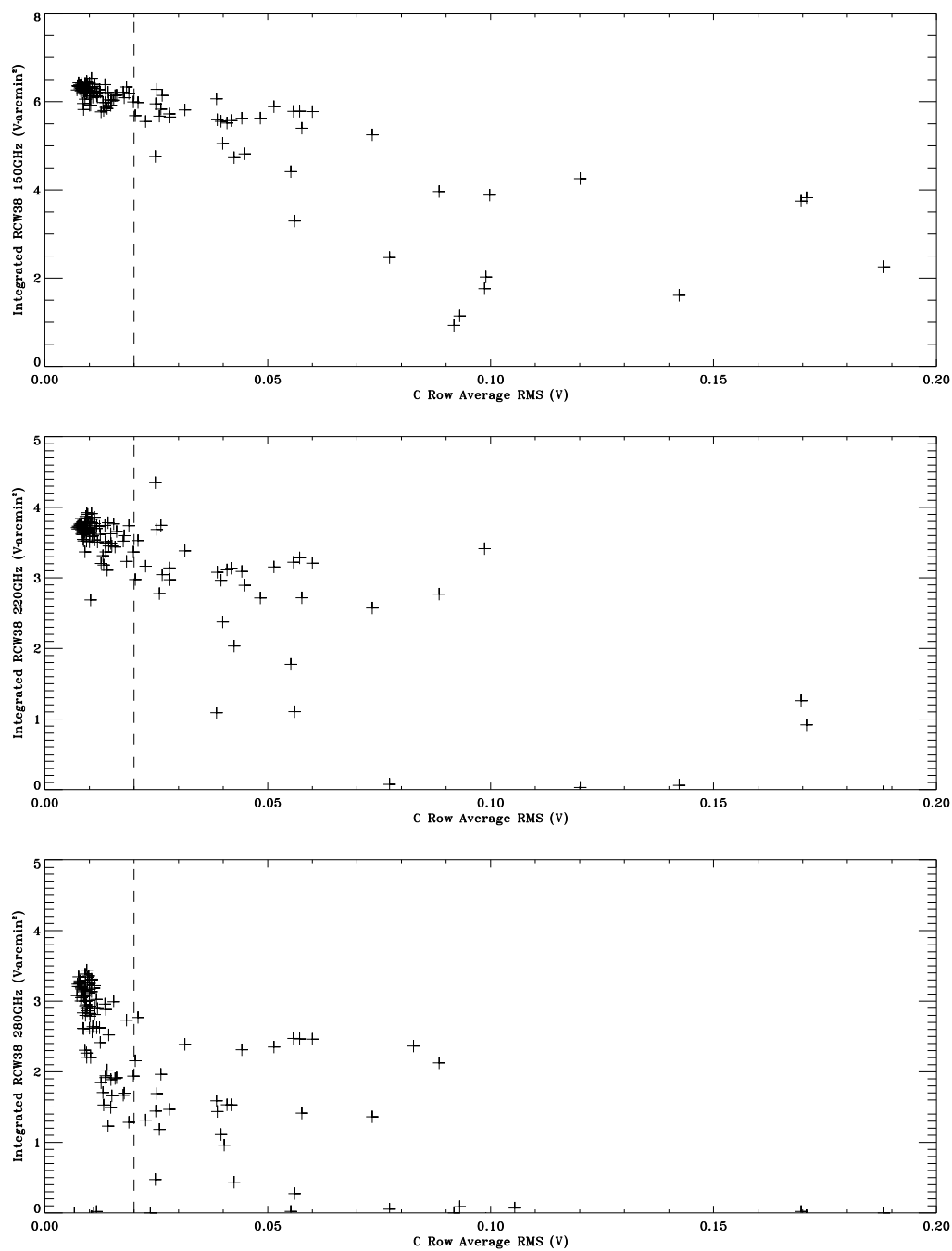


Figure 4.8: Average integrated signal of RCW38 at 150, 220, and 280 GHz versus the average RMS of the four channels in the C row (220 GHz) for 2002. The vertical line corresponds to an average C row RMS of 0.02 V.

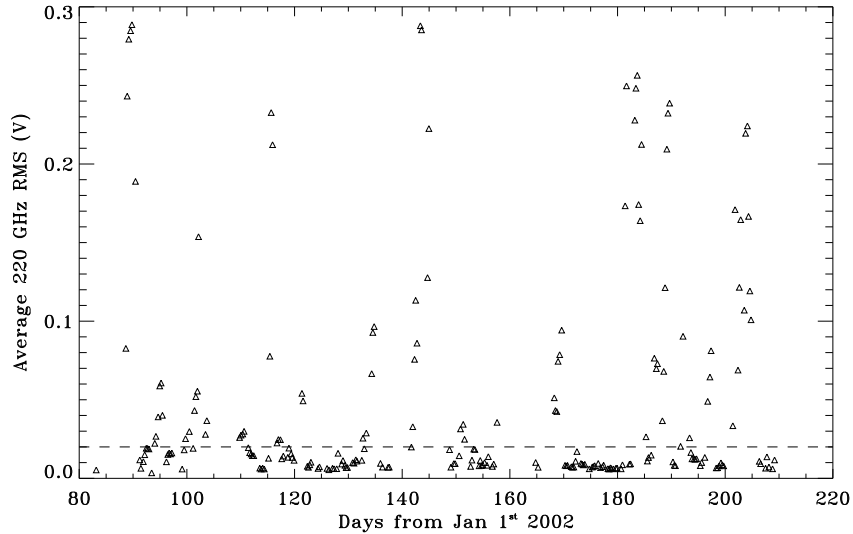


Figure 4.9: Average RMS of the C row (220 GHz) versus time for all CMB5 observations. The dashed horizontal line corresponds to 0.02 V and all observations lying above this threshold are cut from the data sample.

the size of the master map pixels, given explicitly by

$$\begin{aligned} (\text{RA bin})_{ij} &= \text{floor} \left(\frac{\alpha_{ij} - \alpha_{min}}{\Delta\alpha} \right) \\ (\text{DEC bin})_{ij} &= \text{floor} \left(\frac{\delta_{ij} - \delta_{min}}{\Delta\delta} \right), \end{aligned}$$

where α_{min} and δ_{min} are the coordinates of the corner of the master map on the sky and $\Delta\alpha$ and $\Delta\delta$ are the widths of the master map bins.

There are intrinsic sensitivity differences between the individual channels that go into a single frequency's observation map and we use this information to weight the data points rather than simply average the points in each bin. We perform a weighted average of the points within each observation bin using the inverse of the variance of the individual binned maps for that sample as the weight. Given a collection of samples in each bin, X_{mn}^i , from maps, i , with map RMS σ_i , we calculate the weighted average of each bin in the observation map as

$$\bar{X}_{mn}^{obs} = \frac{\sum_i X_{mn}^i / \sigma_i^2}{\sum_i 1 / \sigma_i^2}.$$

Once we have coadded all the channels within a given observation to generate a map at 150 GHz we have sufficient sensitivity on the central quasar to use it as a pointing reference

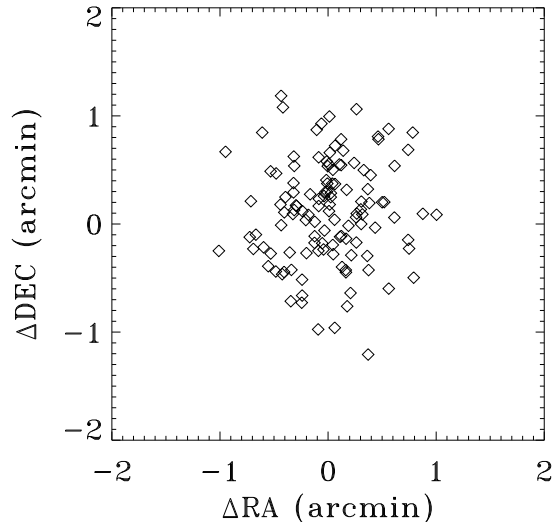


Figure 4.10: Measured position offsets in RA and DEC of the quasar PMN J0253-5441 in the CMB5 field for all files used in the coadded data set. The rms dispersion is $0.39'$ in RA and $0.47'$ in DEC. The dispersion is a combination of pointing jitter and centroiding error.

and remove it from the map. We measure the centroid of the quasar and compare it to the reported pointing model position by smoothing the map with a narrow Gaussian and determine the best-fit position. The scatter of quasar centroid positions for the CMB5 field is shown in Figure 4.10 and represents a combination of actual pointing jitter and centroid uncertainty. We can then use the measured centroid position to shift the coordinates of the coadded map before adding it to the final map. This will produce a minimally sized quasar image in the final map but the resulting size of the quasar may not accurately represent the final coadded beam size since the quasar is used for both positioning and beam size estimation. We remove the quasar by fitting an asymmetric 2-D Gaussian to the 10 arcminutes surrounding the quasar and subtract the best fit Gaussian. This quasar removal works well but we conservatively exclude the $10'$ around the quasar from further analysis because of correlations introduced by the time domain filters.

Once the quasars are removed from all of the coadded observation maps, we measure the variance in each map and use it as a measurement of the atmospheric conditions during the observation for weighting the final coadd. Since the observation maps do not have uniform coverage across the entire map, we only use the overlap region where all channels within that frequency were sampled to generate the weighting. As with the observation maps, we

generate the final coadded map by

$$M_{mn} = \frac{\sum_{\alpha} X_{mn}^{\alpha} / \sigma_{\alpha}^2}{\sum_{\alpha} 1 / \sigma_{\alpha}^2},$$

where X_{mn}^{α} are the individual observation map values and σ_{α}^2 is the variance of the overlap region of observation map α .

The binned maps of the CMB5 MAIN field are shown in Figure 4.11 at all three frequencies and we have intentionally left the quasar in the field and performed no smoothing to illustrate the effective beam size. This effective beam includes the combination of the actual beam sizes along with pointing jitter. The same maps are also shown in Figure 4.12 but we have removed the quasar from the field using the prescription above.

The error bar associated with M_{mn} is not simply the square root of the variance of the points $\{X_{mn}^{\alpha}\}$ because points that are de-weighted because of large map variance should contribute less to the error. We thus use a weighted variance defined as

$$\sigma_M^2 = \frac{1}{N-1} \frac{\sum_{\alpha} (X_{\alpha} - M)^2 / \sigma_{\alpha}^2}{\sum_{\alpha} 1 / \sigma_{\alpha}^2}.$$

Rather than run through the data twice – once to generate M_{mn} for each point and another time to calculate σ_M – we see that expanding the square of the difference term we get

$$\sigma_M^2 = \frac{1}{N-1} (\langle X^2 \rangle - M^2),$$

where the brackets indicate weighted average. So we can keep track of the sums of $X_{\alpha} / \sigma_{\alpha}^2$, $X_{\alpha}^2 / \sigma_{\alpha}^2$, and $1 / \sigma_{\alpha}^2$ and just remove the square of the weighted average at the end of the coadd to determine the variance. One can see that in the limit of equal weights, the weighted variance becomes the standard variance. Maps of σ_M – which are useful for quantifying sky coverage – for the LEAD, MAIN, and TRAIL CMB5 fields at 150 GHz are shown in Figure 4.13. Overplotted on the error maps are boxes indicating the low-noise regions of the three fields used for cluster searching in subsequent sections.

Related to the variance is the noise covariance matrix, C . If the master map has N total points then the noise covariance matrix is $N \times N$ and measures the degree of correlation between each pair of pixels in map. If the points are uncorrelated, then the diagonal elements of C will merely be the variances of each map pixel and the off diagonal points

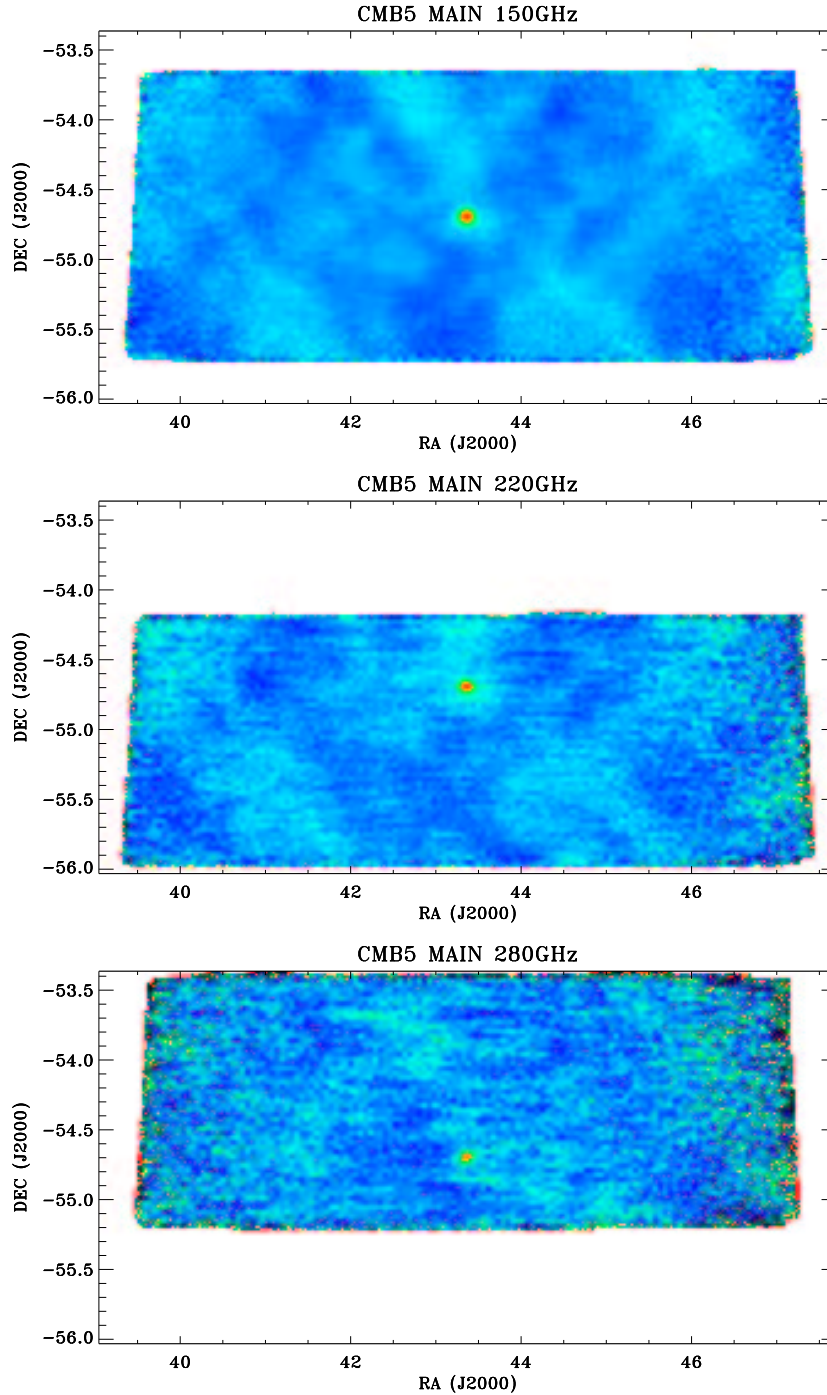


Figure 4.11: Final coadded maps at 150, 220 and 280 GHz of the CMB5 MAIN field after common offset and second order polynomial removal. The maps are pixelated at $1'$ in RA and DEC. All three plots have been converted to thermodynamic temperature and the scale on all three plots is from -1 to 2 mK. This image is useful because the point source quasar shows the final effective beam size of the system which includes pointing jitter. We have only removed a common offset and second-order RA polynomial from these maps to preserve the large-scale structure.

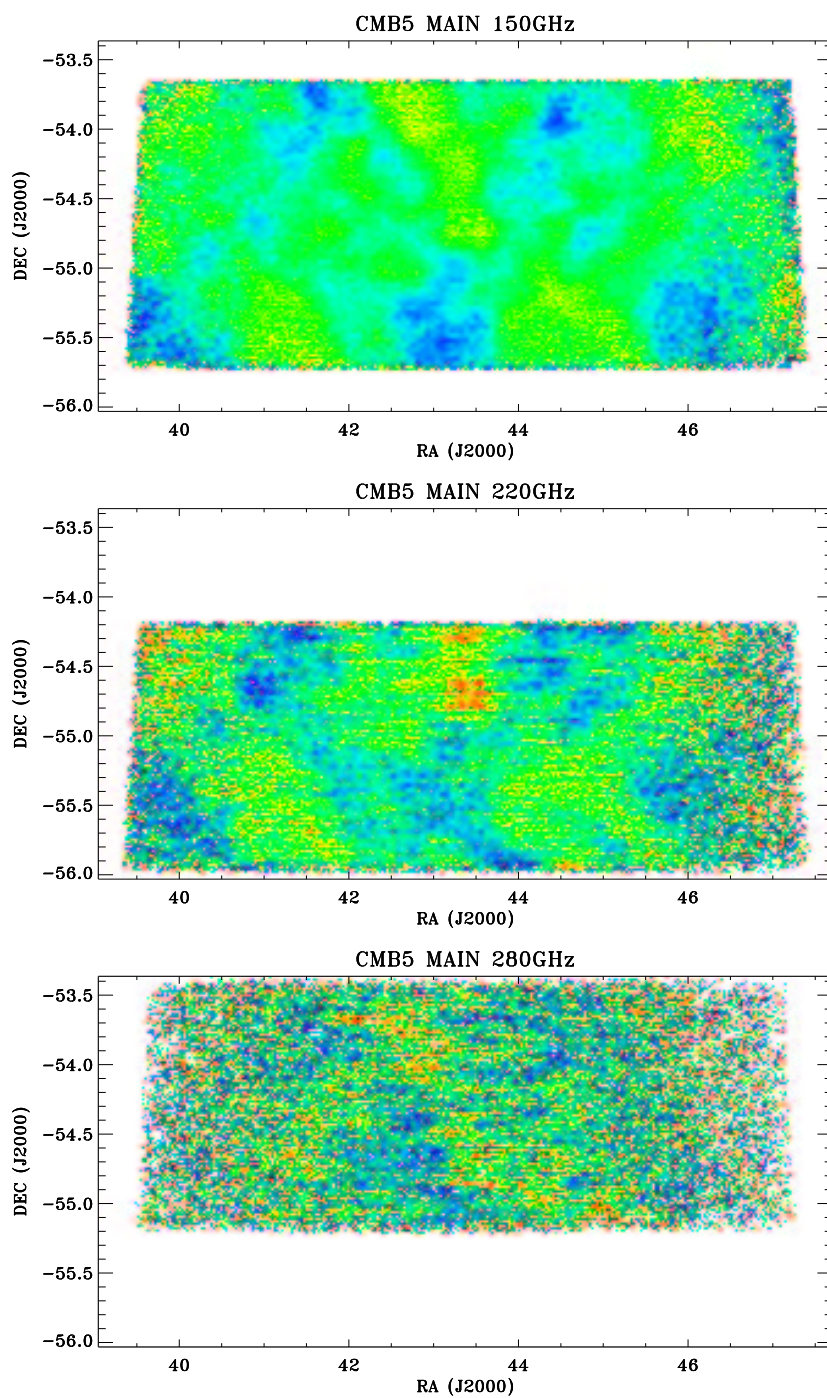


Figure 4.12: Same as Figure 4.11 except the central quasar has been removed and the plots rescaled to $\pm 400 \mu\text{K}$.

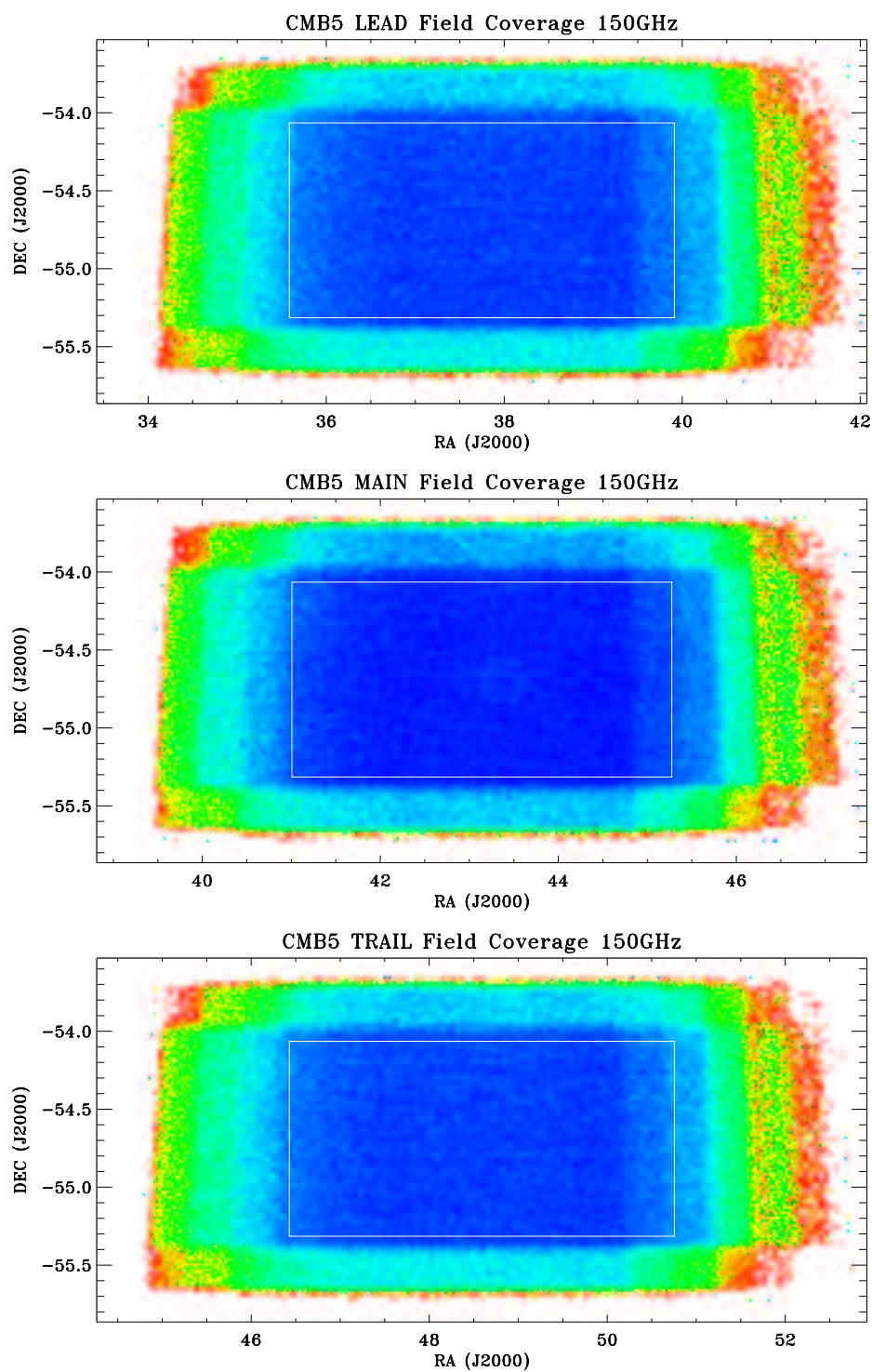


Figure 4.13: Shows the error maps of the three CMB5 fields at 150 GHz. The scales on the images are from 0 to 140, 100, and 140 μK per $1'$ pixel. The white boxes indicate the lowest noise regions of the maps which are used for SZ cluster searching.

will be zero. If we convert the α^{th} observation map and final coadd map into data vectors X_m^α and M_m of length N , then the weighted noise covariance matrix element between the m^{th} and n^{th} pixels of the coadded map is given by

$$C_{mn} = \frac{1}{N-1} \frac{\sum_{\alpha} (X_m^\alpha - M_m)(X_n^\alpha - M_n)/\sigma_{\alpha}^2}{\sum_{\alpha} 1/\sigma_{\alpha}^2},$$

where the sum is over coadded maps $\{\alpha\}$ with variance σ_{α}^2 . Given that not all pixels in the master map are sampled in each individual coadd map, this sum will be incomplete.

The noise covariance matrix of the coadded data vector \vec{M} is related to χ^2 for a model data vector \vec{s} by

$$\chi^2 = (\vec{M} - \vec{s})^T C^{-1} (\vec{M} - \vec{s}),$$

which in the limit of a diagonal noise covariance matrix is equal to the usual expression

$$\chi^2 = \sum_m (M_m - s_m)^2 / \sigma_{M_m}^2.$$

Chapter 5 Data Analysis

5.1 Jackknife Tests

To test whether the structure seen in the maps is repeatable, we can break the data into the first half and second half, process the two halves separately, and compare the average and difference of the two halves. To keep the weighting the same, we also multiply the difference map by 0.5. We remove common offsets from the individual maps along with a third-order polynomial in RA and first-order polynomial in DEC. Approximately 62 raster maps went into each of the halves. The resulting jackknife maps of the 150 GHz LEAD, MAIN, and TRAIL CMB5 fields are shown in Figures 5.1 through 5.3. The maps are pixelated at $1'$ which substantially over-samples the $5'$ FWHM beam and results in a somewhat noisy map. By smoothing the maps with a $5'$ FWHM Gaussian we eliminate most of the small-scale noise while leaving the large-scale power in the maps. The RMSs in the smoothed 150 GHz CMB5 fields are given in Table 5.1 for both the sum and difference. Keep in mind that because the maps are small, the offset removal eliminates the very large-scale CMB anisotropy resulting in a significantly smaller map variance than would be expected from raw CMB ($\sim 100 \mu\text{K}$ for ΛCDM). Note that the difference RMSs are a factor of 3–5 smaller than the sum RMSs even though we removed most of the large-scale CMB power from the map with offset removal.

We can also perform a multi-frequency jackknife by averaging and differencing the signal at two frequencies. Figure 5.4 shows the average and difference of the overlapping regions of 150 and 220 GHz CMB5 MAIN field maps; both have been smoothed with a $5'$ Gaussian.

<i>Field</i>	σ_{avg} (μK)	σ_{diff} (μK)
LEAD	27.0	8.1
MAIN	25.6	5.6
TRAIL	26.6	8.1

Table 5.1: RMS of the $5'$ Gaussian smoothed average and difference 150 GHz CMB5 maps for the first-half/second-half jackknife test.

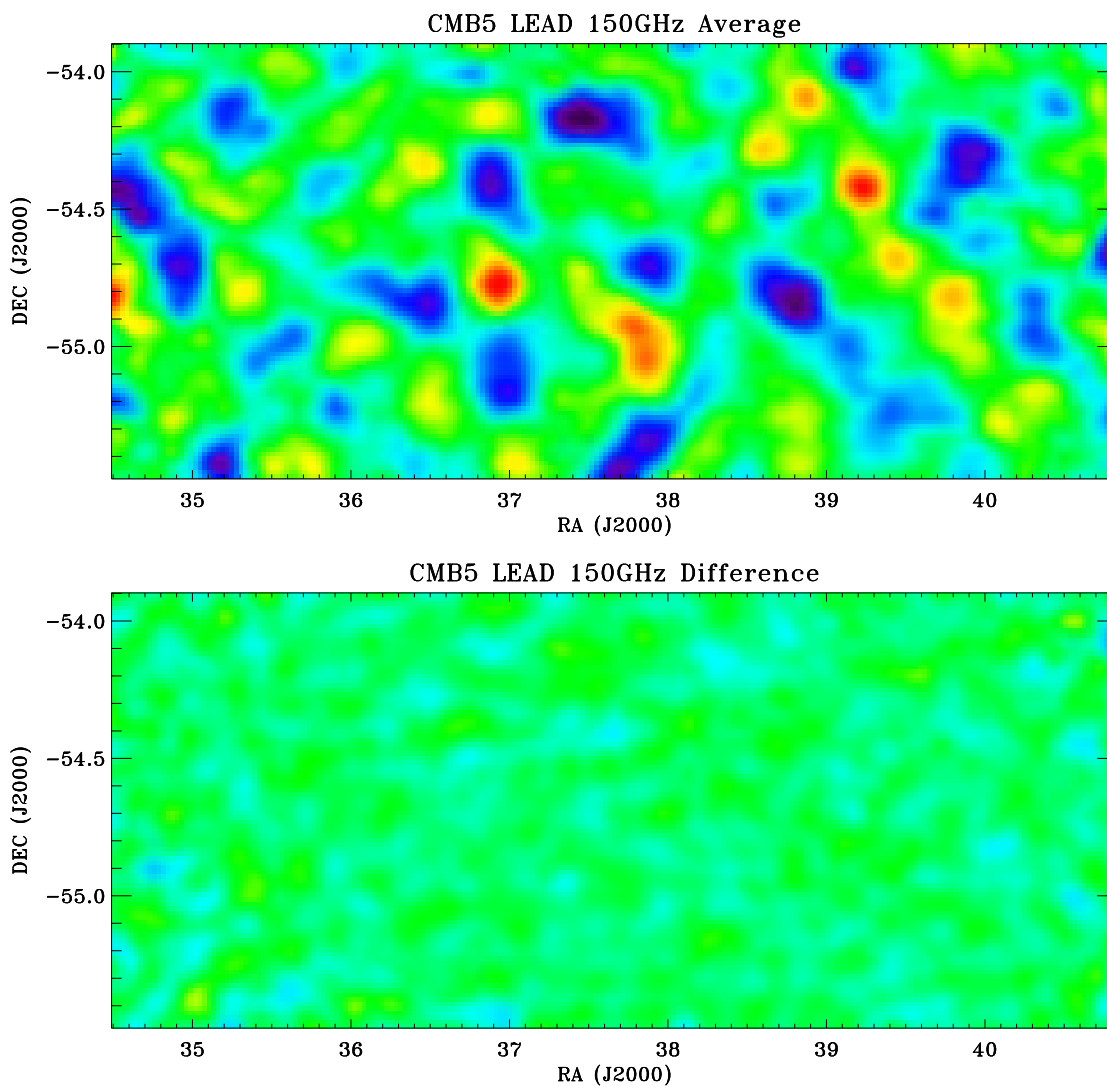


Figure 5.1: First-half versus second-half jackknife for the 150 GHz CMB5 LEAD field. The map is pixelated at $1'$ and the scale is $\pm 100 \mu\text{K}$. A common offset and third-order RA polynomial and first-order DEC polynomial have been removed; this eliminates the largest scale CMB fluctuations from the image.

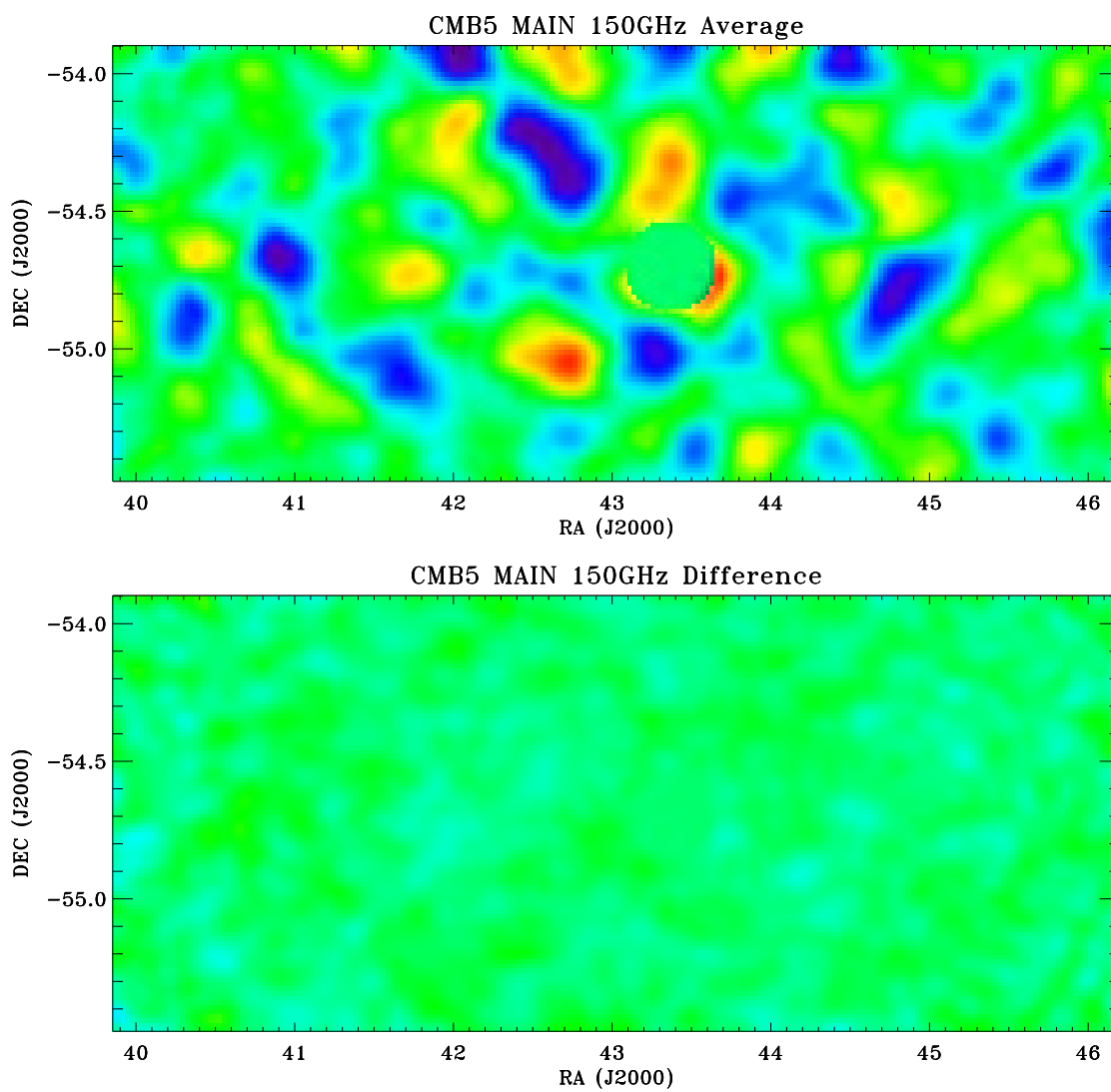


Figure 5.2: First-half versus second-half jackknife for the 150 GHz CMB5 MAIN field. The map is pixelated at $1'$ and the scale is $\pm 100 \mu\text{K}$. The $10'$ around the central pointing quasar has been masked out.

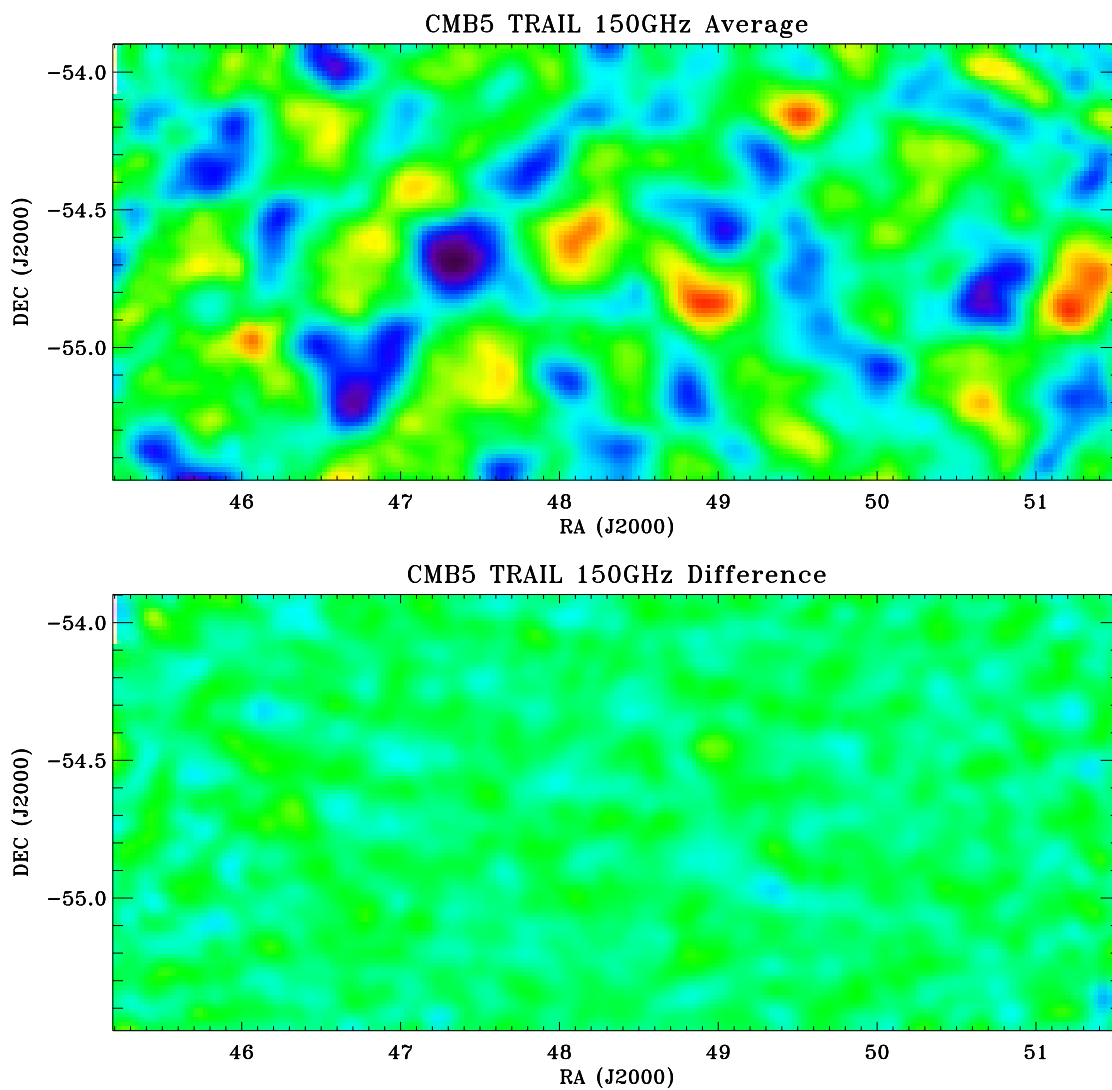


Figure 5.3: First-half versus second-half jackknife for the 150 GHz CMB5 TRAIL field. The map is pixelated at $1'$ and the scale is $\pm 100 \mu\text{K}$.

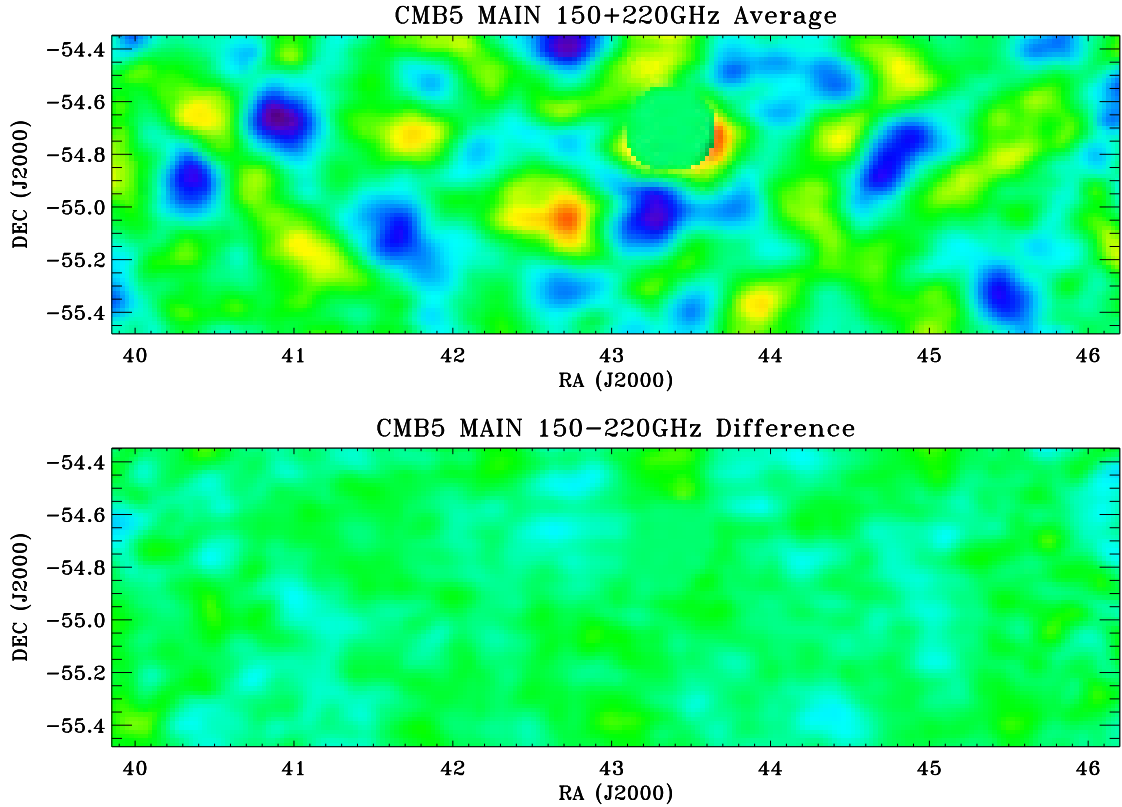


Figure 5.4: Shows the multi-frequency jackknife for the CMB5 MAIN field between 150 GHz and 220 GHz. The 220 GHz map has been scaled by 0.75 to maximize the ratio of average map dispersion to difference map dispersion. The maps have been smoothed with a 5' FWHM Gaussian and are pixelated at 1' with a scale of $\pm 100 \mu\text{K}$. The 10' around the central quasar has been masked out.

We can also test the for a flat spectrum by scaling the 220 GHz map by some factor and measuring the ratio of the dispersion in the average map to the dispersion in the difference map. We find the optimum ratio occurs for a scaling of 0.75. However, this scaling does not account for the large difference (~ 3) between the noise in the 220 versus 150 GHz maps which would tend to drive the “optimum” ratio down. Using the 0.75 scaling we measure the RMSs in the maps to be $23.8 \mu\text{K}$ in the average map and $8.4 \mu\text{K}$ in the difference map indicating that most of the structure in the average map is consistent between frequencies.

5.2 Source Extraction

The topic of extracting compact sources from a noisy background has been the subject of many recent papers. Most of these have targeted the upcoming *Planck* satellite mission¹, which is expected to discover thousands of previously unknown clusters of galaxies [57]. What *Planck* will lack in sensitivity on individual pixels it will more than make up for by mapping the entire microwave sky at many frequencies which will allow the spectral discrimination of SZ sources. This has prompted much development of extraction methods to discern SZ clusters in the presence of a noisy background composed of both instrumental variance and primary CMB anisotropy.

The methods generally fall into two broad categories: Bayesian and Wiener. Bayesian methods attempt to identify clusters in a single-frequency map by probing the likelihood distribution of clusters in a four-dimensional parameter space (two spatial dimensions, a cluster size, and central temperature decrement) using the measured noise properties of the data and an estimate of the power due to the CMB and other foregrounds. Wiener methods, otherwise known as Optimal Filtering, develop a spatial filter that minimizes the contamination of undesirable noise sources (e.g., instrument noise and foregrounds) while maximizing the contribution from sources of a given spatial structure. We elect to use optimal filters for extracting candidate sources from the ACBAR data set.

5.2.1 Optimal Filtering

Optimal filtering makes use of the measured noise properties of a data set and *a priori* knowledge of a source morphology to generate an unbiased spatial filter. This filter maximally enhances objects with the desired shape while minimizing the noise variance in a map. In the present case, we concern ourselves with extracting cluster candidates from a single-frequency map (150 GHz) with an unremovable background of CMB and instrument noise. The matched optimal filter is given, in Fourier space, by the ratio of the source template to the noise power spectrum. This enhances spatial scales where the signal-to-noise is largest. The details of generating a matched filter are given in Herranz et al. (2002). This reference is primarily concerned with the relatively new subject of scale adaptive filters (such as wavelets), but we found that the adaptive filters did not behave as expected for our

¹<http://astro.estec.esa.nl/SA-general/Projects/Planck/>

data set. The traditional matched filter, however, yielded consistent and reliable results. We will focus only on the implementation of the matched optimal filter and use the terms “matched filter” and “optimal filter” interchangeably.

The necessary ingredients for an optimal filter are a spatial template of the desired source, $\tau(x)$, and an estimate of the noise background, $P(q)$. In Fourier space, the matched filter, $\tilde{\psi}(q)$, is given by

$$\tilde{\psi}(q) = \frac{1}{a} \frac{\tau(q)}{P(q)},$$

where the factor a is a normalization factor so that the filter is unbiased. The convolution of the filter with the source profile is a multiplication in Fourier space and for a source at the origin ($\vec{x} = 0$) we have

$$\int d\vec{q} \tau(\vec{q}) \tilde{\psi}(\vec{q}) = 2\pi \int dq q \tau(q) \tilde{\psi}(q) = 1,$$

where we have assumed symmetry in the second equation. This yields the normalization constant for a given source template and noise power spectrum of

$$a = 2\pi \int dq q \frac{\tau^2(q)}{P(q)}.$$

For the case of ACBAR, the $\sim 5'$ FWHM Gaussian beams smooth out the small-scale structure in the cluster and so we assume a symmetric source profile, $\tau(\vec{q}) = \tau(q)$. The oft used β -model cluster profile is found to fit cluster emission well [77] and is given by

$$s(x) = \frac{1}{[1 + (x/r_c)^2]^{3\beta/2 - 1/2}},$$

which for $\beta = 2/3$ equals

$$s(x) = \frac{1}{\sqrt{1 + (x/r_c)^2}}.$$

The β -model has the undesirable features of a diverging spatial integral and Fourier transform. We therefore elect to use the modified $\beta = 2/3$ profile described in Hobson and McLachlan (2002) given as

$$s(x) = \frac{r_c r_v}{r_v - r_c} \left(\frac{1}{\sqrt{r_c^2 + x^2}} - \frac{1}{\sqrt{r_v^2 + x^2}} \right),$$

where r_c is the core radius of the cluster and r_v is a “virial” radius. r_v is not to be confused with the actual virial radius of the cluster, but is used to truncate the extended emission of the cluster at large radii. The authors use $r_v = 3r_c$ and we follow suit. The Fourier transform of the modified β -model has the simple form

$$\tilde{s}(q) = \frac{r_c r_v}{r_v - r_c} \frac{e^{-r_c q} - e^{-r_v q}}{q}.$$

The ACBAR beams are well approximated by a rotationally symmetric Gaussian given by

$$b(x) = e^{-x^2/2\theta^2}$$

$$\tilde{b}(q) = \theta^2 e^{-(q\theta)^2/2},$$

where θ is the Gaussian width of the beam. We can then convolve the beam profile with the source template by multiplying in Fourier space to give

$$\tilde{\tau}(q) = \tilde{b}(q)\tilde{s}(q) = \frac{\theta^2 r_c r_v}{r_v - r_c} e^{-(q\theta)^2/2} \frac{e^{-r_c q} - e^{-r_v q}}{q}.$$

5.2.2 Noise Power Spectrum Estimation

Both matched filter and Bayesian cluster detection methods require knowledge of the “noise” power spectrum (or noise covariance matrix). The noise is composed of both instrumental noise as well as background noise sources. The background noise sources for ACBAR are residual atmosphere and the CMB. In the limit that the data is completely dominated by noise one can use the measured power spectrum of the map as the “noise” power spectrum. However, if there is appreciable signal power in the map, then one must estimate the noise contribution since the signal and noise power spectra are not separable. The instrumental and atmospheric contributions are calculated directly from the dispersion and correlations within the data after removing the astrophysical signal. Estimating the background CMB contribution to the noise power is more difficult.

As detailed above, the calculation of the noise covariance matrix, C_{mn}^N , is mathematically straightforward. In practice, however, it is very memory-intensive and quite cumbersome to calculate for a large number of map pixels. For a map with 10,000 pixels the computer must store 400MB of data (for floating point precision) along with all the computational

overhead to calculate the matrix. This usually involves at least one more matrix of the same size. The situation is somewhat simplified if the correlations in the data are roughly known and the full $N \times N$ matrix need not be measured.

For the case of ACBAR, the raster maps are made by chopping the beams in RA for on the order of a minute for each DEC step. Because of the reasonably long integration time per stare and the time for the telescope to move between stares, the DEC stares can be considered effectively uncorrelated. This approximation is borne out in the measured covariance matrix with the cross-row elements substantially smaller than the diagonal and very random. However, within each row the situation is much less clean because of correlations introduced by the atmosphere as well as time domain filters applied to the TOD and offset removal.

To calculate the contribution of the covariance matrix from the CMB we start by generating the correlation function, $C(\theta)$, which gives the average correlation between two pixels separated by an angle θ on the sky. The correlation function is derived from the CMB power spectrum by

$$C(\theta) = \frac{1}{4\pi} \sum_{\ell} (2\ell + 1) C_{\ell} W_{\ell} P_{\ell}(\cos \theta),$$

where the sum is over the spherical harmonic multipole ℓ . The C_{ℓ} in this expression is the angular power spectrum of the CMB and W_{ℓ} is referred to as the “window function” of the experiment. The window function depends on the beam shape as

$$W_{\ell} = e^{-\ell(\ell+1)\sigma_b^2},$$

where σ_b is the Gaussian width of the beam in radians. The P_{ℓ} are the zeroth order Legendre polynomials and θ is the separation of the pixels on the sky. The CMB covariance matrix only depends on the magnitude of the separation between the two pixels and not their absolute location. Thus, for the pair of points on the sky at locations $\vec{\theta}_m$ and $\vec{\theta}_n$, the theoretical contribution to the CMB covariance matrix is given by

$$C_{mn}^{CMB} = C\left(\left|\vec{\theta}_m - \vec{\theta}_n\right|\right).$$

With both the noise and CMB covariance matrices, the full covariance matrix, C^T , is the

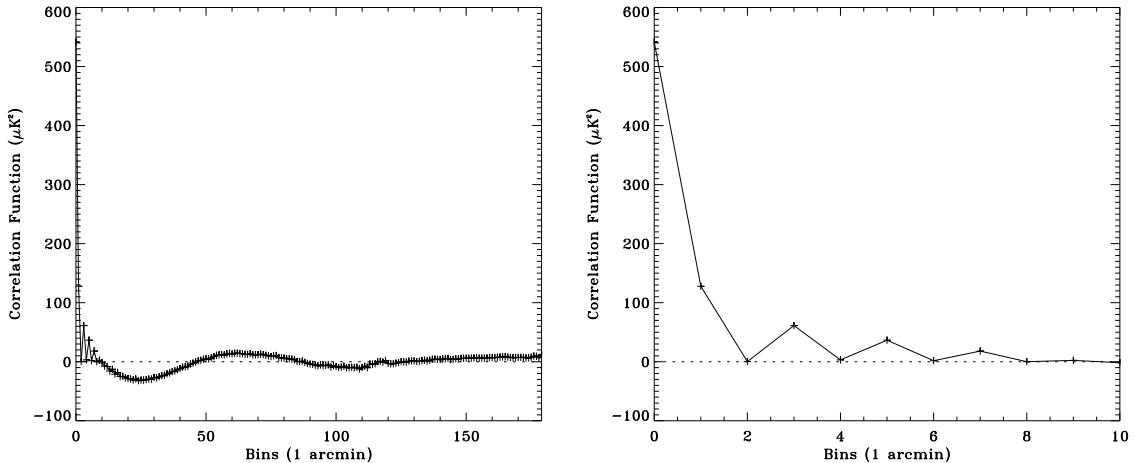


Figure 5.5: Shows the measured noise correlation function for data processed with a 50 Hz low-pass filter and pixelated at $1'$. This function is calculated by averaging the off-diagonal strips of the full noise covariance matrix. The left panel shows the full correlation function and the right panel is a blow-up of the first 10 bins. As discussed in the text, the large-scale correlation is due primarily to offset removal and the small-scale structure visible in the right panel is due primarily to the 50 Hz filter.

sum of these two,

$$C^T = C^N + C^{CMB}.$$

We measured the intra-row noise correlation function by averaging the block diagonal noise covariance matrix. We show the results for a 50 Hz low-pass cutoff filter in Figure 5.5. One can see from the zoomed in plot on the right that the first off-axis pixel correlation is small – but not eliminated – by moving using a 50 Hz LP filter rather than 30 Hz. The morphology of the longer scale correlation from offset and polynomial removal is fairly independent of the LP filter edge.

Uncorrelated Gaussian noise will have a white (flat) spatial power spectrum in the absence of filtering. We have selected our cutoff frequency of 50 Hz to leave the noise power effectively white. Our scan speed of 108 arcmin/s and $1'$ pixelization give a Nyquist frequency of 54 Hz. However, our 2002 data has a narrow noise line in the power spectrum at 55 Hz which we believe is from a mechanical resonance with the muffin fans in the “blue box” that holds the VXI crate on the back of the telescope. Thus, we use a conservative cutoff frequency of 50 Hz; this makes the power spectrum slightly asymmetric but prevents unwanted microphonics from contaminating the data.

The integral of the noise power spectrum gives the total variance due to noise in the map. For a map of uncorrelated Gaussian noise, the variance of the individual pixels is equal to the noise variance in the map ($\sigma_{pixel} = \sigma_{map}$). A map with power spectrum $P(\vec{q})$, where \vec{q} is the 2-D spatial frequency, has a map variance given by

$$\begin{aligned}\sigma_{map}^2 &= \int d\vec{q} P(\vec{q}) \\ &= 2\pi \int_0^\infty dq qP(q) \\ &= 2\pi \sum_q qP_q \Delta q,\end{aligned}$$

where in the second line we have assumed that the noise power spectrum is rotationally symmetric so that it depends only on the magnitude of the spatial frequency and not its direction ($q = |\vec{q}|$). In the last line we have converted the integral to a sum and binned the power spectrum into bins of width Δq .

Because the data is processed such that we believe that $\sigma_{pixel} = \sigma_{map}$ is approximately valid, we assume the noise power spectrum is flat. We then have

$$P^N(\vec{q}) = \frac{\sigma_{map}^2}{\int d\vec{q}} = \frac{\sigma_{pixel}^2}{4q_{max}^2},$$

where in the right-hand expression we've assumed that map bin resolutions are the same in RA and DEC, thus giving the same maximum spatial frequency in both dimensions, $q_{max} = \pi/\Delta\theta$. Total area in spatial frequency space is then $4q_{max}^2$.

To calculate the contribution to the power spectrum from the CMB, we make use of the relation

$$\sigma_{CMB}^2 = \frac{1}{4\pi} \sum_\ell (2\ell + 1) C_\ell W_\ell.$$

Note that there is an implicit lower limit on the sum over ℓ if the map is not full-sky given by $\ell \sim 2\pi/\theta$ where θ is the size of the map in radians. The CMB5 map is approximately 2.5° in extent which gives a minimum ℓ of approximately 140.

With the equation above we can determine the shape of the CMB power spectrum, $P^{CMB}(q)$, by equating the map variances to yield

$$2\pi \sum_q qP_q^{CMB} \Delta q = \frac{1}{4\pi} \sum_\ell (2\ell + 1) C_\ell W_\ell.$$

For $\Delta q = 1 = \Delta \ell$ we have

$$2\pi q P_q^{CMB} = \frac{1}{4\pi} (2\ell + 1) C_\ell W_\ell$$

$$P_q^{CMB} = \frac{1}{8\pi^2 q} (2\ell + 1) C_\ell W_\ell.$$

For ℓ larger than about 100 – which is the case for the ℓ range available to ACBAR – the approximation $\ell \simeq q$ (with q in inverse radians) is valid and the CMB power spectrum can be approximated as

$$P_q^{CMB} \simeq \frac{1}{4\pi^2} C_{\ell=q} W_{\ell=q}.$$

The full “noise” power spectrum for use in generating an optimal filter is then simply

$$P_q = P_q^N + P_q^{CMB}.$$

We now compare the measured power spectrum from the offset removed MAIN CMB5 field with that predicted by a Λ CDM power spectrum and white 27 μ K RMS noise per 1' pixel (see Figure 5.6). The qualitative agreement between the two power spectra is remarkable. The model power spectrum has not been corrected for the effects of offset removal and thus predicts significantly more power at $q < 0.2$ arcmin $^{-1}$ than is measured. As will be seen shortly, the optimal filter will pass no power for spatial frequencies less than about 0.2 arcmin $^{-1}$ and so the over-prediction of large-scale power will not have a significant effect on the optimally filtered data. One can also see from the figure that the approximation of white noise is not quite accurate around $q \sim 1$ arcmin $^{-1}$. This departure could be the desired cluster signal power manifesting in the power spectrum. We will explore the differences produced using optimal filters based on the model power spectrum versus the realized power spectrum below.

5.2.3 Cluster Sizes

Optimal filters require a cluster profile template, $\tau(x)$, which includes a dependence upon the cluster core radius, r_c . The angular core radius of a cluster depends on its mass, formation epoch, observation redshift, and the underlying cosmology of the Universe. For very small clusters, the relatively large ACBAR beams will leave the source unresolved and the source template will be the beam shape. More likely, however, the clusters ACBAR can

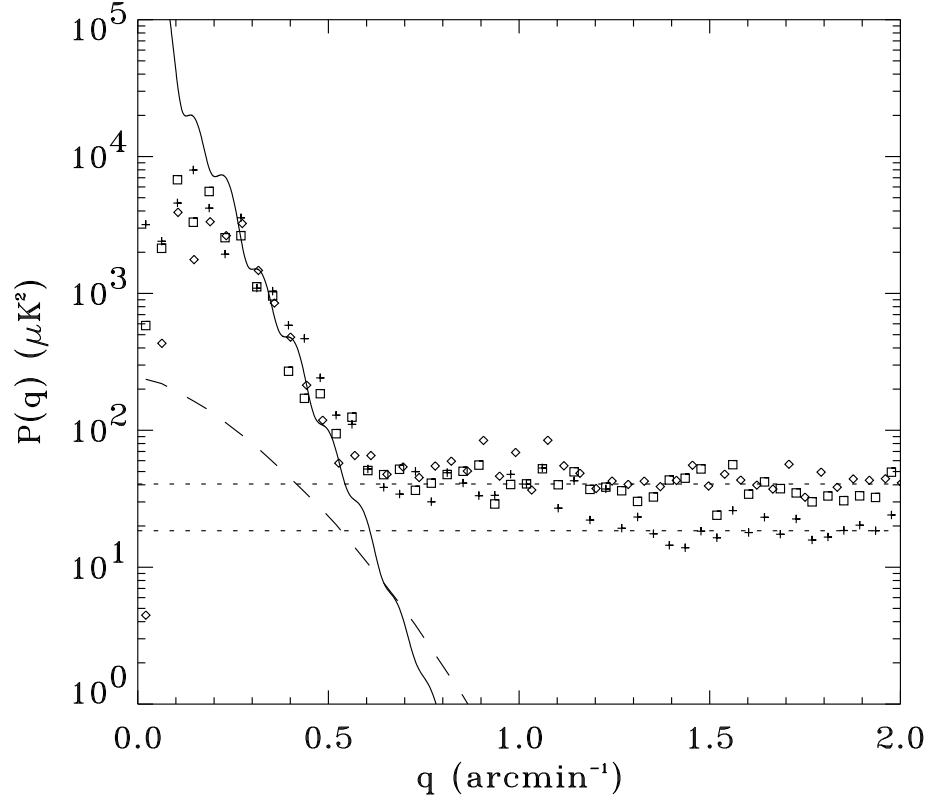


Figure 5.6: Compares the measured power spectra of the CMB5 fields LEAD (diamonds), MAIN (pluses), and TRAIL (boxes) at 150 GHz to that predicted with a Λ CDM cosmology (solid) and 27 and 40 μ K Gaussian noise per $1'$ pixel (dotted). The predicted power spectrum has not been corrected for the effects of offset removal and over-predicts noise power on the largest scales. Also shown is the power spectrum of a cluster (dashed) with a $0.7'$ core radius capable of producing a 100μ K decrement in a $5'$ beam.

detect will be a significant fraction of the beam width in size and the source template will be best modeled as the convolution of the primary beam and an intermediate size cluster. If the source template in the optimal filter is too small, then the extended cluster emission will be filtered out of the map. On the other hand, if the source template is too large, more of the intrinsic CMB anisotropy will pass through the filter and increase the map variance. Thus, we need to determine the most likely range of cluster core radii that ACBAR is capable of detecting.

We accomplish this by using hydrodynamical cluster simulations provided by Mohr and Evrard which image SZ clusters of a range of masses at redshifts 0.06, 0.5, 1.0, 1.5, and 2.3 in Λ CDM, SCDM, and OCDM cosmologies. The simulated clusters are described in detail in Mohr and Evrard (1997). The parameters in the three cosmologies are: 1) Λ CDM: $\Omega_M = 0.3$, $\Omega_\Lambda = 0.7$, $\sigma_8 = 1$, and $h = 0.8$, 2) SCDM: $\Omega_M = 1$, $\Omega_\Lambda = 0$, $\sigma_8 = 0.6$, and $h = 0.5$, 3) OCDM: $\Omega_M = 0.3$, $\Omega_\Lambda = 0$, $\sigma_8 = 1$, and $h = 0.8$. There are sixteen clusters in each cosmology and each cluster is imaged at a distance of $0.06c/H_0$ along three orthogonal axes resulting in 48 cluster images per cosmology. The images are binned in $0.5'$ pixels which are scaled to the appropriate size at the specified redshift with the angular diameter distance relation.

We scale the Hubble constant in the cluster images for Λ CDM and OCDM to the Hubble Key Project value of $h = 0.72$ but retain the SCDM value of $h = 0.5$ to keep the age of the Universe larger than the age of the oldest stars. The physical properties of the simulated clusters scale like $R \propto h^{-1}$, $M \propto h^{-1}$, and $y \propto h$. Few of the simulated clusters have masses exceeding $10^{15} M_\odot$ which, as will be explained later, is the realistic mass range accessible to ACBAR. To extend the cluster sample we assume the cluster properties follow “self-similar” scaling relations, which agrees with the scaling observed in hydrodynamical simulations [80]. Under self-similarity, if the mass of the cluster is increased by a factor α the size of the cluster scales as $\alpha^{1/3}$ and the Compton depth (and temperature decrement) scale as α .

We start by determining the ballpark temperature anisotropy that ACBAR will be able to classify as a detection. To do this, we form an optimal filter with the source template equal to the $5'$ Gaussian beam. This point source response is the best-case situation because the physical scale of the filter will be the smallest, thus introducing the least amount of confusion from primary CMB anisotropy. We apply this optimal filter to the most sensitive region of

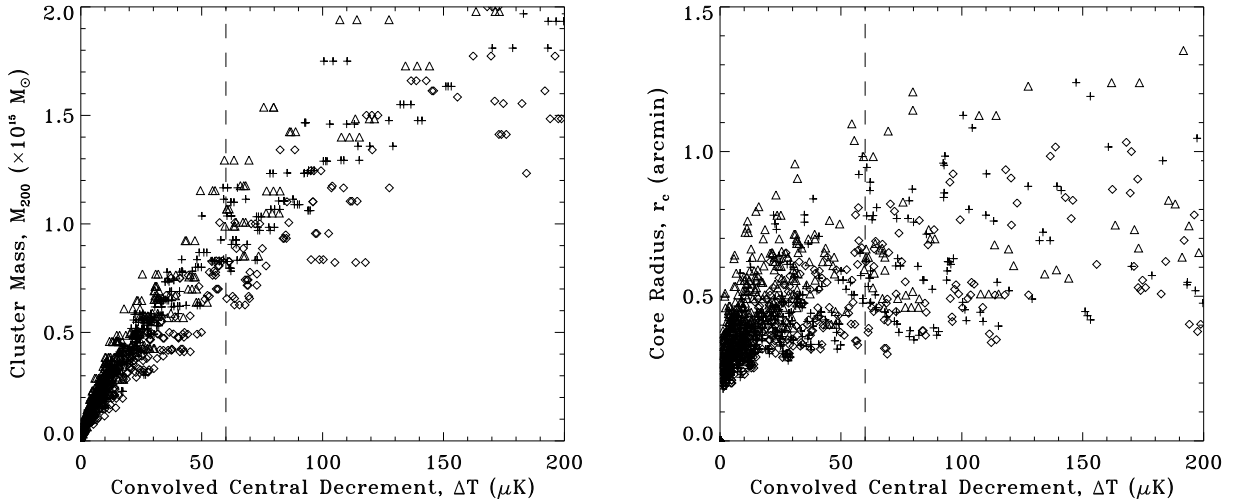


Figure 5.7: Left panel shows cluster mass, M_{200} , versus the expected convolved central decrement for Λ CDM (pluses), OCDM (diamonds), and SCDM (triangles) cosmologies. The central decrement, ΔT , is the maximum temperature decrement at 150 GHz of an SZ cluster after convolution with the $5'$ beam of ACBAR. The right panel shows the cluster core radius, r_c , versus central temperature decrement for the same three cosmologies. The dashed vertical line at $60 \mu\text{K}$ denotes a conservative 4σ lower limit to the optimally filtered maps.

the 150 GHz CMB5 map. The 1σ RMS of the optimally filtered map is approximately $15 \mu\text{K}$ which will require a beam-convolved cluster decrement to exceed $60 \mu\text{K}$ in amplitude for a 4σ detection. Unfortunately, clusters capable of producing a $60 \mu\text{K}$ decrement in a $5'$ beam must be very massive ($\gtrsim 10^{15} M_\odot$), and hence, are quite rare objects in the sky (refer to Figure 1.6).

Now that we have a realistic estimate of the cluster temperature decrement accessible to ACBAR, we need to convert that into a range of core radii for the optimal filter. We do this by taking each of the simulated SZ clusters described above and fit for the core radius of the cluster template, $s(x)$, given above (assuming $r_v = 3r_c$). We then convolve the simulated cluster with a $5'$ Gaussian beam and measure the central temperature decrement that would be measured by ACBAR from that cluster. The results are presented in Figure 5.7, which shows the cluster mass, M_{200} , and core radius, r_c , versus measured central decrement, ΔT , for each of the three cosmologies. The mass estimator M_{200} is the mass contained within a sphere of radius r_{200} in which the average interior density is 200 times the critical density. We have only included the simulations from redshifts $z = 0.5, 1.0,$ and 1.5 because this represents the realistic range of redshift that massive clusters will be present

(refer to Figure 1.6). Overplotted is a line denoting a $60 \mu\text{K}$ measured central temperature decrement which shows that ACBAR will only be able to detect clusters of mass greater than about $10^{15} M_{\odot}$ at 4σ , fairly independent of cosmology.

The parameter we are trying to constrain with these simulations is the likely range of core radii corresponding to detectable clusters. This is shown in the right-hand panel of Figure 5.7. We have drawn a vertical line corresponding to $60 \mu\text{K}$ and we can see that, unlike the cluster mass, the core radii of clusters above this temperature threshold are not well constrained. This is because the SZ temperature decrement is roughly proportional to the total mass of the cluster, but the physical core radius depends upon the redshift of cluster formation and the apparent core radius depends on geometric effects from the angular diameter distance. As seen from the figure, the likely range of detectable core radii lies roughly within the range of $0.4 - 1.0'$.

Because the core radius is small compared to the main Gaussian beam, one may be inclined to assume the source is completely unresolved and simply use the $5'$ Gaussian beam as the source template. To test this approximation, we fit the Gaussian width to the convolution of the primary beam and a model cluster template of varying core radius and plot the fit FWHM versus the core radius in Figure 5.8. One can see that for very small core radii the convolved FWHM is effectively the same size as the raw beam, but for core radii in the detectable range of $0.4 - 1.0'$ the spread in beam size is significant. With no clearly localized optimum cluster scale we will use optimal filters across the likely size range to search for clusters in the maps. It will be shown below in §5.4.2 that the signal-to-noise of a cluster in the filtered maps will not depend strongly upon the assumed cluster core radius.

5.2.4 Application of Optimal Filters

Now that we have both a realistic source template and a noise power spectrum, we can generate optimal filters using the prescription given above. As we saw in Figure 5.6, the measured map power spectrum and the model noise power spectrum are very similar. Figure 5.9 shows the isotropic Fourier transform of the matched filter, $\tilde{\psi}(q)$, with a beam size of $5'$ and a core radius of $0.7'$ for both the measured map noise power spectrum and a model power spectrum generated with a ΛCDM cosmology plus $27 \mu\text{K}$ of white noise. One can see from the figure that the optimal filter based on the measured and model power spectra

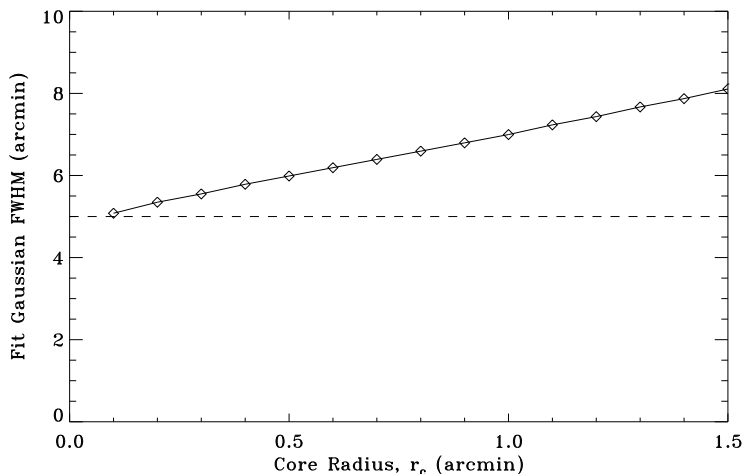


Figure 5.8: Shows the best fit Gaussian FWHM of the convolution of a $5'$ FWHM Gaussian beam and a cluster source profile (given in text) versus the cluster core radius, r_c .

are quite similar. We elect to use the model power spectrum for generating the matched filter least we contaminate the “noise” power spectrum with candidate cluster signal in the deep CMB images. The other feature to take away from Figure 5.9 is that cluster signal power at large angular scales is lost because of the contribution of primary CMB noise power to the denominator of the optimal filter. Figure 5.6 illustrates this point more clearly by comparing the power spectrum of a $r_c = 0.7'$ cluster (convolved with a $5'$ beam) with a Λ CDM power spectrum and white noise. This effects larger clusters significantly more than compact clusters because a larger fraction of their flux is

A related question is the effect of beam size upon the post-filter map RMS; this is illustrated in Figure 5.10. The plot assumes a Λ CDM cosmology and $50 \mu\text{K}$ per $0.5'$ pixel (comparable to the deepest ACBAR maps) and a cluster core radius of $0.7'$. The optimal filter is normalized to be unbiased to this model cluster for all beam widths; the S/N ratio on such a cluster is inversely proportional to the post-filter map RMS. For the cluster model and noise level given above, the “optimum” beam size is about $4'$. The slow rise at large beam size is caused by including an increasing fraction of primary CMB anisotropy. The rise at small beam size results from the fixed pixel instrument noise blowing up as the smaller beam smoothes fewer noise pixels..

If one is optimizing an experiment to search for clusters, this plot does not tell the entire story for a few important reasons. First is that the cluster mass function (and, hence, flux function) is very steep and going to smaller beam sizes will couple more efficiently to the

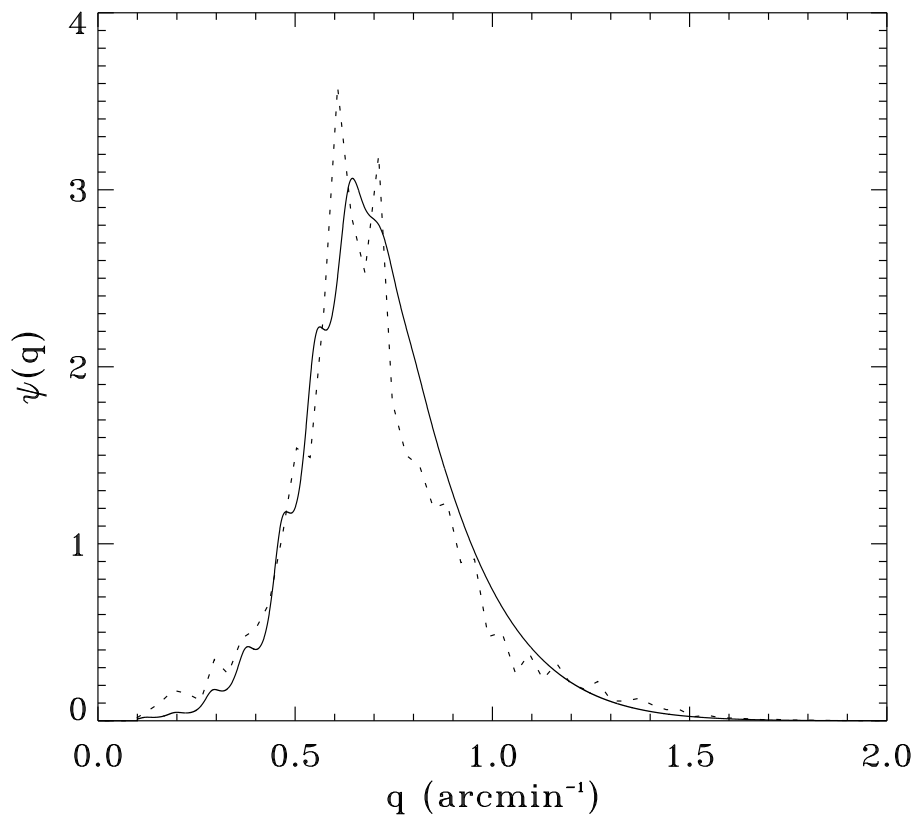


Figure 5.9: Shows the Fourier space representation of the match filter, $\tilde{\psi}(q)$, for a Gaussian beam size of $5'$ and a cluster core radius of $0.7'$ using both the measured CMB5 MAIN map power spectrum (dotted) and a Λ CDM plus $27 \mu\text{K}$ white noise model power spectrum (solid).

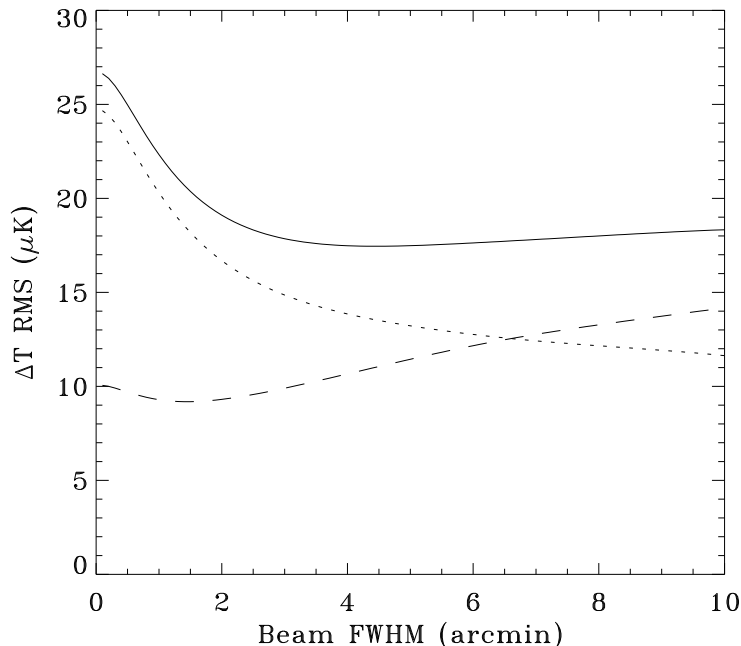


Figure 5.10: Shows the RMS of an optimally filtered Λ CDM anisotropy map versus beam FWHM (solid line) with fixed $50 \mu\text{K}$ instrument noise per $0.5'$ pixel and assuming a cluster core radius of $r_c = 0.7'$. The dashed curve shows the CMB contribution to the total RMS which increases with beam size and the dotted line shows the contribution from instrument noise.

less massive, but significantly more populous, galaxy clusters. Another effect to consider is that the temperature sensitivity of an instrument is independent of beam size and so an instrument with larger beams will map a larger region of sky to a fixed sensitivity than a small beam experiment. In addition, we have assumed the map is pixelated at $0.5'$ and the instrument noise contribution rapidly drops with the smoothing effect of larger beams.

We illustrate the effect of varying the cluster core radius upon the shape of the optimal filter in Figure 5.11. The figure shows how the optimal filter is shifted to slightly larger scales (smaller spatial frequency) as the core radius is increased from 0 to $1'$. Although increasing the core radius improves the coupling to the extended cluster emission, this comes at the price of increasing the post-filter map variance by passing an increasing fraction of primary CMB power. This point is illustrated in Table 5.2 which lists the post-filter map RMS from the CMB as well as total map RMS for a $5'$ Gaussian beam, $27 \mu\text{K}$ of white noise per $1'$ pixel, and Λ CDM cosmology for cluster core radii from 0 to $1'$. One sees from the table that the noise from the CMB increases by about a factor of two between a pure $5'$

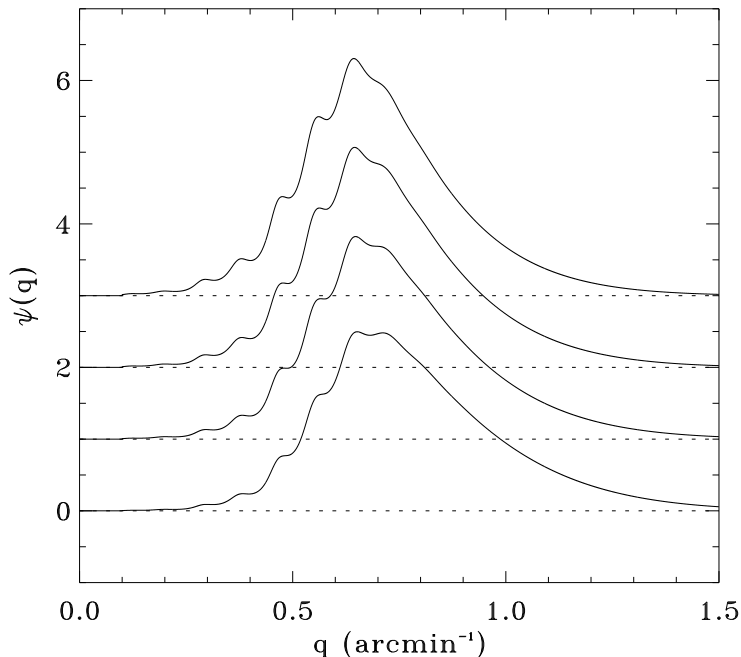


Figure 5.11: Shows the Fourier space representation of the optimal filter for Λ CDM cosmology with $27 \mu\text{K}$ of noise and a $5'$ beam (bottom) as well as for the beam convolved with core radii of $0.4'$, $0.7'$, $1.0'$, from second to bottom to top. The filters have been shifted vertically for ease of visibility.

Gaussian beam and the same beam convolved with a $1'$ core radius cluster. The variance is determined by generating a model power spectrum as described above, performing the convolution in Fourier space, and using Parseval's theorem,

$$\sigma^2 = 2\pi \int dq q \tilde{\psi}^2(q) P(q),$$

where the integral is bounded below by the minimum q determined from the size of the map ($201' \times 201'$ in this case).

A related question is how well the post-filter map variance integrates down with time given a single-frequency map (in which case the CMB is not removable). In the case of ACBAR, the CMB rapidly becomes the limiting “noise” source at 150 GHz because it cannot be removed with the less sensitive 220 and 280 GHz channels. This point is illustrated in Figure 5.12 which shows the total post-filter RMS, the residual RMS from the CMB, and the extra noise power from instrumental variance. It may be noted that the residual CMB power does decrease with integration time. This is because the lower

r_c (l')	σ_{CMB} (μK)	σ_{total} (μK)
0	8.4	15.3
0.4	10.3	16.9
0.7	11.9	18.3
1.0	13.7	19.9

Table 5.2: Post optimal filtering total RMS and CMB-only RMS versus cluster core radius for the parameters listed in the text.

instrumental noise floor allows the optimal filter to push to higher spatial frequencies where there is less CMB power.

The real-space representation of a matched filter with cluster core radius of $r_c = 0.7'$ is shown in Figure 5.13 along with a $5'$ Gaussian for reference. One can see that the physical extent of the filter kernel can extend far beyond the compact beam. The oscillations in the large-scale modes tend to cancel the largest scale structures (dominated by CMB fluctuations) when convolved with the map.

We choose to apply the optimal filter in Fourier space rather than generate a real-space kernel and convolve with the data. To do this, we take the entire map for a given field and pad it with enough zeros so that we do not need to worry about wrap around edge effects. We also zero the edges of the map where the noise rises significantly above the average noise level. We do this because the spatial extent of the filter could couple extra noise into the low noise region of the map. Convolution in Fourier space is done by simply multiplying the Fourier space representation of the filter by the Fourier transform of the map and inverse Fourier transforming the product.

We apply optimal filters to the LEAD, MAIN, and TRAIL fields of CMB5 with the appropriate white noise level for each map as measured from the noise power spectrum (listed in Table 5.3). We do this for cluster template core radii of $0.4'$, $0.7'$, and $1.0'$, as well as for a point source template, denoted $r_c = 0'$. The filtered 150 GHz maps are shown in Figures 5.14 through 5.17. We scaled the z -axis of each image so that sources with amplitude equal to or larger than 4σ appear as white, where σ is the map RMS after optimal filtering. The post-filter map RMS is also listed for each field and core radius in Table 5.3.

Overplotted on these figures are the locations of candidate sources where the signal

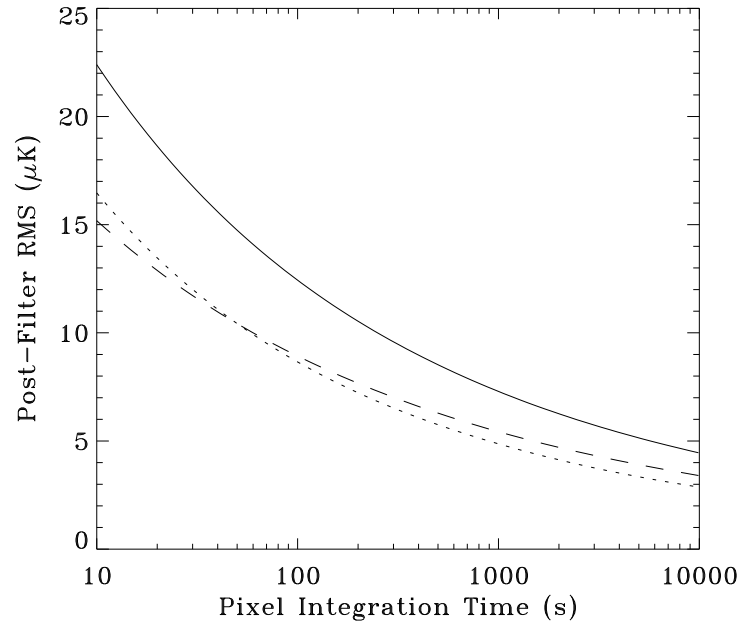


Figure 5.12: Shows the different contributions to the optimally filtered map RMS as a function of pixel integration time. This assumes a Λ CDM cosmology, $5'$ FWHM Gaussian beams, a cluster core radius of $r_c = 1'$, eight $300 \mu\text{K} \sqrt{s}$ detectors pixelated at $1'$ resolution. The solid line is the total map RMS, the dashed line is the residual CMB, and the dotted line is the instrumental noise contribution. Note that the x-axis is on a log scale.

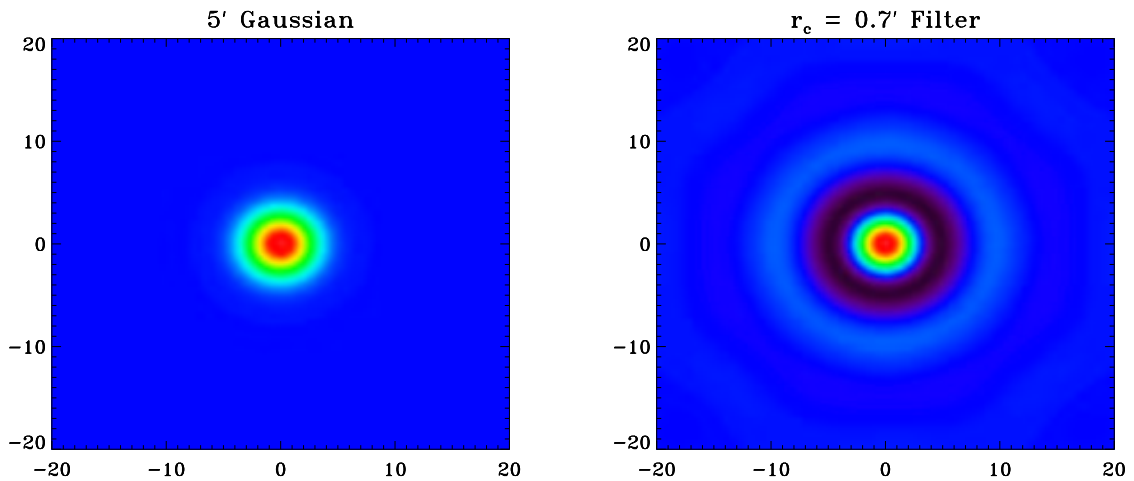


Figure 5.13: Shows the real-space representation of the matched filter for Λ CDM cosmology with noise equivalent to $27 \mu\text{K}$ per $1'$ pixel with a $5'$ beam and cluster core radius of $0.7'$ (right). Also shown is a $5'$ FWHM Gaussian beam (left) for comparison. The filters have been normalized to the same scale for ease of comparison and the axis units are both arcminutes.

CMB5 FIELD	σ_{white} (μK)	$r_c = 0'$ (μK)	$r_c = 0.4'$ (μK)	$r_c = 0.7'$ (μK)	$r_c = 1'$ (μK)
LEAD	40	21.7	22.8	23.8	25.1
MAIN	27	15.9	17.2	18.5	19.9
TRAIL	40	20.6	21.9	23.0	24.4

Table 5.3: Pre-filter $1'$ pixel white noise RMS (first column) and post-filter total map RMS for the 150 GHz CMB5 fields versus filter template core radius assuming a Λ CDM cosmology. The $r_c = 0'$ case refers a $5'$ FWHM point source profile. Compare the post-filter map RMSs to the theoretical values given in Table 5.2.

exceeds $\pm 3\sigma$ in any of the maps – meaning if the source exceeds the threshold in any of the filtered maps for core radii from 0 to $1'$ we mark its position in all of the maps at the location of maximum signal-to-noise. We will discuss candidate source selection in the Source Catalog section below. Also plotted on these figures are the locations of known Abell clusters [1], radio sources from the PMN catalog [39], and bright IRAS sources [54].

The efficacy of the optimal filter is well illustrated in Figure 5.18 which shows the field in the vicinity of the faint radio source PMN J0229-5403 before and after optimal filtering. The left panel of the figure shows the raw map image which is dominated by pixel noise and large-scale CMB power with the source nowhere to be found. The right panel shows the optimally filtered map where we have used a $5'$ FWHM Gaussian as the point source profile and one can see that the radio source is readily identified.

5.3 False Detection Rate

We now investigate the false detection rate in filtered CMB images as a function of cosmology, noise level, and cluster core radius. This should allow us to select an appropriate candidate identification threshold above which we expect few or no false cluster signals. Details of generating CMB and noise realizations from a power spectrum or covariance matrix are provided in Appendix E.

We quantify the false detection rate as the average number of spurious detections in a field (such as the CMB5 MAIN field which is roughly 3.6 deg^2) by generating many realizations of both the CMB and correlated noise and running these maps through the same filtering and source selection criteria as the real data. We generate the CMB sky using power spectra from CMBFAST and the FFT CMB realization method described

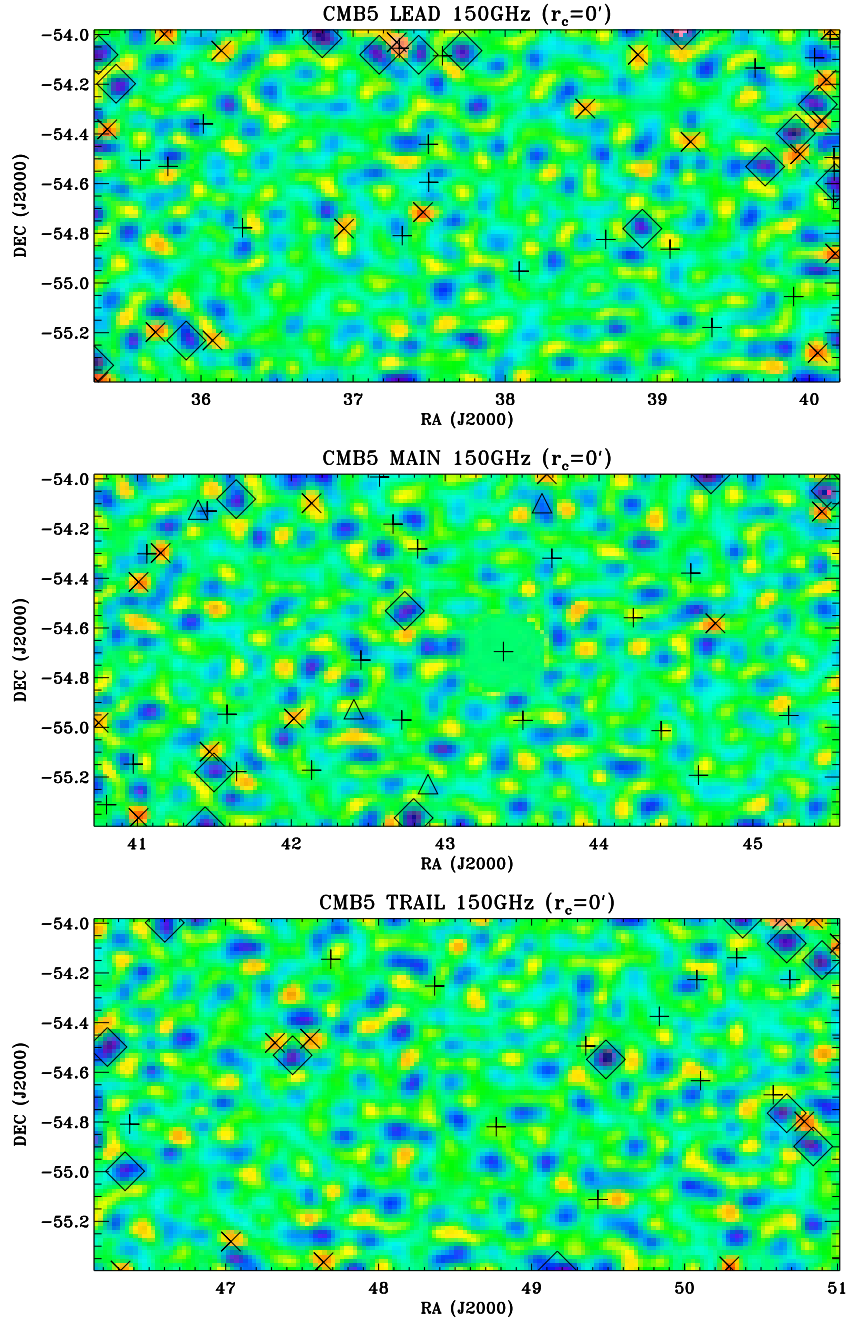


Figure 5.14: Shows the results of applying the matched filter assuming a $5'$ FWHM Gaussian source profile (point source), Λ CDM cosmology, and white noise level appropriate for each of the LEAD, MAIN, AND TRAIL fields of CMB5 at 150 GHz as given in Table 5.3. The maps are scaled so that points ± 4 times the filtered map RMS are shown in white. The map variances are 21.7 , 15.9 , and $20.6 \mu\text{K}$ for the LEAD, MAIN, and TRAIL fields, respectively. The diamonds (crosses) are the locations of sources that exceed -3σ ($+3\sigma$) in at least one of the filtered maps. Overplotted are the locations of known Abell clusters (triangles) as well as radio sources from the PMN radio catalog and IRAS sources (pluses). Although the central quasar in the MAIN field has been removed, we mask out the data within a circle of radius $10'$.

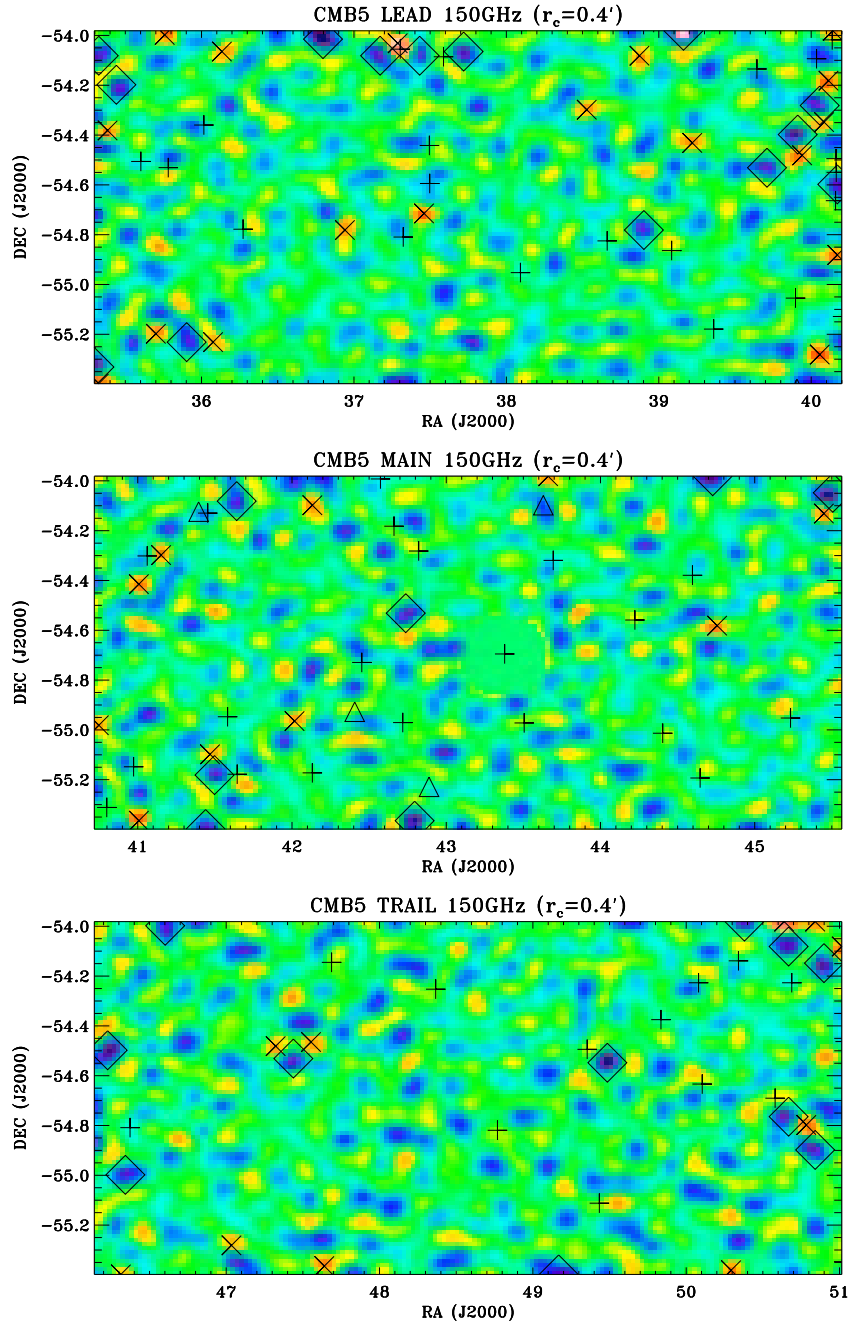


Figure 5.15: Same as Figure 5.14 except a cluster core radius of $r_c = 0.4'$ was used for the optimal filter source profile. The map variances are 22.8, 17.2, and 21.9 μK for the LEAD, MAIN, and TRAIL fields, respectively.

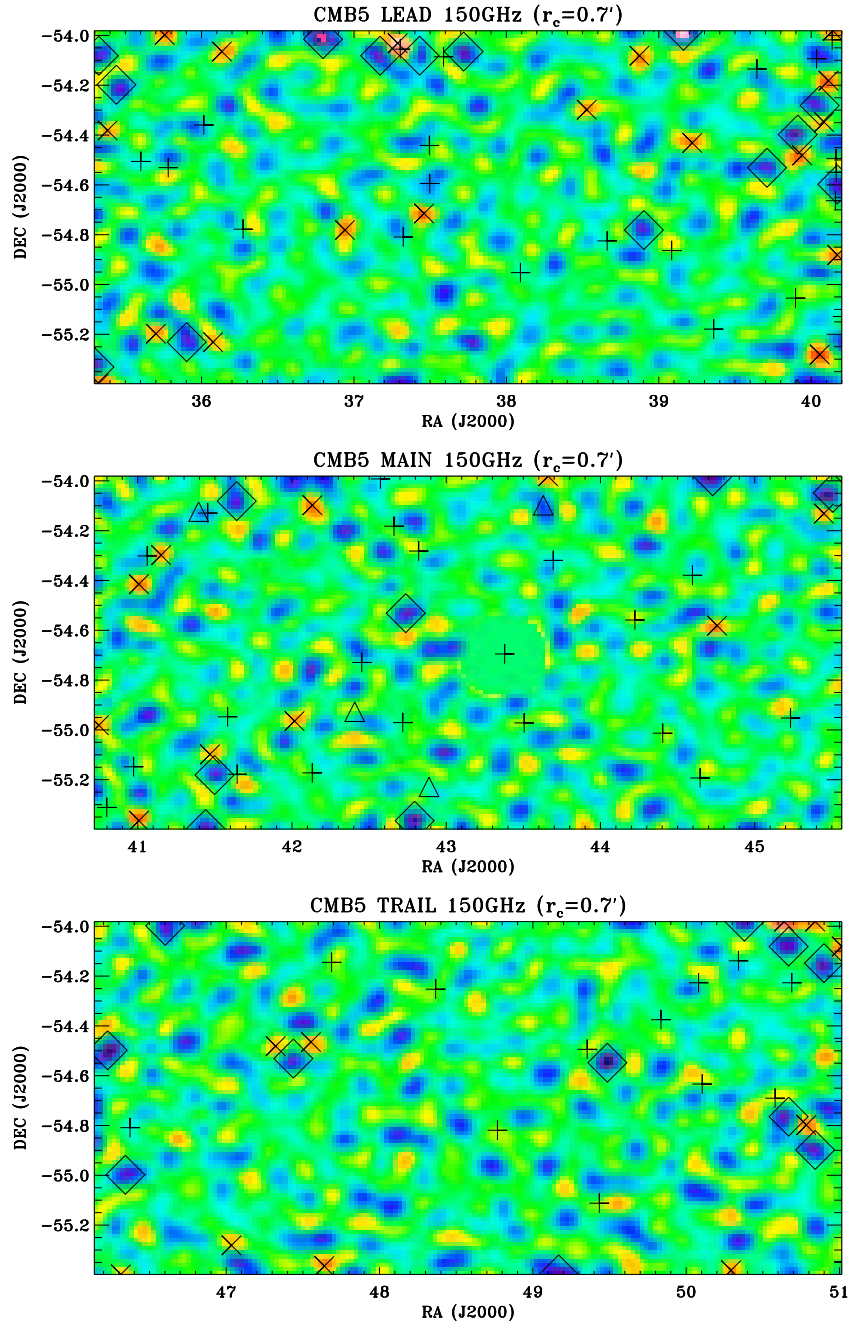


Figure 5.16: Same as Figure 5.14 except a cluster core radius of $r_c = 0.7'$ was used for the optimal filter source profile. The map variances are 23.8, 18.5, and 23.0 μK for the LEAD, MAIN, and TRAIL fields, respectively.

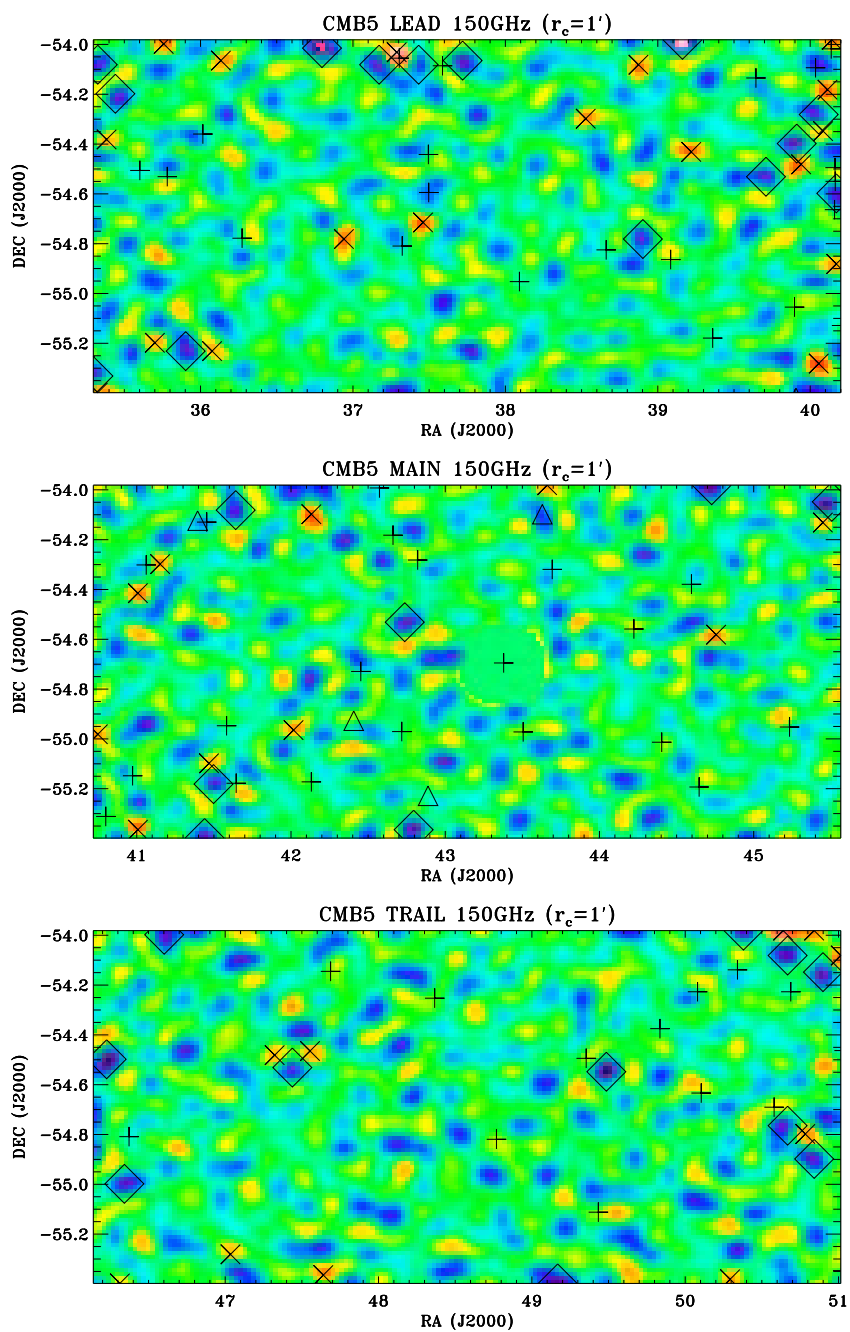


Figure 5.17: Same as Figure 5.14 except a cluster core radius of $r_c = 1.0'$ was used for the optimal filter source profile. The map variances are 25.1, 19.9, and 24.4 μK for the LEAD, MAIN, and TRAIL fields, respectively.

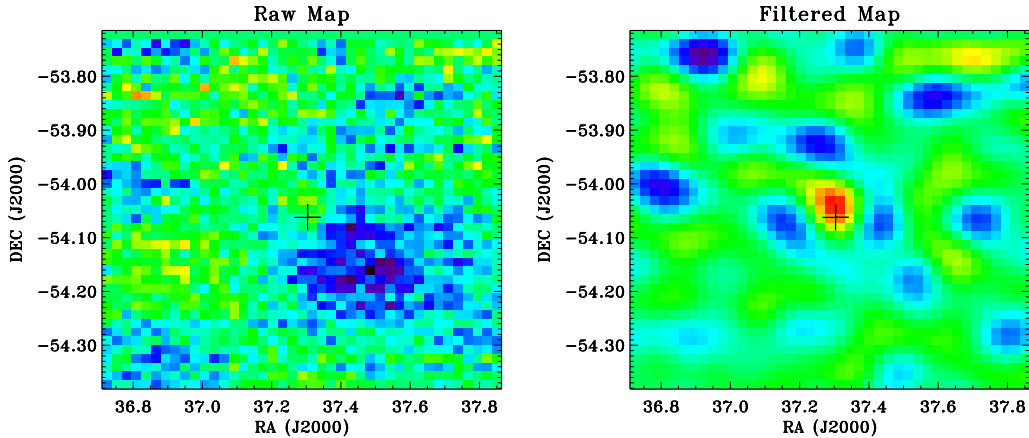


Figure 5.18: Shows the measured microwave sky in the vicinity of the radio source PMN J0229-5403 at 150 GHz. The plus denotes the reported source position. The left panel is the raw image pixelated at $1'$ with a scale of $\pm 250 \mu\text{K}$ and the right panel shows the same field after optimal filtering but the scale has been changed to $\pm 150 \mu\text{K}$. The optimal filter incorporates a ΛCDM power spectrum, $40 \mu\text{K}$ per pixel of white noise, and assumes a $5'$ FWHM Gaussian source profile.

above. We generate CMB maps that are $401' \times 401'$ in size and smooth them with a $5'$ Gaussian beam profile (in real space). We then extract maps that are the same size as the raster fields ($\sim 180' \times 103'$) which eliminates the periodic boundary conditions imposed by the FFT generation method.

The instrument noise is generated with the correlation function method described above. The full noise covariance matrix suggests that the noise between rows in a map is uncorrelated, and thus, we use the average intra-row correlation function derived from the measured covariance matrix of the CMB5 fields at 150 GHz to generate the noise realizations. This simplifies the noise generation greatly because we can use the same L matrix (from $C = LL^T$) to realize the noise for every row.

We then add the noise maps to the CMB maps and apply the same offset removal procedure as used on the raster maps with common offset subtraction plus an additional third-order poly RA and first-order poly DEC removal. These offset removed maps are then padded with zeros and the optimal filters are applied by multiplication in Fourier space. For each CMB plus noise realization, we apply the optimal filter for cluster core radii of $0'$, $0.4'$, $0.7'$, and $1'$ and use the same white noise level as measured in the CMB5 fields at 150 GHz ($27 \mu\text{K}$ per $1'$ pixel in MAIN and $40 \mu\text{K}$ in LEAD/TRAIL).

The cluster candidates are selected if their amplitude exceeds a selection threshold which

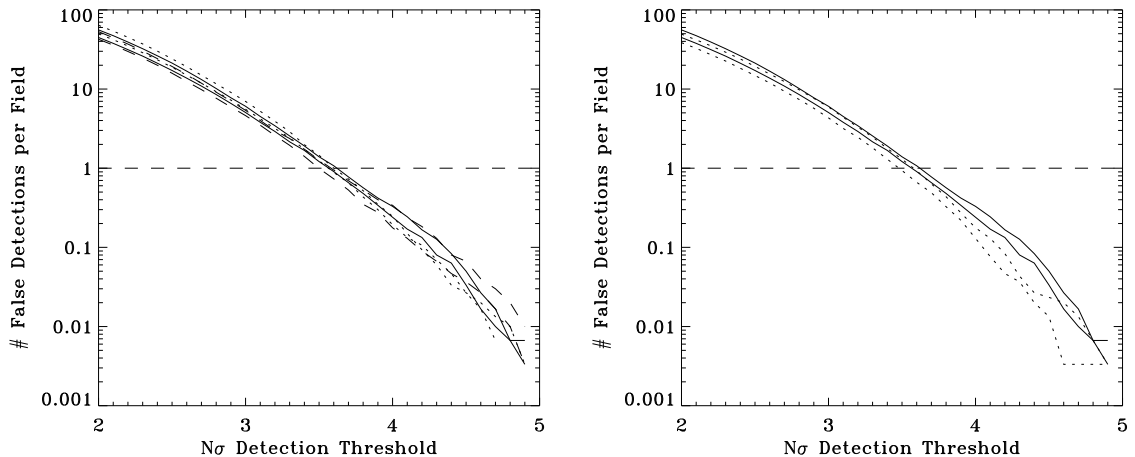


Figure 5.19: Left panel shows the average false detection rate for the simulated 4.1 deg^2 CMB5 MAIN field at 150 GHz for ΛCDM (solid), SCDM (dashed), and OCDM (dotted) cosmologies. The upper line for each cosmology corresponds to a cluster core radius of $r_c = 0'$ and the lower line for $r_c = 1'$. The right panel compares the false detection rate between the MAIN field (solid) and LEAD field (dotted) for a ΛCDM cosmology and measured noise correlation function for each field. The upper (lower) line for each field corresponds to a template cluster core radius of $r_c = 0'$ ($1'$).

we have chosen to be a multiple of the post-filter map RMS. Because of the zero padding of the map before filtering, the width of the filter kernel will correlate junk data into the map. To mitigate this effect, we exclude from consideration the $10'$ strips of data around the edge of the map. We calculate the RMS of the interior region of the map and measure the number of discrete aggregates exceeding the threshold factor times the map RMS. Because massive clusters are rare objects on the sky, we count objects within $5'$ of each other as the same object.

We performed this exercise for 150 CMB plus noise realizations in SCDM, ΛCDM , and OCDM cosmologies and apply the four optimal filters of varying template cluster core radius. We calculate the map variance and then scan the detection threshold between 2 and 5 times the filtered map RMS and measure the number of clusters exceeding the threshold. The results are shown in Figure 5.19 where we have plotted the number of false cluster detections in all three cosmologies for core radii of $0'$ and $1'$ (the $r_c = 0.4'$ and $0.7'$ results fall between these two extremes).

We see from the figure that the false detection rate is remarkably insensitive to cosmology even though the OCDM model should have significantly more small-scale structure than the other two cosmologies. This is most likely due the fact that the increase in coupling of

the optimal filter to beam-size CMB fluctuations is offset by an increase in post-filter map variance. The false detection rate is also reasonably insensitive to the template cluster core radius. We note that the decrease in false detection rate for larger core radii is probably due to larger map RMS. The right-hand panel in the figure shows the agreement between false detection rates for the LEAD and MAIN fields even though the integration times differ by a factor of two. The slightly higher false detection rate for the MAIN field is presumably due to coupling to real small-scale CMB anisotropies where the LEAD field is still dominated by noise.

The horizontal line in the figure denotes the level at which one would expect to find – on average – a single false cluster in the 4.1 deg^2 simulated field; near $\sim 3.6\sigma$ for almost all cosmologies and core radii. A threshold of 4σ yields a single false cluster in roughly 1 out of every 4-5 realizations. If we lower the detection threshold to 3σ we would expect quite a few false objects in the maps ($\sim 5 - 6$ per 4.1 deg^2 field). Note that even though the maps contain roughly $13,000 \text{ } 1' \times 1'$ pixels, we do not expect $0.15\% \times 13,000 \sim 20$ points below -3σ because the pixels are highly correlated from the optimal filter.

Based on this false detection rate simulation we elect to use 4σ as our cluster detection threshold. That being said, however, the steepness of the cluster mass function suggests that a fraction of objects exceeding 3σ should be galaxy clusters even though the CMB and noise will conspire to yield a handful of false detections per field. It would thus be worthwhile to include objects detected at 3σ in a follow-up cluster verification program if the goal is to find massive clusters. We explore the related question of cluster detection efficiency in the next section.

5.4 Bias and Detection Efficiency

We now investigate the probability of detecting a cluster at a given S/N threshold as a function of amplitude and core radius. This will determine the survey selection function from which we can generate realistic expectations for the survey cluster yield. Given the abundance of evidence for a Λ CDM cosmology, we will assume an underlying CMB power spectrum with $\Omega_M = 0.3$, $\Omega_\Lambda = 0.7$, $h = 0.7$, $\Omega_b h^2 = 0.021$, $\tau = 0$, $n = 1$, and COBE normalization (generated with CMBFAST). We will Monte Carlo the detection efficiency for both the MAIN and LEAD/TRAIL fields at 150 GHz using their measured noise properties.

5.4.1 Cluster Realizations

We begin by using the same CMB and noise realizations as used for the false detection rate estimation. We then generate simulated clusters assuming the modified β -model profile given by

$$s(x) = \frac{r_c r_v}{r_v - r_c} \left(\frac{1}{\sqrt{r_c^2 + x^2}} - \frac{1}{\sqrt{r_v^2 + x^2}} \right),$$

where r_c is the cluster core radius and $r_v = 3r_c$ is scale on which the cluster emission is truncated. The clusters are generated with much higher angular resolution than the $1'$ pixel size of the maps and are smoothed with a $5'$ FWHM Gaussian beam before binning down to $1'$ map resolution. We generate clusters with core radii of $0'$, $0.4'$, $0.7'$, and $1.0'$ which correspond to the core radii of the matched filters to test for amplitude bias.

The convolved clusters are normalized to peak central decrements from $-20 \mu\text{K}$ to $-180 \mu\text{K}$ in steps of $20 \mu\text{K}$. By renormalizing the cluster amplitude after convolution we will only test the detection efficiency over the range of clusters likely to be detectable by ACBAR. A measured central decrement of $100 \mu\text{K}$ for a $5'$ beam at 150 GHz corresponds to 96 mJy in-beam (from $\Delta S = (dB/dT)\Delta T\Omega$). It is then a useful approximation to use $1 \mu\text{K} \sim 1 \text{ mJy}$ per beam. After re-binning and normalizing the cluster, we add it to a random location within each CMB+noise realization for a total of 100 realizations per cluster.

We then remove the offsets from the map in the same manner as the raw data with a common offset in RA and DEC as well as a third-order polynomial in RA and first-order polynomial in DEC. This removes a significant amount of CMB from the map and we will verify if the cluster signal is attenuated by $\sim 10\%$ as suggested in the Offset Removal section above. Next we pad the map with zeros in the same manner as the real data and apply the matched filters – with core radii of $r_c = 0'$, $0.4'$, $0.7'$, and $1.0'$ – to the padded map in Fourier space. The matched filters assume the appropriate white noise level for each field: $27 \mu\text{K}$ per $1'$ pixel for the MAIN field and $40 \mu\text{K}$ for the LEAD/TRAIL fields.

We then “detect” the simulated cluster in the map by recording the largest decrement within $2'$ of the input cluster position; this allows for the possibility that the peak cluster signal is not at exactly the same position as the input cluster. We also measure the post-filter map RMS for each realization. This gives us a total of 100 realizations for each of the 4 input cluster core radii, 9 cluster amplitudes, and 4 matched filters.

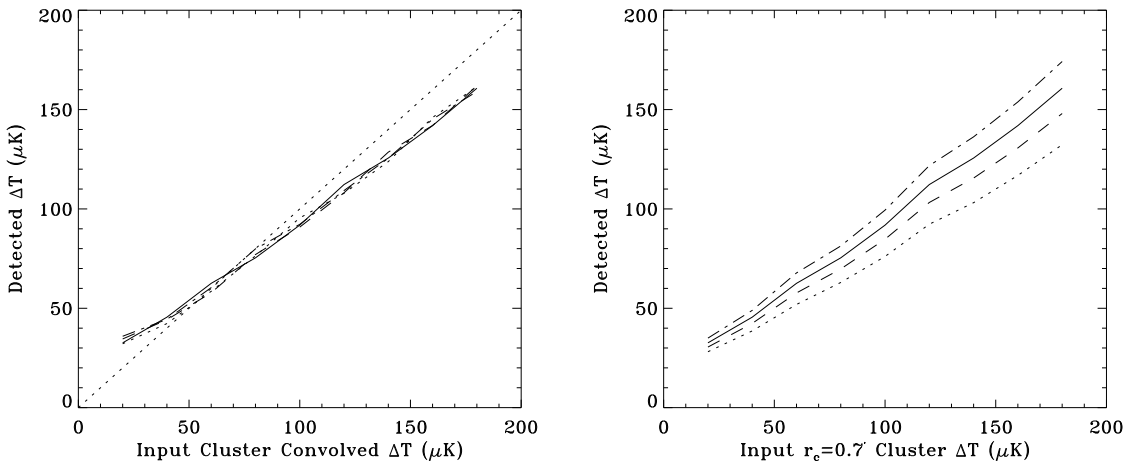


Figure 5.20: Left panel shows the measured central cluster temperature decrement in the MAIN field versus the input cluster decrement for model cluster core radii of $0'$ (dotted), $0.4'$ (dashed), $0.7'$ (solid), and $1'$ (dot-dashed). The values for each core radius are from a matched filter with equal core radius. The measured cluster amplitude versus input cluster amplitude for mismatched optimal filters is presented in the right-hand panel. The input cluster has a core radius of $r_c = 0.7'$ and the lines correspond to filters assuming core radii equal to the left-hand panel.

5.4.2 Bias

We can now compare the measured (beam convolved) cluster amplitude versus the input cluster amplitude as a function of core radius, amplitude, and applied filter. The results are presented in Figure 5.20. The left panel of the figure shows the measured cluster temperature decrement versus the input temperature decrement for clusters of varying core radius. The values presented for each core radius are from the matched filter with the correct cluster core radius. One immediately sees that the detected cluster decrement tends to be lower than the input cluster decrement with the best fit bias of $\sim 90\%$; in agreement with the anticipated 10% signal reduction from offset removal. We repeated the procedure without performing the offset removal and find the matched filter is indeed unbiased. For small amplitudes the detected cluster ΔT exceeds the input temperature. This is because the $2'$ minimum temperature search radius couples to noise in the map when the cluster amplitude drops near the noise level. We also tested the bias for realizations of the LEAD field and find the same 90% amplitude effect with a slightly higher noise level for low amplitude clusters, as would be expected from the larger noise level in the LEAD field.

The right-hand panel of Figure 5.20 illustrates the effect of measuring the beam con-

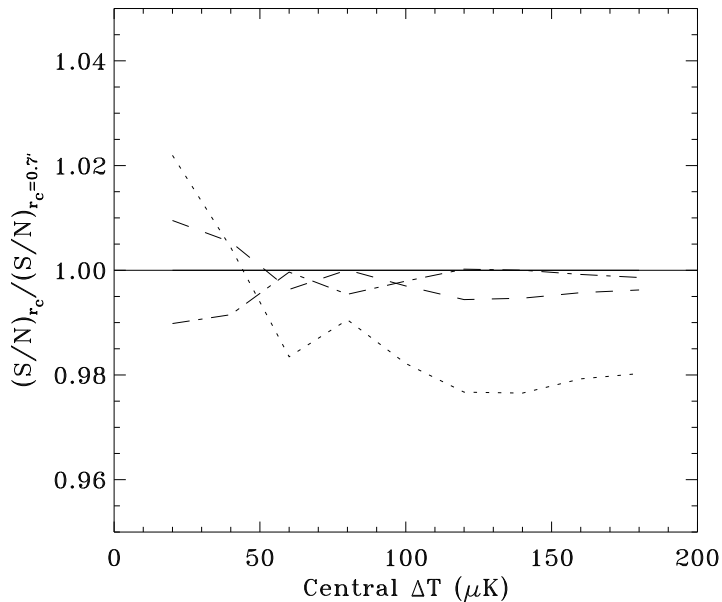


Figure 5.21: Shows the ratio of the detected S/N of a $r_c = 0.7'$ cluster using optimal filters that assume a cluster core radii of $0'$ (dotted), $0.4'$ (dashed), $0.7'$ (solid), and $1'$ (dot-dashed) to the S/N for the properly matched $r_c = 0.7'$ filter. This ratio is plotted versus input convolved cluster temperature decrement.

olved cluster temperature decrement with an “optimal” filter of mismatched core radius. We have used a fiducial cluster of $r_c = 0.7'$ and measured the temperature with all four core radii filters. From the figure one can see that measuring the cluster temperature with a filter that assumes a smaller (larger) core radius will underestimate (overestimate) the cluster amplitude. That being said, we found an interesting effect when we compare the signal-to-noise ratio (S/N) of the cluster for the different filters. The S/N is defined as the measured central cluster decrement divided by the RMS of the filtered map. The ratio of the S/N of the $r_c = 0.7'$ cluster using the incorrect “matched” filter to the S/N with the correct filter (versus central decrement) is shown in Figure 5.21.

The remarkable feature of this figure is that even though the properly matched filter gives the highest signal-to-noise (as would be expected), the improperly matched filters generally give a S/N which is $\gtrsim 95\%$ of the matched value. This is not true for the very weakest clusters which are dominated by coupling to the noise. We interpret this to mean that the loss in cluster signal from using a filter that is undersized for the input cluster is offset by a decrease in post-filter map RMS by reducing the coupling to the CMB. What this says, for the case of ACBAR at least, is that our ability to detect clusters with a S/N

threshold should not depend strongly on the core radius used in the optimal filter.

5.4.3 Average Signal-to-Noise Ratio

We now present the average signal-to-noise of the cluster detections versus a variety of cluster identifiers. Given the results of the previous sub-section, we only present the S/N for each core radius from the properly matched optimal filter. We are presenting the *average* S/N for a given cluster core radius and amplitude, which means that roughly half of the clusters fell above this value and half below this value.

Figure 5.22 shows the average S/N of filtered cluster images versus the integrated 150 GHz flux density of the input cluster in Jy. This is presented for both the MAIN and LEAD/TRAIL realizations in which the input white noise levels are 27 and 40 μK , respectively. For the case of $r_c = 0'$, we assume a point source with flux density sufficient to produce the central beam convolved ΔT . The most notable feature of this figure is the strong drop in S/N as the cluster core radius increases implying an increasing fraction of total cluster flux is lost outside the beam. This immediately tells us that the detection criteria employed here will not produce a uniform cluster selection function based on total integrated cluster flux. As we will see below, the S/N versus the flux within the beam will be much less sensitive to the size of the cluster. The other point to note in the figure is that the average S/N for a given cluster will be a bit lower in the LEAD/TRAIL fields than in the deeper MAIN field.

We can also perform a similar exercise by plotting the average detected S/N of the clusters versus their central Comptonization, y_0 . This is the actual y_0 of the raw cluster; not the value after convolving with the beam. The results are shown in Figure 5.23. There is no corresponding y_0 for a point source so we omit the $r_c = 0'$ data. One notices from the figure that the detectability of a cluster rapidly increases as the core radius increases for fixed central y_0 . This is understood because the larger cluster will fill more of the beam and produce a larger signal for a given value of y_0 .

The last comparison we present is the average measured S/N versus the beam convolved decrement ΔT produced by the cluster (see Figure 5.24). This is equivalent to plotting the S/N versus the in-beam flux density with the conversion $1 \mu\text{K} \sim 1 \text{ mJy}$ mentioned above. The scatter in S/N with varying core radii is greatly reduced from the previous two cluster quantities. This is because the detection criteria of selecting peaks above some

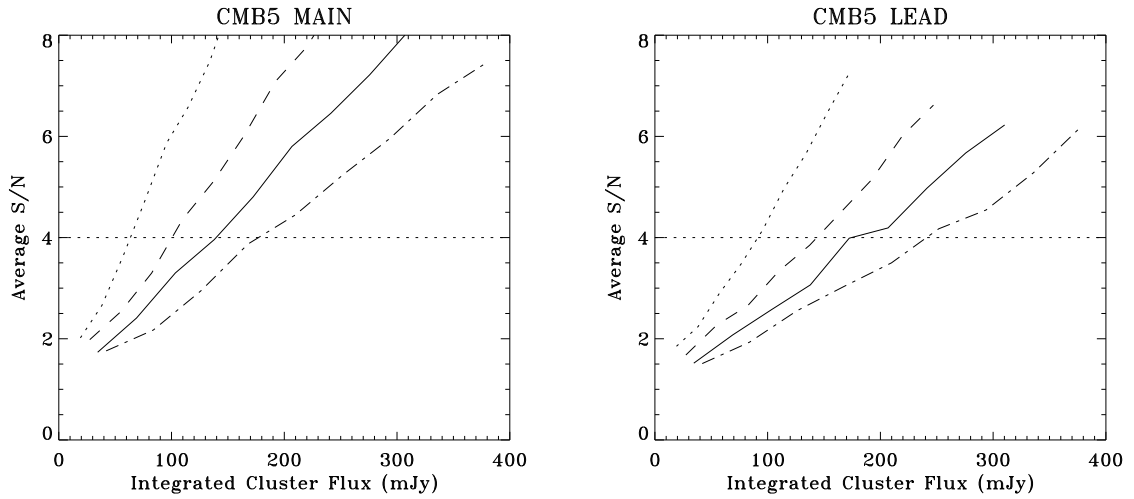


Figure 5.22: Shows the S/N ratio versus integrated 150 GHz flux density of the input clusters for both MAIN (left) and LEAD/TRAIL (right) simulations. The cluster core radii are 0' (dotted), 0.4' (dashed), 0.7' (solid), and 1' (dot-dashed) and the S/N reported are from the properly matched optimal filter. We have drawn a horizontal line at 4σ to guide the eye for comparison.

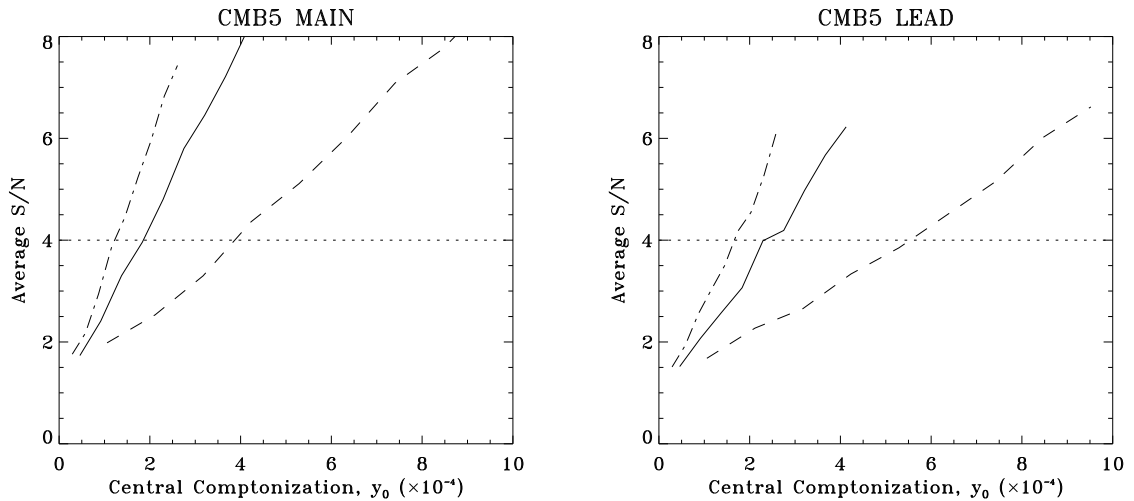


Figure 5.23: Shows the S/N ratio versus central cluster Comptonization, y_0 , of the input clusters for both MAIN (left) and LEAD/TRAIL (right) simulations. The cluster core radii are 0.4' (dashed), 0.7' (solid), and 1' (dot-dashed) and the S/N reported are from the properly matched optimal filter. We have drawn a horizontal line at 4σ to guide the eye for comparison.

factor times the map variance is sensitive to the in-beam flux and not the total cluster flux. Renormalizing the optimal filter to output an estimate of the integrated cluster flux will have no effect on the S/N because the map RMS will be scaled by the same factor. There is a relatively weak dependence upon cluster core radius with higher S/N for more compact clusters. This is because compact objects are inherently easier to detect when the noise power spectrum is steeply falling, as is the case of the CMB. Hence, even if two clusters result in equivalent in-beam fluxes, the more compact object will be easier to detect in the presence of CMB.

The fact that the S/N of a detection depends on the size of the cluster may appear to contradict the claim that a cluster survey selection should depend only on cluster mass (*e.g.*, total cluster flux) [47]. The difference arises from our choice of detection algorithm. We are identifying clusters by their peak temperature decrement above the noise level of the filtered map. The peak decrement depends only on the amount of cluster flux within the beam. The result of Holder et al. (2000) that SZ survey selection functions will not depend strongly upon cluster size is based upon identifying clusters by probing χ^2 -space; fitting to the entire cluster profile with both an amplitude and core radius. This type of object detection scheme should be sensitive to the cluster flux that lies outside the main beam.

For the simulations presented here, the convolved central temperature decrement that will be detected at 4σ (on average) is $\sim 77 \mu\text{K}$ for the MAIN field and $\sim 107 \mu\text{K}$ for the LEAD/TRAIL fields. These are equivalent to in-beam flux densities of $\sim 74 \text{ mJy}$ and $\sim 102 \text{ mJy}$ for the MAIN and LEAD/TRAIL fields, respectively. This means that 50% of the objects with these in-beam flux densities should be detected at 4σ . We explore the detection efficiency as a function of σ threshold in the next sub-section.

5.4.4 Cluster Detection Efficiency

With our simulations, we can estimate the fraction of clusters that will be detected above a given σ threshold as a function of cluster core radius and in-beam flux (or equivalently, beam convolved central ΔT). This is the ACBAR cluster selection function. The results are presented in Figures 5.25 and 5.26 for clusters detected above 4σ and 3σ , respectively, in both the CMB5 MAIN and LEAD/TRAIL simulations. Again we see that for fixed in-beam flux density and detection threshold, compact clusters will be detected somewhat

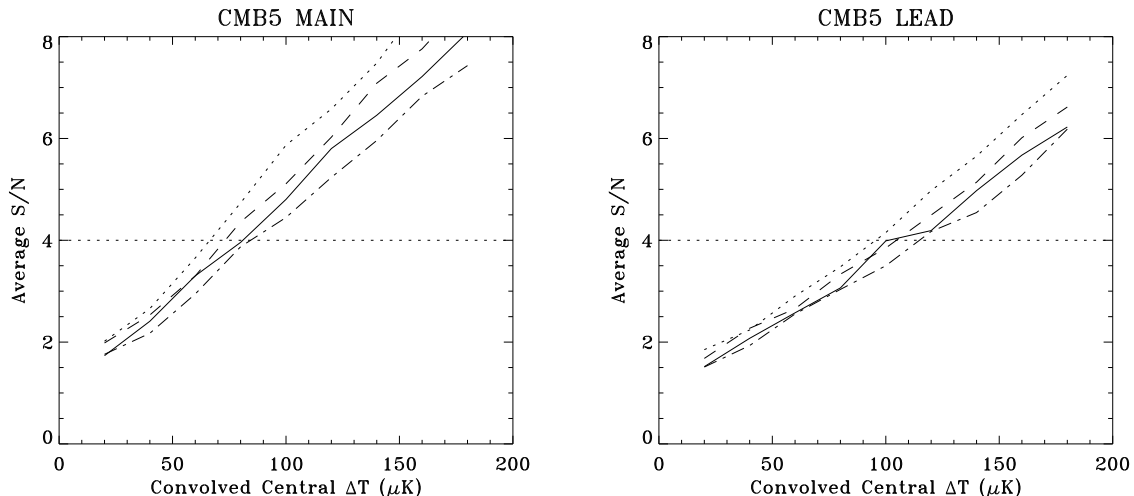


Figure 5.24: Shows the S/N ratio versus beam convolved central temperature decrement, ΔT , of the input clusters for both MAIN (left) and LEAD/TRAIL (right) simulations. The cluster core radii are $0'$ (dotted), $0.4'$ (dashed), $0.7'$ (solid), and $1'$ (dot-dashed) and the S/N reported are from the properly matched optimal filter. We have drawn a horizontal line at 4σ to guide the eye for comparison.

Detected fraction	MAIN 3σ (mJy)	MAIN 4σ (mJy)	LEAD 3σ (mJy)	LEAD 4σ (mJy)
50%	54	75	73	106
90%	78	111	115	146

Table 5.4: Approximate in-beam 150 GHz flux densities for detection thresholds of 3 and 4σ with corresponding fractional detection rates of 50% and 90%. Values are listed for both the MAIN and LEAD/TRAIL simulations and represent the average of the four core radii used in the simulations.

more frequently than extended clusters. One may also note that the slope of the detection efficiency with ΔT changes between the MAIN and LEAD/TRAIL simulations which reflects the higher noise level in the later. We list the approximate in-band fluxes yielding detection efficiencies of 50% and 90% for both 3σ and 4σ detection thresholds in Table 5.4. These values were approximated by averaging the detection efficiencies across the four core radii of the simulations.

5.4.5 Expected Cluster Yield

Using the mass function formalism presented in the introduction and the estimated detection efficiency, we can estimate the expected cluster yield of the ACBAR survey for a given

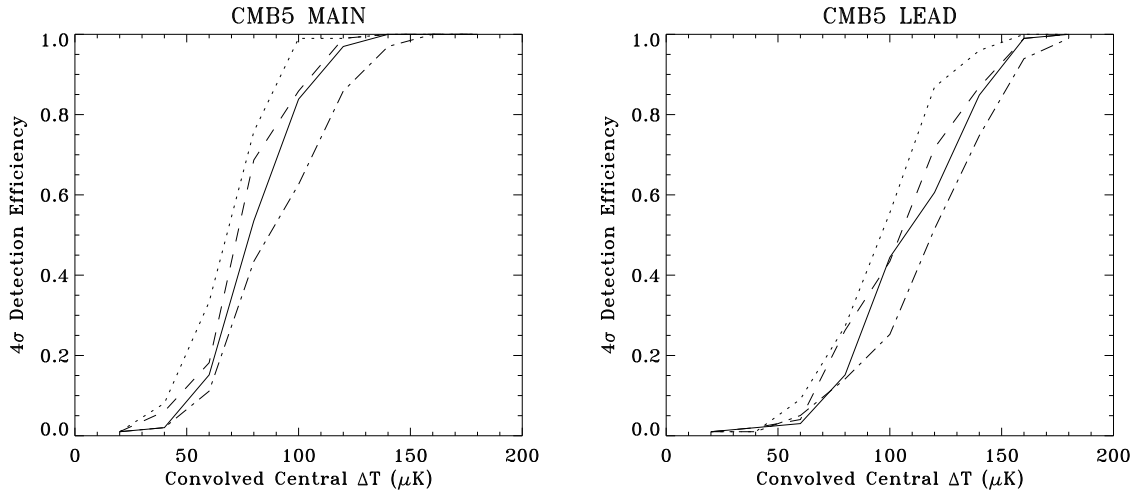


Figure 5.25: Shows the fraction of simulated clusters detected above 4σ versus convolved central temperature decrement, ΔT , for both MAIN (left) and LEAD/TRAIL (right) simulations. The cluster core radii are $0'$ (dotted), $0.4'$ (dashed), $0.7'$ (solid), and $1'$ (dot-dashed) and the S/N reported are from the properly matched optimal filter. The conversion between central ΔT in μK and an in-beam flux in mJy for a $5'$ beam at 150 GHz is approximately $1 \text{ mJy} \sim 1 \mu\text{K}$.

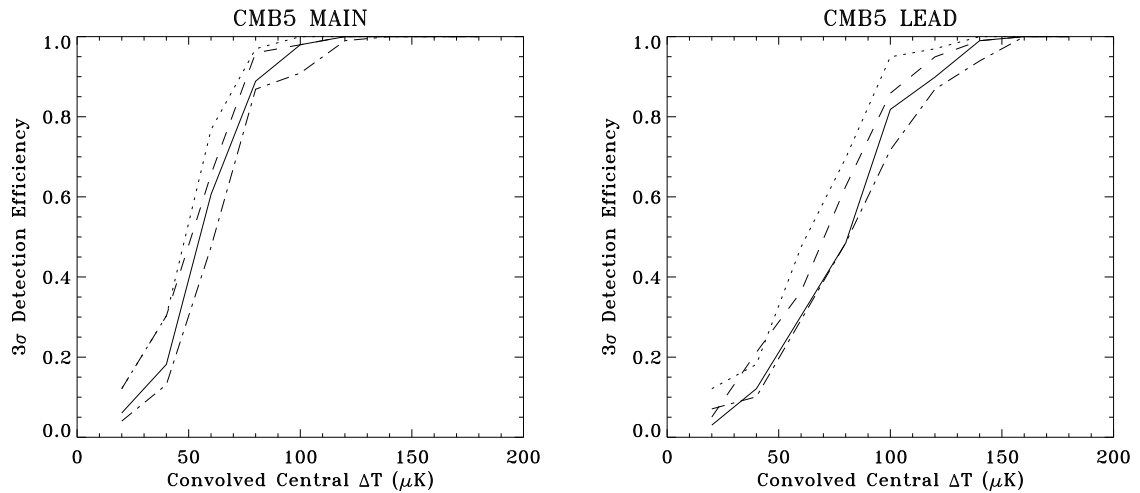


Figure 5.26: Same as Figure 5.25 except for a lower detection threshold of 3σ .

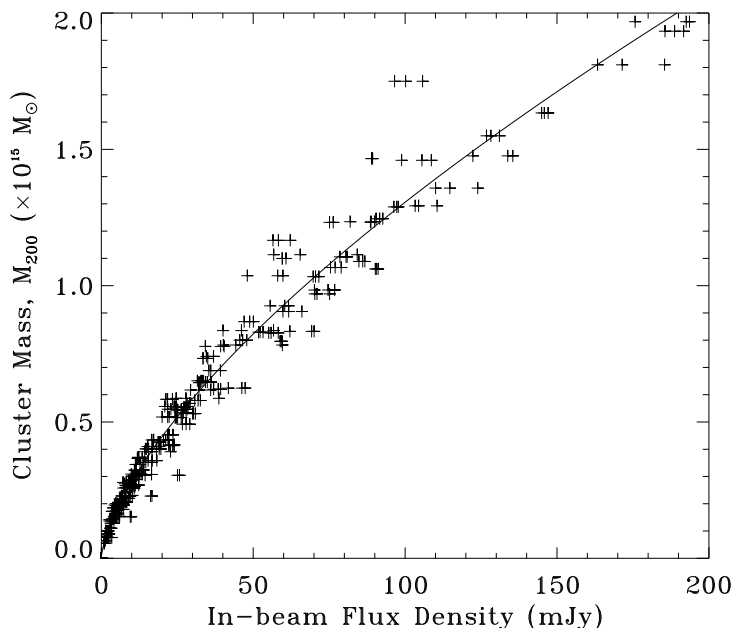


Figure 5.27: Shows the relationship between cluster mass and in-beam flux density assuming a $5'$ beam at 150 GHz for simulated clusters in a Λ CDM cosmology. Simulated clusters from $z = 0.5, 1.0,$ and 1.5 are included in the figure and the solid line is a fit to the data.

cosmology. We have estimated the detection efficiency as a function of in-beam cluster flux, but the number count formalism depends on cluster mass. To estimate the relationship between cluster mass and in-beam flux we return to the cluster simulations used to estimate the like range of core radii of clusters detectable by ACBAR. Again we will focus only on the predicted number counts from a Λ CDM cosmology.

Figure 5.27 shows the cluster mass versus measured in-beam flux (using a $5'$ FWHM Gaussian at 150 GHz) for the simulated clusters in a Λ CDM cosmology. Although the simulated cluster images have been scaled for the difference in assumed Hubble constant, they were generated assuming $\sigma_8 = 1.0$ and we have used $\sigma_8 = 0.93$ for consistency with X-ray observations. The main effect of differing values of σ_8 will be on the expected abundance of clusters (refer to Figure 1.7). However, the different values of σ_8 will also affect the redshift of cluster formation with clusters forming earlier in the universe with larger σ_8 . Clusters that form earlier will be more compact because of the higher mass density at formation but will also be hotter. These two effects will cancel to first order when measuring the in-beam flux after convolution with the large ACBAR beams and, therefore, we will ignore them.

Field Simulation	$S_0^{3\sigma}$ (mJy)	$\Sigma^{3\sigma}$ (mJy)	$S_0^{4\sigma}$ (mJy)	$\Sigma^{4\sigma}$ (mJy)
MAIN	52	19	74	21
LEAD/TRAIL	68	30	102	29

Table 5.5: Best fit parameters S_0 and Σ for the average detection efficiency function, $f(S)$. The values are given for the MAIN and LEAD/TRAIL simulations with detection thresholds of 3σ and 4σ .

We include the clusters from redshifts of $z = 0.5, 1.0,$ and 1.5 in the mass versus in-beam flux figure and find that the dispersion is reasonably small. We therefore assume no evolution of the mass-flux relation for our ballpark estimate of expected cluster yield and find a good fit for $M_{200}(S_{beam}) \sim 10^{15}(S_{beam}/67 \text{ mJy})^{2/3} M_{\odot}$. Now that we have a relationship between cluster mass and in-beam flux density, we need only a functional form of the detection efficiency versus in-beam flux to calculate the expected cluster yield.

The detection efficiency functions plotted in Figures 5.25 and 5.26 are very well fit to an integrated Gaussian with the fraction of clusters producing an in-beam flux S given by

$$f(S) = \frac{1}{\sqrt{2\pi}\Sigma^2} \int_0^S dS' e^{-\frac{(S'-S_0)^2}{2\Sigma^2}},$$

where S_0 is the 50% detection flux and Σ is a measure of the width of the transition. Because the detection fractions in the plots are to first order insensitive to core radius and represent a reasonable cross-section of likely core radii, we simply average the efficiency functions for each of the MAIN and LEAD/TRAIL simulations across core radius for each detection threshold. The average efficiency functions are then fit to the $f(S)$ equation above and the results of the fits are presented in Table 5.5. The 4σ 50% detection fluxes correspond to cluster masses of $\sim 1.1 \times 10^{15} M_{\odot}$ for the MAIN field and $\sim 1.3 \times 10^{15} M_{\odot}$ for the LEAD and TRAIL fields.

The expected cluster yields for a given $N\sigma$ detection threshold are then given by multiplying the detection efficiency times the mass function, integrating over cluster mass and redshift, and multiplying by the solid angle of the survey:

$$N = \Omega \int dz \int dM f[S(M)] \frac{dn}{dM} \frac{dV_c}{d\Omega dz}.$$

The detection efficiency function given above gets quite small for low cluster masses but

is still finite. Because the mass function is very steep, this tends to significantly overcount the number of low-mass clusters likely to be detectable above the noise. Also, our predicted efficiency function is biased high in the low-mass (low in-beam flux) region by false detections of spurious correlations between input low-mass clusters and random cold spots in the filtered CMB realizations. To mitigate this issue, we institute a low-mass cutoff of $M_{limit} = M(S_0 - \Sigma)$ for each simulation. This corresponds to lower mass limits of approximately $\sim 8.5 \times 10^{14}$ and $\sim 10.6 \times 10^{14} M_{\odot}$ for the 4σ detection thresholds of the MAIN and LEAD/TRAIL simulations, respectively. The low mass cutoff has the additional benefit of keeping the power law fit to the variance of the smoothed density field, $\sigma(M, z)$, within the range of mass that the fit is valid.

We generate the expected cluster counts in a Λ CDM cosmology with $\Omega_M = 0.3$, $\Omega_{\Lambda} = 0.7$, $h = 0.7$, $\sigma_8 = 0.93$, $\delta_c = 1.69$, and $\Gamma = 0.23$ and the Sheth-Tormen mass function. Performing the mass integral gives the expected distribution of the cluster surface density with redshift for each field. These $dN/d\Omega dz$ distributions are shown in Figure 5.28 for the 3 and 4σ detection thresholds of MAIN and LEAD/TRAIL. Performing the integral over redshift and multiplying by the solid angle of the filtered maps gives the expected cluster yield for the survey. The full maps are approximately 4 deg^2 per field but we only include the innermost 3.2 deg^2 to avoid the higher noise outer regions of the maps. These results are presented in Table 5.8 which also lists the number of detected decrements in the maps for both 3σ and 4σ thresholds. Note that the expected false detection rate is estimated to be $\sim 4 - 5$ objects for 3σ and ~ 0 for 4σ per 3.2 deg^2 field.

5.5 Results

5.5.1 Source Catalog

Here we present the catalog of candidate sources in the CMB5 fields. We include any source that exceeds $\pm 3\sigma$ in at least one of the four optimally filtered maps ($r_c = 0'$, $0.4'$, $0.7'$, or $1.0'$) and report the S/N and core radius of maximum significance. The S/N is defined as the peak filtered temperature divided by the RMS of the filtered map. We include all objects detected above 3σ in the entire 4.1 deg^2 maps, but mark with an * the S/N values of those objects that lie outside of the innermost 3.2 deg^2 . We exclude the sources in the outer region of the maps from derivation of constraints on cosmological parameters because

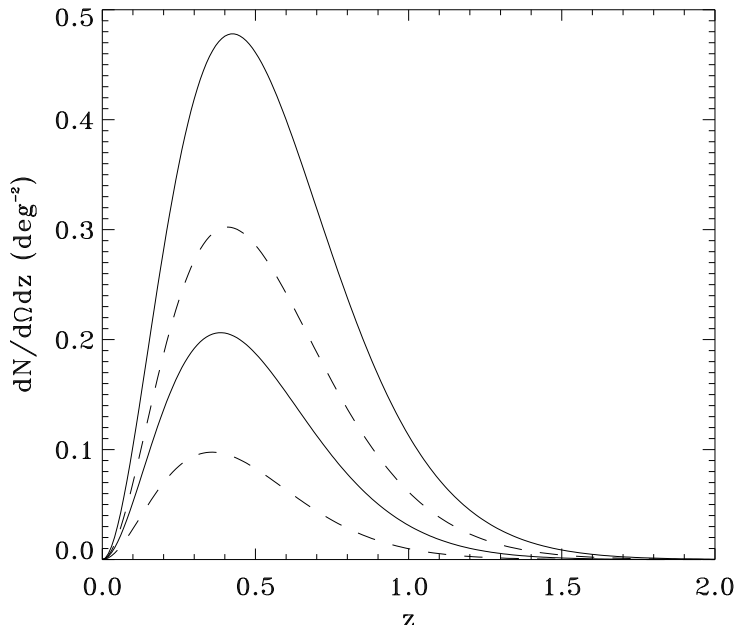


Figure 5.28: Shows the expected redshift distribution of cluster surface density in the MAIN (solid) and LEAD/TRAIL (dashed) fields for a flat- Λ CDM cosmology with $\sigma_8 = 0.93$ and $\Omega_M = 0.3$. The upper (lower) curve for each field represents the results for a 3σ (4σ) detection threshold. Each field is approximately 3.2 deg^2 in area.

they lie within a beam width of the significantly higher noise portion of the maps. The finite width of the optimal filter will couple the high-noise data into the low-noise region of the map and contribute to false detections.

Some source positions vary by $1\text{--}2'$ depending on the core radius of the filter. In the case of multiple detections within $2'$ we only report the source position and core radius of the maximum S/N detection. We also compare the CMB5 source candidates to catalogs of known radio, infrared, optical, UV, and X-ray sources available on the NASA/IPAC Extragalactic Database² by searching for known objects within $5'$ (one beam width) of the candidate source positions. With the exception of a few of the radio sources, the objects reported in the “Near Object” column probably do not correspond to actual object detections because the large $5'$ search radius will include random objects quite frequently.

It should be noted that the matched filter tends to group increments and decrements because of the negative annulus around the central peak of the filter (refer to Figure 5.13). For example, clustered around the radio source PMN J0229-5403 in the LEAD field, we find

²<http://nedwww.ipac.caltech.edu>

two $> 3\sigma$ temperature decrements which are most likely artifacts of the filter and not real clusters. This point is made in Schulz and White (2002) who also employ matched filters to extract clusters from simulated SZ maps. For this reason we should cull decrements within a beam width of bright point sources from the catalog.

RA (J2000)	DEC (J2000)	S/N	r_c (')	FIELD	Near Object	Type	Dist (')
35.297	-55.331	-3.72*	0	L			
35.326	-54.081	-3.37*	0	L			
35.441	-54.198	-3.30*	0	L			
35.903	-55.231	-3.01	1	L			
36.797	-54.015	-4.13*	1	L			
37.172	-54.081	-3.20	0	L	PMN J0229-5403	Radio	4.9
37.431	-54.081	-3.09	0	L	PMN J0229-5403	Radio	4.7
37.720	-54.065	-3.49	0	L	IRAS F02294-5420	Gal	3.5
38.902	-54.781	-3.09	0	L			
39.162	-53.981	-5.14*	1	L			
39.710	-54.531	-3.12	0	L			
39.912	-54.398	-3.93	0	L			
40.056	-54.281	-3.29*	0	L			
40.171	-54.598	-3.11*	0	L	1RXS J024039.0-543252	X-ray	3.0
41.440	-55.398	-3.10*	0.7	M			
41.497	-55.181	-3.11	0	M			
41.642	-54.081	-3.00	0.4	M			
42.738	-54.531	-3.16	0.4	M			
42.795	-55.365	-3.91*	0	M			
44.728	-53.981	-3.45*	0	M			
45.506	-54.048	-4.03*	0	M			
46.227	-54.498	-3.70*	1	T	IRAS F03031-5437	IrS	4.4
46.342	-54.998	-3.03*	1	T			
46.602	-53.998	-3.04*	1	T	CSRG 0235	Gal	4.5
47.438	-54.531	-3.31	0	T			
49.168	-55.398	-3.15*	1	T	many Marano Hole sources		-
49.486	-54.548	-3.92	0	T			
50.380	-53.981	-3.41*	0	T			
50.668	-54.081	-3.50	0	T			
50.668	-54.765	-3.49	0	T			
50.841	-54.898	-3.34*	0	T			
50.899	-54.148	-3.67*	0	T			

Table 5.6: Catalog of candidate source decrements exceeding -3σ in the CMB5 fields. The core radius and source position are for the filter which yields the maximum S/N. The “FIELD” column indicates which of LEAD, MAIN, or TRAIL the source was detected within. Known objects identified within $5'$ of the candidate position are listed in the “Near Object” field and the distance between source position and reported object position is listed in the “Dist” field. S/N values marked with an * lie outside (but within $10'$) of the optimum filtered map region indicating the local RMS may slightly exceed the RMS used to generate the S/N values reported.

RA (J2000)	DEC (J2000)	S/N	r_c (')	FIELD	Near Object	Type	Dist (')
35.326	-55.398	3.89*	0	L			
35.384	-54.381	3.66*	0	L			
35.701	-55.198	3.38	0	L			
35.759	-53.998	3.32*	0.7	L			
36.076	-55.231	3.01	0	L			
36.133	-54.065	3.10	0.7	L			
36.941	-54.781	3.36	1	L			
37.287	-54.031	5.34*	0.7	L	PMN J0229-5403	Radio	1.6
37.460	-54.715	3.46	1	L	ESO 153-IG 036	Gal	3.8
38.527	-54.298	3.07	0.7	L			
38.873	-54.081	3.18	1	L			
39.219	-54.431	3.25	1	L	LSBG F154-040	Gal	0.4
39.940	-54.481	3.40*	1	L			
40.056	-55.281	3.80*	1	L	APMCC 285	Clust	4.1
40.085	-54.348	3.14*	0	L			
40.114	-54.181	3.69*	0.7	L	IRAS F02388-5421	Gal	1.7
40.142	-53.981	3.31*	1	L	PMN J0240-5401	Radio	2.2
40.171	-54.881	3.39*	0	L			
40.747	-54.981	3.02*	1	M			
41.007	-55.365	3.89*	0	M			
41.007	-54.415	3.53	0.4	M	IRAS F02424-5437	IrS	0.7
41.151	-54.298	3.36	0	M			
41.469	-55.098	3.07	0	M			
42.016	-54.965	3.04	1	M	LSBG F154-033	Gal	1.5
42.132	-54.098	3.43	1	M	APMBGC 154-014-037	Gal	4.6
43.660	-53.981	3.11*	0	M	APMCC 314	Clust	2.9
44.756	-54.581	3.43	0	M			
45.449	-54.131	3.80*	0	M	LSBG F154-028	Gal	2.7
46.313	-55.398	3.12*	0	T	[KOS90] 030420-553530	Gal	3.9
47.034	-55.281	3.06	0	T			
47.323	-54.481	3.18	0	T			
47.553	-54.465	3.15	0	T	FSM 005/FSM 015	Gal	4.1/3.9
47.640	-55.365	3.24*	0.4	T			
50.293	-55.381	3.49*	0	T			
50.639	-53.981	4.68*	0.7	T	PMN J0322-5354	Radio	4.5
50.784	-54.798	3.75*	0	T			
50.841	-53.981	3.18*	0	T			
51.014	-54.081	3.69*	1	T			

Table 5.7: Catalog of candidate source increments exceeding $+3\sigma$ in the CMB5 fields.

Field	3σ	3σ	4σ	4σ
	Expected	Detected	Expected	Detected
LEAD	0.6(+4)	7	0.2(+0)	0
MAIN	1.0(+4)	3	0.4(+0)	0
TRAIL	0.6(+4)	4	0.2(+0)	0

Table 5.8: Expected cluster counts and measured number of decrements for each 150 GHz CMB5 field versus detection threshold in a flat- Λ CDM cosmology with $\Omega_M = 0.3$ and $\sigma_8 = 0.93$. We have only included those objects detected within the lowest noise 3.2 deg^2 of the map. The numbers in parentheses are the expected false detection rates for each field and σ threshold.

5.5.2 Comparison with Expectations

The formalism for predicting the number counts was presented in the previous sections. Here we compare the expected number of decrements with S/N above some σ threshold with the number actually measured. The results are presented in Table 5.8 where we have also included an estimate of the false detection rate for each field and σ threshold. The expected and measured 4σ decrements are within reasonable agreement considering that only 0–1 objects are predicted in a Λ CDM cosmology and none are detected. The agreement at 3σ is also reasonable with ~ 14 “objects” (both real clusters and false detections) predicted and 14 detected. However, two of the $> 3\sigma$ decrements in the LEAD field are probably contaminated by a radio source and should not be included as “detected” objects.

The expected cluster yield of the ACBAR survey depends very strongly upon the values of σ_8 and Ω_M assumed for the Universe. We have used values of $\sigma_8 = 0.93$ and $\Omega_M = 0.3$ to be consistent with the values measured by X-ray satellites and CMB observations. However, recent measurements of the CMB power spectrum with the Cosmic Background Imager suggest a higher value of $\sigma_8 \sim 1.0$ to explain an excess of power at high- ℓ than would be expected from primary CMB alone [15]. We compare the expected 4σ cluster yield in all three CMB5 fields for a flat- Λ CDM cosmology with $\Omega_M = 0.3$ as a function of σ_8 in Figure 5.29. The figure also presents the Poisson probability of measuring zero clusters as a function of σ_8 . Note that the Poisson probability of detecting zero objects reduces to $P_\mu(0) = e^{-\mu}$, where μ is the mean expected number of objects [108].

The effects of a 10% error in calibration upon expected cluster yield are also illustrated in Figure 5.29. We have only shown the calibration error in the direction that would produce fewer expected clusters. We see that the calibration error only affects the σ_8 probability

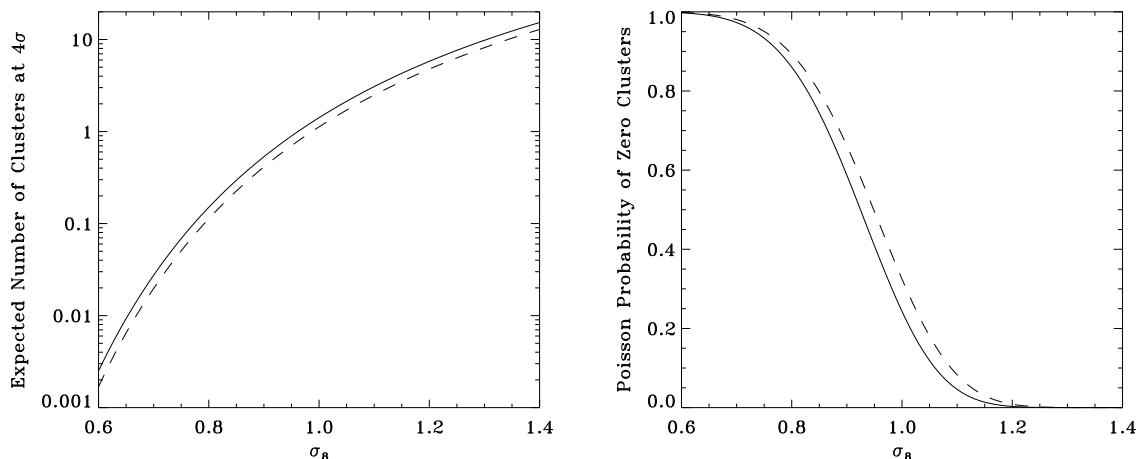


Figure 5.29: Left panel shows the expected 4σ cluster yield of the $\sim 10 \text{ deg}^2$ ACBAR CMB5 cluster survey for a Λ CDM concordance cosmology as a function of σ_8 . Right panel shows the Poisson probability of detecting zero objects at -4σ as a function of σ_8 . The dashed line in both figures represents the effects of a 10% error in flux calibration; we have only shown the error direction that would produce fewer clusters.

curve at the few percent level. The expected number of objects also depends upon the lower mass limit imposed because of the steepness of the mass function. Although statistically motivated, the low-mass cutoff could be too conservative; increasing it to a higher limiting mass would further reduce the number of expected clusters.

The matter density, Ω_M , controls the normalization of the mass function and affects the evolution of $\sigma(M, z)$ and the comoving volume element. Following Lin and Mohr (2002), we also calculate the probability of detecting no clusters at 4σ as a function of σ_8 and Ω_M in a flat- Λ CDM cosmology; the results are shown in Figure 5.30. The 95% confidence contour is well fit by $\sigma_8 < 1.10 (\Omega_M/0.3)^{-0.23}$ for $0.1 \leq \Omega_M \leq 1$.

We have assumed that the selection function and mass-flux relationship do not depend upon core radius or redshift. The assumed universality of the selection function will slightly underestimate the detection fraction of compact clusters and overestimate the fraction of large core radius clusters; these effects should cancel to first order. The cluster mass versus in-beam flux relationship (based on hydrodynamical simulations and shown in Figure 5.27) appears reasonably insensitive to core radius and cluster redshift. We only used simulated clusters in the redshift range 0.5–1.5 and one may argue that neglecting clusters with $z < 0.5$ may bias the results. However, a $10^{15} M_\odot$ cluster at $z < 0.5$ would be clearly detectable in the RASS X-ray survey. Based upon the probability distribution of σ_8 shown in Figure

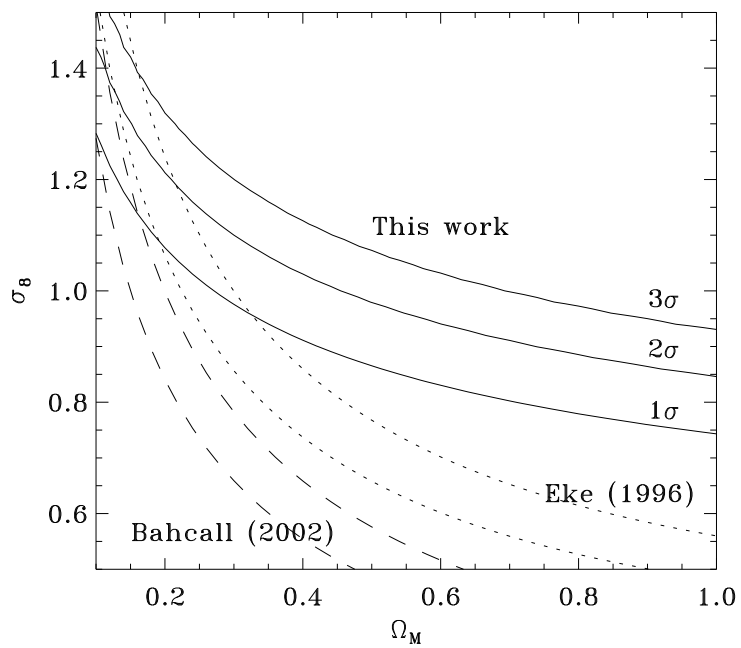


Figure 5.30: Shows the Poisson probability of detecting zero objects at -4σ in the $\sim 10 \text{ deg}^2$ ACBAR CMB5 cluster survey for a flat- Λ CDM cosmology as a function of σ_8 and Ω_M . The solid lines indicate the 68, 95.4, and 99.7% probability contours from this work. Overplotted are the 1 σ contours from X-ray observations [26] (dotted lines) and the SDSS [4] (dashed lines).

5.29 we use the non-detection of clusters at 4σ to place an upper limit of $\sigma_8 < 1.13$ at 95% confidence in a flat- Λ CDM concordance cosmology with $\Omega_M = 0.3$. This result is reasonably robust to uncertainty in the instrument calibration and the value of the low-mass cutoff.

Chapter 6 Other ACBAR Science

6.1 CMB Power Spectrum

ACBAR has made the most precise CMB maps to date with a sensitivity of $\sim 5 \mu\text{K}$ per beam over many square degrees. We have mapped approximately 50 deg^2 to varying levels of sensitivity in an effort to measure the CMB power spectrum from $\ell \sim 150$ to ~ 2500 . The purpose of varying the depth of the CMB maps is to reduce the cosmic variance contribution at low- ℓ by covering a large area of sky but to also go very deep on a few fields to beat down the instrument noise at high- ℓ where the exponential cutoff from the beam size determines the highest significant multipole. The ACBAR power spectrum based on a few months of observation in 2001 and five months in 2002 is presented in Kuo et al. (2002) and shown in Figure 1.2.

The most significant improvement to the measured power spectrum from ACBAR is for $\ell \gtrsim 1000$. This data will be significant for some period of time – even after the MAP satellite [70] releases its full sky power spectrum in early 2003 because its angular resolution will limit it to $\ell < 1000$. Other contemporary experiments designed to measure small scale CMB anisotropy have been limited by a variety of factors. The interferometric CBI in Chile is a very elegantly designed experiment but lacks the intrinsic sensitivity to measure small scale CMB anisotropy over a large amount of sky. The BOLOCAM experiment [31] has the sensitivity, angular resolution, and throughput to be a very powerful CMB experiment but has been plagued by poor weather and sky noise on Mauna Kea and the limited availability of CSO telescope time. There are a handful of small-scale CMB experiments on the horizon (e.g., AMI, AMIBA, and SZA) which should measure complementary CMB power spectra at low-frequency. These experiments are interferometers and should be subject to different systematic effects than ACBAR.

The ACBAR power spectrum has been used to place further constraints on cosmological parameters – both alone and in conjunction with other published power spectrum measurements – and the results are presented in Goldstein et al. (2002). The strongest constraints from ACBAR are on the density of dark energy (Ω_Λ) and the spectral index of scalar density

perturbations (n_s). The probability that the Universe is spatially flat and composed only of matter is extremely unlikely. Most of the evidence points towards roughly 70% of the density in the form of an as of yet unidentified dark energy that is causing the expansion of the Universe to accelerate and an additional $\sim 25\%$ in the form of dark matter whose nature is equally mysterious. The probability that $\Lambda = 0$ based on ACBAR plus COBE data is a mere 2%. It is truly remarkable to contemplate that $\sim 95\%$ of the energy density of the Universe is of a form we know virtually nothing about. There are still significant questions that observational cosmology has yet to answer.

6.2 Pointed Cluster Observations

During 2001 and 2002, we conducted pointed cluster observations with ACBAR of an X-ray luminosity limited sample of clusters in the southern hemisphere ($L_x > 4 \times 10^{44}$ erg/s, $\delta < -44^\circ$) selected from the REFLEX cluster survey [13]. This program is part of the Viper SZ Cluster Survey [98] which combines observations of southern clusters from ACBAR at 150, 220, and 280 GHz with X-ray data from ROSAT, Chandra, and XMM as well as weak lensing data from the 4m CTIO telescope in Chile. The goal of the Viper Cluster Survey is to understand the physical properties of nearby ($z < 0.1$) clusters.

Understanding cluster physics will be vital for estimating the cluster selection function in future deep SZ cluster surveys that will be sensitive to the details of the evolution of cluster gas [46]. The multifrequency observations of ACBAR allow the separation of contaminating primary CMB anisotropy from the SZ emission which is very important for measuring the distribution of cluster gas. An example of a CMB cleaned SZ image made by ACBAR is shown in Figure 6.1 for the Abell cluster A3266 [34]. The multifrequency observations of clusters afforded by ACBAR make it a powerful instrument for the study of SZ emission of nearby clusters.

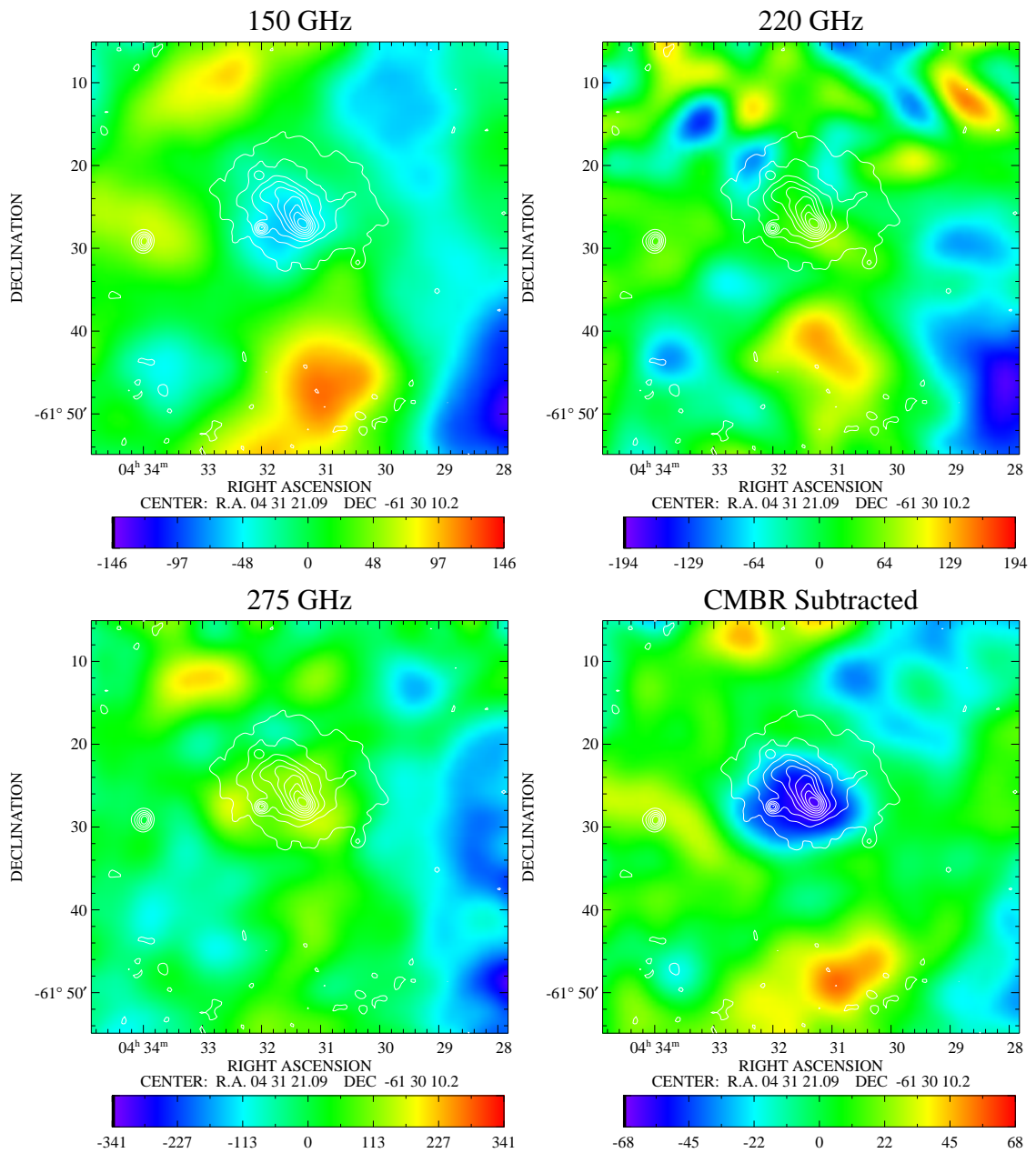


Figure 6.1: Illustrates the ability to remove primary CMB anisotropy from an SZ cluster image with multifrequency ACBAR data. This figure shows ACBAR data at 150, 220, and 280 GHz of Abell 3266 as well as a CMB subtracted image which maximizes the SZ signal to noise. The overlay contours are from ROSAT and they overlap the measured SZ decrement quite well. This figure is from Gomez et al. (2002).

Chapter 7 Conclusions and Future Prospects

We have taken advantage of improvements in bolometric detector technology and the remarkable observing conditions at the South Pole to make the most sensitive maps of the Cosmic Microwave Background to date. ACBAR has demonstrated that the South Pole is an ideal location to conduct large-scale CMB and SZ surveys at millimeter wavelengths. Our deepest CMB field was mapped to a sensitivity of $\sim 5 \mu\text{K}$ per $5'$ beam at 150 GHz over many square degrees with adjacent fields mapped to $\sim \sqrt{2}$ times this sensitivity. We searched within these maps for previously unknown clusters of galaxies using the SZ effect. Because our higher-frequency maps lack the sensitivity to effectively remove the primary CMB signal from the 150 GHz maps, we applied optimal filters tuned to the cluster sizes likely to be detectable by ACBAR to reduce the contamination from primary CMB anisotropy. We found that the cluster size assumed in the optimal filter has remarkably little effect on the expected S/N of a cluster.

We find no clusters with signal greater than 4 times the post-filter map RMS within the most sensitive 10 deg^2 of our optimally filtered maps. This is consistent with the 0–1 expected from a ΛCDM concordance cosmology with $\Omega_M = 0.3$ and power spectrum normalization of $\sigma_8 = 0.93$ based on X-ray observations (refer to Figure 5.29). We determined the expected yield of the ACBAR cluster survey by Monte Carlo simulation of our detection efficiency using realizations of the CMB and the measured noise covariance. We find the cluster selection function to be a fairly uniform function of in-beam cluster flux, but not total cluster flux (or equivalently, cluster mass). This results from our use of a peak-finding cluster detection method. In the future, we intend to employ a Bayesian cluster detection algorithm which should result in a more uniform selection function with cluster mass [47].

We estimate the mass limit of the survey to be $\sim 1.1 \times 10^{15} M_\odot$. Using the simulated cluster selection function and the non-detection of sources above 4σ , we place a 2σ upper limit of $\sigma_8 < 1.10 (\Omega_M/0.3)^{-0.23}$ upon the power spectrum normalization in a flat- ΛCDM cosmology ($h = 0.7$, $\Gamma = 0.23$). This result is consistent with the reported 68% confidence contours on the σ_8 – Ω_M plane from X-ray observations [26], the Sloan Digital Sky Survey [4] for values of $\Omega_M \gtrsim 0.15$ (refer to Figure 5.30). The result is also consistent with the

non-detection of SZ clusters in the deep BIMA fields [68] and the power spectrum excess at high- ℓ detected by CBI [15]. We note in passing that the X-ray and optical results are inconsistent with each other at the $> 1\sigma$ level which may indicate that the systematics of cluster surveys are not entirely understood.

We detect a handful of objects above 4σ just outside of the optimal map region and two objects at $> 3.9\sigma$ within the best parts of the maps. The probability of $\sim 4\sigma$ false detections is low and these objects may be the first discovery of previously unknown clusters using the SZ effect. We have begun a follow-up program using X-ray satellite observations from XMM, optical observations from the 4 m CTIO telescope in Chile, as well as pointed multi-frequency observations with ACBAR to determine cluster redshifts and verify an SZ spectrum of cluster candidates.

In retrospect, it would have been judicious to select fields with at least one known X-ray bright galaxy cluster to verify ACBAR's cluster finding efficacy. However, massive clusters are very rare objects on the sky and this would have biased our result. We will make this a priority for future cluster searches with ACBAR to demonstrate its ability to find clusters in a large survey. Our deepest field has four optically selected galaxy clusters from the Southern Abell catalog [1] but we do not detect any of these above a S/N of 3. This is not surprising because most of these Abell clusters lack sufficient hot gas to be detectable in the RASS. The possible exception is A3067 (43.629° , -54.124° J2000), which overlaps nicely with a cold spot in our filtered maps but does not quite reach the 3σ selection threshold.

ACBAR's relatively large $5'$ beams couple well to the extended emission of very massive galaxy clusters but also to small-scale primary CMB anisotropy. We find that CMB contamination in our single-frequency maps decreases our sensitivity to clusters by $\sim \sqrt{2}$; this has a very large effect on the expected yield of our survey because the cluster mass function is very steep. In 2004, we intend to reconfigure the ACBAR focal plane with enough 220 GHz feeds to provide comparable sensitivity to the 150 GHz channels. The 220 GHz CMB maps will be free of SZ signal and can be used as a template for removing the primary CMB anisotropy from the 150 GHz maps. This should greatly increase the number of clusters detectable by ACBAR. Deep observations at 150 and 220 GHz should also allow the separation of the primary and SZ power spectra at $\ell \gtrsim 1000$ which will put tight limits on σ_8 .

Future SZ surveys, such as SZA in the Owens Valley and the South Pole Telescope,

will have smaller beams than ACBAR. This will not only improve coupling to the more abundant low-mass clusters but will also push the angular scale further down the damping tail of the CMB power spectrum. We also note that near-future X-ray surveys (such as the XMM Cluster Survey [99]) expect to detect hundreds of clusters out to redshifts as high as $z \sim 2$. These deep surveys will be more sensitive to the details of cluster physics at high redshift because they will resolve the clusters rather than integrate their flux over a large beam. We must better understand the evolution of clusters to develop accurate survey selection functions if meaningful cosmological parameters are to be extracted from these deep surveys.

Cluster evolution should eventually be well understood from the wealth of information provided by upcoming deep, high-resolution, multi-frequency SZ surveys and X-ray observations. With this information it should be possible to accurately separate the evolution of structure growth and the comoving volume element in cluster abundance surveys and tightly constrain the cosmological parameters σ_8 , Ω_M , and Ω_Λ . In principle, it may be possible to use these observations in conjunction with distance measurements to constrain the equation of state of the dark energy [79]. This should shed some light on this mysterious dark energy that dominates the energy budget and expansion dynamics of the Universe but whose nature remains one of the most fundamental open questions in cosmology.

Appendix A Bolometer Parameters

A.1 Load Curve Analysis

The steady state of a bolometer is determined by the power balance equation

$$P + Q = \int_{T_{base}}^{T_{bolo}} G(T) dT,$$

where $P = IV$ is the electrical power dissipated by the bolometer, Q is the absorbed optical power, $G(T)$ is the thermal conductivity of the bolometer to the temperature bath and is a function of temperature, T_{base} is the temperature of the bath, and T_{bolo} is the temperature of the bolometer. The thermal conductivity is usually well described by a power law of the form

$$G(T) = G_0 \left(\frac{T_{bolo}}{T_0} \right)^\beta,$$

where T_0 is a merely a reference temperature for which $G(T_0) = G_0$ and β is the power law index of the thermal conductivity. The ratio T_{bolo}/T_0 occurs quite frequently and is usually denoted as $\phi = T_{bolo}/T_0$, and thus the thermal conductivity can be written

$$G(\phi) = G_0 \phi^\beta.$$

Expanding the power balance equation we have

$$P + Q = \frac{G_0}{(\beta + 1)T_0^\beta} \left(T_{bolo}^{\beta+1} - T_{base}^{\beta+1} \right) = \frac{G_0 T_0}{\beta + 1} \left(\phi_{bolo}^{\beta+1} - \phi_{base}^{\beta+1} \right).$$

The impedance of the bolometer is a strong function of temperature and is given by

$$R(T) = R_0 e^{\sqrt{\frac{\Delta}{T}}},$$

where Δ is a property of the thermistor material and R_0 depends on the geometry of the thermistor. Typical values of these characteristic bolometer quantities for ACBAR are $R_0 \sim 150 \Omega$, $\Delta \sim 41.8 \text{ K}$, $G_0 \sim 300 - 700 \text{ pW/K}$, and $\beta \sim 1$.

The equation for thermistor impedance as a function of temperature is only true in the limit of low electric field across the thermistor. Depending on the type of semiconductor used for the thermistor, when the electric field across it exceeds a certain value, electron hopping across the thermistor will occur and the impedance will not obey this simple relation. This is called the electric field effect (or just E-field effect) and usually only manifests when bolometers have very high impedance resulting in large electric fields [35]. The functional form for the impedance including the E-field term is

$$R(T) = R_0 e^{\sqrt{\frac{\Delta}{T}} - \frac{eEL}{kT}},$$

from which you should note the different dependencies upon temperature of the two terms in the exponent.

The physical parameters of a bolometer can be measured from a series of load curves (see Figures 2.10 through 2.13) for which the bolometer is exposed to some optical load and the DC signal voltage of the bolometer (V_s) is recorded for many values of bias voltage (V_b). In most applications, the bias and signal voltages will have some voltage offsets due to FETs or the amplifier as well as gain which must be removed to get the true bias and signal voltages. For the circuit arrangement shown in Figure 2.23, one can determine the impedance of the bolometer for any pair, (V_b, V_s), by analyzing the circuit as a simple voltage divider,

$$R_{bolo} = 2R_L \frac{V_s}{V_b - V_s},$$

where R_L is the impedance of one of the two load resistors (each 30 M Ω in ACBAR). The bias current is

$$I_{bias} = \frac{V_b - V_s}{2R_L}.$$

The electrical power dissipated by the bolometer is given by $P = V_s^2/R_{bolo}$. If the bolometer quantities R_0 and Δ are known, the temperature of the bolometer can be determined by inverting the $R(T)$ relation to get

$$T_{bolo} = \frac{\Delta}{[\ln(R_{bolo}/R_0)]^2}.$$

To determine the parameters R_0 and Δ , one usually “blanks off” the bolometer – so

that it is looking into a very cold load resulting in little optical power – and the impedance of the bolometer is measured across a range of base temperatures. This set of bolometer resistances as a function of base temperature is then fit to the $R(T)$ relation to extract R_0 and Δ . In practice, the bolometer is rigidly mounted to a baseplate which is then attached to a fridge and controlled to a given temperature with a heater. The temperature of the baseplate needs to be accurately measured and this is best achieved with a calibrated thermometer, such as a GRT or Cernox thermometer. At each baseplate temperature a very short load curve is taken. One must be careful not to apply too much power to the bolometer or it will heat significantly above the baseplate temperature. It is a simple matter to determine if too much bias power has been applied because the signal voltage versus bias voltage will deviate from an ohmic straight line. The impedance of the bolometer is then determined by fitting a straight line to $V_s(V_b)$ with

$$V_s = V_b \frac{R_{bolo}}{R_{bolo} + 2R_L}.$$

One can then fit the measured values of R_{bolo} and T_{base} to the $R(T)$ function to determine R_0 and Δ . Taking the natural log of the impedance nicely linearizes this equation,

$$\ln R = \ln R_0 + \sqrt{\Delta}x,$$

where $x = 1/\sqrt{T}$.

Unfortunately, it is unlikely that the true bolometer temperature will be the same as the baseplate because of finite thermal conductivity, Kapitza resistance, or a miscalibrated thermometer. If you know the Δ of the material, *a priori*, then it is useful to include a temperature offset in the fit and replace T_{bolo} with $T_{base} + \delta T$, where δT is the temperature offset between the measured temperature and the true bolometer temperature. For ACBAR, we were told by the thermistor manufacturer that the Δ of the NTD Germanium chips is 41.8 K. We were thus able to measure the temperature offsets for all of our bolometers which were found to be as high as 12 mK from the Cernox thermometer values.

With R_0 and Δ , one can then determine the thermal conductivity parameters G_0 and β from a full load curve. By converting the measured values of V_s and V_b into P and T_{bolo} , as described above, one can then fit for G_0 and β from the derivative dP/dT_{bolo} . Using the

power balance equation we see this derivative is given by

$$\frac{dP}{dT_{bolo}} = G_0 \left(\frac{T_{bolo}}{T_0} \right)^\beta = G_0 \phi^\beta.$$

One can then take the natural log of this equation to linearize it and fit a straight line to determine G_0 and β . Take careful note that E-field effects will most likely corrupt the low bias points where the bolometer impedance is highest; particularly for low base temperature load curves with little optical power. This will manifest itself as a non-linear $\ln(dP/dT)$ vs $\ln T_{bolo}$ curve at low T_{bolo} and care should be taken to exclude these points from the fit.

Unless the load curve is very finely sampled, it is more accurate to use the imperfect differential

$$\frac{\Delta P}{\Delta T_{bolo}} = \frac{G_0}{(\beta + 1)T_0^\beta} \frac{(T_{bolo_1}^{\beta+1} - T_{bolo_2}^{\beta+1})}{(T_{bolo_1} - T_{bolo_2})} = \frac{G_0}{(\beta + 1)} \frac{(\phi_1^{\beta+1} - \phi_2^{\beta+1})}{(\phi_1 - \phi_2)}.$$

The key benefit of these equations is that both the baseplate temperature, T_{base} , and absorbed optical power, Q , do not appear. This implies that one can determine G_0 and β from a load curve at any base temperature and any applied optical power. However, the power law index, β , depends weakly on the temperature of the bolometer. If one is going to use the measured bolometer parameters to determine optical loading (as described in the next paragraph), it is generally a good idea to determine G_0 and β in the range of bolometer temperature similar to where you will be measuring Q (e.g., determine G_0 and β from the same load curve that you want to determine the absorbed optical power).

Re-arranging the power balance equation gives

$$Q = \frac{G_0}{(\beta + 1)T_0^\beta} (T_{bolo}^{\beta+1} - T_{base}^{\beta+1}) - P.$$

With all of the bolometer parameters in hand, one can determine the bolometer temperature and electrical power for each point in a load curve and solve for Q for the entire load curve. Since Q is constant across the load curve, this should be a flat line if the bolo parameters are correct. It is likely that E-field effects will cause the measured Q to deviate from a flat line at low bolometer temperatures. Note that this depends explicitly on knowledge of the base temperature. Temperature offsets can greatly affect the value of Q measured

in this way. For example, a +10 mK offset (bolometer base temperature 10 mK higher than thermometer reads) with a 500 pW/K bolometer will yield a value of Q too high by ~ 5 pW. Because of this, it is useful to have a well-characterized dark bolometer on the cold stage which you can use as a temperature reference – if you measure a non-zero value of Q for the dark bolometer (and have eliminated optical loading or RF heating) you can determine the temperature offset by

$$\Delta T_{base} \approx \frac{Q_{meas}}{G_0} \left(\frac{T_0}{T_{base}} \right)^\beta,$$

for $\Delta T_{base} \ll T_{base}$.

Measuring the optical power with the technique described above has many useful applications. For example, the optical efficiency of a bolometric system is usually measured by looking into two different temperature loads and comparing the measured difference in absorbed optical power (ΔQ_{abs}) to the incident optical power ($\Delta Q_{incident}$). This method for determining optical efficiency is advantageous over the load curve difference method for systems with high optical efficiency because it does not depend on having the bolometers at the same operating temperature. It is occasionally difficult to apply enough electrical power to a load curve looking into LN2 to achieve the same bolometer temperature looking into a room temperature load.

Similarly, by measuring Q for two different loads you can determine how much additional loading is incident upon the bolometers from within the dewar. For example, if you measure Q looking at both a 300 K and 77 K load and take the ratio of Q_{300} to Q_{77} you should measure

$$\frac{Q_{300}}{Q_{77}} = \frac{\int \tilde{f}_\nu B_\nu(300K) A \Omega d\nu}{\int \tilde{f}_\nu B_\nu(77K) A \Omega d\nu} \sim \frac{300}{77} = 3.9$$

if no power is intercepted by an intermediate temperature within the dewar, where \tilde{f}_ν is the optical efficiency normalized frequency response of the system and $B_\nu(T)$ is the blackbody spectral energy density. However, realistic optical systems have finite transmission at each optical element, and thus the ratio is more accurately described by

$$\frac{Q_{300}}{Q_{77}} = \frac{Q_{internal} + \int \tilde{f}_\nu B_\nu(300K) A \Omega d\nu}{Q_{internal} + \int \tilde{f}_\nu B_\nu(77K) A \Omega d\nu} < 3.9,$$

where $Q_{internal}$ is the loading from the optical elements along the path of the beam due to

absorption or reflection.

The initial deployment of ACBAR suffered from a large amount of internal loading from the 77 K filters leading to Q_{300}/Q_{77} ratios as low as 2.0. After the system upgrade in the Austral Summer of 2001/2002, the measured ratios rose to between 3.3 and 3.7 indicating little internal loading. Another useful application for measuring Q is during a skydip, where the telescope is tipped from near the zenith down to very low elevation to measure the emission (and, hence, transmission) of the atmosphere. The problem with using bolometer voltages is that the bolometer is inherently nonlinear and the large changes in loading during a skydip can lead to misleading atmospheric opacity measurements. By determining Q at each point in the skydip one can accurately determine the real variation in optical loading with zenith angle to measure atmospheric opacity. As an aside, it was by analyzing skydips that the excess filter loading in ACBAR was discovered and explained our excess noise. The details of analyzing skydips are presented in an accompanying appendix.

A.2 Bolometer Optimization

With reasonable estimates for the operating parameters of an instrument (e.g., η , Q , T_{base} , amplifier noise, etc.) one can optimize the thermal conductivity of a bolometer to obtain the lowest total NEP . This process is discussed in detail in Griffin and Holland (1988). Figure A.1 shows the various contributions to the 150 GHz system noise as a function of bolometer operating temperature (which is set by the bias current).

If the bolometer is operated in the undesirable “detector noise limit,” then the impedance of the bolometer and thermal conductivity will determine the sensitivity almost irrespective of the background photon noise contribution. If, on the other hand, the detector is dominated by photon noise, then an otherwise less than optimal detector G does not translate into a noise increase as $NEP \propto \sqrt{G}$. Figure A.2 illustrates this point; it shows the minimum NEP_{total} as a function of detector thermal conductivity for four optical loadings. The minimum NEP is set by tuning the operating temperature of the bolometer for a given base plate temperature and optical loading. Although the G corresponding to the minimum NEP tends to be quite low (~ 60 pW/K for ACBAR’s 150 GHz channels), it is usually not practical to use devices with such low G because the detector time constant goes like C/G and would be prohibitively large. Even with thermal conductivities many times the

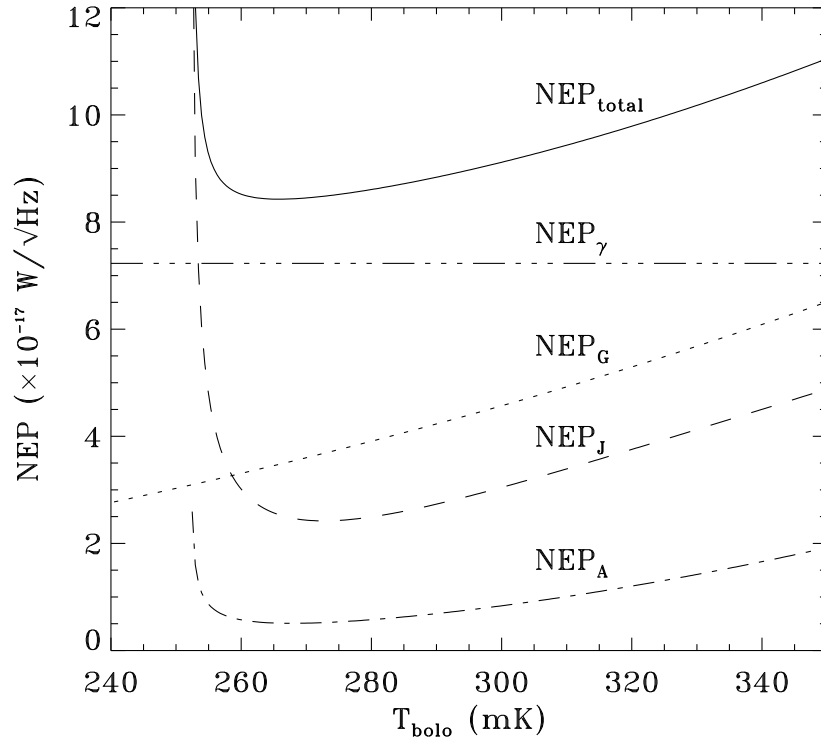


Figure A.1: Noise contributions to ACBAR at 150 GHz versus bolometer operating temperature where we have assumed $Q = 10$ pW, $G_0 = 300$ pW/K, $\beta = 1$ $R_0 = 150$ Ω , $\Delta = 41.8$ K, and $NEV_{amp} = 3 \times 10^{-9}$ V/ $\sqrt{\text{Hz}}$ at 10 Hz. The solid line is the total system NEP , the dotted line is phonon noise, the dashed line is Johnson noise, the dot-dashed line is amplifier noise, and the triple-dot-dashed line is photon noise. We have included both the counting and Bose terms in the NEP_γ .

optimal value, the total system NEP is less than 10% higher the minimum for $Q = 15$ pW and $G_0 = 300$ pW/K.

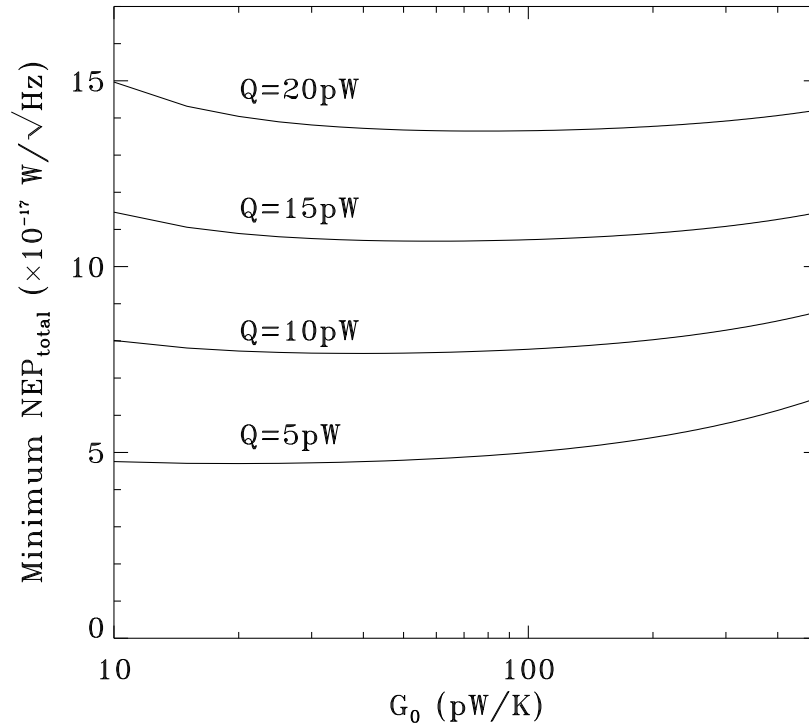


Figure A.2: Minimum total ACBAR 150 GHz NEP versus detector thermal conductivity, G_0 , for various optical loadings. The bolometer parameters are the same as in Figure A.1. The lines correspond to, from bottom to top, $Q = 5, 10, 15,$ and 20 pW optical loading. The average loading for ACBAR is approximately 13 pW at 150 GHz. The actual thermal conductivity of the 150 GHz detectors is approximately 300 pW/K and one can see from the Figure that even though the thermal conductivity is many times the optimal value, the system noise is $\lesssim 10\%$ above the minimum because of the contribution from other noise sources (mainly photon noise).

Appendix B Atmosphere

B.1 Spectrum

The transmission spectrum of the atmosphere is a complex forest of vibrational and rotational molecular lines dominated by water, oxygen, and ozone. The two parameters that are most useful for quantifying the atmospheric spectrum are its temperature, T_{atm} , and frequency dependent zenith opacity, τ_ν . The transmission of the atmosphere at a frequency ν and zenith angle ζ (where the zenith angle is defined as the angle subtended between the point directly overhead and the direction of observation) is given by $e^{-\tau_\nu/\cos\zeta}$. Figure B.1 shows a model of the transmission of the South Pole atmosphere in the winter generated with the AT atmospheric modeling program¹. One can see that there are well-defined “windows” in the far-infrared where the absorption and emission from the atmosphere are minimal; these windows transmit the most astrophysical signal while contributing the least atmospheric power.

The emissivity of the atmosphere contributes to the optical loading of the system (and hence, background noise) and is given by

$$\epsilon_\nu = 1 - e^{-\tau_\nu/\cos\zeta}.$$

The spectral flux density emitted by the atmosphere at temperature T_{atm} is thus

$$I_\nu = \epsilon_\nu B_\nu(T_{atm}),$$

where $B_\nu(T)$ is the emission from a black body at temperature T . In the Rayleigh-Jeans limit, the power received on a detector with optical efficiency normalized frequency response \tilde{f}_ν is then

$$P_{atm} = \int \tilde{f}_\nu \epsilon_\nu \frac{2kT_{atm}\nu^2}{c^2} A\Omega d\nu .$$

¹Airhead Software, Boulder CO

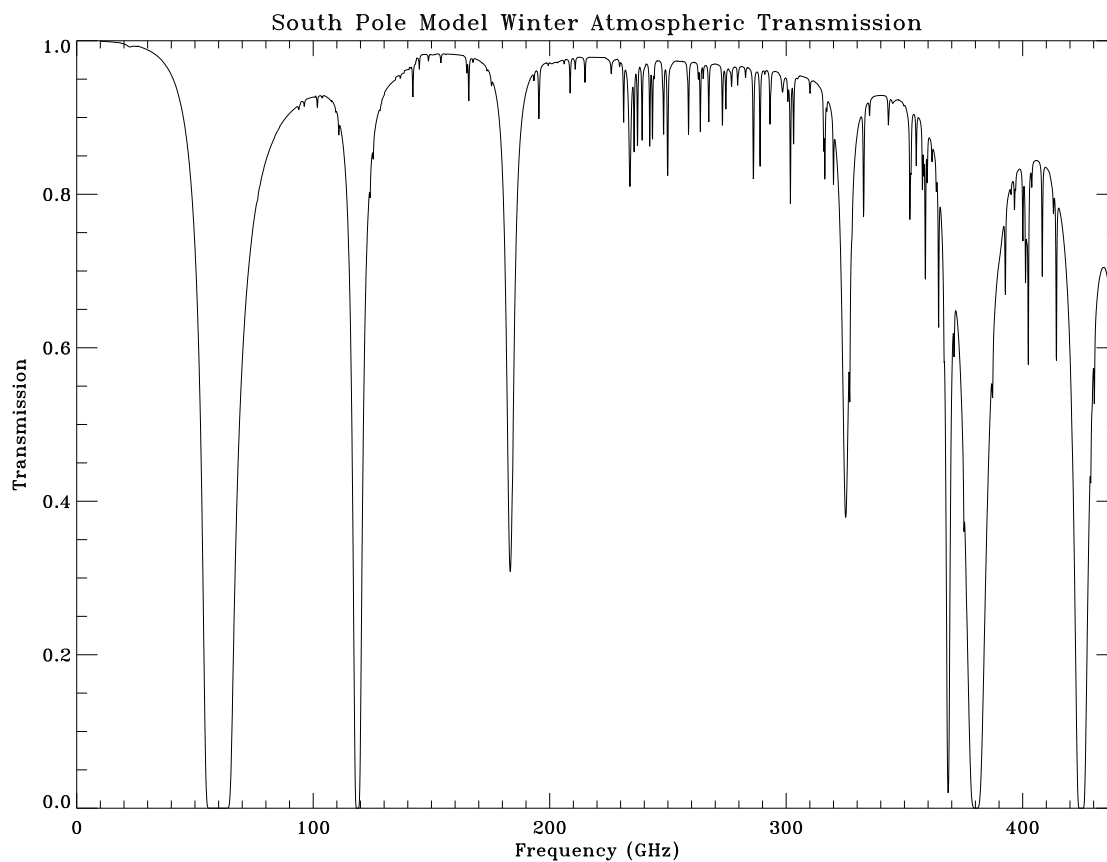


Figure B.1: Model of atmospheric transmission for the South Pole during the Austral Winter generated with the AT atmospheric modeling program. This model assumes an elevation of 2835 m, temperature of -60C, PWV of 0.25 mm, and pressure of 530 torr.

B.2 Skydip Analysis

Although models of the transmission of the atmosphere are useful for selecting spectral band edges, once an instrument is in the field the actual transmission of the atmosphere for each channel needs to be measured. This is usually done with a procedure called a skydip. A skydip is a measurement of the optical power incident on a detector as a function of zenith angle and should follow the relation $a + be^{-\bar{\tau}/\cos\zeta}$, where $\bar{\tau}$ is the effective zenith opacity of the channel. For any point in the skydip there will be many contributions to the total optical power, or equivalently, observed temperature loading:

$$T_{obs}(\zeta) = T_{internal} + \epsilon_{scope}T_{scope} + (1 - \epsilon_{scope}) \left[T_{CMB}e^{-\bar{\tau}/\cos\zeta} + T_{atm} \left(1 - e^{-\bar{\tau}/\cos\zeta} \right) \right],$$

where $T_{internal}$ is the internal loading in the dewar due to absorption or reflection by filters or optical stops, ϵ_{scope} is the total emissivity of the telescope and is a function of frequency and the telescope mirror material, T_{scope} is the temperature of the telescope, T_{CMB} is the temperature of the cosmic microwave background (2.73 K) and is assumed to be the dominant astrophysical source, and T_{atm} is the temperature of the atmosphere. The emissivity of a mirror surface depends on its conductivity and surface finish [122] and is given by

$$\epsilon = \sqrt{\frac{16\pi c\epsilon_0}{\lambda\sigma}},$$

where c is the speed of light, ϵ_0 is the permittivity of free space, λ is the wavelength, and σ is the conductivity of the metal which is approximately $3.7 \times 10^7 \Omega^{-1}\text{m}^{-1}$ for aluminum. Surface roughness and oxidation will degrade the reflectivity of a metal surface and the actual emissivity is usually a few times this value. Note that for Viper there are four mirror surfaces and thus the total emissivity of the telescope is $4\times$ this nominal value.

The optical loading on a detector can change during the course of a skydip. This can cause a bolometer to go non-linear and, thus, fitting to the DC voltage of a bolometer as a function of zenith angle can give incorrect results for the atmospheric opacity. This problem is mitigated by calculating the optical power on the bolometer for each point in the skydip. This can only be done if the bolometers have been well characterized (see the Load Curve Analysis appendix), the bolometer base temperature is monitored, and FET voltage offsets can be removed by either including a zero bias point in the skydip or using a

resistor channel whose voltage does not depend on optical power or base plate temperature as an offset monitor.

For ACBAR's 2001 observing season we performed approximately 350 skydips but only took a grounded bias point for the last ~ 40 dips to measure the FET offsets. Since it is important to know the FET offsets for all channels to accurately determine the optical loading, we needed a way to infer the FET offsets for the skydips without grounded bias points. The solution was to use the fake bolometers (load resistors) as FET offset monitors since their biased signal (DC) should only depend on the FET offsets and the voltage gain (which we assume to be stable). Figure B.2 shows the correlation between the FET offsets of two of the resistor channels of ACBAR and one can see they are well fit by a line with slope of unity indicating a common drift in FET offset voltage.

While biased, only one of our resistor channels was not saturated. But because the FET offsets are correlated, we can use this one channel as an indicator of drifts in all channels. To this end we computed the average of the FET offsets for all channels for the 40 skydips with grounded bias points as well as the change in voltage on the one resistor channel between biased and unbiased states (13.676 V). For all of the skydips where no grounded bias point was taken we then used the biased voltage of this resistor channel, subtracted this voltage difference, and compared the resulting number with the average grounded bias value (-4.275 V) to determine any shift in FET offset voltage. The resultant shift in FET offsets is then added to the average FET offsets for all channels which gives the appropriate offset to remove from the skydip voltages. In 2002, we explicitly included a bias grounded data point in all skydips and this issue was moot.

Once the voltage offsets have been properly removed from the skydip, the optical power for each skydip point is determined by inverting the bolometer power balance equation

$$Q = \int_{T_{base}}^{T_{bolo}} G(T)dT - IV,$$

which makes use of the measured bolometer properties and base plate temperature. One then has $Q(\zeta)$ for each channel. With laboratory load curve measurements looking into two different temperature loads one can take the measured ΔQ for a temperature difference of

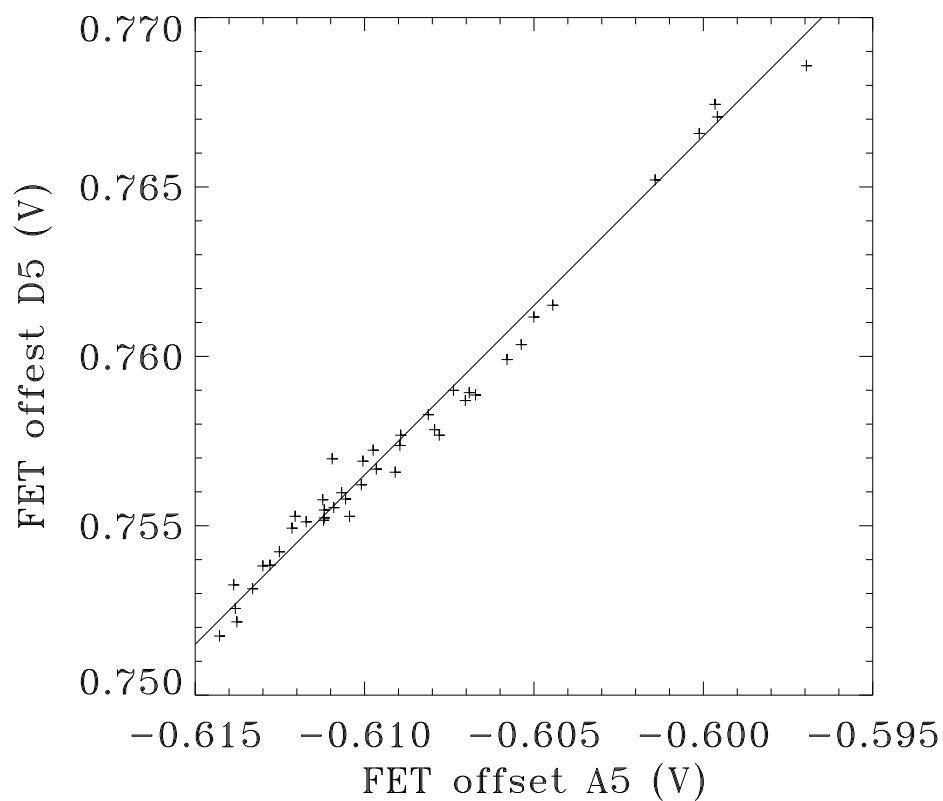


Figure B.2: Comparison of the FET offsets of two resistor channels. The line has slope of unity indicating good correlation of offset drift between channels.

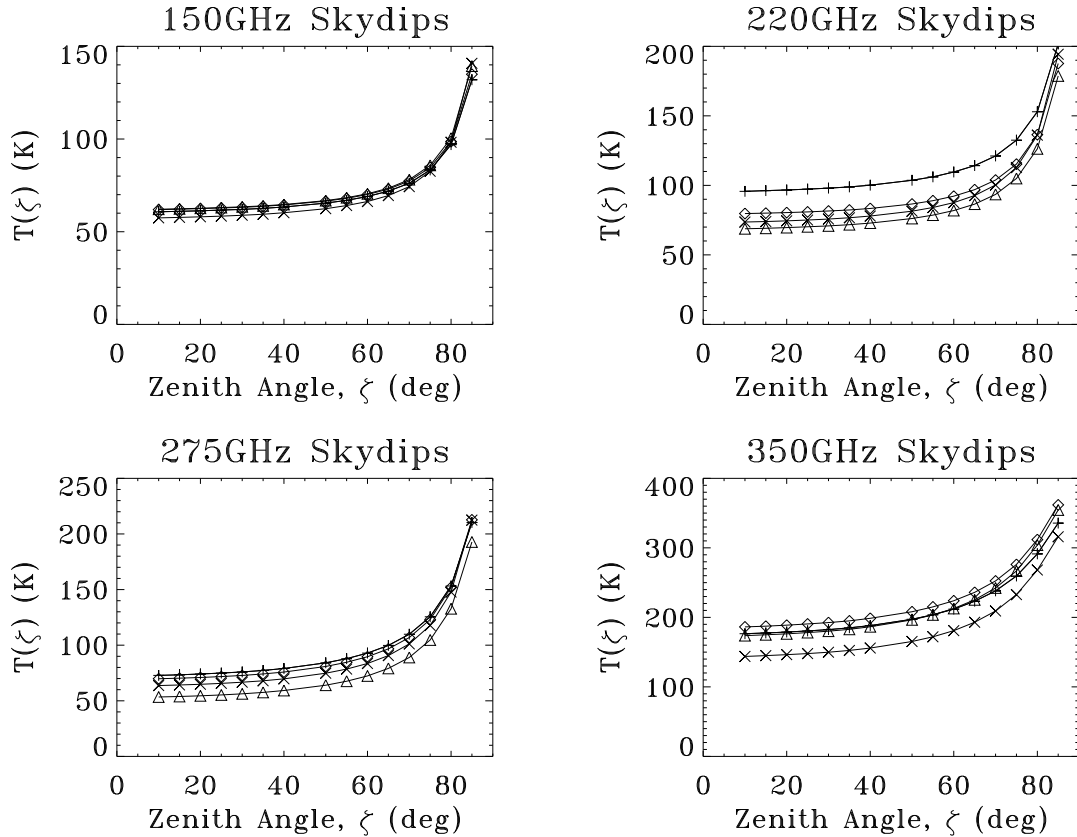


Figure B.3: The observed temperature of all channels as a function of zenith angle, ζ . Within each frequency are four sets of points: plus, diamond, triangle, and times representing channels 1 through 4 of each frequency, respectively. The lines connecting the points are to guide the eye and are not fits to the data.

ΔT and convert $Q(\zeta)$ to $T(\zeta)$ by

$$T(\zeta) = \frac{\Delta T}{\Delta Q} Q(\zeta).$$

Figure B.3 shows a skydip performed on 02/07/01 for all channels.

Fitting $T(\zeta)$ to the functional form $a + T_{atm} (1 - e^{-\bar{\tau}/\cos\zeta})$ without further assumptions can prove difficult because $1 - e^{-x} \sim x$ for $x \ll 1$ leading to a degeneracy between the parameters T_{atm} and $\bar{\tau}$. It is usually the case that $\bar{\tau}/\cos\zeta \ll 1$ unless the skydip is taken to very large zenith angles or the opacity is particularly high. However, this degeneracy can be broken with an estimate of the temperature of the atmosphere and telescope transmission, in which case the term that depends on zenith angle is given by $(1 - \epsilon_{scope}) (T_{CMB} - T_{atm}) e^{-\bar{\tau}/\cos\zeta}$. We were fortunate to be granted access to the archive

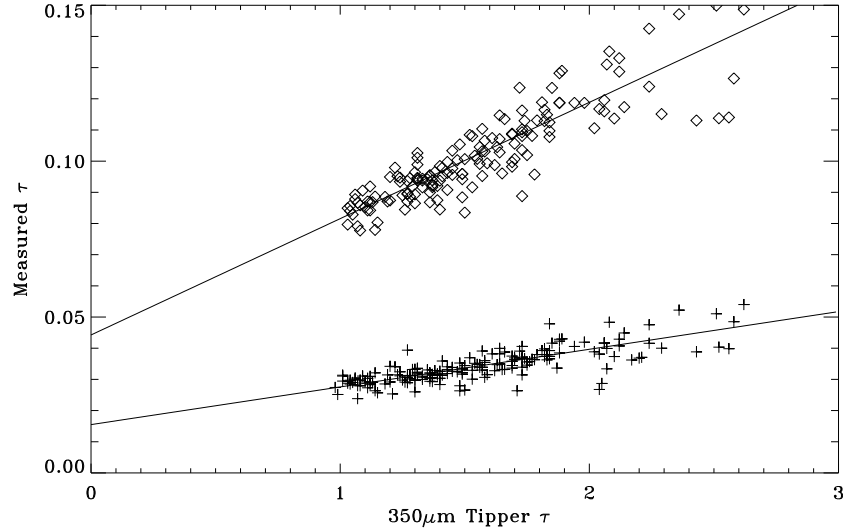


Figure B.4: The correlation between the average measured effective opacity at 275 (diamonds) and 150 GHz (pluses) versus the 350 μm tipper on AST/RO. The solid lines are the best fit linear curves.

Band (GHz)	a	b
150	0.0186	0.0112
220	0.0189	0.0251
280	0.0209	0.0439
350	0.0417	0.0954

Table B.1: Average linear fit between the measured in-band zenith opacity versus reported 350 μm tipper for 2001. The equation is parameterized by $\bar{\tau} = a + b\tau_{350}$.

of atmospheric temperatures measured by the sub-mm tipper on the AST/RO [93] which measures both the temperature of the atmosphere as well as zenith opacity at 350 μm approximately every 15 minutes. Using this archive we were able to break the τ - T_{atm} degeneracy as well as correlate our measured effective opacities for all channels with the values measured at 350 μm . This latter point allows us to use the frequently measured τ_{350} to correct for the atmospheric transmission without having to do time consuming skydips multiple times a day. Figure B.4 shows the correlation between measured effective opacities at 150 and 275 GHz versus the 350 μm values. A straight line was fit to each channel i of the form $\bar{\tau}_i = a_i + b_i\tau_{350}$ and the average values of a and b for each frequency are listed in Tables B.1 and B.2. Figure B.5 shows a histogram of effective zenith opacity at 150 GHz scaled from the entire 350 μm tipper archive from 2001.

Band (GHz)	a	b
150	0.0155	0.0121
220	0.0160	0.0247
280	0.0442	0.0373

Table B.2: Average linear fit between the measured in-band zenith opacity versus reported $350 \mu\text{m}$ tipper for 2002. The equation is parameterized by $\bar{\tau} = a + b\tau_{350}$.

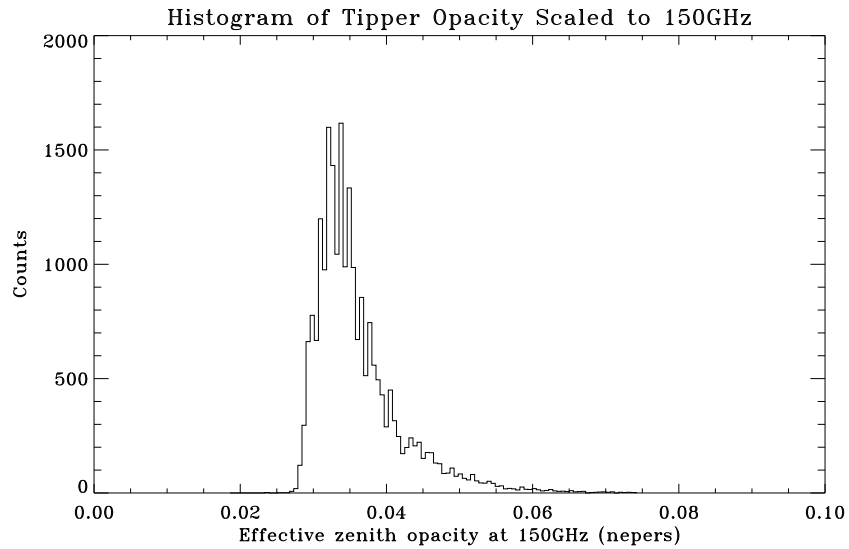


Figure B.5: Histogram of effective zenith opacity at 150 GHz for the 2001 observing season. This data was generated by the NRAO $350 \mu\text{m}$ tipper at the pole [93] and scaled to 150 GHz.

Appendix C Optics

C.1 Gaussian Telescope Optics

A discussion of Gaussian telescope optics is in order before detailing the Viper telescope and feed horn design. The propagation of single moded beams is well described by Gaussian optics [32] and the field distribution is given by the wave equation

$$\nabla^2\psi + k^2\psi = 0,$$

which, for a wave propagating in the \hat{z} direction, the solution is

$$\psi(z) = A \frac{w_0}{w(z)} e^{-r^2/w^2(z)} e^{-ikz} e^{-i\pi r^2/\lambda R(z)} e^{i \tan^{-1}(\lambda z/\pi w_0^2)}.$$

The width of the beam is characterized by $w(z)$ given by

$$w(z) = w_0 \left[1 + \left(\frac{\lambda z}{\pi w_0^2} \right)^2 \right]^{1/2},$$

and a beam waist is defined as the width of the beam when the phase is flat. The effect of a focusing optic is to convert one beam waist to another by varying the phase front of the incident beam. For a beam waist size w_1 a distance d_1 from a focusing element of focal length f , the equations giving the position and size of the re-imaged waist are

$$\frac{d_2}{f} = 1 + \frac{(d_1/f) - 1}{[(d_1/f) - 1]^2 + (\pi w_1^2/\lambda f)^2}$$

$$\left(\frac{w_2}{w_1} \right)^2 = \frac{1}{[(d_1/f) - 1]^2 + (\pi w_1^2/\lambda f)^2}.$$

Thus, the effect of a telescope can be described by multiple applications of these focusing formulae to propagate an initial beam waist – generated by a feed horn – through the system. For distances much larger than a wavelength, the effect of a focusing element reduces to the

familiar geometric optics relation

$$\frac{1}{f} = \frac{1}{d_1} + \frac{1}{d_2}.$$

The resulting far field beam on the sky is given by

$$\theta_{FWHM} = \sqrt{2 \ln 2} \frac{\lambda}{\pi w_p},$$

where w_p is the waist size formed by the primary. It needs to be stressed that this relation is only approximate and that the true beam size will be determined by a diffraction integral of the fields over the finite aperture of the primary which will spread the beam slightly from this nominal value.

An important parameter characterizing a telescope is the effective focal length, f_{eff} . In the geometric optics limit, the effective focal length is given by

$$f_{eff} = DF = \frac{D}{2 \tan \phi_{1/2}},$$

where D is the diameter of an incident ray bundle, F is the $f/\#$ of the beam incident on the focal plane, and $\phi_{1/2}$ is the half-angle of the beam incident on the focal plane. For most purposes a telescope can be approximated as a single focusing element of focal length f_{eff} . The primary waist size for a system with effective focal length f_{eff} , feed waist w_0 , and wavelength λ is equal to

$$w_p = \frac{\lambda f_{eff}}{\pi w_0},$$

and thus the beam size is simply $\theta_{FWHM} = \sqrt{2 \ln 2} w_0 / f_{eff}$ and is independent of frequency to first order. One can see from these equations that matched beam sizes from a multi-frequency instrument requires matched feed waist sizes, w_0 ; this produces primary beam waists that scale with wavelength.

The effective focal length also sets the plate scale of the system which is the separation of two pixels on the sky for a given separation on the focal plane. This is a useful parameter to determine the density of pixels on the sky for close packed focal plane array. The plate scale is given by $PS = 1/f_{eff}$ with units of radians per unit length. The units of length are set by f_{eff} (*e.g.*, for a system with an effective focal length of 4 m the plate scale is 0.25 rad/m or 0.86 '/mm).

For ACBAR we decided upon a nominally $4'$ beam at all frequencies which corresponds to a primary waist size of $w_p = 0.644$ m at 150 GHz and an edge taper of -20dB at the edge of the 2 m primary. However, when the beam pattern is modeled for a feed designed to produce this beam waist, the sidelobe structure results in an actual edge taper of -18dB. Performing the diffraction integral of this distribution over the 2 m aperture implies that the 150 GHz beam should be spread to $\sim 4.5'$ because of edge truncation; this is, in fact, close to the $4.69'$ we observe on the telescope. One may think that the solution to this spreading is to simply make the beam waist larger on the primary to compensate for the finite aperture affects. However, the diffractive effects spread the beam more quickly than it will be reduced by going with large waist sizes. Because the Viper telescope consists of many off-axis reflections from asymmetric mirrors, performing accurate diffraction integral predictions was unrealistic and it was decided the safest approach would be to scale the primary beam waists with wavelength in an attempt to achieve matched beam sizes at all frequencies. In retrospect, the diffraction integral on the primary appears to reasonably predict the values of the beam sizes achieved and it should have been possible to do a better job of matching the beam sizes.

C.2 Viper Telescope and Tertiary Redesign

ACBAR observes from the Viper telescope at the South Pole which is administered by the Center for Astrophysical Research in Antarctica (CARA). Viper has been used to conduct 45 GHz observations of CMB anisotropies with the CORONA receiver [87] and polarization in the CMB with the Dos Equis receiver. Viper was also used to measure large scale magnetic fields through polarization of the dust in the galactic center at $850 \mu\text{m}$ with the SPARO receiver [24]. Viper is an off-axis aplanatic Gregorian telescope with a 2 m diameter primary mirror and an additional 0.5 m skirt around the primary to reduce spillover. The pre-ACBAR optical arrangement is shown in Figure C.1 and consists of a 2 m parabolic primary mirror, an elliptical secondary mirror, a chopping flat at an image of the primary formed by the secondary to sweep the beams across the sky without modulating the position on the primary, and a hyperbolic tertiary mirror that refocuses the beam into the receiver. One should take particular note of the reflection off last optic which is a $\sim 90^\circ$ off-axis reflection that converts the incident $f/5.2$ beam into $f/0.5$ resulting in serious aberration of

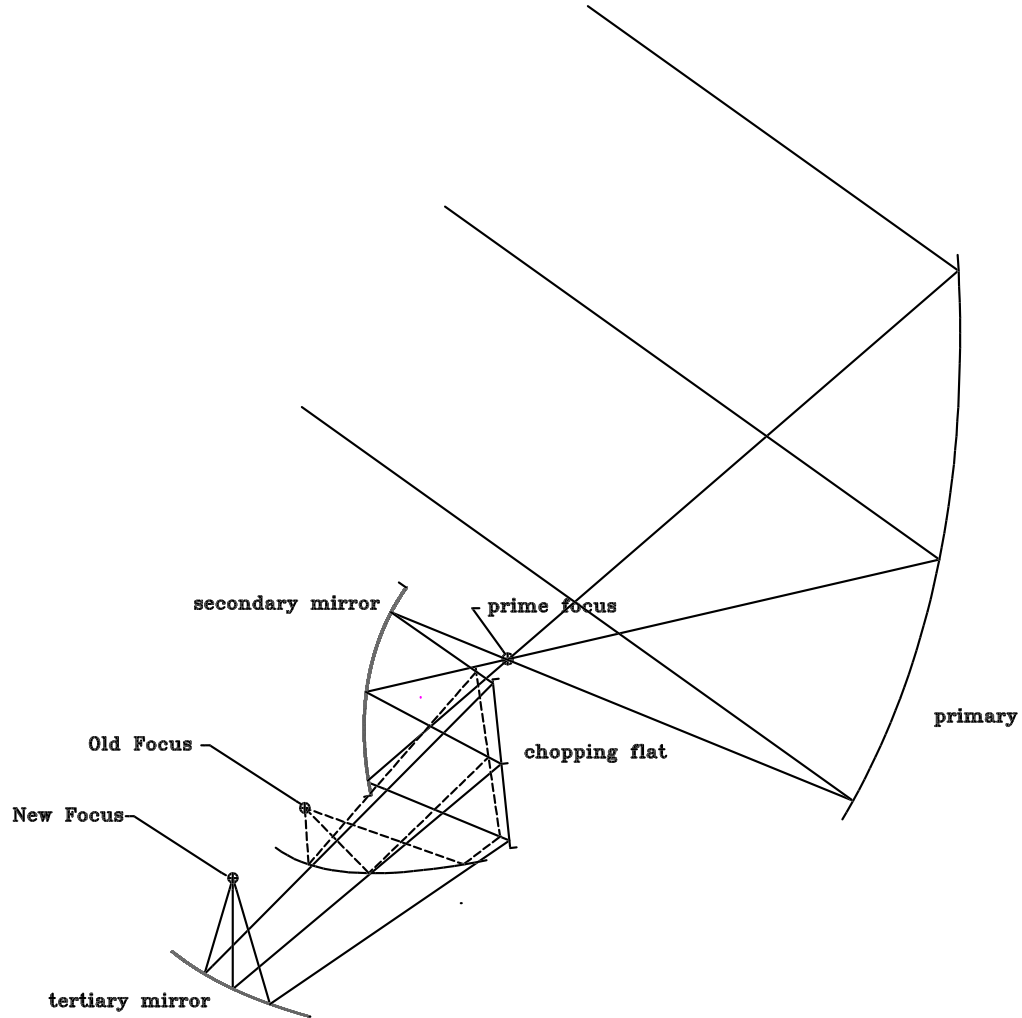


Figure C.1: Comparison of Viper telescope optical layout before (dashed) and after (solid) the tertiary change.

the focal plane.

Our initial design goal for ACBAR was to get as many diffraction limited beams at 150 GHz as possible across the focal plane. With a -18 dB edge taper at 2 m this corresponds to a beam size of approximately $4.5'$ on the sky which is well matched to extended cluster emission as well as small enough to cover the CMB power spectrum down to $\ell \sim 2500$. However, the severe coma of the existing optical system would limit us to a single diffraction limited 150 GHz pixel in the focal plane – if we attempted to put more pixels in the focal plane the spreading of the spot diameters would become comparable to the beam waist sizes of the feeds resulting in significantly enlarged beams on the sky. Because of this we decided

to redesign and reposition the tertiary mirror to improve the optical quality of the system for ACBAR.

Because of existing structural constraints of the telescope, the available degrees of freedom for the redesign were quite limited. The chopper could be moved slightly in both position and angle but we did not want to deviate too much from the image of the primary formed by the secondary; this would modulate the beams on the primary resulting in large chopper synchronous offsets. The position of the tertiary was reasonably free once it was decided that cutting a hole in the floor of the telescope hopper was acceptable. However, the tight confines of the secondary support structure severely limited the position of the ACBAR dewar, and thus, the available position and angle of the new tertiary.

The fixed primary waist size constrains the ratio of the effective focal length to the feed waist size. The effective focal length of the system is determined primarily by the location of the tertiary and the distance of the dewar to the tertiary, but this is tightly constrained by the telescope structure. The feed waist size is determined by the feed geometry and should be much larger than the rms spot diameter due to aberrations on the focal plane which depend strongly on optical quality achieved with the tertiary. To get good optical quality on the focal plane the angle of reflection off the tertiary should be as small as possible and the resulting $f/\#$ should be as high as possible. The high effective focal length also reduces the space between beams on the sky for a close packed array by reducing the plate scale. These constraints left little room for optimization but an acceptable tertiary was found which met all of the design criteria within the physical constraints of the telescope.

With most of the physical criteria set, the surface of the tertiary mirror was optimized to produce the best image quality across the focal plane allowing for the greatest number of pixels. For this we used the optical design package CodeV produced by Optical Research Associates¹. CodeV is a ray tracing package with optimization tools that allow you to specify the convergence criteria (such as image distortion and aberrations) for a target solution while specifying the range of multiple physical dimensions.

¹Pasadena, CA 91107

Appendix D Transfer Functions

D.1 Introduction

A time varying optical signal incident upon a system will undergo multiple layers of processing before the signal is written to a data file. Each element filters the oscillations in the signal as a function of frequency. The transfer function quantifies the conversion of a time varying optical signal, $s(t)$, with Fourier transform, $\tilde{s}(\omega)$, incident on the receiver into the recorded signal voltage time stream, $v(t)$. In Fourier space, the effect of the transfer function, $\tilde{f}(\omega)$, is a multiplication given by $\tilde{v}(\omega) = \tilde{f}(\omega)\tilde{s}(\omega)$. The transfer function is a complex quantity with both amplitude and phase and fully describes the attenuation and phase shift of a signal as a function of frequency.

As described below, the transfer function can cause serious distortion of the time stream signal. It must be measured to correct the recorded voltage time stream to recover the incident optical signal by multiplying the Fourier transform of the recorded signal by the inverse of the transfer function, $\tilde{s}(\omega) = \tilde{f}^{-1}(\omega)\tilde{v}(\omega)$. Note that physical filters have a real impulse response, and hence satisfy $\tilde{f}(-\omega) = \tilde{f}(\omega)^*$. This implies that the recorded time stream voltage is also real. The following sections describe the filtering elements of the ACBAR system and their measurement.

D.2 Filters

The ACBAR transfer function can be broken down into different classes of filters: thermal, electrical, and sampling. The first filter element to process incident light is the bolometer. As discussed in the Bolometer section, the frequency response of a bolometer is described by a single-pole filter with a time constant τ_{bolo} ; typical bolometer time constants are of order of a few milliseconds. The frequency response of a single-pole filter is the same as an RC filter with $\tilde{f}(\omega) = 1/(1 + i\omega\tau_{bolo})$. The effects of this filter can be separated into an

amplitude and phase given by

$$f_{\omega} = \frac{1}{\sqrt{1 + (\omega\tau_{bolo})^2}}$$

$$\phi = -\tan^{-1} \omega\tau_{bolo}.$$

Fitting bolometer time constants is described in more detail below.

The bolometer signal voltage then passes along wires to the FETs where the large impedance of the bolometers and capacitance of the wires and FETs form an RC filter with $\tau = RC$. Since we do not know the value of RC *a priori*, we also include it as a parameter in the fit of the transfer function with typical values around 0.2 ms (consistent with a detector impedance of 20 M Ω and capacitance of 10 pF). The signals are buffered by the FETs and then exit the dewar into the readout electronics where they under go amplification and another stage of electrical filtering. The AC filtering stage has an RC filter with a -3dB point at 650 Hz. The -3dB point of a filter is defined to be where the voltage squared (not the voltage) has fallen to half of the peak value. For a filter with a known -3dB point the equivalent time constant is given by $\tau = 1/2\pi\nu_{3dB}$.

Following amplification, the signals then enter the VXI crate where the signal is anti-alias filtered, sampled, averaged, and converted to digital form. The anti-aliasing (AA) filter used for ACBAR is an Agilent¹ E1503A Signal Conditioning Plug-on (SCP) which is a programmable AA filter with -3dB points at 2, 10, and 100 Hz as well as an “unfiltered” mode with cutoff at 1.5 kHz. We operate the filter at the 100 Hz setting during normal operation. The filtering for this module is advertised as a 2-pole Bessel filter but was discovered to be, in fact, only single pole. By plotting the log of the voltage attenuation versus the log of the frequency we found the filter falls off with a slope of -1 and not -2 at high frequency and is well fit by a single RC filter across our signal band. The AA filter also introduces a 25 ms time delay into the data stream which causes a phase shift of $\phi = -\omega T_{delay}$. But because all of our signals and encoders are processed through the same filtering and averaging, we can ignore time delays because they are common to all channels including the chopper position encoder.

After AA filtering the signal is sampled at 2800 Hz and then averaged on 8 samples to reduce the file size as much as possible without aliasing noise into the signal band. The

¹Palo Alto, CA 94303

effect of averaging can be thought of as a convolution of the time stream data with a boxcar average. For example, with a boxcar of length T and a signal $x(t)$ one has

$$y(t') = \frac{1}{T} \int_{t'-T}^{t'} x(t) dt.$$

For an input signal of frequency ω given by $x(t) = e^{i(\omega t + \phi)}$ one gets

$$y(t') = x(t') e^{-i\omega T/2} \frac{\sin(\omega T/2)}{\omega T/2},$$

which has a sinc low-pass filter as well as a phase shift.

The Nyquist frequency is defined as the maximum frequency component that can be fully reconstructed from sampled data and is equal to one half of the sampling rate. The averaging of the sampled signal reduces the Nyquist frequency of our data and results in signal aliasing. This shifts power at frequencies above the Nyquist frequency back into the signal band as well as inverts the phase of the signal. The purpose of the anti-aliasing filter is to reduce high-frequency noise from being aliased into the signal band as much as possible. Aliasing can be understood easily with the following example (provided by Sunil Golwala):

Given a time stream signal, $g(t)$, which has been sampled on interval Δt , the discrete Fourier transform is given by

$$\tilde{g}(\omega_n) = \sum_{k=-(N/2-1)}^{k=N/2} g(t_k) e^{-i\omega_n t_k},$$

where $t_k = k\Delta t$ and $\omega_n = \frac{n2\pi}{N\Delta t}$ with $n \in [-(N/2 - 1), N/2]$. For an excitation with frequency above the Nyquist frequency ($\omega_{nyquist} = \pi/\Delta t$) given by $g(t_k) = \cos(\omega_0 t_k + \phi)$

with $\omega_0 = \frac{N-m}{N} \frac{2\pi}{\Delta t}$ and $m \in [0, N/2 - 1]$, we have

$$\begin{aligned}
 g(t_k) &= \frac{1}{2} \left[e^{i(\omega_0 t_k + \phi)} + e^{-i(\omega_0 t_k + \phi)} \right] \\
 &= \frac{1}{2} \left[e^{i\left(\frac{N-m}{N} \frac{2\pi}{\Delta t} k \Delta t + \phi\right)} + e^{-i\left(\frac{N-m}{N} \frac{2\pi}{\Delta t} k \Delta t + \phi\right)} \right] \\
 &= \frac{1}{2} \left[e^{-i\left(\frac{m}{N} \frac{2\pi}{\Delta t} k \Delta t - \phi\right)} + e^{i\left(\frac{m}{N} \frac{2\pi}{\Delta t} k \Delta t - \phi\right)} \right] \\
 &= \frac{1}{2} \left[e^{-i(\omega_m t_k - \phi)} + e^{i(\omega_m t_k - \phi)} \right] \\
 &= \cos(\omega_m t_k - \phi),
 \end{aligned}$$

where I have used the fact that $e^{i\left(\frac{N}{N} \frac{2\pi}{\Delta t} k \Delta t\right)} = e^{ik2\pi} = 1$. This result shows that a waveform with frequency ω_{N-m} will be aliased to frequency ω_m after sampling. Pay particular note to the fact that the phase of the input waveform has changed sign after aliasing.

By averaging our 2800 Hz sampled data into 8 samples per bin we reduce the Nyquist sampling rate from 1400 Hz to 175 Hz. Figure D.1 shows the effect of averaging and aliasing on the 100 Hz AA filtered data. The signal bandwidth of ACBAR is less than 50 Hz and one can see from the figure that the AA filter knocks down aliased white noise to the level a few percent below 50 Hz. With the addition of the bolometer time constant filtering this is reduced to less than 1% below 50 Hz. Figure D.2 shows the amplitude attenuation and phase shift from all filter elements, as well as the cumulative transfer function from all filters up to the Nyquist frequency, for a model bolometer.

D.3 Transfer Function Measurement

Measuring the transfer function of a system is, in principle, as simple as placing a chopped optical source in front of an instrument and measuring the signal from the data stream as a function of chop frequency. Accomplishing this *in situ* without disturbing the system, such as changing the optical loading by placing a chopped source in front of the instrument, can prove to be difficult. For ACBAR we drilled a small hole (approximately $\varnothing 3/16''$) in the tertiary mirror and mounted a variable frequency chopped load behind it. Although the load provides approximately 200 K of chop, the small size of the hole allows enough signal through without changing the loading on the bolometers appreciably. This chopped source, referred to as the Calibrator, allows us to measure changes in detector responsivity as well

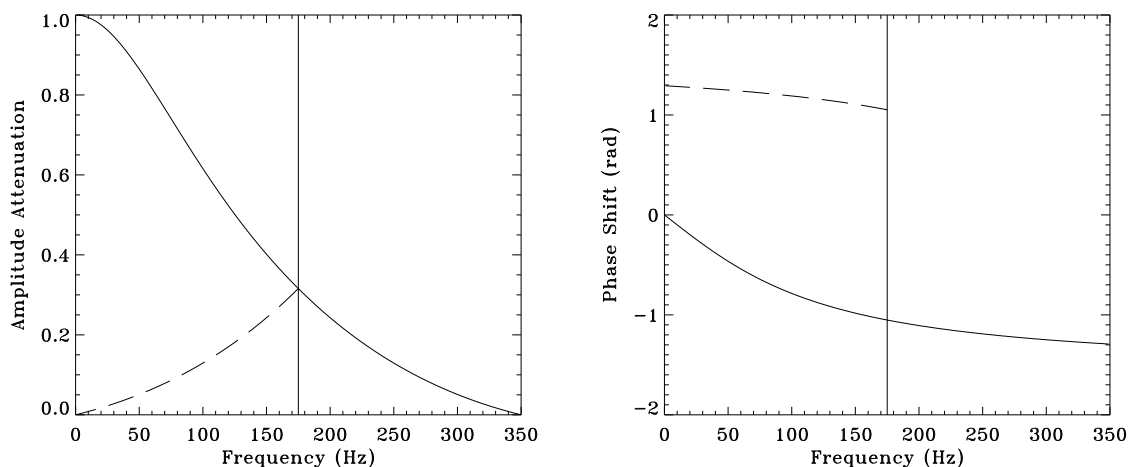


Figure D.1: Transfer function of the VXI electronics including the 100 Hz AA filter and averaging as well as the effects of aliasing for frequencies up to the averaged sample rate (350 Hz). The left panel shows the amplitude of a signal versus measured frequency. The solid line is the filter attenuation and the dashed line shows the aliasing of signals above the Nyquist frequency back into the signal band. The vertical line at 175 Hz denotes the Nyquist frequency. The right panel shows the phase shift for the same data. Notice the phase shift changes sign for aliased frequencies.

as bolometer time constants and the full system transfer function.

To measure the transfer function we turn on the calibrator source and start the chopper wheel spinning. We measure the signal in all detectors for 30 seconds as well as an optical encoder signal from the chopper blade. This is done for chop frequencies from 10 to 160 Hz. The optical encoder signal provides an accurate measurement of the optical chop frequency as well as a phase reference for the bolometer signals. The encoder is physically offset in angle from the wave guide that the optical signal emanates from; this results in a constant phase shift between the encoder signal and bolometers. Since the phase shifts from all filter elements are zero at 0 Hz, this offset is easily fit to and removed from all channels.

A digital frequency lock-in is employed to extract the amplitude and phase of each bolometer from the time stream signal for each chop frequency. A lock-in is a very useful technique to extract small AC signals of known frequency from noisy data. Consider a time varying signal $v(t) = V_0 \cos(\omega t - \phi)$ which is then multiplied by two functions to produce

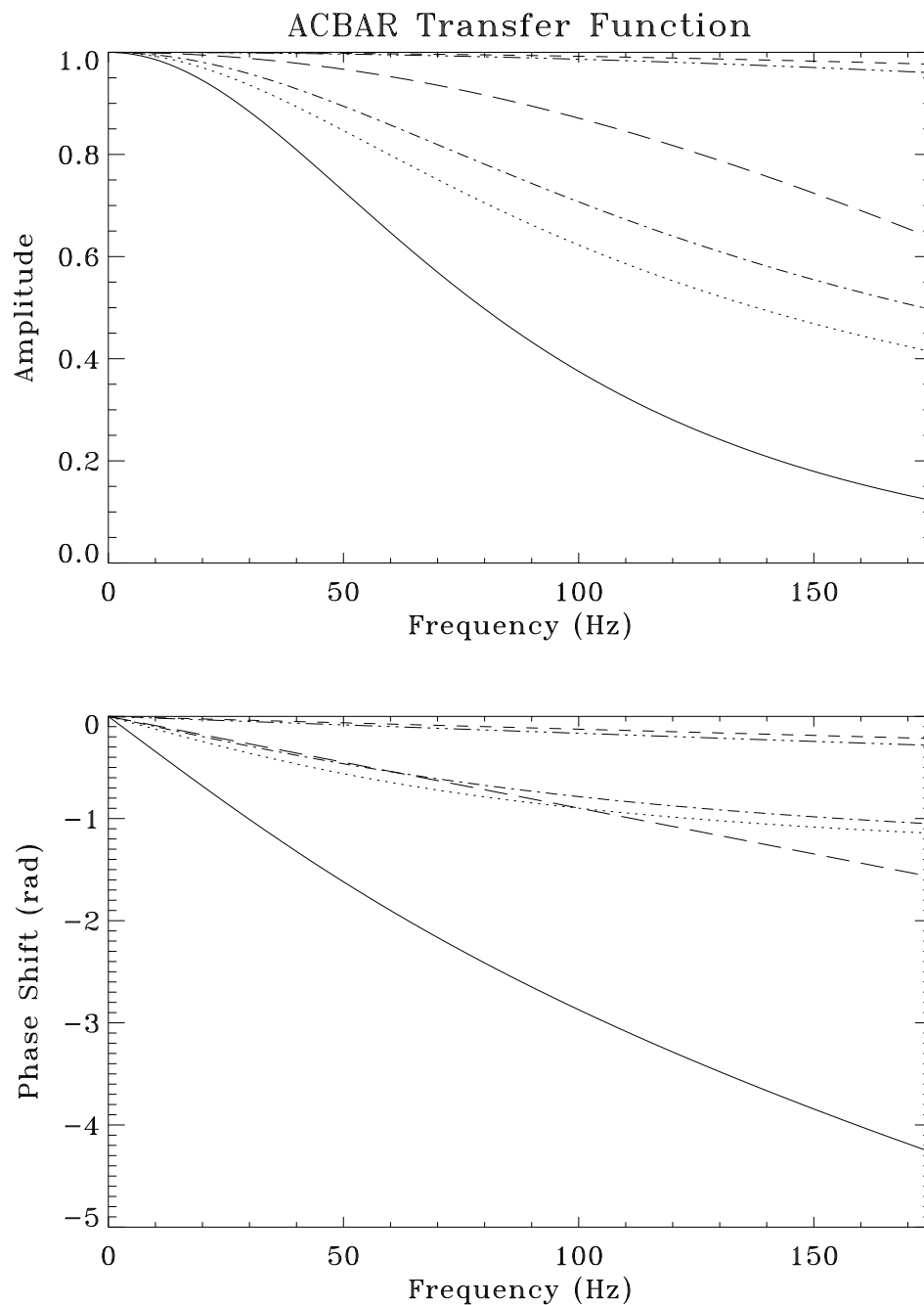


Figure D.2: Amplitude attenuation (upper panel) and phase shift (lower panel) as a function of frequency for all filter elements in the ACBAR signal pipeline for a model $\tau_{bolo} = 2$ ms bolometer with $RC = 0.2$ ms. The curves are bolometer time constant (dotted), RC filtering (dashed), 100 Hz AA filter (dot dashed), 650 Hz AC filter (three dot dashed), sinc filter from averaging (long dashed), and cumulative effect of all five filters (solid).

$$\begin{aligned}
X(t) &= v(t) \cos(\omega't) \\
&= V_0 \cos(\omega t - \phi) \cos(\omega't) \\
&= \frac{V_0}{2} [\cos(\omega t - \phi + \omega't) + \cos(\omega t - \phi - \omega't)] \\
Y(t) &= v(t) \sin(\omega't) \\
&= \frac{V_0}{2} [\sin(-\omega t + \phi + \omega't) + \sin(\omega t - \phi + \omega't)].
\end{aligned}$$

Low-pass filtering these two functions by averaging over a time much longer than ω^{-1} selects the DC component of $X(t)$ and $Y(t)$ with $\omega' = \omega$ resulting in

$$\begin{aligned}
\bar{X} &= \frac{V_0}{2} \cos \phi \\
\bar{Y} &= \frac{V_0}{2} \sin \phi
\end{aligned}$$

and thus

$$\begin{aligned}
\sqrt{\bar{X}^2 + \bar{Y}^2} &= V_0/2 \\
\tan^{-1}(\bar{Y}/\bar{X}) &= \phi.
\end{aligned}$$

Because of the shape of the chopper blade, encoder, and optical signal hole, the harmonic structure of the power spectra of the measured calibrator signal and bolometer signals will differ. However, measuring the transfer function requires knowing the processing of a single frequency component as the frequency is changed. Thus, we select the fundamental frequency of the signal from the calibrator encoder and lock-in to that frequency in the bolometer signals. To determine the fundamental frequency we measure the PSD of the encoder signal and find the peak power. Since we only integrate for 30 seconds the resolution of the PSD is not adequate to accurately determine the fundamental chop frequency. To improve the accuracy, we perform a lock-in on the encoder signal for all frequencies within 0.5 Hz around the PSD peak frequency to determine the actual fundamental frequency value to 1 mHz precision.

With the fundamental chop frequency known, we then measure the amplitude, $A(\omega)$,

and phase, $\phi'(\omega)$, of each bolometer signal as well as the amplitude, $A_{enc}(\omega)$, and phase, $\phi_{enc}(\omega)$, of the encoder signal. We then take the difference of the bolometer and encoder phase to determine their relative phase which removes the phase shift due to the arbitrary start time of each data file,

$$\phi(\omega) = \phi'(\omega) - \phi_{enc}(\omega).$$

The measured transfer function of each bolometer, $A(\omega)$ and $\phi(\omega)$, is the cumulative effects of the bolometer, RC filter of the detector and FETs, AC amplifier filter, anti-aliasing filter, and any low-pass filter from data averaging. Thus, a model of the transfer function must be consistent with both the amplitude attenuation and phase shift produced by all of these elements. Unfortunately, by differencing the phase of the bolometers and optical encoder, we have removed any phase shift common to those channels; this includes the AA filter and averaging phase shifts. To measure the AA filter of the VXI we sent a sine wave into one filtered and one unfiltered channel of system and measured the signal with both averaging on and off for frequencies from 10 to 200 Hz. The AA filter is well fit by a single pole RC filter with -3dB point at 100 Hz and the averaging is well described by the sinc function as described above. This is inconsistent with the manufacture's claim that the AA filter is a 2-pole Bessel filter.

With the effects of these filters known, we then correct the measured transfer function amplitude response, $A(\omega)$, for the attenuation from the AA filter, the 650 Hz AC filter, and the averaging of the VXI crate as well as remove the phase shifts from the AA filter and 650 Hz AC from the measured phase shift function, $\phi(\omega)$. These corrected functions are then simultaneously fit for two one pole filters: the bolometer time constant, τ_{bolo} , and the RC time constant of the detector impedance and the FET and wiring capacitance, τ_{RC} . Figure D.3 shows this fit for a single 150 GHz bolometer and one can see the excellent agreement between amplitude and phase for the two time constant model.

D.4 Effects of Transfer Function

As mentioned previously, the processing of input signals by the system transfer function results in a distortion of the measured time stream data. These effects are well illustrated by the impulse response of the system which is the time response to a delta function input signal. The processed signal that will be recorded for a given input signal is determined by

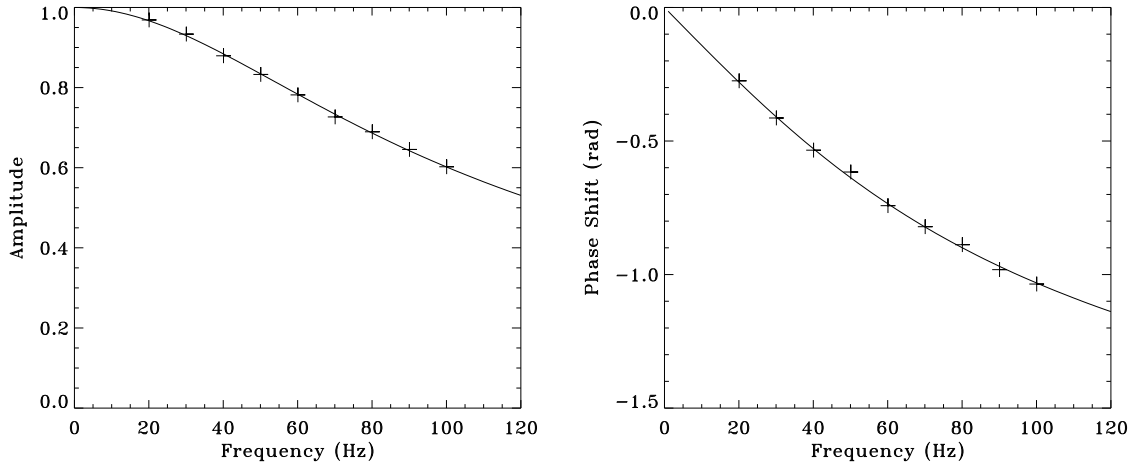


Figure D.3: Amplitude attenuation (left panel) and phase shift (right panel) as a function of frequency for a 150 GHz bolometer after correcting for all filters but bolometer time constant and a residual RC filter. The pluses are the data and the solid line is a fit with bolometer time constant $\tau_{bolo} = 2.1$ ms and $\tau_{RC} = 0.2$ ms.

convolving the impulse response of the system with the time stream data.

The convolution theorem states that the Fourier transform of the convolution of two functions is equal to the product of their Fourier transforms [90]. Specifically, for functions $g(t)$ and $h(t)$, with respective Fourier transforms $G(\omega)$ and $H(\omega)$, the convolution theorem states

$$g \star h = \int_{-\infty}^{\infty} g(\tau)h(t - \tau)d\tau$$

$$g \star h \iff G(\omega)H(\omega),$$

where the \iff indicates Fourier transform. Using the convolution theorem with one function as a delta function to represent the time stream impulse, we see that the impulse response of the system is the inverse Fourier transform of the frequency response transfer function. The impulse response of ACBAR with a few bolometer time constants is shown in Figure D.4. One notices the long delay introduced by the system which is irrelevant to the data analysis since all channels suffer the same delay and can be neglected. The signal then rises rapidly and decays with a time constant that depends strongly on the speed of the bolometer.

When the beams are scanned across a source, the impulse response will smear out signal

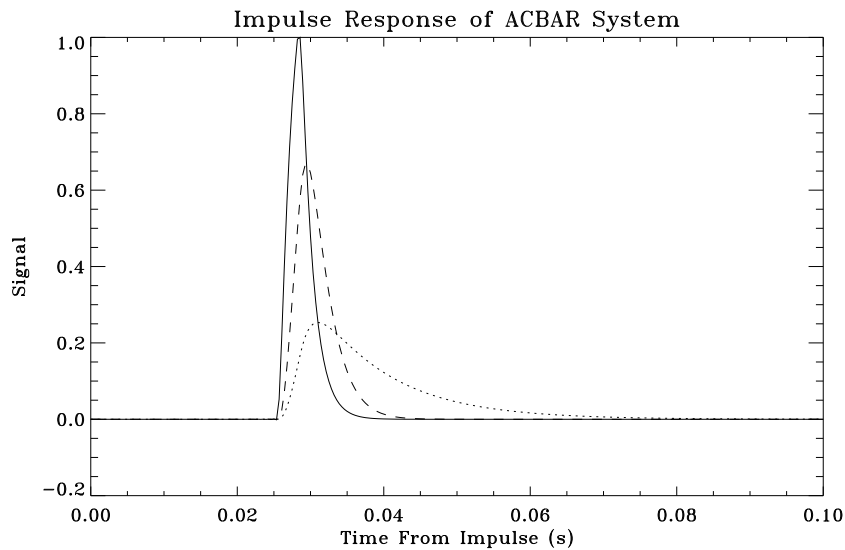


Figure D.4: The impulse response of the ACBAR system for various bolometer time constants. The solid line is for an infinitely fast bolometer ($\tau_{bolo} = 0$ ms), the dashed line has $\tau_{bolo} = 2$ ms, and the dotted line has $\tau_{bolo} = 10$ ms. One can see that the delta function impulse can become severely distorted in the time stream when detector time constants are large.

to a degree which depends on the scan velocity. Faster scan speeds push more of the signal bandwidth to higher frequencies which causes more signal distortion. Figure D.5 shows the effect of scan velocity on a Gaussian beam for a pair of detector time constants.

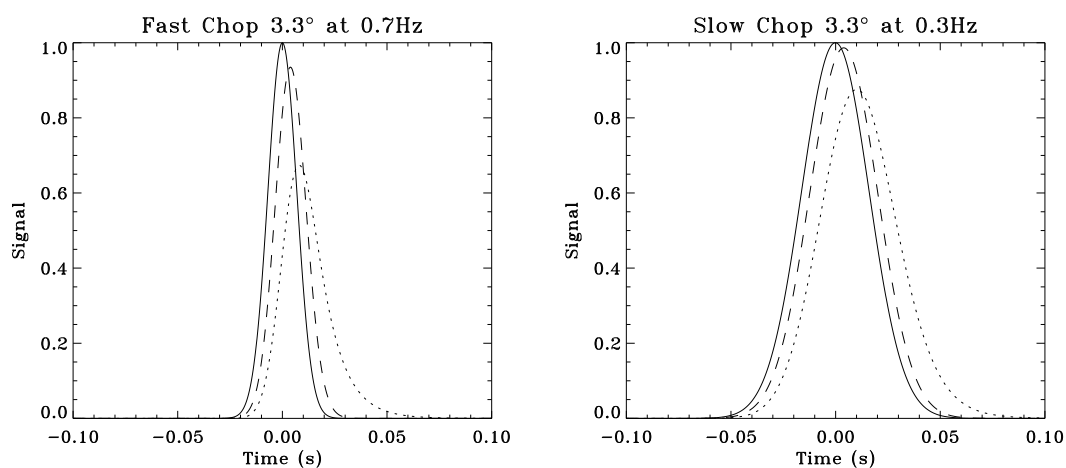


Figure D.5: The effects of scan velocity and detector time constant are illustrated in these two plots. A model 4.5' beam is scanned across a point source at a fast chop velocity of 3.3° amplitude at 0.7 Hz (left panel) and a slow chop velocity of 3.3° at 0.3 Hz. The solid line is the unfiltered time stream data, the dashed line is the response of the ACBAR system with a 2 ms bolometer, and the dotted line is for a 10 ms bolometer. One can see that the 10 ms signal is significantly reduced in amplitude and broadened in extent whereas the 2 ms bolometer suffers very little distortion.

Appendix E CMB Realizations

We need to generate realizations of the CMB and correlated instrument noise for Monte Carlo simulations of cluster detection efficiency and false detection rates. Here we present two methods to generate realizations of the CMB given a power spectrum; the first method can also be used to generate realizations of noise if the covariance matrix is known. These methods are derived from useful discussions with Ken Ganga, Eric Hivon, and Chao-lin Kuo.

E.1 Correlation Function Method

As mentioned above, we can generate the covariance matrix of the CMB, C_{mn}^{CMB} , from the correlation function, $C^{CMB}(\theta)$. To generate the covariance matrix for a map on the sky with pixel positions $\{\vec{\theta}_m\}$ we start by rearranging the pixels into one long vector and calculate the matrix Θ_{mn} which is equal to the angular separation on the sky of each pair of pixels,

$$\Theta_{mn} = |\vec{\theta}_m - \vec{\theta}_n|.$$

Using the correlation function of the CMB generated from a given power spectrum and window function,

$$C^{CMB}(\theta) = \frac{1}{4\pi} \sum_{\ell} (2\ell + 1) C_{\ell} W_{\ell} P_{\ell}(\cos \theta),$$

the CMB covariance matrix is simply

$$C_{mn}^{CMB} = C^{CMB}(\Theta_{mn}).$$

For an ensemble of measurements on sky $\{\Delta T_m\}$ at positions $\{\vec{\theta}_m\}$, we can arrange the temperature measurements into a long vector $\vec{\Delta T}$ and the covariance matrix is given by the ensemble average of the vector product of $\vec{\Delta T}$ with itself,

$$C_{mn} = \left\langle \Delta \vec{T} \Delta \vec{T}^T \right\rangle_{mn}.$$

Since the covariance matrix is symmetric with positive definite eigenvalues, we can find the “square root” of the matrix via Cholesky Decomposition [90] into two tridiagonal matrices

$$C = LL^T.$$

If we generate a normally distributed random vector, \vec{x} , with unity RMS and zero mean and the same length as $\vec{\Delta T}$, then the ensemble average of the vector product of \vec{x} will satisfy $\langle \vec{x}\vec{x}^T \rangle = I$, where I is the unity identity matrix.

Inserting this into the covariance equation above we have

$$\begin{aligned} C &= LL^T \\ &= LIL^T \\ &= L \langle \vec{x}\vec{x}^T \rangle L^T \\ &= \langle (L\vec{x})(L\vec{x})^T \rangle \\ &= \langle \vec{\Delta T}\vec{\Delta T}^T \rangle, \end{aligned}$$

from which we claim that the model temperature map $\vec{\Delta T}_{model} = L\vec{x}$ will have exactly the same ensemble average covariance matrix as the input correlation function. This equation is quite remarkable because it shows that once the matrix L has been determined, a realization of the CMB sky is generated by merely multiplying this matrix times a random vector of the appropriate length. One should also note that this formalism works equally well for any covariance matrix including the noise covariance matrix. This means we can generate realizations of the noise – including any pixel-to-pixel correlations – once we determine the square root matrix L of the measured noise covariance matrix.

Generating realizations of the CMB this way can be remarkably difficult for large map sizes because we must include correlations in both RA and DEC. If we consider generating CMB realizations that are the same size as our raster maps, $180' \times 103'$, then with $1'$ pixel resolution we will have 18,540 pixels on the sky which translates into a floating point covariance matrix occupying approximately 1.4 GB of memory; certainly an unwieldy object to store, let alone perform Cholesky decomposition upon. The situation is much simplified for generating noise realizations for ACBAR because the only non-zero correlations occur within rows, and thus, the covariance matrix is block diagonal. The memory requirements

for a block diagonal matrix based on the raster map dimensions given above is a mere 13 MB. What is even more useful is that, because the covariance matrix is block diagonal, Cholesky decomposition need only be performed on the sub-matrices which are only 180×180 in size. If we assume a common correlation function for all rows in the map, we only need to perform Cholesky decomposition on one of these sub-matrices to generate the full noise realization for the raster map.

E.2 FFT Method

The angular power spectrum is the ensemble average of the coefficients of the spherical harmonic decomposition of the sky. However, for a small enough patch of sky, realizations of the CMB can be generated with the FFT which is much faster than the correlation function method and consumes much less memory. For a given CMB angular power spectrum one generates the spatial power spectrum, $P^{CMB}(\vec{q})$, via the method given in the previous section. For the realizations presented here, we omit the beam window function from the CMB power spectrum and instead convolve the resulting maps with a Gaussian of the appropriate width.

Next, we specify the number of pixels (N_x, N_y) and pixel resolution of the map ($\Delta\theta_x, \Delta\theta_y$) in both the \hat{x} and \hat{y} directions. The corresponding spatial frequency vectors are then

$$q_x^i = 2\pi \frac{(i - N_x/2)}{N_x \Delta\theta_x},$$

where i runs from 0 to N_x , and similarly for \hat{y} . Note that the resolution in spatial frequency is determined by the size of the map in each direction and is given by

$$\Delta q_x = \frac{2\pi}{N_x \Delta\theta_x}.$$

For a full-sky map we have $N_x \Delta\theta_x = 2\pi$ and so the resolution is $\Delta q = 1 \text{ rad}^{-1}$ (corresponding to $\Delta\ell = 1$).

The CMB is believed to be a Gaussian random field which means that its Fourier components are complex and are drawn from independent normal distributions [see, for example, Liddle and Lyth (2000)]. The value of the real, $R_{\vec{q}}$, and imaginary, $I_{\vec{q}}$, parts of

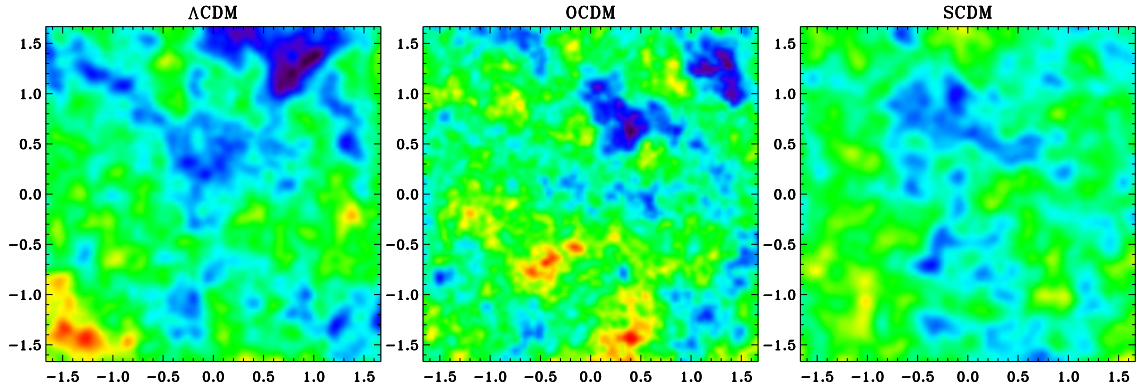


Figure E.1: Shows $3.3^\circ \times 3.3^\circ$ simulations of the CMB for Λ CDM (left), OCDM (middle), and SCDM (right) cosmologies. The scale in the figures is $\pm 400 \mu\text{K}$. Note the excess of small-scale structure in the OCDM simulation. The axes are both in degrees.

each point in Fourier space, \vec{q} , are drawn from the same distributions and satisfy

$$\sigma_{\vec{q}}^2 = \langle R_{\vec{q}}^2 \rangle = \langle I_{\vec{q}}^2 \rangle = P_{\vec{q}}^{CMB} \Delta q_x \Delta q_y / 2 .$$

For each point in Fourier space we generate a random value for the real and imaginary terms and combine them to form the Fourier space map

$$\tilde{\Delta T}_{\vec{q}} = R_{\vec{q}} + i I_{\vec{q}} .$$

The real-space temperature map must be purely real and so the Fourier space map must satisfy the condition

$$\tilde{\Delta T}_{-\vec{q}} = \tilde{\Delta T}_{\vec{q}}^* .$$

One then takes the inverse Fourier transform of the $\tilde{\Delta T}_{\vec{q}}$ field to produce the realization of the CMB. Examples of CMB realizations generated with this method are shown in Figure E.1 for Λ CDM, SCDM, and OCDM cosmologies. The input CMB power spectra used to generate these CMB realizations were generated with CMBFAST. One can see from these figures that the OCDM realization has significantly more small-scale structure than the spatially flat cosmologies as expected from their power spectra (refer to Figure 1.1).

Fourier transforms assume periodicity in the map and so the maps generated in this manner can be shifted by any amount in any direction and remain smoothly varying. On the other hand, if we want to measure the spatial power spectrum of a CMB map by inverting

this procedure, it is unlikely that the map will satisfy the periodic boundary conditions. To solve this problem we can apply an apodizing window (e.g., Hanning window) to the map which will taper to zero at the map edges and mitigate the effects of aperiodicity [90].

Bibliography

- [1] G. O. Abell, H. G. Corwin, and R. P. Olowin, *Astrophysical Journal Supplement Series*, **70**, 1 (1989).
- [2] E. Anders and N. Grevesse, *Geochimica et Cosmochimica Acta*, **53**, 197 (1989).
- [3] N. A. Bahcall, in “Large Scale Structure: Tracks and Traces, Proceedings of the 12th Potsdam Cosmology Workshop,” V. Mueller, S. Gottloeber, J. P. Muecket, J. Wambsganss Eds., World Scientific, 137 (1998).
- [4] N. A. Bahcall et al., astro-ph/0205490, (2002).
- [5] J. G. Bartlett and J. Silk, *Astrophysical Journal*, **423**, 12 (1994).
- [6] A. J. Beasley et al., *Astronomy and Astrophysics Supplement Series*, **124**, 469 (1997).
- [7] A. Benoit et al., astro-ph/0210305, submitted to *Astronomy and Astrophysics Letters*, (2002).
- [8] A. J. Benson, C. Reichardt, and M. Kamionkowski, *Monthly Notices of the Royal Astronomical Society*, **331**, 71 (2002).
- [9] R. S. Bhatia et al., *Cryogenics*, **40** 685 (2000).
- [10] M. Birkinshaw, *Physics Reports*, **310**, 98 (1999).
- [11] A. W. Blain et al., *Astrophysical Journal*, **512**, 2 (1999).
- [12] J. J. Bock, PhD thesis, University of California at Berkeley (1994).
- [13] H. Böhringer et al., *Astronomy and Astrophysics*, **369**, 826 (2001).
- [14] J. R. Bond and G. Efstathiou, *Monthly Notices of the Royal Astronomical Society*, **226**, 655 (1987).
- [15] J. R. Bond et al., astro-ph/0205386, submitted to *Astrophysical Journal* (2002).

- [16] J. E. Carlstrom, G. P. Holder, and E. D. Reese, *Annual Review of Astronomy and Astrophysics*, **40**, 643 (2002).
- [17] S. E. Church et al., in *Proc. 30th ESLAB Symp. Submillimetre and Far-Infrared Space Instrumentation*, ESTEC, Noordwijk, Netherlands, ESA SP-388 (1996).
- [18] S. E. Church, private communication (1996).
- [19] S. E. Church et al., *Astrophysical Journal*, **484**, 523 (1997).
- [20] P. J. B. Clarricoats and P. K. Saha, *Electronics Letters*, **5**, 592 (1969).
- [21] P. J. B. Clarricoats and A. D. Olver, *Corrugated Horns for Microwave Antennas*, IEE Electromagnetic Wave Series 18, Peter Peregrinus (1984).
- [22] G. Cotter et al., *Monthly Notices of the Royal Astronomical Society*, **331**, 1 (2002).
- [23] K. S. Dawson et al., astro-ph/0206012, (2002).
- [24] J. L. Dotson et al., in “Advanced Technology MMW, Radio, and Terahertz Telescopes,” T. G. Phillips, Ed., Proc. SPIE **3357**, 543 (1998).
- [25] L. DuBond, priv. communication.
- [26] V. R. Eke, S. Cole, and C. S. Frenk, *Monthly Notices of the Royal Astronomical Society*, **282**, 263 (1996).
- [27] V. R. Eke et al., *Monthly Notices of the Royal Astronomical Society*, **298**, 1145 (1998).
- [28] D. P. Finkbeiner, M. Davis, and D. J. Schlegel, *Astrophysical Journal*, **524**, 2 (1999).
- [29] FLUXES JCMT Position and Flux Density Calibration Software (available at <http://www.starlink.rl.ac.uk>).
- [30] W. L. Freedman et al. *Astrophysical Journal*, **553**, 47 (2001).
- [31] J. Glenn et al., in “Advanced Technology MMW, Radio, and Terahertz Telescopes,” Phillips T.G. ed., *Proceedings of the SPIE*, **3357**, 326 (1998).
- [32] P. F. Goldsmith, “Quasioptical Systems: Gaussian Beam Quasioptical Propagation and Applications,” IEEE Press, Piscataway, NJ (1998).

- [33] J. H. Goldstein et al., in preperation (2002).
- [34] P. L. Gomez et al., in "Matter and Energy in Clusters of Galaxies," ASP in press (2003).
- [35] S. M. Grannan, A. E. Lange, E. E. Haller, and J. W. Beeman, *Physical Review B*, **45**, 4516 (1992).
- [36] L. Grego et al., *Astrophysical Journal*, **552**, 2 (2001).
- [37] M. J. Griffin et al., *Icarus*, **65**, 244 (1986).
- [38] M. J. Griffin and W. S. Holland, *International Journal of Infrared and Millimeter Waves*, **9**, 861 (1988).
- [39] M. R. Griffith et al., *Astrophysical Journal Supplement Series*, **90**, 179 (1994).
- [40] E. Grossman, "AT User's Manual," Airhead Software, Boulder, CO 80302 (1989).
- [41] M. Guelin, in "Millimeter Interferometry: Proceedings of the IRAM Millimeter Interferometry Summer School," S. Guilloteau, Ed., Institut de Radio Astronomie Millimetrique, p.79 (1999).
- [42] S. Hanany et al., *Astrophysical Journal*, **545**, 5 (2000).
- [43] J. P. Henry et al., *Astrophysical Journal*, **386**, 408 (1992).
- [44] D. Herranz et al., *Astrophysical Journal*, **580**, 610 (2002).
- [45] M. P. Hobson and C. McLachlan, astro-ph/0204457, (2002).
- [46] G. P. Holder and J. E. Carlstrom, in "Microwave Forgrounds," A. de Oliveira-Costa and M. Tegmark eds., (ASP, San Francisco, 1999)
- [47] G. P. Holder et al., *Astrophysical Journal*, **544**, 629 (2000).
- [48] G. P. Holder, Z. Haiman, and J. J. Mohr, *Astrophysical Journal*, **560**, 111 (2001).
- [49] W. L. Holzapfel et al., *Astrophysical Journal*, **481**, 35 (1997).
- [50] W. L. Holzapfel et al., *Astrophysical Journal*, **539**, 57 (2000).

- [51] W. L. Holzapfel et al., *Astrophysical Journal*, **539**, 67 (2000).
- [52] D. Huterer and M. S. Turner, *Physical Review*, **D64**, 123527 (2001).
- [53] W. Hu, N. Sugiyama, and J. Silk, *Nature*, **386**, 37 (1997).
- [54] IRAS Point Source Catalog, Joint IRAS Science Working Group, ver2.0, NASA RP-1190 (1988).
- [55] A. Jenkins et al., *Monthly Notices of the Royal Astronomical Society*, **321**, 372 (2001).
- [56] W. C. Jones et al., astro-ph/0209132 (2002).
- [57] S. T. Kay, A. R. Liddle, and P. A. Thomas, *Monthly Notices of the Royal Astronomical Society*, **325**, 835 (2001).
- [58] R. S. J. Kim et al., *Astronomical Journal*, **123**, 20 (2002).
- [59] C. L. Kuo et al., in preparation (2002).
- [60] A. P. Lane, in “Astrophysics From Antarctica,” G. Novak and R. Landsberg, Eds., ASP Conference Series, **141**, 289 (1998).
- [61] O. P. Lay and N. W. Halverson, *Astrophysical Journal*, **543**, 787 (2000).
- [62] C. Lee et al., *Proc. 30th ESLAB Symp. Submillimetre and Far-Infrared Space Instrumentation*, ESTEC, Noordwijk, Netherlands, ESA SP-388 (1996).
- [63] E. M. Leitch et al., *Astrophysical Journal*, **532**, 37 (2000).
- [64] J. R. Leong, Senior thesis, California Institute of Technology (2001).
- [65] A. R. Liddle and D. H. Lyth, “Cosmological Inflation and Large-Scale Structure,” Cambridge University Press (2000).
- [66] A. R. Liddle et al., *Monthly Notices of the Royal Astronomical Society*, **325**, 875 (2001).
- [67] H. Lin, T. Chiueh, and X. P. Wu, astro-ph/0202174 (2002).
- [68] Y. T. Lin and J. J. Mohr, astro-ph/0208005, submitted to ApJ (2002).

- [69] E. L. Lokas and Y. Hoffman, in “Proceedings of the 3rd International Workshop on the Identification of Dark Matter,” N. J. C. Spooner & V. Kudryavtsev eds., World Scientific, Singapore, p121 (2001).
- [70] Microwave Anisotropy Probe, (<http://map.gsfc.nasa.gov>).
- [71] B. Mason, 1999, PhD thesis, University of Pennsylvania (1999).
- [72] B. Mason et al., astro-ph/0205384, (2002).
- [73] J. Mather, *Applied Optics*, **23**, 584 (1984).
- [74] J. C. Mather et al., *Astrophysical Journal*, **420**, 439 (1994).
- [75] P. D. Mauskopf et al., *Applied Optics*, **36**, 765 (1997).
- [76] J. J. Mohr and A. E. Evrard, *Astrophysical Journal*, **491**, 38 (1997).
- [77] J. J. Mohr, B. Mathiesen, and A. E. Evrard, *Astrophysical Journal*, **517**, 627 (1999).
- [78] J. J. Mohr et al., in “Extrasolar Planets to Cosmology: The VLT Opening Symposium, Proceedings of the ESO Symposium held at Antofagasta, Chile,” Jacqueline Bergeron and Alvio Renzini eds., Springer-Verlag, p150 (2000).
- [79] J. J. Mohr et al., astro-ph/0208102, (2002).
- [80] J. J. Mohr, private communication, (2002).
- [81] NASA/IPAC Extragalactic Database (<http://ned.ipac.caltech.edu>), operated by the Jet Propulsion Laboratory, California Institute of Technology.
- [82] C. B. Netterfield et al., *Astrophysical Journal*, **571**, 604 (2002).
- [83] S. Padin et al., *The Publications of the Astronomical Society of the Pacific*, **114**, 83 (2002).
- [84] P. J. E. Peebles, *Principles of Physical Cosmology*, Princeton University Press (1993).
- [85] P. J. E. Peebles, astro-ph/0208037, (2002).
- [86] S. Perlmutter et al., *Astrophysical Journal*, **517**, 565 (1999).

- [87] J. B. Peterson et al., *Astrophysical Journal*, **532**, 83 (2000).
- [88] B. J. Philhour, PhD thesis, California Institute of Technology (2002).
- [89] W. H. Press and P. Schechter, *Astrophysical Journal*, **187**, 452 (1974).
- [90] W. H. Press, S. A. Teukolsky, W. T. Vetterling, and B. P. Flannery, “Numerical Recipes in C,” Cambridge University Press (1992).
- [91] C. Pryke et al., *Astrophysical Journal*, **568**, 46 (2002).
- [92] J. L. Puchalla et al., *Astronomical Journal*, **123**, 1978 (2002).
- [93] S. Radford, in “Astronomical Site Evaluation in the Visible and Radio Range,” ASP Conf. Ser. 266, J. Vernin, Z. Benkhaldoun, and C. Munoz-Tunon, Eds., 148 (2002).
- [94] A. C. S. Readhead et al., *Astrophysical Journal*, **346**, 566 (1989).
- [95] E. D. Reese, PhD thesis, The University of Chicago, (2002).
- [96] T. H. Reiprich and H. Böhringer, *Astrophysical Journal*, **567**, 716 (2002).
- [97] P. L. Richards, *Journal of Applied Physics*, **76**, 1 (1994).
- [98] A. K. Romer, The Viper SZ Cluster Survey (<http://astrophysics.phys.cmu.edu/research/viper/vszs/>).
- [99] A. K. Romer et al., *Astrophysical Journal*, **547**, 594 (2001).
- [100] P. Rosati, S. Borgani, and C. Norman, *Annual Reviews of Astronomy and Astrophysics*, **40**, 539 (2002).
- [101] J. E. Ruhl et al., in preparation (2002).
- [102] U. Seljack and M. Zaldarriaga, *Astrophysical Journal*, **469**, 437 (1996).
- [103] R. K. Sheth and G. Tormen, *Monthly Notices of the Royal Astronomical Society*, **308**, 119 (1999).
- [104] A. E. Schulz and M. White, astro-ph/0210667, (2002).
- [105] P. F. Scott, et al., astro-ph/0205380, submitted to *Monthly Notices of the Royal Astronomical Society* (2002).

- [106] S. W. Smith, "The Scientist and Engineer's Guide to Digital Signal Processing," California Technical Publishing, (<http://www.dspguide.com>) (1997).
- [107] R. A. Sunyaev and Ya. B. Zel'dovich, *Comments on Astrophysics and Space Physics*, **4**, 173 (1972).
- [108] J. R. Taylor, "An Introduction to Error Analysis," University Science Books, Sausalito, CA (1997).
- [109] M. Tegmark and G. Efstathiou, *Monthly Notices of the Royal Astronomical Society*, **281**, 1297 (1996).
- [110] M. Tornikowski et al., *Astronomy and Astrophysics Supplement Series*, **116**, 157 (1996).
- [111] M. Tornikowski, M. Lainela, and E. Valtaoja, *Astronomical Journal*, **120**, 2278 (2000).
- [112] A. D. Turner et al., *Applied Optics*, **40**, 4921 (2001).
- [113] J. A. Tyson, D. M. Wittman, J. R. P. Angel, "Gravitational Lensing: Recent Progress and Future Goals," ASP Conference Proceedings, **237**, T. G. Brainerd and C. S. Kochanek, Eds. Astronomical Society of the Pacific, p.417 (2001).
- [114] D. Tytler, J. M. O'Meara, N. Suzuki, and D. Lubin, *Physics Reports*, **333**, 409 (2000).
- [115] P. S. Udomprasert, B. S. Mason, A. C. S. Readhead, in "New Century of X-ray Astronomy", ASP Conference Proceedings Vol. 251, H. Inoue and H. Kunieda, Eds. Astronomical Society of the Pacific, (2001).
- [116] B. L. Ulich, *The Astronomical Journal*, **86**, 1619 (1981).
- [117] P. T. P. Viana and A. R. Liddle, *Monthly Notices of the Royal Astronomical Society*, **281**, 323 (1996).
- [118] P. T. P. Viana and A. R. Liddle, *Monthly Notices of the Royal Astronomical Society*, **303**, 535 (1999).
- [119] E. W. Weisstein, PhD thesis, California Institute of Technology (1996).
- [120] M. White, astro-ph/0207185, (2002).

- [121] R. J. Wylde, *IEE Proceedings, Part H - Microwaves, Optics and Antennas*, **131**, 258 (1984).
- [122] J. Xu, A. E. Lange, and J. J. Bock, in *Proc. 30th ESLAB Symp. Submillimetre and Far-Infrared Space Instrumentation*, ESTEC, Noordwijk, Netherlands, ESA SP-388 (1996).
- [123] Y. Yamada, A. Mitsuishi, and H. Yoshinaga, *Journal of the Optical Society of America*, **52**, 17 (1962).
- [124] X. Zhang, *IEEE Transactions on Microwave Theory and Techniques*, **41** 1263 (1993).